

# Droplet Deposition and Evaporation Dynamics on Chemically and Topographically Patterned Surfaces

Frankie Felix Jackson

Submitted in accordance with the requirements for the degree  
of  
Doctor of Philosophy



The University of Leeds  
School of Mechanical Engineering  
September 2021

The candidate confirms that the work submitted is his own, except where work which has formed part of jointly authored publications has been included. The contribution of the candidate and the other authors to this work has been explicitly indicated below. The candidate confirms that appropriate credit has been given within the thesis where reference has been made to the work of others.

Part of the work in Chapter 6 is based on a jointly authored publication: *Droplet Misalignment Limit for Inkjet Printing into Cavities on Textured Surfaces* published in *Langmuir* July 9<sup>th</sup> 2019. The authors include **Frankie Felix Jackson**, Krzysztof J. Kubiak, Mark C. T. Wilson, Marco Molinari, and Viacheslav Stetsyuk. I was responsible for developing the numerical models, gathering and processing data, and writing the manuscript. The contribution of the other authors was to provide guidance while producing the manuscript as well as check for grammatical/ spelling and typing errors.

This copy has been supplied on the understanding that it is copyright material and that no quotation from the thesis may be published without proper acknowledgement.

The right of Frankie Felix Jackson to be identified as Author of this work has been asserted by him in accordance with the Copyright, Designs and Patents Act 1988.

---

## Acknowledgements

---

I would like to sincerely thank my supervisors Dr Kryzstof Kubiak and Dr Mark C. T. Wilson. Both have provided tremendous support throughout my PhD. It is no understatement to say that this PhD would not have been possible without their guidance and feedback over the last few years. I would also like to extend my thanks to Dr Marco Molinari and Dr Viacheslav Stetsyuk, as their engagement in the first year of my research was extremely valuable.

I would especially like to thank my friends and fellow PhD students who have made the journey a thoroughly enjoyable experience.

Finally, a special thanks to my family. Their unwavering support and encouragement are truly appreciated now and forever.

---

## Abstract

---

Inkjet printing is a promising alternative technique for the fabrication of functional devices such as organic light emitting diode displays. However, with ever increasing requirements for finer display resolutions, it becomes increasingly challenging to precisely position inkjet printed droplets. Even once the droplet is in the required location, there are challenges in achieving a uniform particle deposit of the functional material, once the solvent evaporates.

In this thesis, a multiphase lattice Boltzmann method is used to investigate the deposition processes of droplets deposited into idealised pixel geometries (square cavities). Specific attention is given to droplets deposited with positioning errors, to see which factors have the greatest influence on the droplets ability to self-align. Additionally, the model is coupled with an energy equation to investigate cavity properties on evaporation rate, internal flows, and particle deposition.

A review of different multiphase models leads to the choice of the pseudopo-

tential method, as recent developments allow for the simulation of moderate density ratios, thermodynamic consistency, and the ability to couple with an energy equation to simulate thermal flows with phase change. Implementation is then discussed, with attention given to parallelising the multiphase algorithm to run on high-performance computers.

Different wetting models are evaluated, and a new model is suggested, which allows for additional control of adhesive forces over the liquid-vapour interface. Furthermore, the importance of boundary treatment in computing the pseudopotential forces is highlighted.

The new wetting model is used to explore the limits of positioning error for the deposition of droplets into square cavities. A regime map is suggested which highlights the conditions required for print success, relating droplet size, cavity size, and printer positioning errors.

Finally, investigations of evaporation in heated square cavities show the influence of receding contact angle on evaporation rate, internal flows, and particle deposition.

---

## Contents

---

<b>1</b>	<b>Introduction</b>	<b>1</b>
1.1	Motivation . . . . .	1
1.2	Inkjet Printing . . . . .	2
1.2.1	Ink Requirements . . . . .	6
1.3	Wetting and Evaporation . . . . .	6
1.3.1	Evaporation and Particle Deposits . . . . .	10
1.4	Numerical Modelling of Fluids . . . . .	12
1.4.1	Continuum-based Solvers . . . . .	12
1.4.2	Particle-based Solvers . . . . .	13
1.4.3	Numerical Modelling of Inkjet Printed Droplets . . . . .	15
1.4.4	Modelling Approach . . . . .	16
1.5	Aim and Objectives . . . . .	18
1.5.1	Aim . . . . .	18
1.5.2	Objectives . . . . .	18
1.6	Thesis Layout . . . . .	18

<b>2</b>	<b>The Lattice Boltzmann Method</b>	<b>20</b>
2.1	Background of the LBM . . . . .	20
2.1.1	Cellular Automata . . . . .	20
2.1.2	Lattice Gas Cellular Automata . . . . .	23
2.2	Theoretical Basis of the Lattice Boltzmann Method . . . . .	24
2.2.1	The Discrete Lattice Boltzmann Method . . . . .	27
2.2.2	Chapman-Enskog Expansion . . . . .	32
2.3	Model Extensions . . . . .	37
2.3.1	Multiple Relaxation Time Modelling . . . . .	37
2.3.2	Entropic Lattice Boltzmann Model . . . . .	41
2.4	Thermal Extension of the LBM . . . . .	42
2.5	Chapter Summary . . . . .	43
<b>3</b>	<b>Multiphase Lattice Boltzmann Modelling</b>	<b>44</b>
3.1	Introduction . . . . .	44
3.2	Multiphase and Multicomponent Modelling . . . . .	45
3.2.1	Colour Modelling . . . . .	45
3.2.2	Free-Energy Modelling . . . . .	50
3.2.3	He-Chen-Zhang Modelling . . . . .	53
3.3	Shan-Chen Pseudopotential Method . . . . .	58
3.3.1	Thermodynamic Consistency . . . . .	61
3.3.2	Strengths and Weaknesses . . . . .	67
3.4	Thermal Multiphase Modelling . . . . .	69
3.5	Chapter Summary . . . . .	70
<b>4</b>	<b>Numerical Implementation</b>	<b>72</b>
4.1	Introduction . . . . .	72
4.2	Non-Dimensionalisation . . . . .	73

4.2.1	Conversion Factors . . . . .	74
4.3	Boundary and Initial Conditions . . . . .	76
4.3.1	Periodic Boundary . . . . .	76
4.3.2	No-Slip Boundary . . . . .	77
4.3.3	Open Boundary . . . . .	79
4.3.4	Symmetry Boundary . . . . .	80
4.3.5	Initial Conditions . . . . .	82
4.4	Computing Performance: Parallelisation . . . . .	85
4.5	Hydrodynamic Boundary Validation . . . . .	91
4.5.1	Multiphase Convergence . . . . .	91
4.5.2	Flow in a Square Duct: Gravity Driven . . . . .	92
4.5.3	Flow in a Square Duct: Pressure Driven . . . . .	94
4.6	Chapter Summary . . . . .	96
<b>5</b>	<b>Wetting Model Evaluation and Development</b>	<b>98</b>
5.1	Introduction . . . . .	98
5.2	Multiphase Wetting Modelling . . . . .	99
5.2.1	Existing Wetting Models . . . . .	100
5.2.2	New Wetting Model . . . . .	101
5.2.3	Boundary Treatment . . . . .	103
5.3	Evaluation of Wetting Models . . . . .	105
5.3.1	Equilibrium Contact Angles on Homogeneous Surface . . . . .	106
5.3.2	Simulation Configuration . . . . .	108
5.3.3	Spurious Velocities . . . . .	120
5.3.4	Maximum and Minimum Densities . . . . .	124
5.3.5	Spreading on a Homogeneous Surface . . . . .	129
5.4	Wetting Chemically Heterogeneous Surfaces . . . . .	132
5.4.1	Spreading on Chemically Heterogeneous Surface . . . . .	133

5.5	Experimental Validation . . . . .	137
5.6	Chapter Summary . . . . .	141
5.6.1	Further Considerations . . . . .	141
<b>6</b>	<b>Droplet Deposition on Structured Surfaces</b>	<b>145</b>
6.1	Introduction . . . . .	145
6.2	Deposition within a Square Micro-cavity . . . . .	146
6.2.1	Model Validation . . . . .	149
6.2.2	Ideal Deposition into a Cavity . . . . .	153
6.3	Deposition with Single-axis Positional Inaccuracy . . . . .	157
6.3.1	Droplet Morphologies . . . . .	157
6.3.2	Cavity Wetting Times . . . . .	161
6.3.3	Evolution of Wetted Fraction . . . . .	163
6.4	Deposition with Dual-axis Positional Inaccuracy . . . . .	166
6.4.1	Droplet Morphologies . . . . .	170
6.4.2	Cavity Wetting Time . . . . .	170
6.4.3	Evolution of Wetted Fraction . . . . .	174
6.4.4	Additional Dual-Axis Positional Inaccuracy Configuration . . . . .	177
6.5	Maximum Permissible Positioning Error . . . . .	178
6.5.1	Influence of Dual-axis Misalignment on Deposition . . . . .	179
6.5.2	Influence of Droplet Properties on Deposition . . . . .	184
6.5.3	Determination of Maximum Permissible Overlap . . . . .	187
6.5.4	Printable Parameter Map . . . . .	190
6.6	Chapter Summary . . . . .	193
<b>7</b>	<b>Evaporation on Textured Surfaces</b>	<b>194</b>
7.1	Introduction . . . . .	194

7.2	Background	195
7.3	Thermal Model Validation	196
7.3.1	Dirichlet Boundary Conditions	198
7.3.2	Outflow Boundary Condition	202
7.4	Sessile Droplet Evaporation	204
7.4.1	Evaporative Cooling	208
7.4.2	Internal Flow of Evaporating Droplets	208
7.5	Evaporation in Cavities	212
7.5.1	Influence of Cavity Wettability on Evaporation Rate	214
7.5.2	Internal Flow of Droplets Evaporating in Cavity	220
7.6	Deposits	225
7.6.1	Deposition on a Smooth Surface	226
7.6.2	Deposition in a Square Cavity	230
7.7	Chapter Summary	236
<b>8</b>	<b>Conclusions</b>	<b>237</b>
8.1	Conclusions	237
8.2	Future Work	242
<b>A</b>	<b>Publications and Presentations</b>	<b>244</b>
<b>B</b>	<b>Geometric Wetting Boundary</b>	<b>245</b>
B.1	Identification of Node Types	245
B.2	Discretisation	246
B.2.1	Corner Treatment	247
<b>C</b>	<b>Lattice Isotropy</b>	<b>250</b>
C.1	Moments of the Equilibrium Distribution Function	251



---

## List of Figures

---

1.1	Map of parameters suitable for inkjet printing. . . . .	5
1.2	Photograph of a rain droplet sitting on a leaf illustrating non-wetting characteristics. . . . .	7
2.1	Snapshots of the time evolution of simple 1D cellular automata.	21
2.2	Snapshots of the time evolution of John Conway's 2D cellular automata, <i>life</i> . . . . .	22
2.3	Illustration of the D2Q9 and D3Q19 velocity sets. . . . .	29
2.4	Illustration of the streaming step for post-collision populations. . . . .	31
3.1	Coexistence curves of reduced densities from Maxwell equal-area construction (MWC) and Free-Energy LB model with van der Waals EOS. . . . .	52

3.2	Coexistence curves of reduced index function from Maxwell equal-area construction and HCZ LB model with Carnahan-Starling EOS. . . . .	57
3.3	Illustration of spurious velocities surrounding a suspended droplet in a fully periodic domain. . . . .	60
3.4	Pressure-volume plot for Peng-Robinson EOS for varying temperature. . . . .	63
3.5	Reduced coexistence densities from the Maxwell equal-area construction and pseudopotential LB model with Peng-Robinson EOS. . . . .	65
3.6	Young-Laplace validation of pseudopotential model to determine the surface tension. . . . .	67
4.1	Illustration of the periodic boundary condition applied to each side of a 2D simulation, giving a toroidal geometry. . . . .	77
4.2	Illustration of half-way bounce-back boundary condition. . . . .	78
4.3	Illustration of free-slip boundary condition. . . . .	82
4.4	Validation of the symmetry boundary condition for pseudopotential model. . . . .	83
4.5	Scaling performance of 3D pseudopotential model with multiple threads. . . . .	86
4.6	Illustration of simple one-dimensional domain decomposition for MPI parallelisation. . . . .	87
4.7	Illustration of message passing with distributed memory systems. . . . .	87
4.8	Strong scaling performance for multiphase lattice Boltzmann models in 2D parallelised with MPI. . . . .	89
4.9	Scaling performance for 3D pseudopotential multiphase model parallelised with MPI. . . . .	90

4.10	Convergence residuals for density and velocity magnitude in multiphase simulation of a stationary droplet in a fully periodic domain. . . . .	92
4.11	Illustration of flow velocity ( $u_x(y, z)$ ) for gravity driven Poiseuille flow in a square duct. . . . .	93
4.12	Grid convergence for 3D gravity driven Poiseuille flow with single-phase LBM. . . . .	94
4.13	Validation of pressure distribution in 3D pressure driven Poiseuille flow with Zou-He boundary conditions. . . . .	95
4.14	Grid convergence for 3D gravity driven Poiseuille flow with single-phase LBM. . . . .	96
5.1	Profiles of adhesive force computed for different wetting models for a single droplet wetting a smooth surface. . . . .	103
5.2	Illustration of the computation of cohesive forces at boundary nodes in which neighbouring pseudopotentials in solid nodes ( $\psi(\mathbf{x}_w)$ ) need to be defined. . . . .	104
5.3	Illustration of the ambiguity in defining a precise <i>interface</i> location for diffuse interface models. . . . .	107
5.4	Equilibrium contact angles ( $\theta$ ) against adhesion strength parameter, $G_{adh}$ , for $\rho$ - and $\psi$ -based wetting models. . . . .	112
5.5	Equilibrium contact angles ( $\theta$ ) against adhesion strength parameter, $G_{adh}$ , for $\psi^2$ -based and IFM wetting models. . . . .	115
5.6	Equilibrium contact angles for geometric wetting model with different interface thicknesses and incorporated stability condition. . . . .	117
5.7	Evaluation of equilibrium spreading factor for each wetting model and boundary treatment. . . . .	119

5.8	Evaluation of maximum spurious velocities for different contact angles for each wetting model and boundary treatment. . . . .	122
5.9	Illustration of velocity field for wetting model and boundary treatment configuration which resulted in the largest spurious velocity. . . . .	123
5.10	Deviation from coexistence density both in the liquid phase (boundary node beneath the droplet) and vapour phase (boundary node at the top of the simulation domain) for $\rho$ - and $\psi$ -based wetting models. . . . .	126
5.11	Deviation from coexistence density both in the liquid phase (boundary node beneath the droplet) and vapour phase (boundary node at the top of the simulation domain) for $\psi^2$ -based and IFM wetting model. . . . .	128
5.12	Evolution of droplet radius on a smooth surface with an equilibrium contact angle of $\theta = 40^\circ$ . . . . .	131
5.13	Illustration of a droplet deposited onto a chemically patterned surface. . . . .	133
5.14	Evolution of droplet radius spreading on a chemically patterned surface. . . . .	136
5.15	Experimental validation of multiphase model for simulating dynamical spreading and droplet height oscillation. . . . .	139
5.16	Deviation from coexistence density both in the liquid phase (boundary node beneath the droplet) and vapour phase (boundary node at the top of the simulation domain) for the LAD model. . . . .	143
5.17	Evaluation of maximum spurious velocities for different contact angles for LAD model. . . . .	143

5.18	Evolution of droplet radius on smooth surface with an equilibrium contact angle of $\theta = 40^\circ$ for LAD model. . . . .	144
6.1	Illustration of droplet angular deflection ( $\theta^D$ ) and print-head positioning error ( $E_{PH}$ ) during droplet deposition. . . . .	147
6.2	Idealised cavity geometry for investigating droplet deposition with off-centre positioning. . . . .	148
6.3	Determination of suitable critical density value, $\rho_c$ , for correctly computing the wetted fraction (equation 6.1) for both hydrophobic and hydrophilic cavities. . . . .	150
6.4	Determination of suitable lattice resolution through evaluation of the wetted fraction. . . . .	152
6.5	Evaluation of the effect of kinematic viscosity ratios $\mu_R$ on the evolution of the WF. . . . .	154
6.6	Snapshots of ideal droplet deposition into a cavity with different dynamic viscosity ratios. . . . .	155
6.7	Dimensionless wetted time for ideal droplet deposition as a function of the inverse Ohnesorge number. . . . .	156
6.8	Distinct droplet morphologies for single-axis misalignment with overlap value of $\alpha_\beta = 0.5$ and $\alpha_{\bar{\beta}} = 0.0$ . . . . .	159
6.9	Identification of distinct droplet morphologies at $t_{\max}^*$ for droplet deposition with single-axis misalignment. . . . .	160
6.10	Wetting time for cavities in which ideal wetting is achieved for droplet deposition with single-axis misalignment. . . . .	162
6.11	Evolution of wetted fraction for droplet deposition with single-axis misalignment. . . . .	164

6.12	Illustrations of droplets spreading in cavities with different substrate and wall contact angles with single-axis misalignment ( $\alpha_\beta = 0.5$ and $\alpha_{\bar{\beta}} = 0.0$ ).	165
6.13	Illustration of the volume of droplet initially placed outside of the cavity for dual-axis positioning error ( $\alpha_\beta$ and $\alpha_{\bar{\beta}} > 0$ ).	167
6.14	Volume fraction for different configurations of dual-axis misalignment.	168
6.15	Approximations for the volume fraction with dual-axis overlap.	169
6.16	Distinct droplet morphologies for dual-axis misalignment with overlap values of $\alpha_\beta = \alpha_{\bar{\beta}} = 0.355216$ (VF = 0.5).	171
6.17	Identification of distinct droplet morphologies at $t = t_{max}$ for droplet deposition with dual-axis misalignment.	172
6.18	Wetting time for cavities in which ideal wetting is achieved for droplet deposition with dual-axis misalignment.	173
6.19	Evolution of wetted fraction for droplet deposition with dual-axis misalignment.	175
6.20	Illustrations of droplets spreading in cavities with different substrate and wall contact angles with dual-axis misalignment ( $\alpha_\beta = \alpha_{\bar{\beta}} = 0.355216$ ).	176
6.21	Illustration of cavity spacing for display configuration.	178
6.22	Investigation of print success for varying cavity height $H/D$ , width $W/D$ for single- and dual-axis misalignment.	180
6.23	Final state morphologies for droplet impact cavity with a single-axis overlap.	182
6.24	Final state morphologies for droplet impact cavity with a dual-axis overlap.	183

6.25	Investigation of print success for varying cavity height $H/D$ , width $W/D$ and We number. . . . .	185
6.26	Snapshots of the droplet evolution with high and low We numbers. . . . .	186
6.27	Determination of maximum achievable overlap for different cavity wall widths and heights. . . . .	188
6.28	Illustration of final state morphologies for points (a) and (b) highlighted in figure 6.27. . . . .	189
6.29	Printable parameter map based on determined maximum overlap value, $\alpha_{MAX}$ . . . . .	191
6.30	Validation of printable parameter map. . . . .	192
7.1	Validation of $D^2$ law for droplet vaporisation with hybrid pseudopotential model. . . . .	199
7.2	Validation of temperature distribution in a multiphase system in which different fluid-vapour levels are explored. . . . .	201
7.3	Open boundary condition effects on system mass. . . . .	203
7.4	Relationship between attraction parameter in Peng-Robinson EOS and liquid-vapour interface thickness. . . . .	204
7.5	Transient evolution of normalised volume, normalised radius and contact angle for droplet evaporating in CCA and CCR modes. . . . .	206
7.6	Density contours at different stages of the evaporation processes for droplets evaporating in either the CCA or CCR mode on a flat heated surface. . . . .	207
7.7	Temperature distribution (in lattice units) of evaporating sessile droplets in which effects of evaporative cooling are observed. . . . .	209

7.8	Velocity streamlines highlighting Marangoni flows in sessile droplet evaporation. . . . .	210
7.9	Average velocity magnitude for evaporating droplets in CCA and CCR mode. . . . .	211
7.10	Illustration of simulation configuration for evaporating droplet in a heated cavity. . . . .	213
7.11	Time dependence of non-dimensional droplet volume evaporating in a square cavity with no hysteresis. . . . .	215
7.12	Snapshots of droplet evaporation in a square cavity with $\theta = 90^\circ$ and no hysteresis. . . . .	216
7.13	Time dependence of non-dimensional droplet volume evaporating in a square cavity with pinned contact lines. . . . .	217
7.14	Snapshots of droplet evaporation in a square cavity with pinned contact lines. . . . .	218
7.15	Time dependence of non-dimensional droplet volume evaporating in a square cavity with different receding contact angles. . . . .	219
7.16	Snapshots of droplet morphologies during evaporating in a square cavity with different receding contact angles. . . . .	219
7.17	Illustration of thermal Marangoni flows inside a heated square cavity. . . . .	221
7.18	Time dependence of spatial averaged velocity magnitude of a droplet evaporating in a heated square cavity with no hysteresis. . . . .	222
7.19	Time dependence of spatial averaged velocity magnitude of a droplet evaporating in a heated square cavity with $30^\circ$ receding contact angle on cavity wall. . . . .	223

7.20	Time dependence of spatial averaged velocity magnitude of a droplet evaporating in a heated square cavity with pinned contact line. . . . .	224
7.21	Illustration of particle concentration in evaporating droplets in CCA mode for different Péclet numbers. . . . .	228
7.22	Illustration of particle concentration in evaporating droplets in CCR mode for different Péclet numbers. . . . .	229
7.23	Snapshots illustrating the evolution of particle concentration on the substrate surface for a droplet evaporating in a heated cavity with $Pe \approx 9.315$ . . . . .	231
7.24	Snapshots of particle concentration for thermal and isothermal evaporation in a cavity. Cavity contact angles of $\theta = 90^\circ$ and with no hysteresis. . . . .	232
7.25	Snapshots illustrating the evolution of particle concentration on the substrate surface for a droplet evaporating in a heated cavity with $Pe \approx 6.21$ . . . . .	234
7.26	Snapshots of particle concentration for thermal and isothermal evaporation in a cavity. Cavity contact angles of $\theta_A = 90^\circ$ and receding contact angle of $\theta_R = 30^\circ$ . . . . .	235
B.1	Identification of unique node types within a square cavity for discretisation of the geometric boundary condition to control wetting. . . . .	246
B.2	Illustration of solid ghost nodes in convex and concave corners.	248
B.3	Neighbouring node to a concave corner to be determined from geometric wetting condition. . . . .	249

---

## List of Tables

---

1.1	Printer characteristics. . . . .	3
3.1	Coexistence liquid and vapour densities from Maxwell's equal-area rule for the Peng-Robinson EOS. . . . .	66
4.1	Physical quantities and conversion factors for LBM simulations.	75
5.1	Polynomial coefficients for relating adhesion strength $G_{adh}$ to equilibrium contact angle $\theta$ with the $\rho$ -based wetting model. .	109
5.2	Polynomial coefficients for relating adhesion strength $G_{adh}$ to equilibrium contact angle $\theta$ with the $\psi$ -based wetting model. .	111
5.3	Polynomial coefficients for relating adhesion strength $G_{adh}$ to equilibrium contact angle $\theta$ with the $\psi^2$ -based wetting model.	113
5.4	Polynomial coefficients for relating adhesion strength $G_{adh}$ to equilibrium contact angle $\theta$ with the IFM wetting model. . . .	114
5.5	Comparison of wetting model performance for static and dynamic scenarios. . . . .	140

---

## Acronyms

---

**BBGKY** Bogoliubov–Born–Green–Kirkwood–Yvon.

**BGK** Bhatnagar-Gross-Krook.

**CA** cellular automata.

**CCA** constant contact angle.

**CCR** constant contact radius.

**CFD** computational fluid dynamics.

**CIJ** continuous inkjet.

**CM** colour model.

**DDF** double-distribution function.

**DOD** drop on demand.

**DPD** dissipative particle dynamics.

**ELBM** entropic lattice Boltzmann model.

**FHP** Frisch-Hasslacher-Pomeau.

**HCZ** He-Chen-Zhang.

**HPP** Hardy-Pomeau-de Pazzis.

**IFM** interface force modification.

**LAD** local average density.

**LBM** lattice Boltzmann method.

**LGCA** lattice-gas cellular automata.

**LS** level-set.

**MCSC** multi-component Shan-Chen.

**MLUPS** million lattice updates per second.

**MPI** message passing interface.

**MRT** multiple relaxation time.

**MS** multi-speed.

**NS** Navier-Stokes.

**OLEDs** organic light emitting diodes.

**PDF** probability density function.

**SC** Shan-Chen.

**SRT** single relaxation time.

**VOF** volume of fluid.

**WF** wetted fraction.

**ZH** Zou-He.

# CHAPTER 1

---

## Introduction

---

### 1.1 Motivation

The drive towards cheaper and more functional electronic devices has resulted in the exploration of fabrication technologies such as inkjet printing as a means of directly applying material in the required location. Inkjet printing offers the ability to deposit material in a precise repeatable pattern, allowing the printing of text and images with ease and without the need for a physical template. These qualities of inkjet printing result in it being a low cost and highly scalable alternative to traditional printing techniques. Examples of inkjet printed electronics include thin-film transistors [1], sensors [2] and organic light emitting diodes (OLEDs) [3, 4]. As the functional material can be deposited onto a wide range of substrates, inkjet printing gives a viable means for manufacturing wearable electronic devices [5].

The current manufacturing procedure for the mass production of OLEDs involves expensive evaporative based techniques, which heat up the required material to the point of vaporisation, then through the use of fine masks, allow it to condense in the required location [6, 7]. This process also places constraints on the substrates due to the high temperature requirement. The aforementioned qualities of inkjet printing make it a potential alternative fabrication technique for OLEDs, and as such has received much research interest [3, 4, 7, 8, 9, 10]. However, the main challenge with the use of inkjet printing for the fabrication of OLEDs is depositing a uniform layer of functional material in the desired location. Furthermore, as demand consistently increases for higher resolution displays, the requirement to print with finer tolerance also increases.

The remainder of this chapter gives an introduction of the basics of inkjet printing and the associated physical phenomena i.e. wetting and evaporation as well as describe computational modelling techniques available to simulate the process. Finally, the thesis aim and objectives are presented along with a description of the thesis layout.

## **1.2 Inkjet Printing**

There are two primary inkjet printing technologies: continuous inkjet (CIJ) and drop on demand (DOD), which as the names suggest produce either a stream of continuous equidistant droplets or a single droplet when required [11].

CIJ printers produce a continuous stream of droplets which are subsequently deflected onto the substrate or collected in a reservoir to be reused. The pressurised ink is passed through the print head, which through the phe-

nomenon of Rayleigh instability creates a stream of droplets. These droplets are given a potential relative to ground, which allows them to be deflected as they travel from the print head.

With DOD printers, the liquid is held in place within a nozzle by the interfacial surface tension. To eject a droplet from the nozzle a pressure pulse is created forcing a single droplet to be ejected. There are two methods of generating a pressure pulse: rapid heating of the ink causing local vaporisation, or mechanical compression using a piezoelectric transducer. Positioning of the droplet is achieved by moving the print head to the desired location. When the droplet is formed, there is a tail produced which stretches from the droplet to the nozzle. This tail breaks up as the droplet falls to the substrate and creates smaller satellite drops, which catch up with the main droplet and coalesce before impact on the substrate. To allow this to occur, the print head must be positioned a suitable distance away from the substrate, typically  $2 - 3mm$ . For the fabrication of functional devices, DOD printers are preferable as they typically achieve finer resolutions. Typical droplet properties of CIJ and DOD are summarised in table 1.1.

	<b>CIJ</b>	<b>DOD</b>
Droplet size ( $\mu m$ )	100	20-50
Generation frequency ( $kHz$ )	20-60	1-20
Droplet velocity ( $ms^{-1}$ )	>10	5-8

Table 1.1: Printer characteristics. Data obtained from [12] & [13].

There are a number of different physical steps which comprise the process of inkjet printing such as the generation of droplets, the positioning of single or multiple interacting droplets on a substrate, and finally the evaporation or

solidification of the ink to give a solid deposit. Each of these steps encompasses complex phenomena spanning a wide range of industrial and academic interests.

The characteristics of the applied pressure pulse in addition to the nozzle diameter control the size and velocity of the ejected droplet. With these droplet properties in addition to fluid properties such as density, viscosity, and surface tension, dimensionless numbers can be constructed such as the Reynolds (Re) and Weber (We) numbers. The Reynolds number describes the ratio of inertial to viscous forces and is given as

$$\text{Re} = \frac{u_0 D_0}{\nu}, \quad (1.1)$$

where  $u_0$  is the in-flight droplet velocity,  $D_0$  is the in-flight droplet diameter and  $\nu$  is the kinematic viscosity. The Weber number gives the ratio of inertial forces to surface tension forces and is expressed as

$$\text{We} = \frac{\rho u_0^2 D_0}{\sigma}, \quad (1.2)$$

where  $\rho$  is the density and  $\sigma$  is the liquid-vapour surface tension. Additionally, the Ohnesorge (Oh) number defined as

$$\text{Oh} = \frac{\sqrt{\text{We}}}{\text{Re}}, \quad (1.3)$$

is used for categorising the droplets without the influence of velocity. Typically, the inverse of the Ohnesorge number ( $Z = 1/\text{Oh}$ ) is used to determine suitable properties for printing. Ranges suitable for printing are given as  $10 > Z > 1$  [14] and  $14 > Z > 4$  [15]. Additional requirements are that the jet possess sufficient kinetic energy to be ejected from the nozzle, giving  $\text{Re} = 2/\text{Oh}$  and that splashing is avoided upon impact with the solid surface

giving  $OhRe^{5/4} = 50$  [12]. These dimensionless numbers can be used to give a map of properties suitable for inkjet printing, figure 1.1.

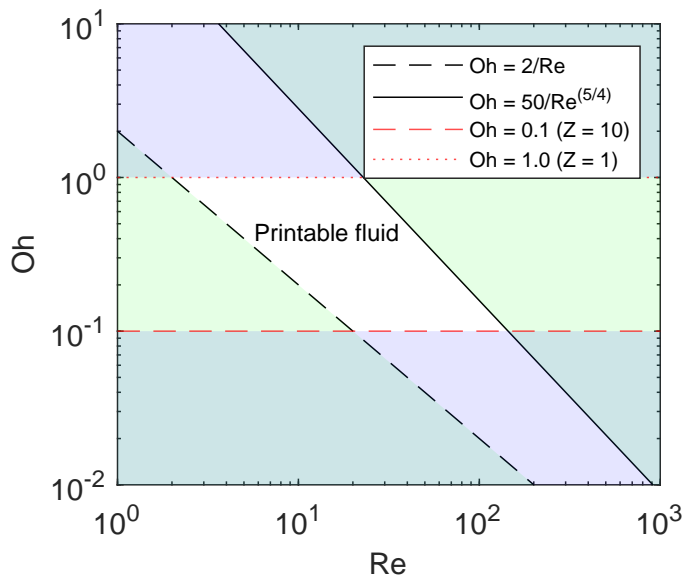


Figure 1.1: Map of parameters suitable for inkjet printing. Constructed using the relationships identified in [12].

Following the ejecting from the print nozzle, the droplet will fall until it reaches the substrate. When the droplet impacts the substrate, the behaviour can be driven by either inertial forces or capillary forces. The nature of the droplet substrate interaction is complex and depends on both the liquid and solid surface properties. Considerable research has been directed towards understanding the interactions of droplets on surfaces, which is summarised in §1.3.

### 1.2.1 Ink Requirements

As highlighted above, there is a narrow range of conditions in which a successful print can be achieved. Furthermore, the requirement to print functional materials can significantly affect the rheological properties of the ink and depending on the concentration, the fluid can become non-Newtonian, affecting the printability. The inks used in inkjet printing are complex, and comprise four main components: colourant, solvent, binder and additives [16]. For inkjet fabrication of electrical devices, the colourant is replaced by the required functional material such as silver particles [17] or poly(3,4-ethylenedioxythiophene) polystyrene sulfonate (PEDOT:PSS) [18] etc., a review of conductive inks is given in [19]. For the fabrication of OLEDs through inkjet printing, the inks typically contain particle dispersions of the functional material to be deposited, which due to the viscosity requirements to maintain printability need to be of low concentration ( $< 5\%$ ) [16].

## 1.3 Wetting and Evaporation

The wetting of solid surfaces by droplets is encountered in numerous situations. A key wetting phenomenon encountered in nature is the interaction between plant leaves and water droplets. The typically non-wetting nature of the plant leaves (illustrated in figure 1.2) leads to droplets rebounding or sliding, making the application of pesticides and herbicides inefficient [20]. In an industrial setting, wetting examples include coatings, spray cooling and inkjet printing.

In the bulk of a liquid, molecules experience cohesive forces with other liquid molecules, resulting in a net force equal to zero. However, at the interface between a liquid and a gas, molecules are interacting with both gas and



Figure 1.2: Photograph of a rain droplet sitting on a leaf illustrating non-wetting characteristics.

liquid molecules in an approximately equal manner, which due to the weaker cohesive forces between the liquid and gas results in a force (surface tension) pointing towards the bulk of the liquid. This is the driving mechanism for shaping small droplets to a spherical shape and also generates excess pressure inside the droplet. The difference between the pressure inside and outside the droplet is referred to as Laplace pressure and is expressed as

$$\Delta p = p_{in} - p_{out} = \frac{2\sigma}{R}, \quad (1.4)$$

where  $\sigma$  is the surface tension and  $R$  is the radius of the drop. When a liquid drop is brought into contact with a solid surface, the shape it adopts is one that minimises its free energy. When gravity can be neglected, this shape is approximated as a spherical cap. The length scale at which gravity becomes relevant is determined by the capillary length of the liquid  $\lambda_c$ , which

is expressed as

$$\lambda_c = \sqrt{\frac{\sigma}{\Delta\rho g}}, \quad (1.5)$$

where  $g$  is the acceleration due to gravity and  $\Delta\rho$  is the difference between the liquid and vapour phase densities,  $\rho_l$  and  $\rho_v$  respectively. Due to the small size of the droplets in inkjet printing, gravitational forces are assumed to be negligible and thus the equilibrium shape of a droplet wetting a surface is well approximated with a spherical cap. Due to the presence of a solid, there are additional adhesive forces experienced by the liquid and vapour with the solid. The wetting or wettability of a surface is normally described by the equilibrium contact angle,  $\theta$ , which on a flat smooth surface given by Young's equation as

$$\cos(\theta) = \frac{\sigma_{sv} - \sigma_{sl}}{\sigma_{lv}}, \quad (1.6)$$

where  $\sigma_{sv}$ ,  $\sigma_{sl}$  and  $\sigma_{lv}$  are the surface tensions between the solid-vapour, solid-liquid and liquid-vapour respectively. A surface is characterised as wetting or hydrophilic if the contact angle  $\theta < 90^\circ$ . Alternatively, the surface is described as non-wetting or hydrophobic if the contact angle is greater than  $\theta > 90$ . Finally, superhydrophobic surfaces are characterised by a contact angle  $\theta > 150^\circ$ .

Although the Young equation gives a single equilibrium contact angle, there are in practice a range of contact angles that can be seen for a droplet wetting a surface, which is the result of chemical or topographical imperfections (surface roughness). The range of angles exhibited will however be in-between maximum and minimum values  $\theta_A$  and  $\theta_R$ , which describe the advancing and receding contact angles respectively. The difference between these two extreme contact angles is called the contact angle hysteresis,  $\theta_H = \theta_A - \theta_R$ .

For the case where a droplet is deposited onto a rough surface, there are two possible configurations: the homogeneous case in which the droplet fully wets the surface, and the heterogeneous case where vapour remains underneath the droplet. Two popular models exist to give the equilibrium contact angles on these rough surfaces. When the surface is completely wetted by the droplet, the apparent contact angle ( $\theta_{App}$ ) is described by the Wenzel model [21], expressed as

$$\cos(\theta_{App}) = R\cos(\theta), \quad (1.7)$$

where  $\theta_{App}$  is the apparent contact angle,  $\theta$  is the inherent contact angle of a droplet on a smooth surface and  $R$  is the roughness ratio, comparing the true surface area to the apparent surface area. Alternatively, the droplet may rest upon the protruding features of the rough surface, trapping vapour underneath the droplet, which is referred to as Cassie-Baxter type wetting [22]. The expression for the apparent contact angle is expressed as

$$\cos(\theta_{App}) = R_w f' \cos(\theta) + f' - 1, \quad (1.8)$$

where  $R_w$  is the roughness ratio of the wetted surface area and  $f'$  is the fraction of surface area wetted by the droplet. For the case of a droplet wetting a smooth surface with chemical patterning, the Cassie-Baxter equation becomes

$$\cos(\theta_{App}) = f' \cos(\theta^{(1)}) + (1 - f') \cos(\theta^{(2)}), \quad (1.9)$$

where  $\theta^{(1)}$  and  $\theta^{(2)}$  are the inherent contact angles of chemical components 1 and 2 respectively. The models are useful, however, it is argued by [23] that instead of using contact areas to determine the change in contact angle, the contact line is the key quantity determining a change in contact angle.

In addition to equilibrium configurations, the dynamic process of droplet impact with a solid surface is of key importance for inkjet printing. As highlighted by Rioboo *et al.* [24] and summarised in [13] there are six possible outcomes for a droplet impacting a flat surface: deposition, prompt splash, corona splash, receding breakup, partial rebound and complete rebound. The spreading and evolution of the droplet radius on a wetting surface have been investigated [25]. During the initial impact stage, inertial wetting is dominant and large spreading speeds result which is independent of wettability.

### 1.3.1 Evaporation and Particle Deposits

During the evaporation of a droplet, liquid molecules which possess enough energy break free from the cohesive force in the bulk into the surrounding atmosphere. Macroscopically, this process is described by an evaporative flux leaving the surface. As evaporation continues, the temperature lowers at the droplet surface due to latent heat effects. However, if the evaporation occurs at a slow enough rate, the process can be assumed to be isothermal [26].

There is a non-uniform evaporative flux for sessile droplet when the contact angle  $\theta \neq 90^\circ$  [27, 28]. For droplets with contact angles  $\theta < 90^\circ$  the evaporation flux is enhanced at the contact line, whereas for droplets with  $\theta > 90^\circ$  the evaporative flux is reduced at the contact line. When the contact line is pinned and there is enhanced evaporation flux due to  $\theta < 90^\circ$ , there is an outward replenishing flow inside the droplet. This causes solutes in the droplet to collect at the droplet periphery, leaving a ring-like deposit on the substrate once the solvent has fully evaporated [27]. This phenomenon is commonly referred to as the *coffee-ring* effect. The Péclet number (Pe), provides a means of determining whether the diffusion of a material in the solute will dominate over convection, and is defined as

$$\text{Pe} = \frac{Lu}{D_c}, \quad (1.10)$$

where  $L$  is the length scale of the drop,  $u$  is the characteristic internal flow velocity and  $D_c$  is the diffusivity. When the Pe number is less than 1, uniform deposits can be expected, whereas for  $\text{Pe} > 1$ , non-uniform deposition results [29, 30].

For an evaporating sessile droplet on a flat surface, there are three distinct modes which are observable: constant contact radius (CCR) where the droplet-substrate area remains constant and the height and contact angle reduce, constant contact angle (CCA) in which the droplet shrinks in a self-similar way, reducing the height and droplet-substrate contact area and finally, a combination of the two modes in which the contact angle and radius shrink simultaneously [31, 32]. For heterogeneous surfaces, there is however another mode of droplet evaporation referred to as the stick-slip evaporation model [33]. Here, the droplet evaporates in a CCR mode until a critical angle is reached after which the droplet radius rapidly decreases until it becomes re-pinned.

For evaporating droplets in which there are non-uniform surface tensions, either through the presence of thermal gradients or compositional gradients in binary solvents, there will be a resulting recirculating flow, from regions of low surface tension to high referred to as Marangoni flow [34]. For small droplets where the effects of gravity can be neglected, the presence of Marangoni flows can cause deviation from a spherical cap shape [35]. Hu and Larson [36] showed how Marangoni flows could be used to suppress the coffee-ring effect.

## 1.4 Numerical Modelling of Fluids

Tools such as computational fluid dynamics (CFD) are used for solving fluid dynamic problems in which no analytical solution exists or the solution is difficult to obtain. As opposed to experimental investigations of fluid flows, CFD offers a cost and time effective way to explore different parameters and perform optimisation studies.

### 1.4.1 Continuum-based Solvers

The most common and commercially available CFD packages treat the fluid as a continuum, thus are applicable to scales at which the molecular motion is sufficiently well averaged. Flows can be characterised by their Knudsen number,  $\text{Kn} = \frac{l_{\text{mfp}}}{l_0}$ , which compares the characteristic length scale of the flow to the mean free path between particle collisions,  $l_0$  and  $l_{\text{mfp}}$  respectively. When  $\text{Kn} \ll 1$  the continuum assumption is valid. The behaviour of the fluid is therefore characterised by macroscopic properties such as density, pressure, velocity and temperature.

These macroscopic quantities are defined for a small region of space but are still large enough to statistically average out particle motion. The motion of a fluid is described by conservation laws for mass and momentum. Typically, these are used with simplifying assumptions such as that of incompressibility and that the fluid behaves in a Newtonian way. The incompressible version of the Navier-Stokes (NS) equation, which describes the conservation of momentum is given as

$$\frac{\partial \mathbf{u}}{\partial t} + (\mathbf{u} \cdot \nabla) \mathbf{u} = \nu \nabla^2 \mathbf{u} - \frac{1}{\rho} \nabla p, \quad (1.11)$$

where  $\mathbf{u}$ ,  $\rho$ ,  $p$  and  $\nu$  are the velocity, density, pressure and kinematic viscosity

respectively. For an incompressible fluid, it is also required that the velocity be divergence free, formally

$$\nabla \cdot \mathbf{u} = 0. \quad (1.12)$$

These equations will also be solved with a Poisson equation for the pressure. For numerical simulation, these equations are discretised with commonly used techniques such as the *finite-difference* [37], *finite-element* [38] or *finite-volume* [39] methods.

For modelling the inkjet printing process with conventional CFD techniques, additional equations are required to capture the free surface<sup>1</sup>(interface) of the ink and gas. To track the interface there are different techniques such as the volume of fluid (VOF) [40] or the level-set (LS) [41] methods among others.

### 1.4.2 Particle-based Solvers

Unlike conventional CFD techniques which work at the macroscopic level, with conserved quantities of mass and momentum, the modelling of the fluid can also be approached from the micro- or meso-scale perspectives [42]. Considering the fact that all fluids are made up of particles, simple numerical models can be constructed to track the motion of the particles based on Newton's second law,

$$\mathbf{F}_i = m\mathbf{a}_i, \quad (1.13)$$

where  $m$  is the mass of the fluid particle,  $\mathbf{a}_i$  is the acceleration of particle  $i$

---

<sup>1</sup>A free surface describes a region in which two media are in contact, one of which cannot support an applied pressure gradient or shear stress.

and  $\mathbf{F}_i$  is the total force acting on the particle. Neglecting gravity, the force can be written as

$$\mathbf{F}_i = \sum_{j=1, j \neq i} -\nabla \phi(|\mathbf{r}_{ij}|), \quad (1.14)$$

where  $\mathbf{r}_{ij}$  is the distance between two particles and  $\phi$  is the inter-particle potential, of which the Lennard-Jones 12-6 potential is widely adopted:

$$\phi(\mathbf{r}_{ij}) = 4\epsilon \left[ \left( \frac{\sigma}{r} \right)^{12} - \left( \frac{\sigma}{r} \right)^6 \right], \quad (1.15)$$

where  $\epsilon$  controls the interaction strength and  $\sigma$  controls the range of interaction. The particle position at time  $t + \Delta t$  can then be obtained by

$$\mathbf{x}_i(t + \Delta t) = 2\mathbf{x}_i(t) - \mathbf{x}_i(t - \Delta t) + \frac{\mathbf{F}_i(t)}{m} \Delta t^2, \quad (1.16)$$

among other methods [43]. To obtain the macroscopic quantities of interest, averaging steps are required. As such, the temperature is calculated by first considering the average kinetic energy per degree of freedom,

$$\left\langle \frac{1}{2} m v_\alpha^2 \right\rangle = \frac{1}{2} k_b T. \quad (1.17)$$

Therefore, the instantaneous temperature is given as

$$T(t) = \sum_{i=1}^{N_f} \frac{m v_{\alpha,i}^2(t)}{k_b N_f}, \quad (1.18)$$

where  $k_b$  is the Boltzmann constant and  $N_f$  is the number of degrees of freedom. This simple model is able to capture complex phenomena with the appropriate tuning of the force parameters. However, the main limitation is that the required number of particles quickly makes the method impractical for anything other than short length and time scales [44]. Alternatively, dissipative particle dynamics (DPD) originally proposed by Hoogerbrugge and

Koelman [45] can be considered a coarse-grained MD method, in which the particles represent a cluster of molecules, and is thus suitable for simulating larger length and time scales. The method combines features of MD and LGCA such as Newtonian mechanics and an evolution consisting of collision and streaming. While the method can be used for simulating a variety of mesoscale flows, configuring simulations can be challenging due to the large number of parameters affecting the hydrodynamic behaviour. Furthermore, pair-wise interactions between particles are limited by a cut-off distance, which requires a relatively large length to model fluids with large viscosity, increasing the simulation time [44, 46]. Other particle based approaches such as the lattice-gas cellular automata (LGCA) and the lattice Boltzmann method (LBM), which instead of tracking individual particles use statistical information of particle distributions are described in detail in chapter 2.

### 1.4.3 Numerical Modelling of Inkjet Printed Droplets

Due to the multiple length scales involved with wetting phenomenon, numerical modelling can be challenging and as such there are numerous approaches each with its own strengths and weaknesses [47]. Different CFD methodologies and challenges associated with droplet generation for different printing techniques are reviewed by Hoath [13]. For continuum-based models of multiphase flows, challenges include but are not limited to: enforcing mass conservation, momentum and kinetic energy conservation and handling complex topologies [48]. For interface-tracking (Lagrangian methods) in which the mesh evolves with the free surface, difficulties can arise when dealing with droplet coalescence and breakup [48]. With the VOF method, there can be difficulties in reconstructing the interface, resulting in modelling errors. Furthermore, the dynamic contact angle usually has to be prescribed as a

simulation input.

Nevertheless, continuum-based solvers have been utilised for investigating various scenarios relating to inkjet printing of functional devices, including droplet impact onto rough surfaces [49], wetting of anisotropic surfaces [50] and deposition into cavities [51, 52, 53].

At the micro-scale, molecular dynamic simulations have been used to explore the physics of moving wetting lines [54, 55]. However, due to high computational requirements, these investigations are limited to small space and time scales.

Operating at the *meso-scale*, the lattice Boltzmann method is well suited to modelling multiphase flows as interactions among fluid particles can easily be incorporated without the computational demands of molecular dynamics simulations. As such, the lattice Boltzmann method has been used to explore droplet deposition on smooth surfaces [56, 57] as well as onto a variety of topographically patterned surfaces, including cavities [58, 59], idealised scratched surfaces [60], small protrusions [61], porous surfaces [62]. Furthermore, the LBM has been used to model deposition on smooth, chemically patterned surfaces consisting of stripes [63, 64] and chemical gradients [65].

#### 1.4.4 Modelling Approach

For the research conducted in this thesis, the lattice Boltzmann method is used which is described in detail in the following chapters. The LBM is particularly well suited to multiphase flow, furthermore, the algorithm is highly parallelizable, allowing for implementation on high-performance computers and even graphical processing units. Some of the commonly quoted strengths and weaknesses of the LBM method [66, 67, 44] are summarised below:

**Strengths:**

- The LBM recovers the incompressible Navier-Stokes equation without the need to solve the Poisson equation.
- The kinetic nature of the LBM allows for ease in incorporating interactions among fluid particles and the environment to enable modelling of complex multiphase and multicomponent flows.
- The method performs well at simulating mass conserving flows in complex geometries, with the straightforward implementation of no-slip boundary conditions.
- The lattice based nature as well the simple algorithm allows for efficient implementation on parallel computers.

**Weaknesses:**

- The generation of spurious velocities<sup>2</sup> at curved interfaces with multiphase and multicomponent simulations.
- Time dependant algorithm which is not efficient for the simulation of steady flows.
- A memory intensive algorithm, as a number discrete particle probabilities need to be modelled at each lattice node in addition to macroscopic quantities.
- Implementing boundaries with macroscopic quantities such as density, pressure or velocity is not straightforward.

---

<sup>2</sup>An illustration of spurious velocities is shown in §3.3, figure 3.3.

## 1.5 Aim and Objectives

### 1.5.1 Aim

The aim of this thesis is to use computational fluid dynamic simulations to elucidate the behaviour of inkjet printed droplets on patterned substrate pertaining to the fabrication of organic light emitting diode displays. First, multiphase modelling aspects are explored and developed in order to produce an accurate model, then with this model, two different stages of the printing process are investigated, including the deposition onto the substrate and then the subsequent evaporation of the carrier liquid.

### 1.5.2 Objectives

- Develop an appropriate multiphase simulation model to allow the modelling of droplet deposition into cavities.
- Investigate the deposition process and self-alignment properties of droplets falling into cavities with positional inaccuracies.
- Investigate the process of evaporation and particle flow of droplets inside a cavity.

## 1.6 Thesis Layout

The remainder of this thesis is organised as follows, chapter 2 describes the history of the lattice Boltzmann method from its roots in cellular automata and describes the derivation from a statistical mechanics perspective. The Chapman-Enskog multi-scale expansion is performed to show that at the macroscopic scale the Navier-Stokes equations are recovered. Additionally,

recent advances are described which are able to improve the accuracy and stability of the method. Chapter 3 explores the various multiphase and multi-component extensions to the LBM, with a detailed description of the pseudopotential method used for this research. Chapter 4 gives details about the implementation of the LBM algorithm, taking advantage of the inherent parallelisation capabilities with distributed memory systems. The relationships between LB models and physical dimensional units are given and conversion factors are introduced. Boundary and initial conditions are described which are used throughout this research and a validation case for no-slip boundaries is presented. Chapter 5 describes various methods of incorporating fluid-solid interactions into the pseudopotential method and explores performance in terms of wetting characteristics for static and dynamic scenarios. A new wetting model is described which is able to reduce undesirable effects present in other models. Chapter 6 explores the dynamics of deposition into idealised pixel geometries (square cavities). A discussion on the relevant literature regarding deposition into pre-fabricated cavities is presented first, then results are given for droplet self-alignment with different cavity wetting properties, Weber numbers and cavity spacing. A printable regime map is constructed, highlighting conditions for a successful print. In chapter 7, the pseudopotential model is coupled with an energy equation to investigate droplet evaporation in heated cavities. The model is used to explore wettability effects on evaporation rate, internal flows and particle deposits. Finally, in chapter 8 concluding remarks are given.

---

### The Lattice Boltzmann Method

---

#### 2.1 Background of the LBM

In this section, an overview of the developments leading to the lattice Boltzmann method is presented. The origins of the LBM are rooted in cellular and lattice gas automata, which is summarised in the following sections. The same equations which arose through this natural evolution are also obtained through a statistical mechanics perspective, giving a sound foundation for the LBM, this is briefly described in §2.2.

##### 2.1.1 Cellular Automata

The lattice Boltzmann method evolved from cellular automata (CA) in a process of systematic improvements and modifications. In order to best understand the nature of the LBM, it is helpful to first know about the CA

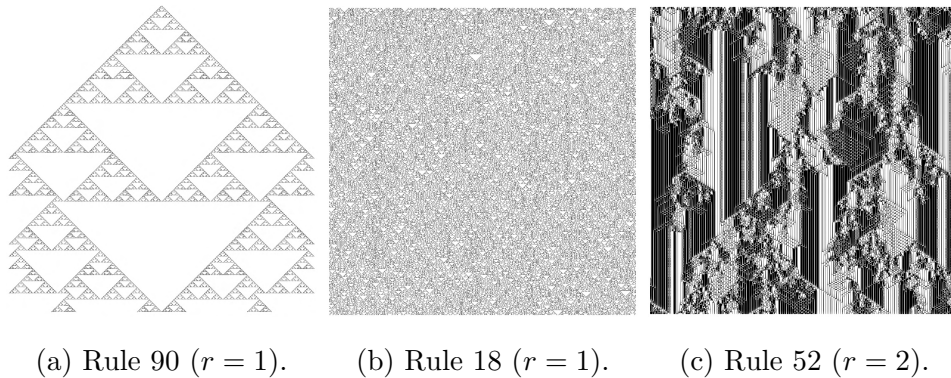


Figure 2.1: Snapshots of the time evolution of simple 1D cellular automata, where  $r$  is the range on influence in the update rule.

which came before it. The development of CA began in the 1950's by John von Neumann and Stanislas Ulam [68]. The basic characteristics of the CA are as follows:

- An array of cells all of the same type.
- Each cell has a binary state.
- Each cell is updated simultaneously at discrete time intervals.
- Each cell is updated by a single deterministic rule depending on the state of neighbouring cells.

Some examples of 1D CA following classification by Stephen Wolfram [69] are given in figure 2.1. The top row of the images represents the system at time  $t = 0$  and subsequent rows are the time  $t + 1$ . A popular 2D CA was introduced in the 1970s by John Horton Conway called *Life* which again had simple totalistic update rules producing complex behaviour. This was subsequently popularised by Martin Gardner in a series of papers [70, 71, 72,

73]. From an initial random distribution of states (*alive* or *dead*), the state at each location is updated depending on the state of the neighbouring cells until a stable configuration is reached, an example of which is shown in figure 2.2. Here, the domain consists of  $100 \times 100$  nodes, where at initialisation, each node is equally likely to be *alive* or *dead*. Each cell has 8 neighbours, if at the current time-step the cell is *alive* and has 2 or 3 neighbours which are also *alive*, the cell will remain *alive* for the next iteration. Alternatively, if the cell is *dead* and has precisely 3 neighbours which are *alive* the cell will change to *alive* for the next iteration. All other configurations default to a *dead* cell at the next iteration.

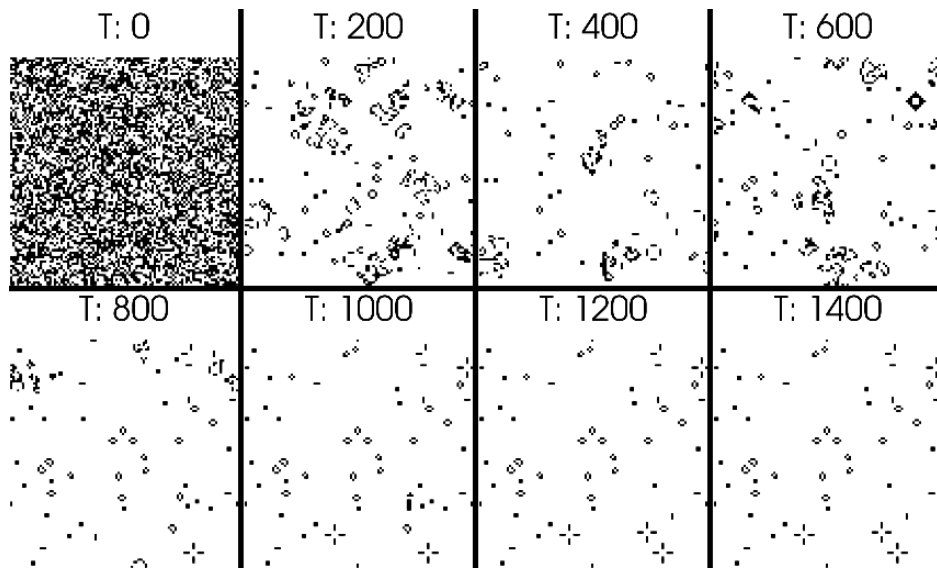


Figure 2.2: Snapshots of the time evolution of John Conway's 2D cellular automata, *life*. From  $T = 1200$ , populations have stabilised.

### 2.1.2 Lattice Gas Cellular Automata

A special type of CA, referred to as lattice-gas cellular automata (LGCA) was proposed in 1973 by Hardy, Pomeau and de Pazzis [74] which is coined the HPP model from the authors initials. The key idea was that different micro dynamical systems can lead to the same behaviour on a macroscopic scale. This special type of CA was developed such that mass and momentum were conserved to allow the simulation of physical phenomena such as fluid flow. With the LGCA, space is filled with equidistant lattice nodes connected by a vector  $\mathbf{e}_i$ . A Boolean variable,  $n_i$ , is associated with each vector to represent the presence or absence of a particle. Each lattice node has four vectors connecting it to its nearest neighbours, configured in a square lattice structure. The evolution of the system is then described as

$$n_i(\mathbf{x} + \mathbf{e}_i\Delta t, t + \Delta t) - n_i(\mathbf{x}, t) = \Delta_i(\mathbf{n}(\mathbf{x}, t)), \quad (2.1)$$

where  $\Delta_i$  is the collision operator. The left-hand side is responsible for streaming and the right-hand side redistributes the particles with the constraints of mass and momentum conservation imposed by the collision operator. Later, in 1986 Frisch, Hasslacher and Pomeau [75] proposed a LGCA model which was able to recover the Navier-Stokes equations in the macroscopic limit. Their approach is commonly referred to as the FHP model, again named after the inventors' initials. They were able to recover the Navier-Stokes equations by identifying the required lattice isotropy (Described in Appendix C). The square lattice structure was replaced by a hexagonal configuration with 6 lattice vectors (7 if including rest particles). This increased the complexity, as now there were multiple possible collision events that would respect the conservation requirements. The outcome of collision would therefore be chosen randomly, with an equal probability between dif-

ferent states. The model was a substantial step forward, however, it suffered from noise due to the Boolean nature of the particles, violation of Galilean invariance, velocity dependent pressure, restriction to low Reynolds number flows, and spurious invariants<sup>1</sup>.

Subsequent developments were able to remove these undesirable effects from the model. To remove the noise and thus the need for statistical averaging of the whole simulation, the Boolean values were replaced with real number distribution functions representing the average occupation at each site by McNamara and Zanetti [76]. Simplified collision operators were then introduced under the assumption that the distribution function is close to its equilibrium value [77]. A key final modification was proposed by numerous authors [78, 79, 80] in which the collision operator was re-expressed in a form such that the distribution functions all relax towards equilibrium at a constant rate, resembling the Bhatnagar-Gross-Krook (BGK) collision operator [81].

## 2.2 Theoretical Basis of the Lattice Boltzmann Method

As mentioned in §1, fluids can be modelled at different scales. Describing a fluid system using statistical mechanics involves a large number of degrees of freedom, as knowledge of all the positions  $\mathbf{p}_i$  and momenta  $\mathbf{q}_i$  of the particle constituting the fluid are required. The evolution of this system is described by derivatives of the Hamiltonian  $H(\mathbf{q}, \mathbf{p})$  as:

$$\dot{\mathbf{q}}_i = \frac{\partial H}{\partial \mathbf{p}_i} \quad \text{and} \quad \dot{\mathbf{p}}_i = -\frac{\partial H}{\partial \mathbf{q}_i}, \quad (2.2)$$

---

<sup>1</sup>Conservation of phenomena other than mass and momentum.

where  $i = 1, 2, \dots, N$ , with  $N$  being the number of particles in the system, typically exceeding  $10^{23}$  and the dotted quantities representing a derivative with respect to time. Due to the large number of particles, it is beneficial to take a different approach to modelling the system, such as the *kinetic theory*. With kinetic theory, the interest is shifted towards probabilities rather than the knowledge of each individual particle. The probability density function (PDF),  $f_N(\mathbf{q}, \mathbf{p}, t)$  is introduced which gives the probability that the state of the system is in the volume  $[\mathbf{p}, \mathbf{p} + d\mathbf{p}] \times [\mathbf{q}, \mathbf{q} + d\mathbf{q}]$  in phase space. The benefit of  $f_N$  is that it gives all the statistical properties which would otherwise have had to be obtained from directly performing statistical averages on molecular dynamic simulations. The evolution of the  $f_N$  is described by the Liouville equation,

$$\frac{df_N}{dt} = \frac{\partial f_N}{\partial t} + \sum_{i=1}^N \left[ \frac{\partial f_N}{\partial \mathbf{q}_i} \cdot \dot{\mathbf{q}}_i + \frac{\partial f_N}{\partial \mathbf{p}_i} \cdot \dot{\mathbf{p}}_i \right] = 0. \quad (2.3)$$

However, the Liouville equation still contains too many degrees of freedom to be of practical use computationally. A reduced PDF,  $F_s$ , is introduced

$$F_s(\mathbf{q}_1, \mathbf{p}_1, \dots, \mathbf{q}_s, \mathbf{p}_s) = \int f_N(\mathbf{q}_1, \mathbf{p}_1, \dots, \mathbf{q}_N, \mathbf{p}_N) d\mathbf{q}_{s+1} d\mathbf{p}_{s+1} \dots d\mathbf{q}_N d\mathbf{p}_N. \quad (2.4)$$

The evolution of  $F_s$  is given by the so called BBGKY hierarchy after Bogoliubov, Born, Green, Kirkwood and Yvon who derived the equations. In full, this hierarchy is identical to the Liouville equation. However, a truncated form of the BBGKY equation can be obtained under the assumption of the Boltzmann gas limit [82], which at the first order gives the Boltzmann equation as

$$\frac{\partial f}{\partial t} + \boldsymbol{\xi} \cdot \frac{\partial f}{\partial \mathbf{x}} = \Omega(f), \quad (2.5)$$

where  $f$  is the velocity distribution function in physical space and  $\Omega$  represents the rate of change of  $f$  due to binary molecular collisions. The velocity distribution function  $f$  is defined as

$$f(\mathbf{x}, \boldsymbol{\xi}, t) = NmF_1(\mathbf{q}_1, \mathbf{p}_1, t), \quad (2.6)$$

where  $\boldsymbol{\xi} = \mathbf{p}_1/m$  is the particle velocity. Useful macroscopic quantities are easily obtained from the velocity distribution function through its moments, such as

$$\rho = \int f d^3\xi, \quad (2.7)$$

$$\rho \mathbf{u} = \int f \boldsymbol{\xi} d^3\xi, \quad (2.8)$$

$$\rho e = \frac{1}{2} \int |\mathbf{v}|^2 f d^3\xi, \quad (2.9)$$

$$\rho E = \frac{1}{2} \int |\boldsymbol{\xi}|^2 f d^3\xi, \quad (2.10)$$

where  $e$  is the internal energy,  $E$  is the total energy and  $\mathbf{v} = \boldsymbol{\xi} - \mathbf{u}$  is the relative velocity.

### **$\mathcal{H}$ -Theorem**

Derived by Boltzmann, the  $\mathcal{H}$ -Theorem states that the particle collisions drive the distribution towards equilibrium. The  $\mathcal{H}$ -function is defined as

$$\mathcal{H} = \int f \ln f d^3\xi, \quad (2.11)$$

which is shown always to decrease, i.e.,

$$\frac{d\mathcal{H}}{dt} \leq 0, \quad (2.12)$$

where the equality holds only if the distribution function reaches its time invariant (equilibrium) state, which is the Maxwell-Boltzmann distribution

$$f^{eq} = \frac{\rho}{(2\pi RT)^{3/2}} \exp\left[-\frac{(\boldsymbol{\xi} - \mathbf{u})^2}{2RT}\right], \quad (2.13)$$

where  $R = k_b/m$  is the gas constant and  $k_b$  is the Boltzmann constant.

The originally proposed collision operator takes the form of a complicated integral, and as such simpler collision operators were suggested. The simplest and one of the most popular of these operators is the BGK [81] model. The BGK model works by relaxing velocity distribution functions towards the Maxwell-Boltzmann equilibrium as

$$\Omega(f) = -\frac{1}{\lambda}(f - f^{eq}), \quad (2.14)$$

where  $\lambda$  is the relaxation time. This then takes the place of the collision operator in equation 2.5 to give

$$\frac{\partial f}{\partial t} + \boldsymbol{\xi} \cdot \frac{\partial f}{\partial \mathbf{x}} = -\frac{1}{\lambda}(f - f^{eq}). \quad (2.15)$$

Finally, arriving at the Boltzmann equation with the BGK collision operator, all that remains is discretisation in velocity, space and time. The details of which are given by He and Luo [83, 84] and a summary of the discretised equations is given in the following section.

### 2.2.1 The Discrete Lattice Boltzmann Method

The standard particle distribution function,  $f(\mathbf{x}, \boldsymbol{\xi}, t)$  spans seven-dimensional space defined by the spatial coordinates  $x$ ,  $y$  and  $z$ , velocity components  $\xi_x$ ,  $\xi_y$  and  $\xi_z$  and time  $t$ . However, working with a finite set of discrete velocities,  $\boldsymbol{\xi}$ , the correct hydrodynamic moments can still be recovered but with

the benefit of reduced computational cost. There are however requirements for the discrete velocities in order to be able to correctly recover the Navier-Stokes equations as discussed in section 2.1.2. The construction of a suitable set of discrete velocities,  $\boldsymbol{\xi}$ , is typically followed by a re-scaling by the factor  $1/\sqrt{3}$  to give the discrete lattice velocity  $\mathbf{e}_i$  of which the abscissae are in integer form. Combining the discrete lattice velocities with appropriate weights  $w_i$  gives a *velocity set*. The most common two- and three-dimensional velocity sets for recovering the NS equations, D2Q9 and D3Q19<sup>2</sup>, which are illustrated in figure 2.3. The velocities for the D3Q19 velocity set can be expressed as

$$\mathbf{e}_i = \begin{cases} 0, 0, 0 & i = 0, \\ (\pm 1, 0, 0), (0, \pm 1, 0), (0, 0, \pm 1) & i = 1, \dots, 6, \\ (\pm 1, \pm 1, 0), (\pm 1, 0, \pm 1), (0, \pm 1, \pm 1) & i = 7, \dots, 18. \end{cases} \quad (2.16)$$

where the weights are

$$w_i = \begin{cases} \frac{1}{3} & i = 0, \\ \frac{1}{18} & i = 1, \dots, 6, \\ \frac{1}{36} & i = 7, \dots, 18. \end{cases} \quad (2.17)$$

The continuous space  $\mathbf{x}$  and time  $t$  are also discretised to lattice points separated by distance  $\Delta x$  and time steps in interval  $\Delta t$  respectively. Neighbouring lattice points are connected by one of the lattice vectors,  $\mathbf{e}_i \Delta t$ , ensuring the discrete particle distribution function  $f_i(\mathbf{x}, t)$  arrives at a neighbouring lattice node  $f_i(\mathbf{x} + \mathbf{e}_i \Delta t)$  in one time-step.

---

<sup>2</sup>The common notation for describing velocity sets is  $DdQq$ , where  $d$  is the number of spatial dimensions and  $q$  is the number of discrete velocity paths [80].

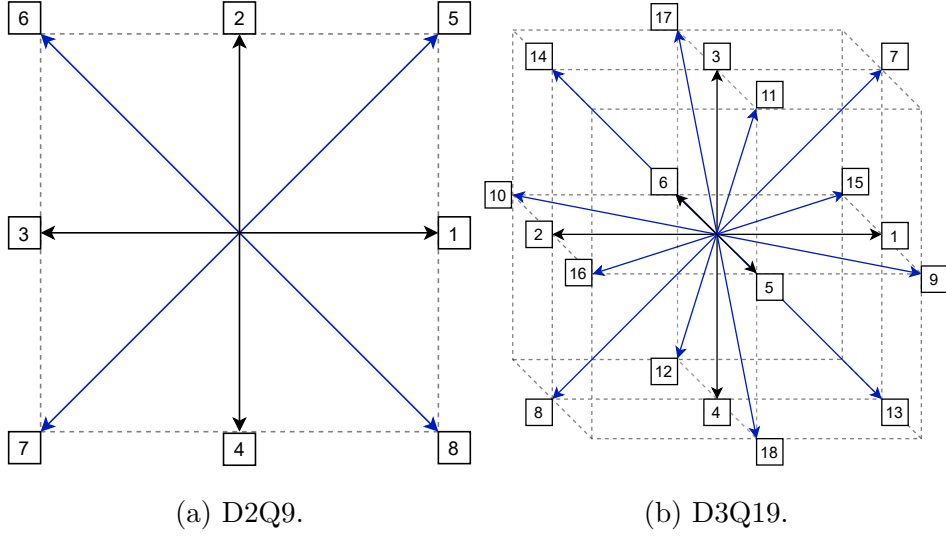


Figure 2.3: Illustration of the D2Q9 and D3Q19 velocity sets.

The discrete lattice Boltzmann equation is expressed with an arbitrary collision operator ( $\Omega_i(\mathbf{x}, t)$ ) as follows

$$f_i(\mathbf{x} + \mathbf{e}_i \Delta t, t + \Delta t) - f_i(\mathbf{x}, t) = \Omega_i(\mathbf{x}, t). \quad (2.18)$$

As with the continuous Boltzmann equation, the simplest and most popular collision operator is the BGK [81] model, which is expressed for the discrete LB model as

$$\Omega_i(f) = -\frac{1}{\tau}(f_i - f_i^{eq})\Delta t, \quad (2.19)$$

where  $\tau$  is the relaxation time and  $f_i^{eq}$  is the discrete isothermal equilibrium distribution function, which is expressed as

$$f_i^{eq} = w_i \rho \left( 1 + \frac{\mathbf{u} \cdot \mathbf{e}_i}{c_s^2} + \frac{(\mathbf{u} \cdot \mathbf{e}_i)^2}{2c_s^4} - \frac{(\mathbf{u} \cdot \mathbf{u})^2}{2c_s^2} \right), \quad (2.20)$$

where  $\rho$  is the density,  $\mathbf{u}$  is the macroscopic velocity and  $c_s = 1/\sqrt{3}$  is the

lattice speed of sound. Obtaining a discrete form of the equilibrium distribution function can be achieved by first expressing equation 2.13 as a series of Hermite polynomials, then using the rules of Gauss-Hermite quadrature, discrete velocities can be obtained which then give discrete equilibrium values,  $f_i^{eq}$ <sup>3</sup>. The macroscopic quantities of density and velocity are recovered through weighted sums of the distribution functions at each node as

$$\rho(\mathbf{x}, t) = \sum_i f_i(\mathbf{x}, t) \quad \text{and} \quad \mathbf{u}(\mathbf{x}, t) = \frac{1}{\rho(\mathbf{x}, t)} \sum_i f_i(\mathbf{x}, t) \mathbf{e}_i. \quad (2.21)$$

Furthermore, the kinematic viscosity for the LB simulation is determined from the relaxation time as

$$\nu = c_s^2 \left( \tau - \frac{1}{2} \right). \quad (2.22)$$

One time-step of the LB equation 2.18 comprises two steps, first the particle *collision* processes and secondly, the *streaming* (or *propagation*) step. During collision, the discrete particle distribution function is relaxed towards the local equilibrium value, which for the BGK collision operator is expressed as

$$f_i^* = f_i - \frac{1}{\tau} (f_i - f_i^{eq}) \Delta t, \quad (2.23)$$

where  $f_i^*$  is used to describe post collision populations. These values are then streamed along lattice vectors to neighbouring lattice nodes, as illustrated in figure 2.4.

---

<sup>3</sup>This procedure is described in detail in [44].

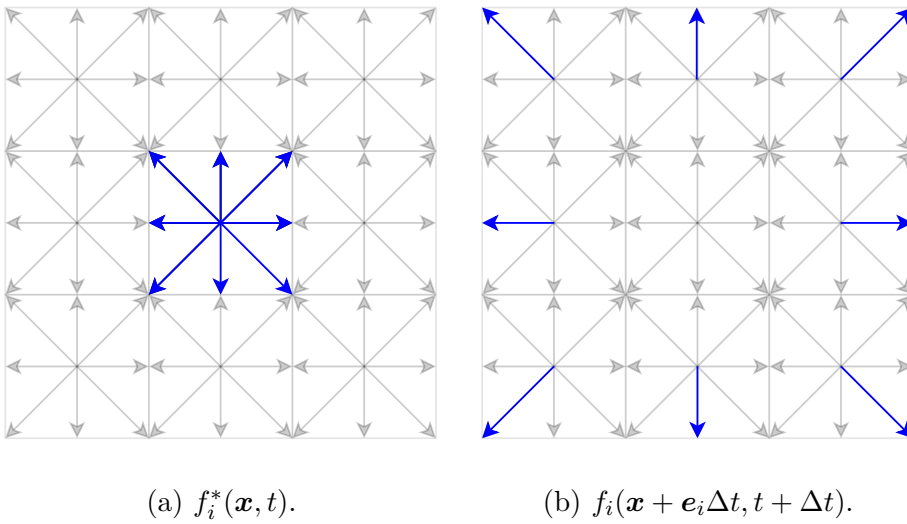


Figure 2.4: Illustration of the streaming step for post-collision populations.

### 2.2.2 Chapman-Enskog Expansion

To understand the behaviour of the discrete lattice Boltzmann equation at macroscopic scales, a common expansion (*Chapman-Enskog expansion* [85]) is used, which reveals that at the macroscopic scale, the lattice Boltzmann equation recovers the Navier-Stokes equations. To begin the expansion, the distribution function is first expressed as a perturbation expansion around the equilibrium distribution as

$$f_i = f_i^{eq} + \epsilon f_i^{(1)} + \epsilon^2 f_i^{(2)} + \dots, \quad (2.24)$$

where  $\epsilon$  is a small parameter, typically the Knudsen number. Here the expansion is performed on the fully discretised lattice Boltzmann equation with BGK collision operator:

$$f_i(\mathbf{x} + \mathbf{e}_i \Delta t, t + \Delta t) - f_i(\mathbf{x}, t) = -\frac{\Delta t}{\tau} (f_i(\mathbf{x}, t) - f_i^{eq}(\mathbf{x}, t)). \quad (2.25)$$

The higher order terms  $f_i^{(1)}$  and  $f_i^{(2)}$ , are subject to the following solvability conditions

$$\sum_i f_i^{(n)} = 0 \quad \text{and} \quad \sum_i \mathbf{e}_i f_i^{(n)} = 0 \quad \text{for } n \geq 1. \quad (2.26)$$

A Taylor series expansion up to second order on the first term on the left-hand side of equation 2.25 gives

$$\begin{aligned} f_i(\mathbf{x} + \mathbf{e}_i \Delta t, t + \Delta t) &= f_i(\mathbf{x}, t) + (\partial_t f_i \Delta t + \partial_\alpha f_i e_{i\alpha} \Delta t) \\ &\quad + \frac{\Delta t^2}{2} (\partial_t^2 f_i + 2\partial_t \partial_\alpha f_i e_{i\alpha} + \partial_\alpha^2 f_i e_{i\alpha}^2) + \mathcal{O}(\Delta t^3), \end{aligned} \quad (2.27)$$

which after manipulation is expressed in a simplified form as

$$\Delta t(\partial_t + e_{i\alpha}\partial_\alpha)f_i = -\frac{\Delta t}{\tau}f_i^{neq} + \frac{\Delta t^2}{2\tau}(\partial_t + e_{i\alpha}\partial_\alpha)f_i^{neq} + \mathcal{O}(\Delta t^3), \quad (2.28)$$

where  $f_i^{neq} = f_i - f_i^{eq}$ . In addition to the expanded distribution function in equation 2.24, the time and space derivatives are expanded as

$$\partial_t = \epsilon\partial_t^{(1)} + \epsilon^2\partial_t^{(2)} \quad \text{and} \quad \partial_\alpha = \epsilon\partial_\alpha^{(1)}. \quad (2.29)$$

Which are then substituted into the Taylor expanded LBM (equation 2.28) to give

$$\begin{aligned} \Delta t(\epsilon\partial_t^{(1)} + \epsilon^2\partial_t^{(2)} + e_{i\alpha}\epsilon\partial_\alpha^{(1)})(f_i^{eq} + \epsilon f_i^{(1)} + \epsilon^2 f_i^{(2)}) = \\ -\frac{\Delta t}{\tau}(\epsilon f_i^{(1)} + \epsilon^2 f_i^{(2)}) + \frac{\Delta t^2}{2\tau}(\epsilon\partial_t^{(1)} + \epsilon^2\partial_t^{(2)} \\ + e_{i\alpha}\epsilon\partial_\alpha^{(1)})(\epsilon f_i^{(1)} + \epsilon^2 f_i^{(2)}). \end{aligned} \quad (2.30)$$

Dividing both sides by  $\Delta t$ , terms of  $\mathcal{O}(\epsilon)$  and  $\mathcal{O}(\epsilon^2)$  are grouped together. Terms of order  $\mathcal{O}(\epsilon)$  are:

$$\partial_t^{(1)}f_i^{eq} + e_{i\alpha}\partial_\alpha f_i^{eq} = -\frac{1}{\tau}f_i^{(1)}. \quad (2.31)$$

Similarly, terms of order  $\mathcal{O}(\epsilon^2)$  are:

$$\partial_t^{(2)}f_i^{eq} + (\partial_t^{(1)} + e_{i\alpha}\partial_\alpha)f_i^{(1)} - \frac{\Delta t}{2\tau}(\partial_t^{(1)} + e_{i\alpha}\partial_\alpha)f_i^{(1)} = -\frac{1}{\tau}f_i^{(2)}. \quad (2.32)$$

The moments are then taken for the grouped terms of each order. For equation 2.31 (order  $\mathcal{O}(\epsilon)$ ), the  $0^{th}$ ,  $1^{st}$  and  $2^{nd}$  moments are taken. For equation 2.32 (order  $\mathcal{O}(\epsilon^2)$ ) the  $0^{th}$  and  $1^{st}$  order moments are taken.

The  $0^{th}$  moment of  $\mathcal{O}(\epsilon)$  is obtained by multiplying equation 2.31 by 1 and summing over  $i$ :

$$\partial_t^{(1)}\rho + \partial_\alpha\rho u_\alpha = 0. \quad (2.33)$$

The 1<sup>st</sup> moment of  $\mathcal{O}(\epsilon)$  is obtained by multiplying equation 2.31 by  $e_{i\alpha}$  and summing over  $i$ :

$$\partial_t^{(1)}\rho u_\alpha + \partial_\beta\Pi_{\alpha\beta}^{eq} = 0. \quad (2.34)$$

The 2<sup>nd</sup> moment of  $\mathcal{O}(\epsilon)$  is obtained by multiplying equation 2.31 by  $e_{i\alpha}e_{i\beta}$  and summing over  $i$ :

$$\partial_t^{(1)}\Pi_{\alpha\beta}^{eq} + \partial_\gamma\Pi_{\alpha\beta\gamma}^{eq} = -\frac{1}{\tau}\Pi_{\alpha\beta}^{(1)}. \quad (2.35)$$

The 0<sup>th</sup> moment of  $\mathcal{O}(\epsilon^2)$  is obtained by multiplying equation 2.32 by 1 and summing over  $i$ :

$$\partial_t^{(2)}\rho = 0 \quad (2.36)$$

The 1<sup>st</sup> moment of  $\mathcal{O}(\epsilon^2)$  is obtained by multiplying equation 2.32 by  $e_{i\alpha}$  and summing over  $i$ :

$$\partial_t^{(2)}\rho u_\alpha + \partial_\beta\left(1 - \frac{\Delta t}{2\tau}\right)\Pi_{\alpha\beta}^{(1)} = 0 \quad (2.37)$$

The moments are then re-combined following the expanded distribution function (equation 2.24) and expanded derivatives (equation 2.29) to give

$$\partial_t\rho + \partial_\alpha(\rho u_\alpha) = 0, \quad (2.38)$$

and

$$\partial_t(\rho u_\alpha) + \partial_\beta\Pi_{\alpha\beta}^{eq} = \partial_\beta\left(1 - \frac{\Delta t}{2\tau}\right)\Pi_{\alpha\beta}^{(1)}. \quad (2.39)$$

The expansion thus far has recovered the continuity equation (equation 2.38). However, it is still required to obtain the momentum equation from equation 2.39. The term  $\Pi_{\alpha\beta}^{eq} = \rho c_s^2 \delta_{\alpha\beta} + \rho u_\alpha u_\beta$ <sup>4</sup> is known from the lattice isotropy requirements and the form of the equilibrium distribution function, see appendix C.3. From equation 2.35, an expression for  $\Pi_{\alpha\beta}^{(1)}$  is known, therefore, equation 2.39 becomes

$$\partial_t(\rho u_\alpha) + \partial_\beta(\rho u_\alpha u_\beta) = -\partial_\beta(\rho c_s^2 \delta_{\alpha\beta}) - \partial_\beta \left(1 - \frac{\Delta t}{2\tau}\right) \tau (\partial_t^{(1)} \Pi_{\alpha\beta}^{eq} + \partial_\gamma^{(1)} \Pi_{\alpha\beta\gamma}^{eq}). \quad (2.40)$$

The last term of the equation ( $\partial_t^{(1)} \Pi_{\alpha\beta}^{eq} + \partial_\gamma^{(1)} \Pi_{\alpha\beta\gamma}^{eq}$ ) is now expanded with the known forms of the equilibrium moments (appendix C.3) as

$$\partial_t^{(1)} \left( c_s^2 \rho \delta_{\alpha\beta} + \rho u_\alpha u_\beta \right) + \partial_\gamma^{(1)} \left( c_s^2 \rho (u_\alpha \delta_{\beta\gamma} + u_\beta \delta_{\alpha\gamma} + u_\gamma \delta_{\alpha\beta}) \right). \quad (2.41)$$

Using the product rule for three components as  $\partial_t(abc) = a\partial_t(bc) + b\partial_t(ac) - ab\partial_t(c)$ , the first term in equation 2.41 is expanded as

$$\partial_t^{(1)} \left( c_s^2 \rho \delta_{\alpha\beta} + \rho u_\alpha u_\beta \right) = c_s^2 \delta_{\alpha\beta} \partial_t^{(1)} \rho + u_\alpha \partial_t^{(1)} (\rho u_\beta) + u_\beta \partial_t^{(1)} (\rho u_\alpha) - u_\alpha u_\beta \partial_t^{(1)} \rho. \quad (2.42)$$

Expressions for the scaled time derivatives ( $\partial_t^{(1)}$ ) for  $\rho$  and  $\rho u_\alpha$  are given in equations 2.33 and 2.34 respectively, thus can be substituted into the right-hand side of equation 2.42:

$$\begin{aligned} & - c_s^2 \delta_{\alpha\beta} (\partial_\gamma^{(1)} \rho u_\gamma) - u_\alpha \partial_\gamma^{(1)} (\rho c_s^2 \delta_{\beta\gamma} + \rho u_\beta u_\gamma) \\ & - u_\beta \partial_\gamma^{(1)} (\rho c_s^2 \delta_{\alpha\gamma} + \rho u_\alpha u_\gamma) + u_\alpha u_\beta (\partial_\gamma^{(1)} \rho u_\gamma). \end{aligned} \quad (2.43)$$

---

<sup>4</sup>Here  $c_s$  is the lattice speed of sound and  $\delta_{\alpha\beta}$  is the usual Kronecker delta.

Further expansion and applying summations over repeated indices yields

$$\begin{aligned}
& - c_s^2 \delta_{\alpha\beta} (\partial_\gamma^{(1)} \rho u_\gamma) - c_s^2 (u_\alpha \partial_\beta \rho + u_\beta \partial_\alpha \rho) \\
& - [u_\alpha \partial_\gamma (\rho u_\beta u_\gamma) + u_\beta \partial_\gamma (\rho u_\alpha u_\gamma) - u_\alpha u_\beta \partial_\gamma (\rho u_\gamma)]. \quad (2.44)
\end{aligned}$$

The term in the square brackets can be written compactly as  $(\partial_\gamma (\rho u_\alpha u_\beta u_\gamma))$ . Additionally, the second term on the right-hand side of equation 2.41, is expanded to give:

$$c_s^2 (\partial_\beta (\rho u_\alpha) + \partial_\alpha (\rho u_\beta)) + c_s^2 \delta_{\alpha\beta} \partial_\gamma (\rho u_\gamma), \quad (2.45)$$

which after expanding the first term with the product rule becomes

$$c_s^2 (\rho \partial_\beta u_\alpha + u_\alpha \partial_\beta \rho + \rho \partial_\alpha u_\beta + u_\beta \partial_\alpha \rho) + c_s^2 \delta_{\alpha\beta} \partial_\gamma (\rho u_\gamma). \quad (2.46)$$

Finally, combining expression 2.46 and 2.44, an expression for the tensor  $\Pi_{\alpha\beta}^{(1)}$  can be given as

$$\Pi_{\alpha\beta}^{(1)} = -\tau c_s^2 (\rho \partial_\beta u_\alpha + \rho \partial_\alpha u_\beta) + \tau \partial_\gamma (\rho u_\alpha u_\beta u_\gamma). \quad (2.47)$$

Substituting this expression back into equation 2.40 while neglecting the term  $\tau \partial_\gamma (\rho u_\alpha u_\beta u_\gamma)$  gives

$$\partial_t (\rho u_\alpha) + \partial_\beta (\rho u_\alpha u_\beta) + \partial_\beta (\rho c_s^2 \delta_{\alpha\beta}) = \partial_\beta \left( 1 - \frac{\Delta t}{2\tau} \right) \tau c_s^2 \rho (\partial_\beta u_\alpha + \partial_\alpha u_\beta). \quad (2.48)$$

Which is recognisable as the Navier-Stokes equation with dynamic viscosity given by

$$\mu = \rho c_s^2 \left( \tau - \frac{\Delta t}{2} \right). \quad (2.49)$$

Additionally, as the term  $\partial_\beta(\rho c_s^2 \delta_{\alpha\beta})$  simplifies to  $\partial_\alpha(\rho c_s^2)$  when summing over repeated indices, the pressure is given as  $p = \rho c_s^2$ . The cubic velocity term,  $\tau \partial_\gamma(\rho u_\alpha u_\beta u_\gamma)$ , is negligible for small Mach number, incompressible flows.

## 2.3 Model Extensions

Although the standard single-relaxation-time LBM is commonly used, it does however have some limiting features, such as viscosity dependent accuracy and reduced stability at high Reynolds numbers. As such, there are many different extensions, which improve the model's applicability to a wider range of fluid flows. A brief overview of some of the extensions available and the strengths and weaknesses of each modification are given in the following sections.

### 2.3.1 Multiple Relaxation Time Modelling

One way to improve the models stability and accuracy is to use multiple-relaxation-time (MRT) collision operators. Here, unlike the traditional single relaxation time (SRT) models, where each distribution function is relaxed towards an equilibrium state at the same rate, the multiple relaxation time (MRT) method performs collisions in *moment space* [86, 44], and each moment is relaxed at a different rate. The individual relaxation rates,  $\omega_i$ , are given as  $\omega_i = 1/\tau_i$  and the individual moments,  $m_k$ , are obtained by multiplying the populations with a  $q \times q$  transformation matrix  $\mathbf{M}$  as

$$m_k = \sum_i M_{ki} f_i. \quad (2.50)$$

Alternatively, the moments can be expressed in vector form where  $\mathbf{m} = (m_0 \dots m_{q-1})^T$  and  $\mathbf{f} = (f_0 \dots f_{q-1})^T$ , giving  $\mathbf{m} = \mathbf{M}\mathbf{f}$ . The post-collision

moments with a force term in moments space,  $\mathbf{S}$ , can then be expressed as

$$\mathbf{m}^* = \mathbf{m} - \mathbf{\Lambda}(\mathbf{m} - \mathbf{m}^{eq}) + \left(\mathbf{I} - \frac{\mathbf{\Lambda}}{2}\right) \mathbf{S}\Delta t, \quad (2.51)$$

where  $\mathbf{m}^{eq}$  is the equilibrium moment vector,  $\mathbf{m}^{eq} = \mathbf{M}\mathbf{f}^{eq}$ ,  $\mathbf{I}$  is the identity matrix, and  $\mathbf{\Lambda}$  is a diagonal relaxation rate matrix

$$\mathbf{\Lambda} = \begin{bmatrix} \omega_0 & 0 & \dots & 0 \\ 0 & \omega_1 & \dots & 0 \\ \vdots & \vdots & \ddots & \vdots \\ 0 & 0 & \dots & \omega_{q-1} \end{bmatrix} \quad (2.52)$$

It is convenient to perform the streaming step in the population space rather than the moment space, thus the post-collision moments are transformed to post-collision populations through multiplication with the inverted transformation matrix  $\mathbf{M}^{-1}$  as  $\mathbf{f}^* = \mathbf{M}^{-1}\mathbf{m}^*$  and are then streamed as normal.

In addition to improved stability and accuracy, the MRT allows for independently setting the shear and bulk viscosities. This is particularly beneficial for multiphase simulations, in which increasing the bulk viscosity can be used to stabilise simulations [87]. The bulk viscosity for two- and three-dimensional simulations are expressed as follows

$$\eta_B = \begin{cases} \rho c_s^2 \left(\frac{1}{\omega_\xi} - \frac{\Delta t}{2}\right) - \frac{\eta}{3} & \text{for D2Q9,} \\ \frac{2}{3} \rho c_s^2 \left(\frac{1}{\omega_e} - \frac{\Delta t}{2}\right) & \text{for D3Q19.} \end{cases} \quad (2.53)$$

The transformation matrices can be constructed from Hermite polynomials or via the Gram-Schmidt procedure, producing orthogonal basis vectors. However, as mentioned in [88, 89], the transformation matrix does not need to be an orthogonal one, with non-orthogonal matrices offering a potential computation speed-up due to more zero elements. Here, the D3Q19 trans-

formation matrix from [44], which was constructed via the Gram-Schmidt procedure, is used, equation 2.54. The inverse of this matrix ( $\mathbf{M}^{-1}$ ), which is used to transform from moment space to population space is obtained with the use of MATLAB.

$$\mathbf{M} = \begin{bmatrix} 1 & 1 & 1 & 1 & 1 & 1 & 1 & 1 & 1 & 1 & 1 & 1 & 1 & 1 & 1 & 1 & 1 & 1 \\ -30 & -11 & -11 & -11 & -11 & -11 & -11 & 8 & 8 & 8 & 8 & 8 & 8 & 8 & 8 & 8 & 8 & 8 \\ 12 & -4 & -4 & -4 & -4 & -4 & -4 & 1 & 1 & 1 & 1 & 1 & 1 & 1 & 1 & 1 & 1 & 1 \\ 0 & 1 & -1 & 0 & 0 & 0 & 0 & 1 & -1 & 1 & -1 & 0 & 0 & 1 & -1 & 1 & -1 & 0 & 0 \\ 0 & -4 & 4 & 0 & 0 & 0 & 0 & 1 & -1 & 1 & -1 & 0 & 0 & 1 & -1 & 1 & -1 & 0 & 0 \\ 0 & 0 & 0 & 1 & -1 & 0 & 0 & 1 & -1 & 0 & 0 & 1 & -1 & -1 & 1 & 0 & 0 & 1 & -1 \\ 0 & 0 & 0 & -4 & 4 & 0 & 0 & 1 & -1 & 0 & 0 & 1 & -1 & -1 & 1 & 0 & 0 & 1 & -1 \\ 0 & 0 & 0 & 0 & 0 & 1 & -1 & 0 & 0 & 1 & -1 & 1 & -1 & 0 & 0 & -1 & 1 & -1 & 1 \\ 0 & 0 & 0 & 0 & 0 & -4 & 4 & 0 & 0 & 1 & -1 & 1 & -1 & 0 & 0 & -1 & 1 & -1 & 1 \\ 0 & 2 & 2 & -1 & -1 & -1 & -1 & 1 & 1 & 1 & 1 & -2 & -2 & 1 & 1 & 1 & 1 & -2 & -2 \\ 0 & -4 & -4 & 2 & 2 & 2 & 2 & 1 & 1 & 1 & 1 & -2 & -2 & 1 & 1 & 1 & 1 & -2 & -2 \\ 0 & 0 & 0 & 1 & 1 & -1 & -1 & 1 & 1 & -1 & -1 & 0 & 0 & 1 & 1 & -1 & -1 & 0 & 0 \\ 0 & 0 & 0 & -2 & -2 & 2 & 2 & 1 & 1 & -1 & -1 & 0 & 0 & 1 & 1 & -1 & -1 & 0 & 0 \\ 0 & 0 & 0 & 0 & 0 & 0 & 0 & 1 & 1 & 0 & 0 & 0 & 0 & -1 & -1 & 0 & 0 & 0 & 0 \\ 0 & 0 & 0 & 0 & 0 & 0 & 0 & 0 & 0 & 0 & 0 & 1 & 1 & 0 & 0 & 0 & 0 & -1 & -1 \\ 0 & 0 & 0 & 0 & 0 & 0 & 0 & 0 & 0 & 1 & 1 & 0 & 0 & 0 & 0 & -1 & -1 & 0 & 0 \\ 0 & 0 & 0 & 0 & 0 & 0 & 0 & 1 & -1 & -1 & 1 & 0 & 0 & 1 & -1 & -1 & 1 & 0 & 0 \\ 0 & 0 & 0 & 0 & 0 & 0 & 0 & -1 & 1 & 0 & 0 & 1 & -1 & 1 & -1 & 0 & 0 & 1 & -1 \\ 0 & 0 & 0 & 0 & 0 & 0 & 0 & 0 & 0 & 1 & -1 & -1 & 1 & 0 & 0 & -1 & 1 & 1 & -1 \end{bmatrix} \quad (2.54)$$

The equilibrium moments  $\mathbf{m}^{eq}$  and the forcing term  $\mathbf{S}$  are determined analytically with  $\mathbf{M}_k \mathbf{f}^{eq}$  and  $\mathbf{M}_k \mathbf{F}$  respectively. Switching from SRT to MRT does increase computation times, typically by 15-20% [86]. The resulting moments in matrix 2.54 are

$$\mathbf{m} = (\rho, e, \epsilon, j_x, q_x, j_y, q_y, j_z, q_z, p_{xx}, \pi_{xx}, p_{ww}, \pi_{ww}, p_{xy}, p_{yz}, p_{xz}, m_x, m_y, m_z)^T. \quad (2.55)$$

where  $e$  is the energy,  $\epsilon$  is the energy squared,  $j_\alpha$  are the momentum components,  $q_\alpha$  are the heat flux components,  $p_{\alpha\beta}$  are the shear stress components

and  $\pi_{\alpha\beta}$  and  $m_\alpha$  correspond to fourth and third order polynomials respectively. The corresponding relaxation matrix is given as

$$\mathbf{\Lambda} = \text{diag}(0, \omega_e, \omega_e, 0, \omega_q, 0, \omega_q, 0, \omega_q, \omega_\nu, \omega_\pi, \omega_\nu, \omega_\pi, \omega_\nu, \omega_\nu, \omega_m, \omega_m, \omega_m), \quad (2.56)$$

where conserved moments have a 0 relaxation rate. Finally, the equilibrium moments are given as

$$\mathbf{m}^{eq} = \left( \rho, -11\rho + 19(u_x^2 + u_y^2 + u_z^2), 3\rho - \frac{11}{2}(u_x^2 + u_y^2 + u_z^2), j_x, -\frac{2}{3}j_x, \right. \\ \left. j_y, -\frac{2}{3}j_y, j_z, -\frac{2}{3}j_z, 2u_x^2 - (u_y^2 + u_z^2), -\frac{1}{2}(2u_x^2 - (u_y^2 + u_z^2)), \right. \\ \left. u_y^2 - u_z^2, -\frac{1}{2}(u_y^2 - u_z^2), u_x u_y, u_y u_z, u_x u_z, 0, 0, 0 \right)^T. \quad (2.57)$$

### Cascaded and Cumulant LBM

Similar to the idea of the MRT, the cascaded LBM or central moment LBM [90] uses central moments in the form of

$$\rho \tilde{M}_{(p)} = \sum_i (\mathbf{e}_i - \mathbf{u})^p f_i. \quad (2.58)$$

This change gives the model Galilean invariance and allows for stable simulations down to the limit of zero viscosity [90]. Criticisms of the model are that extensions to 3D are cumbersome and incorporating forcing terms are challenging, although progress has been made recently to rectify these issues [91]. For cumulant-based models, the distribution functions are transformed to statistically independent quantities [88] and collisions are performed in *cumulant space*.

### 2.3.2 Entropic Lattice Boltzmann Model

The entropic lattice Boltzmann model (ELBM) is beneficial for overcoming instabilities due to low viscosities. Ansumali and Karlin [92] proposed a method of locally adjusting the relaxation rate to satisfy the  $\mathcal{H}$ -theorem. The discrete  $\mathcal{H}$ -function is given as:

$$\mathcal{H}(f) = \sum_i f_i \ln \left( \frac{f_i}{w_i} \right). \quad (2.59)$$

The equilibrium distribution function is given as an extremum of  $\mathcal{H}(f)$ , with the constraints of mass and momentum conservation:

$$f_i^{eq} = \rho w_i \prod_{\alpha=1}^D \left( 2 - \sqrt{(1 + 3u_\alpha^2)} \right) \left( \frac{2u_\alpha + \sqrt{(1 + 3u_\alpha^2)}}{1 - u_\alpha} \right)^{e_{i\alpha}}, \quad (2.60)$$

where  $D$  is the total number of spatial dimensions,  $\alpha$ . The modification to the relaxation process is achieved by ensuring the following:

$$\mathcal{H}(\mathbf{f} + \gamma(\mathbf{f}^{eq} - \mathbf{f})) = \mathcal{H}(\mathbf{f}), \quad (2.61)$$

which requires a root finding algorithm to determine the value of  $\gamma$  such as the Newton-Raphson or the bisection method. The final modified LB algorithm is thus given as

$$f_i(\mathbf{x} + \mathbf{e}_i \Delta t, t + \Delta t) - f_i(\mathbf{x}, t) = \gamma(f_i^{eq}(\mathbf{x}, t) - f_i(\mathbf{x}, t))/2\tau. \quad (2.62)$$

If equation 2.61 is not used to determine  $\gamma$ , and instead  $\gamma$  is fixed at  $\gamma = 2$  the method is equivalent to the standard single-relaxation-time model [93, 94].

## 2.4 Thermal Extension of the LBM

The equilibrium distribution function in equation 2.20 is derived under the isothermal assumption. Additionally, the D2Q9 and D3Q19 velocity sets illustrated in figure 2.3 do not possess enough velocity components to correctly recover the third- and fourth-order velocity moments required for the energy equation. Within the LBM framework, there are three main methods to model thermal flows: the multi-speed (MS) method, the double-distribution function (DDF) method and the hybrid method.

The MS approach requires a velocity set with more discrete velocities as well as modification of the equilibrium distribution function, thus allowing the method to correctly recover higher order moments [95, 96]. A major benefit of this approach is that the coupling between the momentum and energy equations is automatically captured, accounting for viscous heat and compression work. However, MS models are usually criticised for having poor numerical stability and a fixed Prandtl number when used with the BGK collision operator.

The DDF method uses a distribution function  $\mathbf{f}$  for the calculation of the standard isothermal LBM and an additional distribution function,  $\mathbf{g}$ , for computing an advection-diffusion equation for temperature. The velocity which is computed through the moments of  $\mathbf{f}$  is used in computing the equilibrium distributions  $\mathbf{g}^{eq}$ , giving a one-way coupling and treating the temperature as a passive scalar. There are different approaches to model the temperature influence on the velocity [97]. Typically, the Boussinesq approximation may be assumed for cases where buoyant forces are dominant. The DDF approach offers better numerical stability compared to the MS method, although there is not an automatic two-way coupling between the temperature and velocity.

Finally, the hybrid approach couples the standard isothermal LBM to an additional numerical solver for the temperature, typically a finite-difference method. This approach behaves similarly to the DDF method and has the same limitations, in that the two-way coupling needs to be specified. This is the approach used in this thesis, as explained in detail in §3.4. Further details on each thermal expansion method can be found in chapter 5 of [66].

## 2.5 Chapter Summary

The lattice Boltzmann method, in its simplest single-relaxation-time form, evolved through incremental improvements from cellular automata. Examples of 1D and 2D cellular automata are presented along with discussions on the contributions which lead to the LBM. Furthermore, a more theoretical derivation of the Boltzmann equation is presented from a statistical mechanics perspective.

The discrete LBM is then shown, through a Chapman-Enskog expansion, to recover the Navier-Stokes equations. Model extensions to improve stability and accuracy, such as the multiple-relaxation-time (MRT) method are then discussed, and implementation steps are given for the D3Q19 velocity set. Furthermore, thermal modelling extensions are also summarised.

## CHAPTER 3

---

### Multiphase Lattice Boltzmann Modelling

---

#### **3.1 Introduction**

This chapter comprises an overview of some of the most popular multiphase and multicomponent models for the lattice Boltzmann method. The theory and implementation procedure are presented along with key model developments. Strengths and weaknesses are discussed along with example case studies available in the literature. Specific attention is given to the pseudopotential model, including implementation with a 3D MRT algorithm and extensions to incorporate thermal flows as this is used for investigations further in the thesis.

## 3.2 Multiphase and Multicomponent Modelling

One of the main strengths of the LBM is its ability to model multiphase and multicomponent flows. The method's mesoscopic nature allows for ease in the incorporation of inter-particle forces. The interface between components or phases results from the included inter-particle forces, however, they are often under-resolved in order to allow for sufficient computation times. From each individual model's inception, there have been numerous modifications and improvements enabling a wider range of parameters to be explored and reducing undesirable artefacts. From the numerous works investigating multiphase/ multicomponent phenomena with different models, it is clear that no one model offers the best performance in all aspects. Many of the models described in this section require the calculation of spatial gradients. These are calculated with the following isotropic central difference schemes

$$\partial_\alpha \varphi(\mathbf{x}, t) \approx \frac{1}{c_s^2 \Delta t} \sum_i w_i \varphi(\mathbf{x} + \mathbf{e}_i \Delta t, t) e_{i\alpha}, \quad (3.1)$$

$$\nabla^2 \varphi(\mathbf{x}, t) \approx \frac{2}{c_s^2 \Delta t^2} \sum_i w_i [\varphi(\mathbf{x} + \mathbf{e}_i \Delta t, t) - \varphi(\mathbf{x}, t)], \quad (3.2)$$

where the weights  $w_i$  are the same as those used in the chosen velocity set.

### 3.2.1 Colour Modelling

One of the first multicomponent models was developed by Rothman and Keller in 1998 [98]. Their model extended the single phase LGCA to allow for two immiscible components with surface tension. The standard indistinguishable particles of the LGCA are replaced by two (or more) distinct particles, usually referred to as red and blue particles. The rules of the model are similar to the standard LGCA, in that the collisions conserve the num-

ber of red and blue particles. However, additional rules include encouraging the grouping of like colours and the generation of surface tension force. This model was subsequently incorporated into the LBM by Gunstensen *et al.* [99] in 1991 and later, in 1993, Grunau *et al.* [100] modified the model to allow for variation in density and viscosity ratios. Another key modification came in 2005 when Latva-Kokko and Rothman [101] proposed a recolouring step that significantly reduced the computational requirements while minimising the spurious currents and removing the lattice pinning effect<sup>1</sup>. The model works by introducing a PDF for each of the fluid components  $f_i^k(\mathbf{x}, t)$ , where  $k$  is the index for fluid components. The evolution equation is thus expressed as

$$f_i^k(\mathbf{x} + \mathbf{e}_i \Delta t, t + \Delta t) = f_i^k(\mathbf{x}, t) + \Omega_i^k(\mathbf{x}, t), \quad (3.3)$$

where  $\Omega_i^k$  is the multistage collision operator expressed as

$$\Omega_i^k = (\Omega_i^k)^{(3)} [(\Omega_i^k)^{(1)} + (\Omega_i^k)^{(2)}]. \quad (3.4)$$

Each of these collision operators serves a specific purpose:

- $(\Omega_i^k)^{(3)}$  is the recolouring operator responsible for phase segregation.
- $(\Omega_i^k)^{(2)}$  is the perturbation operator, producing interfacial tension.
- $(\Omega_i^k)^{(1)}$  is the normal single-phase collision operator for each component.

Macroscopic quantities are recovered by taking the usual moments of  $f_i^k(x, t)$ :

---

<sup>1</sup>The lattice pinning effect is a problem that may prevent the interface from moving.

$$\rho^k = \sum_i f_i^k, \quad (3.5)$$

$$\rho \mathbf{u} = \sum_{i,k} \mathbf{e}_i f_i^k, \quad (3.6)$$

where  $\rho = \sum_k \rho_k$ . Therefore, the velocity  $\mathbf{u}$  is referred to as the colour-blind velocity. To determine where surface tension forces are to be applied, the colour gradient  $\mathbf{F}$  is defined as,

$$\mathbf{F} = \sum_i \left( \rho^r(\mathbf{x} + \mathbf{e}_i \Delta t) - \rho^b(\mathbf{x} + \mathbf{e}_i \Delta t) \right) \mathbf{e}_i. \quad (3.7)$$

The perturbation step, which generates the surface tension at the interface between two phases is given as

$$(\Omega_i^k)^{(2)} = \frac{A_k}{2} |\mathbf{F}| \left[ w_i \frac{(\mathbf{e}_i \cdot \mathbf{F})^2}{(|\mathbf{F}|)^2} - B_i \right], \quad (3.8)$$

where the variable  $A_k$  is responsible for controlling the strength of the surface tension and  $B_i$  are constants specific to the chosen velocity set. For the D2Q9 velocity set,  $B_i$  are given as

$$\begin{aligned} B_0 &= -\frac{\chi}{3\chi + 6} c^2, & B_{1,\dots,4} &= \frac{\chi}{6\chi + 12} c^2 \quad \text{and} \\ B_{5,\dots,8} &= \frac{1}{6\chi + 12} c^2. \end{aligned} \quad (3.9)$$

Equivalently, for the D3Q19 velocity set,  $B_i$  are given as

$$\begin{aligned} B_0 &= -\frac{2 + 2\chi}{3\chi + 12} c^2, & B_{1,\dots,6} &= \frac{\chi}{6\chi + 24} c^2 \quad \text{and} \\ B_{7,\dots,18} &= \frac{1}{6\chi + 24} c^2, \end{aligned} \quad (3.10)$$

where  $\chi$  is a free parameter. The final step of the colour model is recolouring. The original model of Rothman [98] involves the minimisation of the work,  $W$ , which is given as

$$W(f^r, f^b) = -\mathbf{F} \cdot \mathbf{q}(f^r, f^b), \quad (3.11)$$

where  $\mathbf{q}$  is the local flux, given as,

$$\mathbf{q} = \sum_i \mathbf{e}_i (f_i^r - f_i^b). \quad (3.12)$$

However, this method of recolouring could cause pinning, examples of which include the advection of droplets in a stream becoming pinned to a lattice node once below a critical diameter. This was rectified by Latva-Kokko and Rothman [101] by allowing the red and blue components to mix by ensuring symmetric colour distribution with respect to the colour gradient. The post-recolouring particle distributions are expressed as:

$$(\Omega_i^r)^{(3)}(f_i^r) = \frac{\rho_r}{\rho} f_i' + \beta \frac{\rho_r \rho_b}{\rho^2} f_i^{eq}(\rho, \mathbf{u} = 0) \cos(\lambda_i), \quad (3.13)$$

$$(\Omega_i^b)^{(3)}(f_i^b) = \frac{\rho_b}{\rho} f_i' - \beta \frac{\rho_r \rho_b}{\rho^2} f_i^{eq}(\rho, \mathbf{u} = 0) \cos(\lambda_i), \quad (3.14)$$

where  $\beta$  should be between 0 and 1 and is used for controlling the thickness of the interface,  $f_i' = \sum_k f_i'^k$  where  $f_i'^k$  is the post-collision state after  $(\Omega_i^k)^{(1)}$  and  $(\Omega_i^k)^{(2)}$  have been applied. Additionally,  $\lambda_i$  is the angle between the colour gradient (equation 3.7) and the discrete lattice vector  $\mathbf{e}_i$  and the term  $\cos(\lambda_i)$  is conveniently expressed as

$$\cos(\lambda_i) = \frac{\mathbf{e}_i \cdot \mathbf{F}}{|\mathbf{F}|}. \quad (3.15)$$

After the application of all three collision operators, the usual streaming step is applied for each colour.

## Model Performance

The benefits of the colour model are that it is straightforward to extend the model beyond just two components, additionally, it allows for independent control over the interface thickness and surface tension. Recent advancements have also enabled the model to simulate fluids with moderate density and viscosity ratios. A potential drawback, depending on the modelling requirements is that the model has no ties to thermodynamics, in that it is a purely heuristic model. An additional drawback is the generation of spurious velocities at curved interfaces, though this is common among multiphase models.

## Case Studies

Liu *et al.* [102] used a 3D colour model which they validated with both static and dynamic simulations. In their static test measuring the Laplace surface tension, they successfully achieved density ratios of 1000 with numerical results of surface tension matching well with predictions. For dynamic simulations, the model was validated for density ratios of 5 and stable simulations were achieved with density ratios as high as 80. Cheng *et al.* [103] used the colour model for generating non-circular contact lines on micro pillar arrays. Their model produced results consistent with experimental findings. Akai *et al.* [104] used the colour model to investigate the displacement of oil in porous media by water. Wetting in the model has also been studied by Akai *et al.* [105].

### 3.2.2 Free-Energy Modelling

In 1995, Swift *et al.* [106] proposed a thermodynamically consistent model based on the concept of free energy. The equilibrium distribution is modified such that the pressure tensor is consistent with the tensor derived from the free-energy functional of non-uniform fluids. A van der Waals fluid has the following free energy functional [107]

$$\Psi(\mathbf{x}) = \int [\psi(T, \rho) + \frac{k}{2}(\nabla\rho)^2]dV, \quad (3.16)$$

where  $\psi(T, \rho)$  is the bulk free energy density, and the parameter  $k$  is related to the surface tension. The pressure tensor is given as

$$P_{\alpha\beta} = p\delta_{\alpha\beta} + k\frac{\partial\rho}{\partial x_\alpha}\frac{\partial\rho}{\partial x_\beta}, \quad (3.17)$$

where,

$$p = p_0 - k\rho\nabla^2\rho - \frac{k}{2}|\nabla\rho|^2, \quad (3.18)$$

and  $p_0$  is the pressure given by the van der Waals equation of state,

$$p_0 = \frac{\rho T}{1 - \rho b} - a\rho^2. \quad (3.19)$$

Once the pressure tensor  $P_{\alpha\beta}$  is obtained, it can be incorporated into the LBM. One method, originally utilised by Swift *et al.* [106] was to absorb the pressure tensor into the equilibrium distribution function. However, it is also possible to incorporate the pressure tensor through an additional forcing term [44]. Following the original method of modification to the equilibrium distribution function, a generalised expression for the equilibrium distribution function is first given for the D2Q9 velocity, following the procedure highlighted in [67] as

$$f_{i=1,\dots,4}^{eq} = A_1 + B_1 u_\beta e_{i\beta} + C_1 u^2 + D_1 u_\alpha u_\beta e_\alpha e_\beta + G_{\alpha\beta 1} e_{i\alpha} e_{i\beta}, \quad (3.20)$$

$$f_{i=5,\dots,8}^{eq} = A_2 + B_2 u_\beta e_{i\beta} + C_2 u^2 + D_2 u_\alpha u_\beta e_\alpha e_\beta + G_{\alpha\beta 2} e_{i\alpha} e_{i\beta}, \quad (3.21)$$

$$f_{i=0}^{eq} = A_0 + C_0 u^2. \quad (3.22)$$

where the coefficients are calculated subject to the following constraints

$$\sum_i f_i^{eq} = \rho, \quad (3.23)$$

$$\sum_i f_i^{eq} e_{i\alpha} = \rho u_\alpha, \quad (3.24)$$

$$\sum_i f_i^{eq} e_{i\alpha} e_{i\beta} = P_{\alpha\beta} + \rho u_\alpha u_\beta. \quad (3.25)$$

For a D2Q9 velocity set, the full list of coefficients are given in [67] and details for construction on a D3Q19 velocity set are given in [108].

## Model Performance

The Free-Energy model adheres to local momentum conservation, and as such, the spurious velocities are greatly reduced. Furthermore, the Free-Energy model allows for independent control of the surface tension and EOS. However, the simulation stability is affected by the choice of surface tension and the liquid-vapour interface size varies with surface tension. This can be seen in figure 3.1, where simulation results of the coexistence densities are compared to the values obtained from the Maxwell equal-area construction (explained in §3.3.1) for different values of the surface tension parameter,  $k$ . One of the major criticisms of the original model is its lack of Galilean invariance. Shortly after the original model was proposed, Holdych *et al.* [109] reduced the lack of Galilean invariance to  $\mathcal{O}(u^2)$ . Zheng *et al.* [110] proposed a Galilean invariant model capable of large density ratios. However,

this was later demonstrated by Fakhari and Rahimian to be valid for only density-matched cases [111]. Inamuro *et al.* [112] also proposed a model which allows for the simulation of high density and viscosity ratios, however, the main criticism of their model is the large computational demand. A review of the existing models can be found in [113].

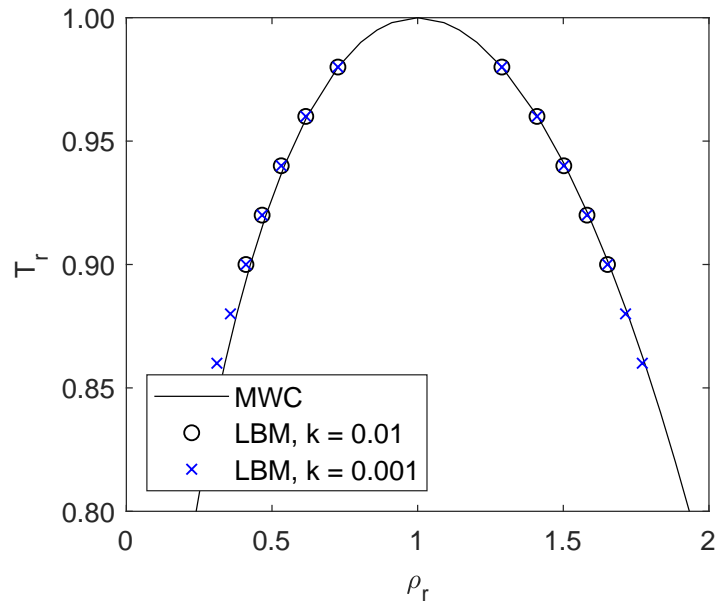


Figure 3.1: Coexistence curves of reduced densities from Maxwell equal-area construction (MWC) and Free-Energy LB model with van der Waals EOS and two different surface tension parameters.

### Case studies

Wetting can easily be incorporated by accounting for the additional free energy at the surface in the bulk free-energy functional [114]. Subsequently, the Free-Energy LBM has been used to investigate droplet motion on chemically and topologically patterned surfaces [115, 116, 117, 118]. In addition to

modelling multiple phases, the Free-Energy method can be used for multiple components [119].

### 3.2.3 He-Chen-Zhang Modelling

The He-Chen-Zhang (HCZ) model proposed in 1999 [120], is an incompressible extension of the He-Chen-Doolen multiphase model [121]. The derivation of this model starts with the non-ideal Boltzmann equation,

$$\frac{Df}{Dt} \equiv \frac{\partial f}{\partial t} + \boldsymbol{\xi} \cdot \nabla f + \mathbf{F} \cdot \nabla_{\boldsymbol{\xi}} f = -\frac{f - f^{eq}}{\lambda}, \quad (3.26)$$

where  $f$  and  $f^{eq}$  are the standard distribution function and equilibrium distribution function respectively,  $\boldsymbol{\xi}$  is the molecular velocity,  $\mathbf{F}$  is the molecular interaction force per unit mass and  $\lambda$  is the relaxation time. The term  $\nabla_{\boldsymbol{\xi}} f$  is unknown and thus approximated with,

$$\nabla_{\boldsymbol{\xi}} f \approx \nabla_{\boldsymbol{\xi}} f^{eq} = -\frac{\boldsymbol{\xi} - \mathbf{u}}{RT} f^{eq}. \quad (3.27)$$

For solving the non-ideal Boltzmann equation numerically while enhancing numerical stability, the HCZ model introduced a new variable,

$$g = fRT + \psi(\rho)\Gamma(\mathbf{0}), \quad (3.28)$$

where  $\psi(\rho) = p - \rho RT$  is the hydrodynamic pressure and  $\Gamma(\mathbf{u})$  is a function of the macroscopic velocity, expressed as

$$\Gamma(\mathbf{u}) = \frac{1}{(2\pi RT)^{D/2}} \exp\left[-\frac{(\boldsymbol{\xi} - \mathbf{u})^2}{2RT}\right]. \quad (3.29)$$

The evolution of the new variable is

$$\frac{Dg}{Dt} = -\frac{g - g^{eq}}{\lambda} + (\boldsymbol{\xi} - \mathbf{u}) \cdot [\Gamma(\mathbf{u})\mathbf{F} - (\Gamma(\mathbf{u}) - \Gamma(\mathbf{0}))\nabla\psi(\rho)], \quad (3.30)$$

where

$$g^{eq} = \rho RT \Gamma(\mathbf{u}) + \psi(\rho) \Gamma(\mathbf{0}). \quad (3.31)$$

The authors of the HCZ model remark that equation 3.30 is computationally superior to equation 3.26 in calculation of the velocity field as the term  $\nabla\psi(\rho)$  is now multiplied by a small quantity. With equation 3.30 the pressure and velocity are recovered as

$$\begin{aligned} p &= \int g d\xi, \\ \rho RT \mathbf{u} &= \int \boldsymbol{\xi} g d\xi. \end{aligned} \quad (3.32)$$

For keeping track of the different densities and maintaining a sharp interface, an index function is utilised. For this, equation 3.26 is used and thus after discretisation (procedure described in [120]) the lattice Boltzmann equations for the evolution of pressure/velocity and the index function are

$$\bar{g}_i(\mathbf{x} + \mathbf{e}_i \Delta t, t + \Delta t) - \bar{g}_i(\mathbf{x}, t) = -\frac{1}{\tau_g} (\bar{g}_i(\mathbf{x}, t) - \bar{g}_i^{eq}(\mathbf{x}, t)) + S_i(\mathbf{x}, t) \Delta t \quad (3.33)$$

and

$$\bar{f}_i(\mathbf{x} + \mathbf{e}_i \Delta t, t + \Delta t) - \bar{f}_i(\mathbf{x}, t) = -\frac{1}{\tau_f} (\bar{f}_i(\mathbf{x}, t) - \bar{f}_i^{eq}(\mathbf{x}, t)) + Q_i(\mathbf{x}, t) \Delta t \quad (3.34)$$

respectively. The variables  $S_i$  and  $Q_i$  represent source terms and  $\tau_g$  and  $\tau_f$  are the relaxation times relating to kinematic viscosity and interface mobility respectively. As in [67] the relaxation times are made to be equivalent  $\tau_g = \tau_f$ . The barred symbols are the result of modifications to keep the scheme

implicit, which results in an explicit dependence on pressure,  $p$ , which is computed through

$$p = \sum_i \bar{g}_i - \frac{\Delta t}{2} \mathbf{u} \cdot \nabla \psi(\rho), \quad (3.35)$$

where  $\psi(\rho) = p - \rho RT$ . As the pressure difference and discrete time step are small values,  $\psi(\rho)$  is calculated with the values of  $p$  and  $\rho$  from the previous time-step [122].

The index function used for maintaining a sharp interface between the two phases is given as

$$\phi = \sum_i \bar{f}_i. \quad (3.36)$$

The macroscopic velocity is recovered as,

$$\rho c_s^2 \mathbf{u} = \sum_i \mathbf{e}_i \bar{g}_i + \frac{\Delta t c_s^2}{2} \mathbf{F}, \quad (3.37)$$

where  $\mathbf{F}$  is the force associated with surface tension and is expressed as,

$$\mathbf{F} = k\rho \nabla(\nabla^2 \rho) \quad \text{or} \quad \mathbf{F} = k\phi \nabla(\nabla^2 \phi), \quad (3.38)$$

where the  $\phi$ -based expression was given later by Zhang *et al.* [123]. The equilibrium distribution functions are given as

$$\bar{g}_i^{eq} = w_i \left[ p + c_s^2 \rho \left( \frac{\mathbf{e}_i \cdot \mathbf{u}}{c_s^2} + \frac{(\mathbf{e}_i \cdot \mathbf{u})^2}{2c_s^4} - \frac{\mathbf{u}^2}{2c_s^2} \right) \right], \quad (3.39)$$

and

$$\bar{f}_i^{eq} = w_i \phi \left[ 1 + \frac{\mathbf{e}_i \cdot \mathbf{u}}{c_s^2} + \frac{(\mathbf{e}_i \cdot \mathbf{u})^2}{2c_s^4} - \frac{\mathbf{u}^2}{2c_s^2} \right]. \quad (3.40)$$

The additional terms in 3.33 and 3.34 are given as

$$S_i = \left(1 - \frac{1}{2\tau_g}\right) (e_{i\alpha} - u_\alpha) \cdot [\Gamma_i(\mathbf{u})F_\alpha - \nabla\psi(\rho)(\Gamma_i(\mathbf{u}) - \Gamma_i(0))], \quad (3.41)$$

and

$$Q_i = \left(1 - \frac{1}{2\tau}\right) \frac{(e_{i\alpha} - u_\alpha) \cdot \nabla\psi(\phi)}{2c_s^2} \Gamma_i(\mathbf{u}), \quad (3.42)$$

where  $\Gamma_i(\mathbf{u}) = \bar{f}_i^{eq}/\phi$ . The function,  $\psi(\phi)$  is related to the thermodynamic pressure and thus is recovered from the equation of state. As with the original HCZ model, the Carnahan-Starling equation of state is used:

$$\begin{aligned} \psi(\phi) &= RT^2\phi \frac{1 + (b\phi/4) + (b\phi/4)^2 - (b\phi/4)^2}{(1 - (b\phi/4))^3} - a\phi^2 - RT\phi \quad (3.43) \\ &= \frac{\phi^2 RT(4 - 2\phi)}{(1 - \phi)^3} - a\phi^2. \end{aligned}$$

In the original model [120], the variables were chosen as  $a = b = 4$  and  $R = 1$ . The critical temperature is given as  $T_c = 0.3773a/bR$ , thus at temperatures below this, two distinct phases coexist. Through the Maxwell equal-area construction (explained in §3.3.1), the coexistence values of  $\phi_l$  and  $\phi_v$  for a chosen temperature are determined. Once initialised, the values of  $\phi$  are used to determine physical properties such as density and kinematic viscosity as

$$\begin{aligned} \rho(\phi) &= \rho_v + \frac{\phi(\mathbf{x}) - \phi_v}{\phi_l - \phi_v} (\rho_l - \rho_v), \quad (3.44) \\ \nu(\phi) &= \nu_v + \frac{\phi(\mathbf{x}) - \phi_v}{\phi_l - \phi_v} (\nu_l - \nu_v). \end{aligned}$$

The values of  $\rho_l$  and  $\rho_v$  are the densities of the liquid and vapour phase respectively, and can be chosen somewhat freely, however, the choice has been shown to affect the numerical stability [67]. The simulated equilibrium values of  $\phi$ , however, deviate significantly from these computed values as illustrated in figure 3.2.

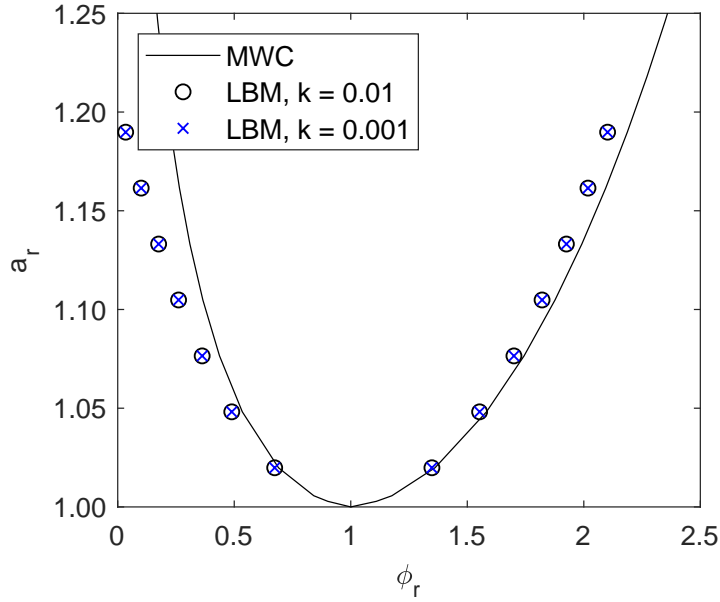


Figure 3.2: Coexistence curves of reduced index function from Maxwell equal-area construction (MWC) and HCZ LB model with Carnahan-Starling EOS. The critical values for obtaining reduced variables are  $a_c = 3.53$  and  $\phi_c = 0.13$ .

## Model Performance

Multiple extensions of the HCZ model exist for expanding the achievable density ratio [124, 125, 126, 67]. Lee and Lin [127] proposed a method capable of modelling high density and viscosity ratios, however their model is quite complex, including two distribution functions, numerous 1<sup>st</sup> and 2<sup>nd</sup> order gradients, and requires three steps comprising pre-streaming collision, streaming and post-streaming collision in order to complete one time-step.

## Case studies

A simple wetting model utilising the bounce back boundary condition and a wall density value was presented by Yiotis *et al.* [124]. Subsequently, the method was used to study droplet spreading [62].

## 3.3 Shan-Chen Pseudopotential Method

In 1993/1994 Shan and Chen proposed two extensions for the LBM for simulating multicomponent [128] and multiphase [129] flows. These extensions are commonly referred to as pseudopotential models or Shan-Chen models. The model works by introducing microscopic interactions between fluid elements which lead to automatic phase segregation. The coexistence of multiple phases of a substance is due to attractive forces in the liquid phase. Similarly, different substances in a multicomponent mixture will have different molecular interactions. The force acts on pairs of molecules located at  $\mathbf{x}$  and  $\tilde{\mathbf{x}} \neq \mathbf{x}$ . It is also assumed that a larger density ( $\rho(\mathbf{x})$ ) of molecules will lead to larger interaction forces. The total interaction force is therefore given as the integral of all possible interactions as

$$\mathbf{F}(\mathbf{x}) = - \int (\tilde{\mathbf{x}} - \mathbf{x}) G(\mathbf{x}, \tilde{\mathbf{x}}) \psi(\mathbf{x}) \psi(\tilde{\mathbf{x}}) d^3 \tilde{\mathbf{x}}, \quad (3.45)$$

where  $G(\mathbf{x}, \tilde{\mathbf{x}})$  gives the strength of the interaction over a distance and the density has been replaced by the pseudopotential  $\psi(\rho)$ <sup>2</sup>.

The pseudopotential can be given in different forms. The originally proposed and regularly used form is expressed as

$$\psi(\rho) = \rho_0 \left[ 1 - \exp \left( - \frac{\rho}{\rho_0} \right) \right], \quad (3.46)$$

---

<sup>2</sup>Using a pseudopotential instead of the density allows for improved numerical stability.

where  $\rho_0$  is a freely chosen reference density. There are different methods for obtaining a discrete form of the interaction force, by limiting interactions to nearest and next-nearest lattice sites, the discrete form of the interaction force is given as follows

$$\mathbf{F}_m(\mathbf{x}) = -\psi(\mathbf{x})G \sum_i w(|\mathbf{e}_i|^2)\psi(\mathbf{x} + \mathbf{e}_i\Delta t)\mathbf{e}_i. \quad (3.47)$$

The sum does not necessarily run over all links of the velocity set, thus the weights  $w(|\mathbf{e}_i|^2)$  are not necessarily the same as the weights used to generate velocity sets. The attraction force can also be expressed as a finite difference approximation to the gradient of the pseudopotential (equation 3.1). As shown in [130], the Taylor expansion of  $\psi(\mathbf{x} + \mathbf{e}_i)$  around  $\mathbf{x}$  is given as

$$\mathbf{F}_m = -Gc^2 \left[ \psi \nabla \psi + \frac{c^2}{2} \psi \nabla (\nabla^2 \psi) + \dots \right]. \quad (3.48)$$

This gives the non-ideal equation of state as  $p = \rho c_s^2 + Gc^2\psi^2/2$ . In the original multicomponent model proposed by Shan and Chen, they proposed a simple forcing scheme for incorporating the interactions,

$$\mathbf{u}^{eq} = \mathbf{u} + \frac{\tau \mathbf{F}_m}{\rho}, \quad (3.49)$$

where  $\mathbf{u}^{eq}$  is the velocity used in calculating the equilibrium distribution function,  $f_i^{eq}(\rho, \mathbf{u}^{eq})$ . The actual fluid velocity to be outputted from the simulation is expressed as

$$\mathbf{u} = \mathbf{u} + \frac{\mathbf{F}_m}{2\rho}. \quad (3.50)$$

An illustration of the resulting spurious velocities of a droplet suspended in a fully periodic domain is displayed in figure 3.3.

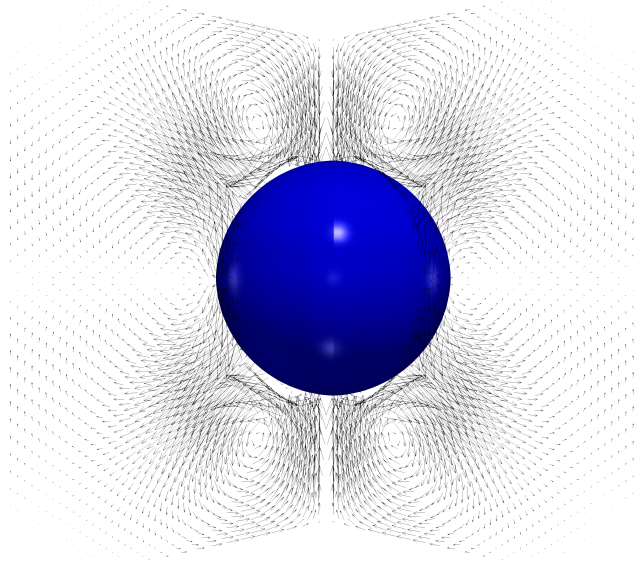


Figure 3.3: Illustration of spurious velocities surrounding a suspended droplet in a fully periodic domain.

### Shan-Chen Multicomponent Modelling

The original model proposed by Shan-Chen was for modelling multiple components and multiple phases [128], their following model was a simplification for a single component with multiple phases. A distribution function is introduced,  $f_i^k$ , for each of the components,  $k$ . The evolution equation of each component is simply

$$f_i^k(\mathbf{x} + \mathbf{e}_i \Delta t, t + \Delta t) - f_i^k(\mathbf{x}, t) = \Omega_i^k(\mathbf{x}, t), \quad (3.51)$$

where  $\Omega_i^k(\mathbf{x}, t)$  is the usual BGK collision operator. To incorporate interactions between different components, the force is expressed as

$$\mathbf{F}^k(\mathbf{x}) = -\psi^k(\mathbf{x}) \sum_{\tilde{k}} G_{\tilde{k}k} \sum_i w_i \psi^{(\tilde{k})}(\mathbf{x} + \mathbf{e}_i \Delta t) \mathbf{e}_i. \quad (3.52)$$

where  $G_{\tilde{k}k}$  is a  $k \times k$  matrix for the interaction strength between components.

For a purely multicomponent mixture, the diagonals of the matrix are 0. The pseudopotential in multicomponent simulations is typically  $\psi = \rho$ . As with the multiphase model, there are different approaches to incorporate the force [44]. Examples of the use of multicomponent models include: wetting in porous media [131], droplet displacement in ducts [132] and high density ratio multicomponent multiphase flows [133, 134].

### 3.3.1 Thermodynamic Consistency

In the pseudopotential model, the coexistence densities are determined by the mechanical stability condition [135]. However, from thermodynamic theory, the coexistence densities can also be computed from the Maxwell equal-area rule [136], which is expressed as

$$\int_{v_l}^{v_g} p dv = p_0(v_v - v_l), \quad (3.53)$$

where  $v_l = 1/\rho_l$  and  $v_v = 1/\rho_v$  are the molar volumes of the liquid and vapour phases respectively and  $p_0$  is a constant pressure. If the mechanical stability condition is to match the thermodynamic description, ensuring that the two descriptions give the same coexistence densities, it is required that the form of the pseudopotential be  $\psi \propto \exp(-1/\rho)$ , constraining the EOS. However, it is desirable to incorporate different EOS from thermodynamic theory, which have a well-defined temperature dependence, for this, the pseudopotential is defined as

$$\psi(\rho) = \sqrt{\frac{2(p_{EOS} - c_s^2 \rho)}{c^2 G}}, \quad (3.54)$$

where  $p_{EOS}$  is the pressure defined by the chosen EOS, the choice of which can allow the model to achieve density ratios in excess of 1000 [137]. When using

an EOS with defined temperature, the role of  $G$  is no longer a temperature-like parameter, but instead is used to ensure the term inside the square root remains positive. This is usually achieved by setting  $G = -1$ , however pressure waves during initialisation may make the term inside the square root negative, causing instability. Modifications to ensure the root term remains positive are given in [87] along with other algorithms to improve stability. For investigations in this thesis, the Peng-Robinson EOS is chosen, as it is shown to produce low spurious velocities and allow for the generation of large density ratios [137]. The Peng-Robinson EOS is expressed as,

$$p_{EOS} = \frac{\rho RT}{1 - b\rho} - \frac{a\alpha(T)\rho^2}{1 + 2b\rho - b^2\rho^2}, \quad (3.55)$$

where  $T$  is the temperature,  $R$  is the gas constant,  $a$  and  $b$  are the attraction and repulsion parameters respectively and  $\alpha(T)$  is given as:

$$\alpha(T) = [1 + (0.37464 + 1.54226\omega - 0.26992\omega^2)(1 - \sqrt{T/T_c})]^2, \quad (3.56)$$

where  $\omega$  is the acentric factor, which for water is equal to 0.344 and  $T_c$  is the critical temperature. When the temperature is below the critical value, the pressure-volume relation no longer changes monotonically and there exist three distinct volumes for a given pressure, illustrated in figure 3.4. At the critical temperature, both the first and second derivatives of the pressure with respect to volume/ density are equal to 0. Solving these derivatives gives the critical density of  $\rho_c \approx 0.25308/b$ , thus at temperatures below this, two distinct values of density will be generated.

The critical values are related to the attraction and repulsion parameters as  $a = 0.45724R^2T_c^2/p_c$  and  $b = 0.0778RT_c/p_c$ , where  $p_c$  is the critical pressure. Typically in LB simulations  $a$  and  $b$  are defined, fixing the critical temperature and density. From these critical values, it is common to define reduced

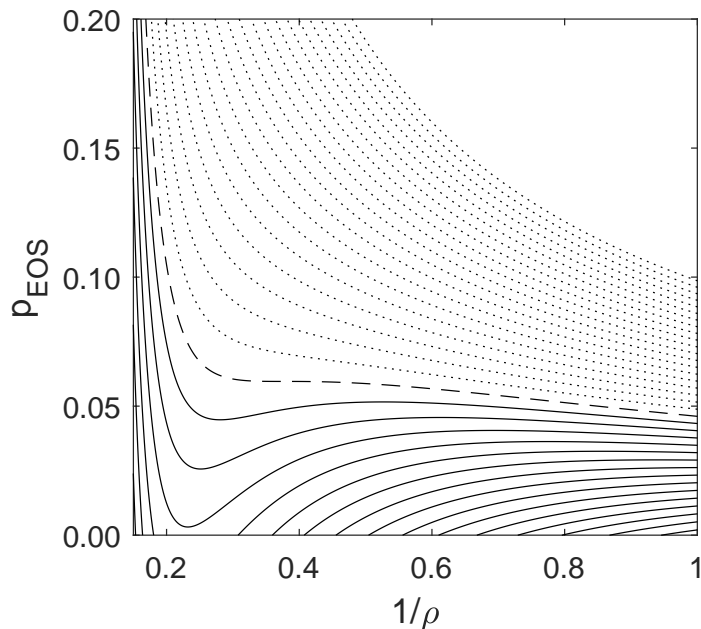


Figure 3.4: Pressure-volume plot for Peng-Robinson EOS. Dotted lines represent  $T > T_c$ , dashed line represents  $T = T_c$  and solid lines represent  $T < T_c$ .

(dimensionless) variables such as the reduced density  $\rho_r = \rho/\rho_c$  and reduced temperature  $T_r = T/T_c$  for ease of comparison to physical systems.

For a fixed reduced density and temperature, the attraction parameter,  $a$ , can be used to control the thickness of the diffuse interface. Increasing the thickness of the interface by changing the attraction parameter  $a$  lowers the spurious velocities. However, as shown by Li and Luo [138], this reduces the speed of sound in the vapour phase,  $\sqrt{(\partial p/\partial \rho)_v}$ . This is problematic for simulating droplets, where due to additional Laplace pressures there is pronounced vapour density variation with droplet size. Thus, to minimise vapour phase density dependence on droplet size the vapour phase speed of sound needs to be the same order of magnitude as the lattice speed of sound,  $c_s$  [138]. A piecewise linear equation of state may be used [139] to control

the speed of sound in each phase directly, however, this is only suitable for isothermal simulations. Therefore, the attraction parameter,  $a$ , needs to be optimised for minimal spurious velocities and density change.

As the pseudopotential is defined by equation 3.54, the model is termed to be *thermodynamically inconsistent*, in that the coexistence densities given by the mechanical stability condition are not the same as the ones obtained from Maxwell's equal-area rule. Therefore, a forcing scheme developed by Li *et al.* [140, 141] is used, which allows for modification of the mechanical stability through a free parameter  $\varepsilon$  to better approximate thermodynamic consistency. For the D3Q19 velocity set and the MRT moment transformation matrix expressed in §2.3.1, the forcing term is expressed as

$$\begin{aligned} \mathbf{S} = & (0, 38(u_x F_x + u_y F_y + u_z F_z) + \frac{114\varepsilon \mathbf{F}_m^2}{\psi^2(1/s_2 - 0.5)}, & (3.57) \\ & -11(u_x F_x + u_y F_y + u_z F_z), F_x, -\frac{2}{3}F_x, F_y, -\frac{2}{3}F_y, \\ & F_z, -\frac{2}{3}F_z, 2(2u_x F_x - u_y F_y - u_z F_z), \\ & -2u_x F_x + u_y F_y + u_z F_z, 2(u_y F_y - u_z F_z), \\ & -u_y F_y + u_z F_z, u_y F_x + u_x F_y, u_z F_y + u_y F_z, \\ & u_z F_x + u_x F_z, 0, 0, 0)^T, \end{aligned}$$

where  $\mathbf{F}_m^2 = (F_{m,x}^2 + F_{m,y}^2 + F_{m,z}^2)$  is the intermolecular interaction force and  $F_\alpha$  is used to represent the total force, including gravity and fluid-solid interactions.

As the parameter  $a$  in the EOS affects the mechanical stability and thus the coexistence densities, but not the values obtained from the Maxwell equal-area construction,  $\varepsilon$  needs to be varied for each value to approximate thermodynamic consistency. To illustrate this, a study is performed with a flat liquid-vapour interface in a computational domain comprising  $3 \times 101 \times 3$

lattice nodes in the  $x$ ,  $y$  and  $z$  directions respectively. The bottom half of the domain ( $0 \leq y \leq 50$ ) consists of liquid whereas the top half consists of vapour. Each of the free relaxation times in the MRT model is fixed at 1 and the repulsion parameter is set to  $b = 2/21$ . As can be seen in figure 3.5, the value of  $\varepsilon$  changes for each value of the attraction parameter,  $a$  in order to approximate thermodynamic consistency.

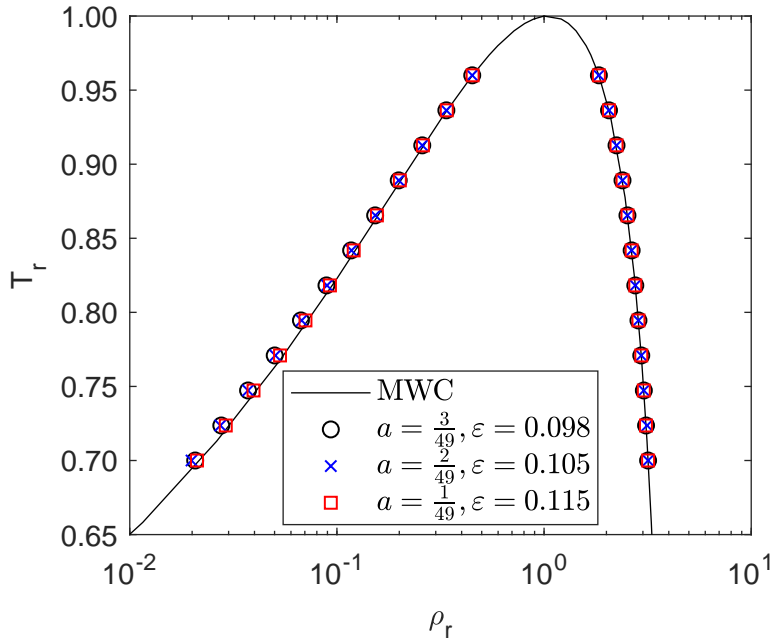


Figure 3.5: Reduced coexistence densities from the Maxwell equal-area construction and pseudopotential LB model with Peng-Robinson EOS. Attraction parameters  $a = \frac{3}{49}$ ,  $\frac{2}{49}$  and  $\frac{1}{49}$  correspond to force corrections  $\varepsilon = 0.098$ ,  $\varepsilon = 0.105$  and  $\varepsilon = 0.115$  respectively.

Through tuning  $\varepsilon$ , the coexistence densities are shown to agree well with the Maxwell equal-area construction when simulating fluids separated by a flat interface. However, for curved interfaces such as droplets, there is

	$\rho_l$	$\rho_v$	$\rho_R$
$T = 0.86T_c$	6.499	0.3797	17.12
$T = 0.80T_c$	7.204	0.1971	36.55

Table 3.1: Coexistence liquid and vapour densities from Maxwell’s equal-area rule for the Peng-Robinson EOS.

additional Laplace pressure to consider, which would require tuning  $\varepsilon$  for different droplet sizes. For investigations in the following chapters of this thesis, the free parameter is set to  $\varepsilon = 0.085$  as this value was found to give suitable results for the droplet sizes considered in this research. In table 3.1, coexistence densities from the Maxwell equal-area construction are given for the temperatures used in the remainder of the thesis.

### Young-Laplace Validation

The surface tension is not readily adjustable and its value is determined by the equation of state. To obtain the numerical value of the surface tension, it is common to perform the Young-Laplace study, where the pressure difference,  $\Delta p$ , is measured in the liquid and vapour for droplets of different sizes. Here, a domain comprising  $150 \times 150 \times 150$  lattice nodes is configured, with droplet sizes varying from  $R_0 = 16$  to  $R_0 = 35$ . The relaxation time for the bulk viscosity is  $\tau_\beta = 1.1$ , with all other free relaxation rates fixed to unity. The results are plotted over the inverse of the radius, giving a linear trend, the slope of which gives the surface tension<sup>3</sup>. The results for droplets at different saturation temperatures are plotted in figure 3.6.

For both temperatures, the linear trend is well captured. For  $T = 0.86T_c$ , the computed surface tension is  $\sigma = 0.0795$ . At the lower temperature  $T = 0.8T_c$

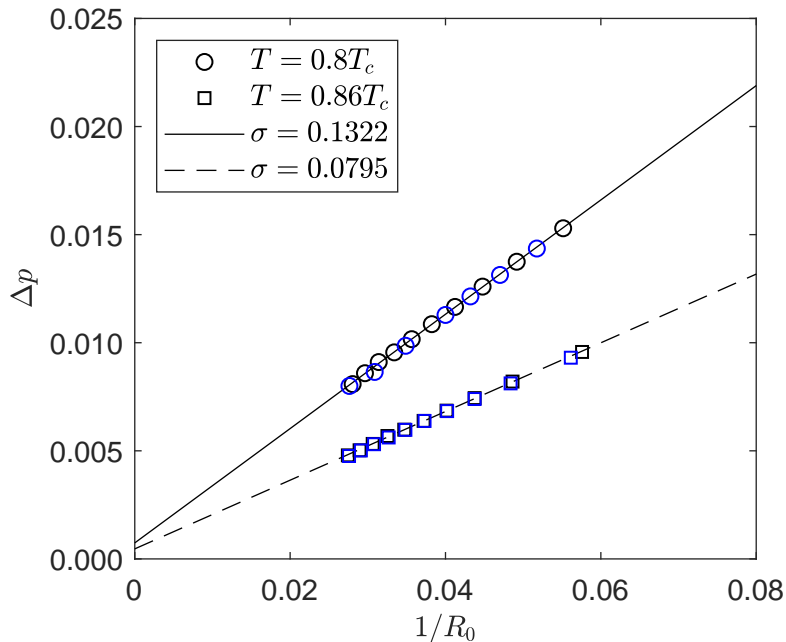


Figure 3.6: Young-Laplace validation of pseudopotential model to determine the surface tension. All quantities are in lattice units. Solid line is a linear fitting for  $T = 0.8T_c$  and dashed line is a linear fitting for  $T = 0.86T_c$ . Blue and black symbols illustrate relaxation times of  $\tau_\nu = 1$  and  $\tau_\nu = 0.6$  respectively.

the computed surface tension is  $\sigma = 0.1322$ . The results obtained showed little deviation for relaxation times of  $\tau_\nu = 1$  and  $\tau_\nu = 0.6$ .

### 3.3.2 Strengths and Weaknesses

One of the key strengths of the method is that it is easy to implement. However, the method received criticism for not being able to introduce a temperature that is consistent with thermodynamics and having a surface

---

<sup>3</sup>In 3D, the slope is  $2\sigma$ .

tension that is coupled to the equation of state [142]. Additionally, if the force is incorporated via equation 3.49, the density ratio and the surface tension change with kinematic viscosity. Numerous different forcing schemes have been suggested such as Luo [143], Guo *et al.* [144], He *et al.* [145], Li *et al.* [140] and Kupershtokh [146]. Huang *et al.* [147] investigated the effects of different forcing schemes in terms of dependence on kinematic viscosity, thermodynamic consistency and spurious currents. Later, Lycett-Brown and Luo [148] performed a third-order analysis of the LBM with a general forcing term to identify errors affecting the mechanical stability condition. They also suggested a new forcing term based on this higher order analysis which allows for independent control of the density ratio, surface tension and interface thickness. Alternative methods for achieving independence between the equation of state and surface tension have been proposed by Sbragaglia *et al.* [149] through the introduction of a multi-range potential. Kharmiani *et al.* [150] modified the original forcing term with two new additional terms identified from Taylor expanding the interaction force, allowing for mechanical stability and surface tension to be modified independently. Li and Luo [151] extended the 2D MRT model of [141] to allow for adjustable surface tension without the need to consider multiple ranges in the expression for the inter-particle force. This was subsequently extended to 3D by Xu *et al.* [152] for the D3Q15 velocity set and [153] for the D3Q19 velocity set. Shan [154] reported on how higher order isotropic discrete gradient operators can reduce the spurious currents. For use with the MRT model, the method of Li *et al.* [141] allows for thermodynamic consistency to be better approximated through the introduction of a free parameter to control the mechanical stability.

### 3.4 Thermal Multiphase Modelling

Within the pseudopotential framework, there have been numerous studies investigating the effects of temperature on multiphase flows with liquid-vapour phase change. Most of these models have used either the DDF or hybrid approach described in §2.4. The first of these models is attributed to Zhang and Chen who used the hybrid approach to simulate the boiling process [155]. Typically, for the hybrid approach a second- or fourth-order Runge-Kutta finite difference scheme is used to solve a temperature/energy equation. Examples of which include modelling of boiling and heat transfer [156], two- and three-dimension sessile droplet evaporation on patterned hydrophilic and hydrophobic strips [157, 158], two-dimensional droplet evaporation on a rough surface [159] and two-dimensional self-propelled Leidenfrost droplets on ratchet surfaces [160].

For the DDF method, care must be taken to ensure additional error terms highlighted through Chapman-Enskog expansion do not significantly affect the solution. Li *et al.* [161] highlighted the error terms and presented corrections both in the single- and multiple-relaxation time framework. Additionally, for single-relaxation time models Ahad *et al.* [162] investigated different force incorporation methods in terms of thermodynamic consistency and stability. Examples of DDF thermal multiphase modelling include thin film evaporation [163], thermal inkjet droplet ejection [164], suspended droplet evaporation with Marangoni effects [165] and droplet evaporation on heated micro-pillared surface [166]. For a review of thermal models for multiphase flow see the review by Li *et al.* [135] and references therein.

The temperature equation for multiphase simulations with phase change is derived from the local balance law for entropy [167, 168]. Effects of compression and viscous heating are neglected to give the governing equation

as

$$\frac{\partial T}{\partial t} = -\mathbf{u} \cdot \nabla T + \frac{1}{\rho C_v} \nabla \cdot (\lambda \nabla T) - \frac{T}{\rho C_v} \left( \frac{\partial p_{EOS}}{\partial T} \right) \nabla \cdot \mathbf{u}, \quad (3.58)$$

where  $C_v$  is the specific heat at a constant volume and  $\lambda$  is the thermal conductivity. The right-hand side term captures effects due to phase change, where the derivative of pressure, given by the equation 3.55, with respect to temperature is

$$\frac{\partial p_{EOS}}{\partial T} = \frac{\rho}{1 - \rho b} + \frac{C_1 a \rho^2 (C_2 - C_1 \sqrt{\frac{T}{T_c}})}{(1 + 2\rho b - \rho^2 b^2) T c \sqrt{\frac{T}{T_c}}} \quad (3.59)$$

where  $C_1 = 0.873373787$  and  $C_2 = 1.873373787^4$ .

An additional LB solver can be used to solve equation 3.58 [168], however, this still requires finite-difference schemes to compute each of the gradient terms. Furthermore, the pseudopotential forcing term has unwanted effects on the temperature equation, which need to be corrected [169]. Therefore, in this research, the temperature equation is solved with a 4<sup>th</sup> order Runge-Kutta method as

$$T^{t+\Delta t} = T^t + \frac{\Delta t}{6} (h_1 + 2h_2 + 2h_3 + h_4), \quad (3.60)$$

where  $h_1 = K(T^t)$ ,  $h_2 = K(T^t + \frac{\Delta t}{2} h_1)$ ,  $h_3 = K(T^t + \frac{\Delta t}{2} h_2)$  and  $h_4 = K(T^t + \Delta t h_3)$ .  $K(T^t)$  represents the right-hand side of equation 3.58.

## 3.5 Chapter Summary

There are numerous multiphase and multicomponent extensions to the original lattice Boltzmann method. In this chapter, popular models are described,

---

<sup>4</sup>Constants based on  $\omega = 0.344$  in Peng-Robinson equation of state.

and comments are made on their respective strengths and weaknesses.

For the investigations in this thesis, the pseudopotential method is adopted, as with appropriate extensions, it is capable of modelling fluids with moderate density ratios, achieving good thermodynamic consistency and incorporating realistic equations of state. Using the 3D MRT method described in chapter §2.3.1, the model is validated by comparing coexistence densities from simulations to values obtained analytically from the Maxwell equal-area construct. Furthermore, the Young-Laplace validation is performed to obtain information on the surface tensions.

Finally, extensions to the pseudopotential model for thermal flows are presented. A brief overview of past work leads to the choice of a hybrid modelling approach, where the chosen energy equation is described which is capable of capturing temperature effects due to phase change.

## CHAPTER 4

---

### Numerical Implementation

---

#### 4.1 Introduction

This chapter describes the processes of numerical implementation of the lattice Boltzmann algorithm. The process of transforming the discrete physical units into dimensionless form is first presented, in order to allow the conversion between computational results and the corresponding physical system. Secondly, the initial and boundary conditions are described along with algorithmic considerations for ease of implementation. Thirdly, a brief overview of the implementation and parallelisation techniques are described along with performance benchmarks of different multiphase models. Finally, benchmark studies are compared to analytical solutions to ensure the correct implementation of the algorithms.

## 4.2 Non-Dimensionalisation

When performing computational simulations, numbers are used without any physical scale, and it is the job of *post-processing* to assign the correct dimensions to variables. Simulation results thus far have been presented in dimensionless *lattice units* or in *reduced* form, meaning that the results are given as a ratio ( $T/T_c$  or  $\rho/\rho_c$ ), which are comparable for both simulation and experiment. Therefore, to map physical properties to simulation or *vice versa*, the conversion between dimensional and dimensionless quantities needs to be understood. To illustrate this process, the discrete lattice Boltzmann equation is rewritten for clarity as

$$f_i(\mathbf{x} + \mathbf{e}_i \Delta t, t + \Delta t) - f_i(\mathbf{x}, t) = -\frac{\Delta t}{\tau} (f_i(\mathbf{x}, t) - f_i^{eq}(\mathbf{x}, t)). \quad (4.1)$$

The moments of this equation give hydrodynamic quantities such as density and velocity at discrete lattice nodes and time intervals in physical units. The spacing between lattice nodes have units of  $[\Delta x] = m$ , the time-step interval has units of  $[\Delta t] = s$  and the relaxation time has units of  $[\tau] = s$ . The equivalent dimensionless lattice variables are marked with a ( $\tilde{\phantom{x}}$ ), giving  $\Delta \tilde{x}$ ,  $\Delta \tilde{t}$  and  $\tilde{\tau}$ . It is common with LB simulations that the lattice spacing and time step are scaled such that  $\Delta \tilde{x} = \Delta \tilde{t} = 1$ . To ensure that simulations are configured correctly, relevant dimensionless numbers such as the Reynolds, Mach, Weber, etc. need to be matched. Flows with the same dimensionless numbers and geometric similarity are considered identical. For the Re number, this is given as

$$\text{Re} = \frac{lu}{\nu} = \tilde{\text{Re}} = \frac{\tilde{lu}}{\tilde{\nu}}. \quad (4.2)$$

The Mach number, Ma, is useful for characterising compressibility effects

and is defined as

$$\text{Ma} = \frac{|u|}{c_s} = \tilde{\text{Ma}} = \frac{|\tilde{u}|}{\tilde{c}_s}, \quad (4.3)$$

where  $\tilde{c}_s$  is the lattice speed of sound  $\tilde{c}_s \approx 0.577$ . As the LBM is used as a solver for the incompressible Navier-Stokes equations, the only requirement for the lattice Mach number is that it is sufficiently small,  $\tilde{\text{Ma}} < 0.3$  [44]. Allowing for differences in  $\tilde{\text{Ma}}$  allows for much quicker computation speeds, as the time-step can be much larger, thus there is no attempt to match the Mach number in simulations.

### 4.2.1 Conversion Factors

To map simulation units to physical units and *vice versa*, three basic independent conversion factors are required. The conversion factors are dimensional values with the constraint that none of the three basic conversion factors can be comprised of the other two. For example, the conversion factor for length,  $C_l$ , is given by

$$C_l = \frac{\Delta x}{\Delta \tilde{x}}, \quad (4.4)$$

where as a consequence of  $\Delta \tilde{x} = \Delta \tilde{t} = 1$ ,  $\Delta x = C_l$  and  $\Delta t = C_t$ . If a droplet with a diameter of  $D_0 = 50\mu\text{m}$  is modelled with 25 lattice nodes then  $\Delta x = C_l = 2 \times 10^{-6}\text{m}$ . Therefore, any *length* measured in the simulation is converted to a physical dimensional value by multiplication with the conversion factor. The choice of density as a second independent conversion factor is also straightforward. Although the models used in this thesis capture both the liquid and vapour phases each with their own density value, the liquid phase value is taken for conversion as  $C_\rho = \rho_l / \tilde{\rho}_l$ . Finally, a conversion

factor is required which contains the time dimension, this could be directly  $C_t$  (units of  $s$ ),  $C_u$  (units of  $ms^{-1}$ ) or  $C_\nu$  (units of  $m^2s^{-1}$ ). The choice will determine how all other conversion factors are determined, examples of which are given in table 4.1.

For clarity and compactness of notation throughout the rest of the thesis,  $\Delta x$  and  $\Delta t$  will be used to refer to the dimensionless lattice counterparts unless mentioned otherwise. Furthermore, all variables, unless otherwise stated will be assumed to be given in dimensionless lattice units.

Physical Property	Physical Units	Conversion Factor
$L$	$m$	$C_l$
$\rho$	$\frac{kg}{m^3}$	$C_\rho$
$\mathbf{u}$	$\frac{m}{s}$	$C_u$
$t$	$s$	$\frac{C_l}{C_u}$
$\mathbf{g}$	$\frac{m}{s^2}$	$\frac{C_u^2}{C_l}$
$\nu$	$\frac{m^2}{s}$	$C_u C_l$
$\eta$	$Pa \cdot s$	$C_\rho C_u C_l$
$\sigma$	$\frac{N}{m}$	$C_\rho C_u^2 C_l$
$p$	$Pa$	$C_\rho C_u^2$

Table 4.1: Physical quantities and conversion factors for LBM simulations. Rows highlighted in grey are the three basic conversion factors which are used to derive other conversion factors.

## 4.3 Boundary and Initial Conditions

The LBM is often praised for its ability to handle complex geometries [44]. Specifically, the no-slip boundary condition is easily implemented at nodes identified to be solid as will be described in the following sections. However, unlike conventional CFD methods, where macroscopic values can be prescribed at boundaries, the LBM has to define values for each of the unknown populations, which then recover the desired macro-scale phenomena.

When characterising LBM boundaries, the order of accuracy describes how the error scales with resolution ( $\Delta x$ ) and the level of exactness describes the method's ability to correctly resolve a flow of certain order. The bulk LBM is spatially second order accurate and second order exact [122], however, unless boundaries are correctly modelled, the overall accuracy and exactness of the method is reduced.

Typically, at a boundary there are more unknown populations,  $f_i$ , than there are macroscopic constraints, consequently, there are many unique solutions to defining these missing values [170, 171, 172, 173, 174, 175, 176, 177, 178, 179]. Reviews of different boundary conditions for single-phase flows can be found in [180, 181, 182]. For multiphase flows, open boundary conditions are reviewed in [183].

### 4.3.1 Periodic Boundary

Possibly the simplest boundary condition used in LB simulations is the periodic boundary, in which populations that are leaving one side of the domain then return at the opposite side. This boundary condition essentially joins opposites sides of the domain together (illustrated in figure 4.1), and is expressed as

$$f_i(\mathbf{x} + \mathbf{e}_i \Delta t, t + \Delta t) = f_i^*(\mathbf{x} + \mathbf{L}, t), \quad (4.5)$$

where  $\mathbf{L}$  is the length in the direction of periodicity. Implementation is straightforward and is encompassed in the streaming step. It is also possible to extend the periodic boundary conditions to include pressure variations at opposite ends of the domain [184].

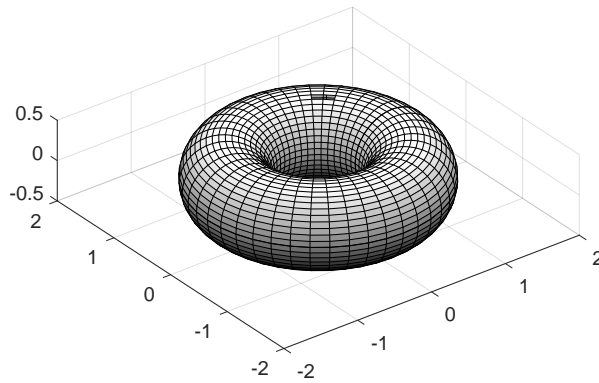


Figure 4.1: Illustration of the periodic boundary condition applied to each side of a 2D simulation, giving a toroidal geometry.

### 4.3.2 No-Slip Boundary

The no-slip boundary condition ensures the fluid velocity at a boundary is equal to the boundary velocity,  $\mathbf{u}(\mathbf{x}_b, t) = \mathbf{u}_b(\mathbf{x}_b, t)$ . For the case of a stationary boundary ( $\mathbf{u}_b = 0$ ), there are simple *bounce-back* methods which have their roots in LGA. The bounce-back method comes in two variants: *full-way* and *half-way*. The names refer to the interpretation of the path travelled by a population  $f_i^*(\mathbf{x}_b, t)$  travelling to a solid node. In the full-way variant, the population is assumed to travel to a solid node, whereas in the

half-way variant, the population is assumed to travel halfway towards the solid node before it is reflected back. Depending on the method, implementation can be achieved by modifying either the streaming or collision steps. Despite what the names may suggest, the actual location of the boundary is approximately mid-way between the boundary and solid node. Ziegler *et al.* [185] showed that if the boundary is assumed to be located between the solid and boundary node then the bounce-back scheme is second order accurate. For the *half-way* bounce-back method, solid nodes are not strictly required, however, including them means boundary nodes do not need to be identified for modification to the streaming step. When including solid nodes, the post-collision populations can be allowed to stream into them, where an additional routine is performed to reverse and stream the populations back within the same time step. This method makes incorporating arbitrary geometries straightforward and is illustrated in figure 4.2 for a straight boundary. For the remainder of this thesis, the *half-way* variant is used and is henceforth referred to as just the *bounce-back* condition.

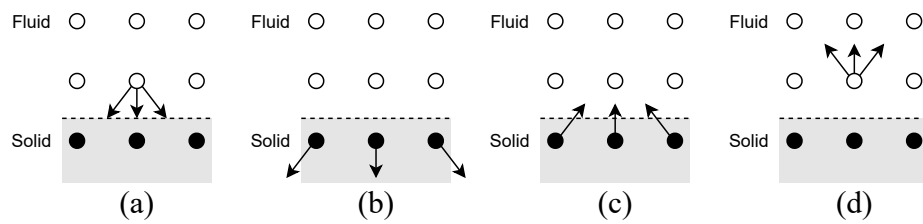


Figure 4.2: Illustration of half-way bounce-back boundary condition. (a) post-collision populations ( $t = t$ ), (b) populations streamed to solid node, (c) population velocities reversed and (d) reversed velocity populations streamed back to boundary ( $t = t + \Delta t$ ).

Formally, the bounce-back boundary condition can be expressed as

$$f_{\bar{i}}(\mathbf{x}_b, t + \Delta t) = f_i^*(\mathbf{x}_b, t), \quad (4.6)$$

where  $f_{\bar{i}}$  is the population in the opposite direction to  $f_i$  and  $f_i^*$  is the post-collision value of the population.

### 4.3.3 Open Boundary

The non-equilibrium bounce-back boundary of Zou-He (ZH) [174] can be used to specify the pressure or velocity at simulation boundaries. This boundary condition specifies the unknown boundary populations, which are then involved in the collision process. Unlike the bounce-back conditions, it is assumed to place the boundary exactly on the lattice nodes. The original ZH model was derived in 2D and a generalised extension for the 3D simulations was given by Hecht and Harting [186]. An example is given for setting the pressure/ density at the top of a 3D multiphase simulation (D3Q19 velocity set in figure 2.3). The macroscopic quantities are first expanded in terms of the known ( $f_i$ ) and unknown ( $\bar{f}_i$ ) populations:

$$\rho = f_0 + f_1 + f_2 + f_3 + \bar{f}_4 + f_5 + f_6 + f_7 + \bar{f}_8 + f_9 \quad (4.7)$$

$$+ f_{10} + f_{11} + \bar{f}_{12} + \bar{f}_{13} + f_{14} + f_{15} + f_{16} + f_{17} + \bar{f}_{18},$$

$$\rho u_x = f_1 + f_7 + f_9 + \bar{f}_{13} + f_{15} \quad (4.8)$$

$$- (f_2 + \bar{f}_8 + f_{10} + f_{14} + f_{16}) + \frac{F_x}{2},$$

$$\rho \bar{u}_y = f_3 + f_7 + f_{11} + f_{14} + f_{17} \quad (4.9)$$

$$- (\bar{f}_4 + \bar{f}_8 + \bar{f}_{12} + \bar{f}_{13} + \bar{f}_{18}) + \frac{F_y}{2},$$

$$\rho u_z = f_5 + f_9 + f_{11} + f_{16} + \bar{f}_{18} \quad (4.10)$$

$$- (f_6 + f_{10} + \bar{f}_{12} + f_{15} + f_{17}) + \frac{F_z}{2}.$$

For simplicity, it is assumed  $F_y = 0$ . Equations 4.7 and 4.9 can be combined and rearranged to find an expression for either the density,  $\rho$ , or the velocity  $u_y$ . For a specified pressure/ density pressure boundary condition, the velocity,  $\bar{u}_y$ , is solved for as

$$\bar{u}_y = 1 - \frac{1}{\rho_0}(f_0 + f_1 + f_2 + f_5 + f_6 + f_9 + f_{10} + f_{15} + f_{16} + 2(f_3 + f_7 + f_{14} + f_{11} + f_{17})), \quad (4.11)$$

which is expressed using only known populations. Finally, the unknown populations ( $\bar{f}_4, \bar{f}_8, \bar{f}_{12}, \bar{f}_{13}$  and  $\bar{f}_{18}$ ) are expressed as

$$\bar{f}_4 = f_3 - \frac{1}{3}\rho\bar{u}_y, \quad (4.12)$$

$$\bar{f}_8 = f_7 + \frac{\rho}{6}(-\bar{u}_y + u_x) + N_x, \quad (4.13)$$

$$\bar{f}_{12} = f_{11} + \frac{\rho}{6}(-\bar{u}_y - u_z) + N_z, \quad (4.14)$$

$$\bar{f}_{13} = f_{14} + \frac{\rho}{6}(-\bar{u}_y + u_x) - N_x, \quad (4.15)$$

$$\bar{f}_{18} = f_{17} + \frac{\rho}{6}(-\bar{u}_y + u_z) - N_z, \quad (4.16)$$

where  $N_x$  and  $N_z$  are correction terms given as

$$N_x = \frac{1}{2}[(f_1 + f_9 + f_{15}) - (f_2 + f_{10} + f_{16})] - \frac{1}{3}\rho u_x + \frac{F_x}{4}, \quad (4.17)$$

$$N_z = \frac{1}{2}[(f_5 + f_9 + f_{16}) - (f_6 + f_{10} + f_{15})] - \frac{1}{3}\rho u_z + \frac{F_z}{4}. \quad (4.18)$$

#### 4.3.4 Symmetry Boundary

In order to increase computational efficiency, symmetry boundary conditions can be used where appropriate. For multiphase simulations which involve a stationary droplet, such as Young-Laplace validation for determining the

surface tension, three planes of symmetry can be identified in 3D, and two planes in 2D. Therefore, with appropriate symmetry boundary conditions, run times can be reduced significantly. To implement symmetry boundary conditions in a multiphase simulation, the pseudopotential must be copied from the boundary nodes into ghost nodes ( $\psi(\mathbf{x}_s)$ ) before computation of the inter-particle force ( $\mathbf{F}_m$ ). For a plane of symmetry on the left-hand side of the domain, the pseudopotential is simply copied into the ghost node as

$$\psi(\mathbf{x}_s, t) = \psi(\mathbf{x} + 1). \quad (4.19)$$

In the bulk, the post-collision populations pointing towards the symmetry boundary are also then copied into the ghost nodes. The directions of the populations are then reversed in the direction normal to the boundary, which again for the D3Q19 velocity set in figure 2.3 is expressed as

$$\begin{aligned} f_1(\mathbf{x}_s, t) &= f_1(\mathbf{x} + 1, t), \\ f_7(\mathbf{x}_s, t) &= f_{14}(\mathbf{x} + 1, t), \\ f_9(\mathbf{x}_s, t) &= f_{16}(\mathbf{x} + 1, t), \\ f_{13}(\mathbf{x}_s, t) &= f_8(\mathbf{x} + 1, t), \\ f_{15}(\mathbf{x}_s, t) &= f_{10}(\mathbf{x} + 1, t). \end{aligned} \quad (4.20)$$

Finally, the normal streaming step is performed everywhere, including the ghost nodes. This is also equivalent to a free-slip boundary, illustrated in figure 4.3.

To ensure that the multiphase symmetry boundary is working as intended, a stationary free droplet is examined and the resulting density and velocity profiles are compared to the corresponding free droplet modelled in full. As ghost nodes are used for implementing the symmetry boundary, and they are

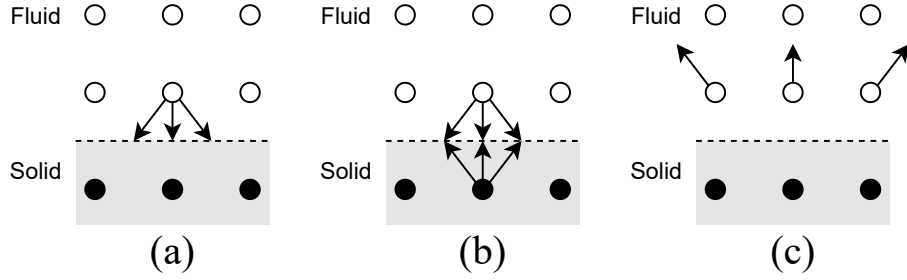


Figure 4.3: Illustration of free-slip boundary condition. (a) post-collision populations at  $t = t$ , (b) populations copied to ghost nodes with velocities normal to the boundary reversed and (c) populations streamed back to the domain  $t = t + \Delta t$ .

required to be at opposite sides of the domain, the number of nodes required in the full study is given as

$$N_{\alpha}^F = 2N_{\alpha}^S - 4. \quad (4.21)$$

where  $N_{\alpha}^F$  is the number of nodes in a fully periodic domain and  $N_{\alpha}^S$  is the total number of nodes (including ghost nodes) with symmetry boundary conditions applied to opposite sides of the domain. The density and velocity profiles after  $2000\Delta t$  are displayed in figure 4.4 for both simulations, the results of which are exactly the same. The total time elapsed for the simulation with symmetry boundary conditions was  $t = 49.9s$  whereas for the full periodic domain the time takes was  $t = 217.9s$ .<sup>1</sup>

### 4.3.5 Initial Conditions

When initialising LB simulations, not only do macroscopic quantities such as velocity and density need to be specified at  $t = 0$ ,  $\rho_0$  and  $\mathbf{u}_0$  respectively,

<sup>1</sup>Simulations run on desktop PC with Intel® Core™ i7-4770K Processor.

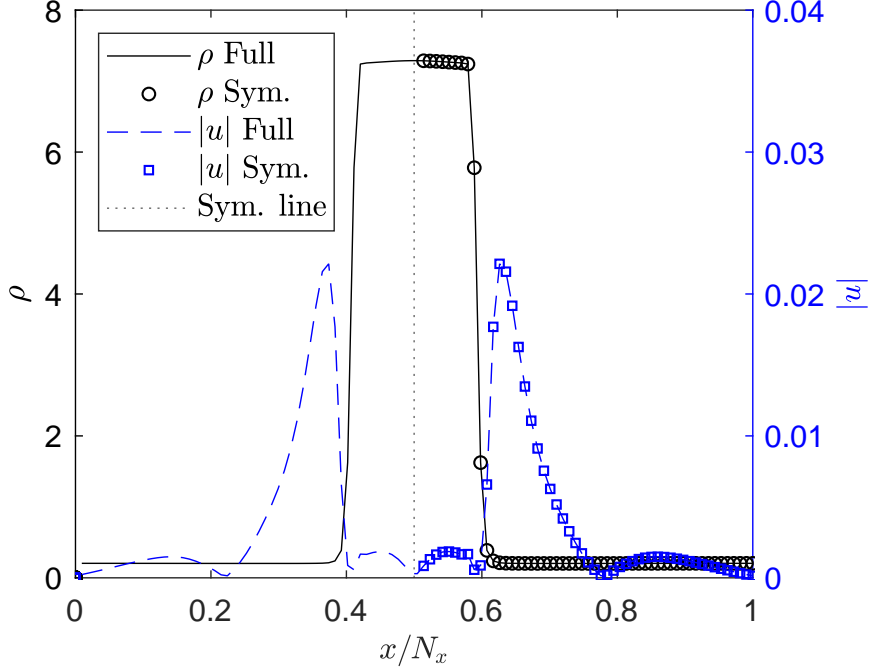


Figure 4.4: Validation of the symmetry boundary condition for pseudopotential model. Symbols illustrate symmetry boundary results and solid lines show results from comparable full domain.

but also the discrete velocity distribution function  $f_i(\mathbf{x}, t = 0)$  needs to be specified. The simplest strategy, and the one utilised throughout this thesis is to set populations at  $t = 0$  to the computed equilibrium values  $f_i(x, t_0) = f_i^{eq}(\rho_0, \mathbf{u}_0)$ . Although convenient in terms of implementation, this simple scheme has noticeable drawbacks for multiphase simulations such as the generation of pressure waves at the start of simulations, however, these tend to dissipate after a few time-steps. For multiphase simulations in which a droplet is to be simulated, the density field is initialised as

$$\rho(\mathbf{x}, t_0) = \frac{(\rho_l + \rho_v)}{2} - \frac{(\rho_l - \rho_v)}{2} \tanh\left(\frac{|\mathbf{x} - \mathbf{x}_0| - R_0}{w}\right), \quad (4.22)$$

where  $\mathbf{x}_0$  is the specified centre location of the droplet,  $R_0$  is the radius and  $w$  is the interface thickness. Similarly, if the droplet has a specified initial velocity,  $\mathbf{u}_D$ , the velocity field is initialised as

$$\mathbf{u}(\mathbf{x}, t_0) = \begin{cases} \frac{\rho(\mathbf{x}, t_0)}{\rho_l \mathbf{u}_D} & \text{if } \rho(\mathbf{x}, t_0) \geq \rho_a, \\ 0 & \text{otherwise,} \end{cases} \quad (4.23)$$

where  $\rho_a$  is a chosen density that is larger than the vapour density. In all multiphase simulations in this thesis, the value of  $\rho_a = 0.1(\rho_l - \rho_v) + \rho_v$  is used.

## 4.4 Computing Performance: Parallelisation

The lattice Boltzmann codes used in this thesis are written in the C programming language. As a compiled language, it is typically faster than languages that need to be interpreted [44]. Furthermore, once the codes are written, compiler optimisation is used for performance gains during execution. There are different levels of optimisation, starting from the lowest level of optimisation `-O0`, to the highest level of optimisation, `-Ofast`. For the codes used in this thesis, either `-O3` or `-Ofast` optimisation is used.

As often described in the literature, the LBM is very amenable to parallelisation. Tremendous speed-up of the LBM algorithm can be obtained by running on *graphical processing units* [187]. However, it is not the goal of this thesis to produce the quickest simulations. Rather, relatively simple and easy to implement techniques are used to increase the computational speed a sufficient amount for the required number of simulations to be performed. Therefore, in this research two different parallelisation techniques are used: *shared memory parallelism* using OpenMP and *distributed memory parallelism* using the message passing interface (MPI).

The standard single-phase LBM algorithm performs most of its operations locally, such as computing macroscopic variables, calculating equilibrium distributions and performing collision. The non-local operations are simple information transfers to neighbouring lattice nodes to complete the streaming step. When modelling multiphase flow with the pseudopotential model, additional information from the nearest neighbouring nodes is required and as such, the algorithm loses efficiency. OpenMP parallelisation is easily implemented into the existing pseudopotential codes. There are two main functions within the code for implementing the pseudopotential model, the first of which is the computation of density/ pseudopotential at each lattice node,

and the second is responsible for computing forces, collisions and streaming. OpenMP directives of `parallel for` are added to these functions, which split the code into threads, and are then executed in parallel. The performance of a lattice Boltzmann algorithms are typically measured in terms of how many lattice sites are updated per second, typically this is a large number, so the performance is given in terms of million lattice updates per second (MLUPS). The performance of the pseudopotential algorithm with an increasing number of threads is illustrated in figure 4.5. Where good speed-up is obtained, with a maximum speed of 52MLUPS.

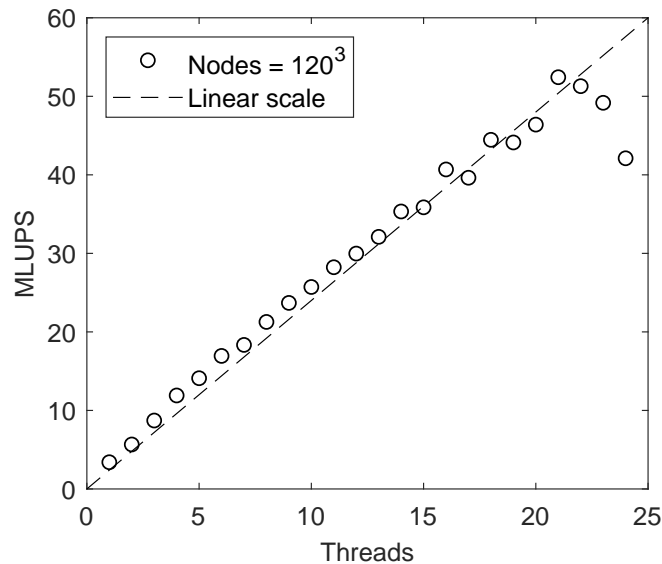


Figure 4.5: Scaling performance of 3D pseudopotential model with shared memory parallelisation. Domain comprised of  $120^3$  lattice nodes.

For distributed memory parallelism with MPI, the domain is divided into sections and a dedicated processor will compute the properties at a specific portion of the domain. In this thesis, a simple 1-Dimensional domain decomposition is applied, which is illustrated in figure 4.6.

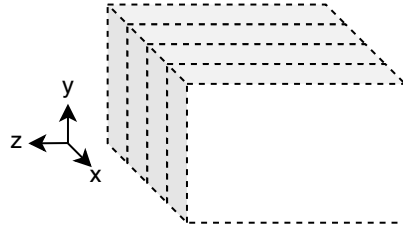


Figure 4.6: Illustration of simple one-dimensional domain decomposition for MPI parallelisation.

As the memory is distributed over a network, information will need to be sent to different processors in order to ensure the whole system is updated as expected. An illustrative example is provided in figure 4.7. Here, values of the pseudopotential at the right-hand side of the domain in rank  $n$  will need to be known by nodes at the left-hand side of rank  $n + 1$  in order to compute the inter-particle force. These values will therefore be sent to *ghost nodes*, which are used for computational convenience to temporarily store values until they are no longer needed.

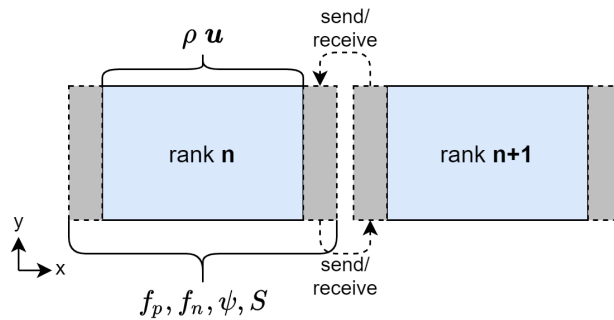


Figure 4.7: Illustration of message passing with distributed memory systems. Grey shaded regions represent *ghost layers* which are shared between processors.

The strong scaling<sup>2</sup> performance of each of the multiphase models described in section 3.2 is investigated for the case of a stationary droplet in a fully periodic domain. A two-dimensional domain of  $N_x = N_y = 2048$  lattice nodes, with relaxation times equal to 1 and a droplet radius of  $R = 500$  placed in the centre of the domain was configured. Each of the models was compiled with -O3 optimisation, and run with an increasing number of processes on the ARCHER UK supercomputer. For an increasing number of processes, the number of time-steps was increased to give an approximate total run time of 20s, allowing for accurate measurement of the performance. The results are plotted in figure 4.8. Linear scaling is displayed for each of the models, and the pseudopotential (Shan-Chen), and Free Energy models are shown to exhibit the best performance.

As the subsequent investigations in this thesis use the pseudopotential multiphase model, the performance of the algorithm is investigated in three dimensions, figure 4.9, where again a linear scaling is displayed and a maximum speed of 205MLUPS is obtained.

---

<sup>2</sup>Performance can be categorised by *strong scaling* or *weak scaling*, which shows speedup with the number of cores or the ability to simulate a larger domain for the same time with more cores respectively.

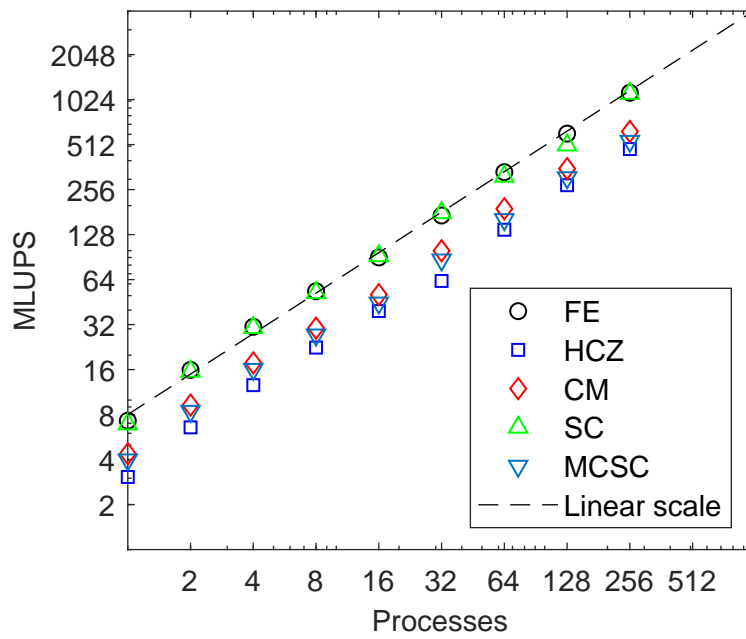


Figure 4.8: Strong scaling performance for multiphase lattice Boltzmann models in 2D parallelised with MPI. Models include Free-Energy (FE), He-Chen-Zhang (HCZ), colour model (CM), Shan-Chen (SC) and multi-component Shan-Chen (MCSC).

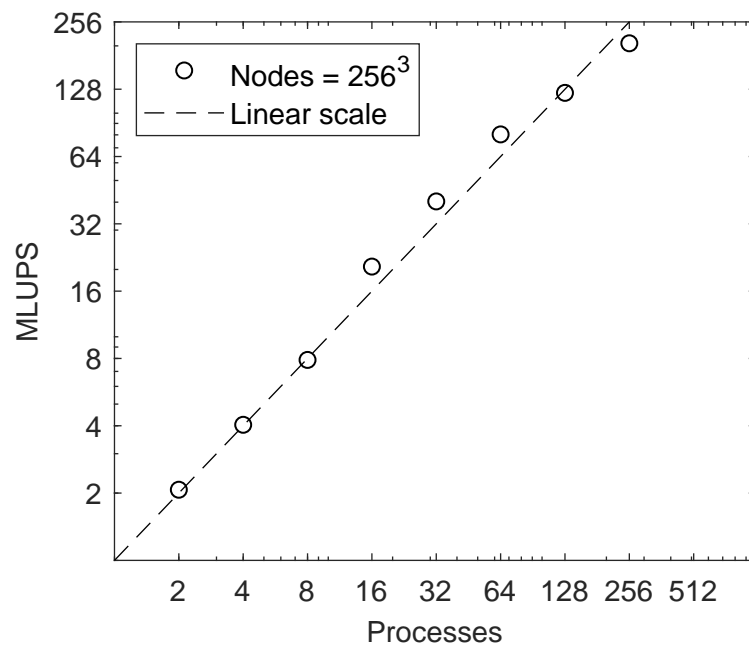


Figure 4.9: Scaling performance for 3D pseudopotential multiphase model parallelised with MPI.

## 4.5 Hydrodynamic Boundary Validation

### 4.5.1 Multiphase Convergence

To determine the convergence level of a simulation in which a steady state exists, the  $L_2$  error norm is used. For this, macroscopic quantities ( $\varphi$ ) at time  $t = t$  are compared to quantities at a previous time-step  $t = t - N\Delta t$ . The  $L_2$  error norm is thus defined as:

$$L_2 := \sqrt{\frac{\sum_x (\varphi(\mathbf{x}, t) - \varphi(\mathbf{x}, t - N\Delta t))^2}{\sum_x \varphi^2(\mathbf{x}, t - N\Delta t)}}. \quad (4.24)$$

For multiphase simulations, quantities such as density or velocity could be used for evaluating the level of convergence. Illustrated in figure 4.10 are the density and the velocity magnitude errors for the simulation of a stationary droplet in a fully periodic domain. Here it can be seen that in the early stages of the simulations, the velocity is changing consistently and not converging. This is due to the creation of spurious velocities in multiphase simulations, which are not accounted for in the initialisation. However, once the spurious velocities are generated, both the density and velocity error converge at the same rate. Included in the figure is a dashed black line that shows the point at which  $L_2 = 10^{-7}$ , which could represent a threshold for determining if the simulation is sufficiently well converged. However, as can be seen, the error values do not decay at a smooth rate, and the error can pass below the threshold triggering the simulation to be stopped prematurely. To overcome this, a simple counter is utilised which is used to check that the convergence criteria are met in a number of consecutive steps.

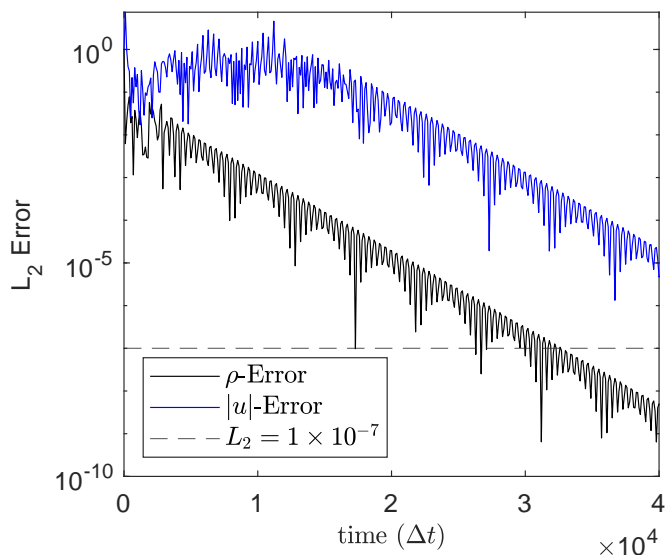


Figure 4.10: Convergence residuals for density and velocity magnitude in multiphase simulation of a stationary droplet in a fully periodic domain.

## 4.5.2 Flow in a Square Duct: Gravity Driven

To validate the implemented boundary conditions, the 3D-MRT model with a single-phase fluid is used to simulate force driven Poiseuille flow through a square duct. The simulation results at different lattice resolutions are compared to the analytical solution [188] for the fluid flow

$$u_x(y, z) = \frac{16a^2 F_x}{\rho\nu\pi^3} \sum_{i=1,3,5,\dots}^{i=\infty} (-1)^{(i-1)/2} \left[ 1 - \frac{\cosh(i\pi z/2a)}{\cosh(i\pi/2)} \right] \frac{\cos(i\pi y/2a)}{i^3}, \quad (4.25)$$

where  $a$  is half the duct width and  $F_x$  is the body force. Although the solution to the velocity field required an infinite sum, a sufficiently accurate velocity profile is obtained by including terms up to and including  $i = 51$ . An illustration of the resulting velocity profile is given in figure 4.11.

To validate the 2<sup>nd</sup> order accuracy of the boundary condition, as well as

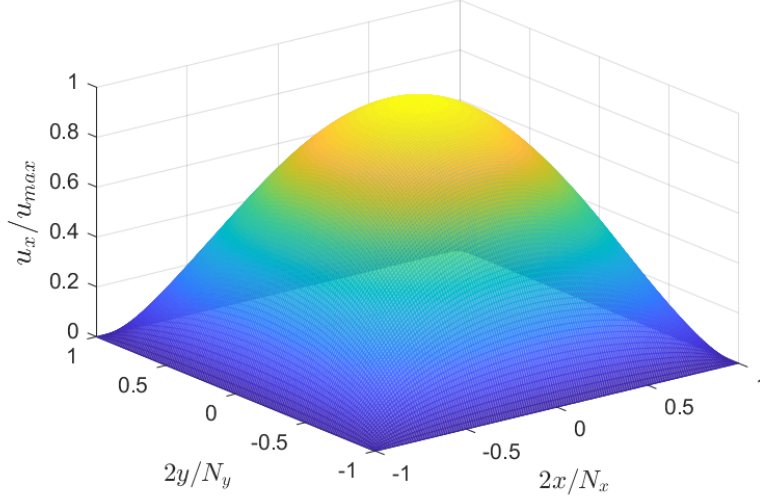


Figure 4.11: Illustration of flow velocity ( $u_x(y, z)$ ) for gravity driven Poiseuille flow in a square duct.

ensure correct implementation of the LB algorithm, simulation results at different lattice resolutions are compared to the analytical solution for flow in a square duct (equation 4.25). As the flow is invariant in the  $x$ -direction, only 3 lattice nodes are used. The Reynolds number was fixed at  $\text{Re} = 10$  and the lattice viscosity was fixed at  $\nu = 0.05$  ( $\tau_\nu = 0.65$ ), with all other relaxation rates set to unity. For each lattice resolution, the gravitational acceleration force  $F_x$  is set to ensure the target Reynolds number ( $\text{Re} = 10$ ) is reached.

The simulations are run until a convergence threshold of  $10^{-7}$  is obtained, after which, the lattice velocity  $u_x$  is compared to the analytical solution. However, the velocity is only available at discrete lattice nodes  $u_x(x_i, y_j, z_k)$ , where  $x_i (i = 0, \dots, N_x - 1)$  etc., thus to compare with the continuous analytical solution, the discrete lattice values are mapped to the physical space as  $z = k - (N_z - 2)/2 - 0.5$ . The error between simulation and analytical

solution is also calculated with the  $L_2$  error norm, in equation 4.24 where  $\varphi(\mathbf{x})$  and  $\varphi(\mathbf{x}, t - N\Delta t)$  replaced with  $u_x(\mathbf{x})_{\text{LBM}}$  and  $u_x(\mathbf{x})_{\text{ANA}}$ , the lattice Boltzmann results and the analytical solution respectively. The computed error for increasing lattice resolution is displayed in figure 4.12, where the error can be seen to reduce at a second order rate.

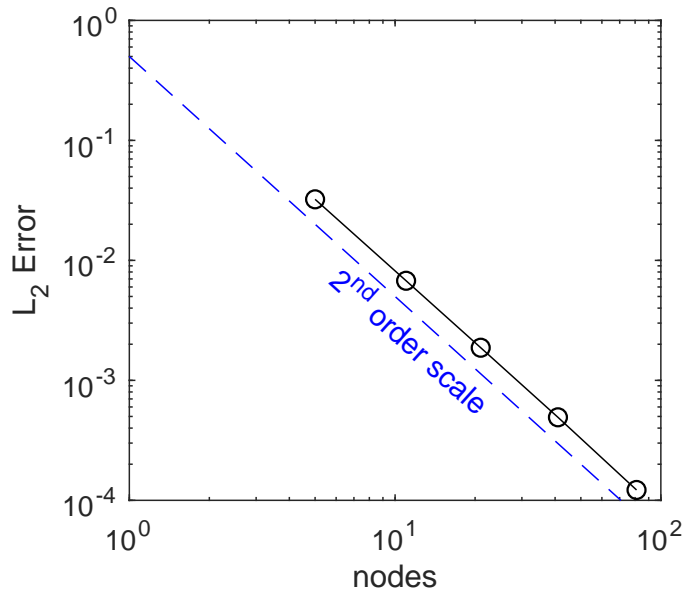


Figure 4.12: Grid convergence for 3D gravity driven Poiseuille flow with single-phase LBM. For each lattice resolution the Reynolds number is fixed at  $\text{Re} = 10$  and kinematic viscosity fixed at  $\nu = 0.05$  ( $\tau_\nu = 0.65$ ).

### 4.5.3 Flow in a Square Duct: Pressure Driven

To validate the 3D Zou-He boundary implementation described in §4.3.3, pressure driven Poiseuille flow through a square duct is simulated. The no-slip boundaries are still handled with the bounce-back method, whereas instead of constant gravitational acceleration, the Zou-He boundary sets con-

stant pressures at the inlet and outlet of the simulation domain. For each simulation, the outlet pressure is  $p_{out} = c_s^2$ , or equivalently, the outlet density  $\rho_{out} = 1$ . The same domain sizes and Reynolds numbers are used as in the gravity driven study, therefore, the equivalent inlet pressure for each simulation is calculated as  $p_{in} = \frac{1}{c_s^2}(F_x(N_x - 1) + p_{out})$ . Due to the pressure gradient at the inlet and outlet, the length of the channel was set to be  $N_x = 2N_y$ , which substantially increases the computation time. The simulations are again run until a convergence threshold of  $10^{-7}$  is obtained.

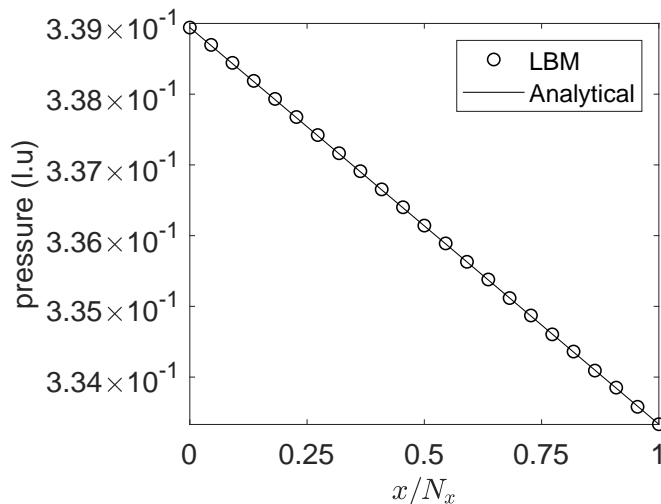


Figure 4.13: Validation of pressure distribution in 3D pressure driven Poiseuille flow with Zou-He boundary conditions.

For coarser lattice resolutions, the inlet pressure/density is required to be larger for the required Re number, this introduces additional compressibility errors into the simulation. As the lattice resolution increases, the difference between the inlet and outlet pressure/density reduces and the compressibility effects are minimised. An illustration of the pressure profile along the centre of the channel is displayed in figure 4.13, where the expected linear profile

is observed. The velocity error is again computed with the  $L_2$  norm and displayed in figure 4.14, where again the error can be seen to reduce at a second order rate.

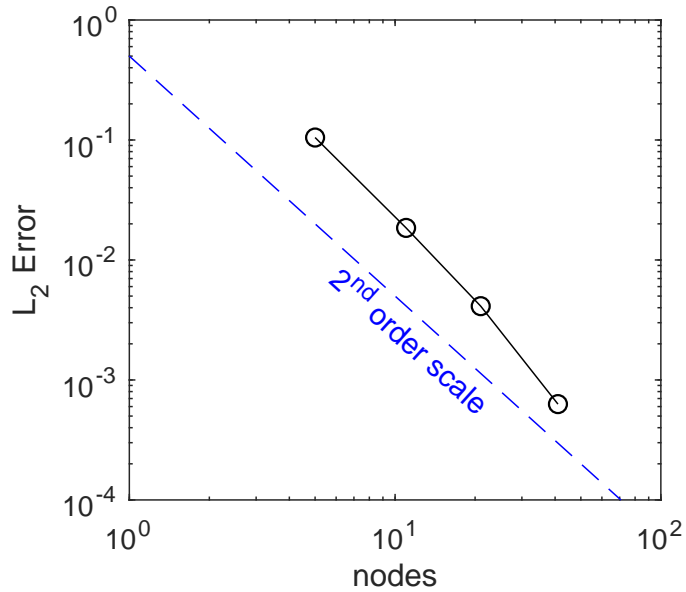


Figure 4.14: Grid convergence for 3D pressure driven Poiseuille flow with single-phase LBM. For each lattice resolution the Reynolds number is fixed at  $Re = 10$  and kinematic viscosity fixed at  $\nu = 0.05$  ( $\tau_\nu = 0.65$ ).

## 4.6 Chapter Summary

In this chapter, aspects regarding the implementation of the lattice Boltzmann method are presented, starting with the process of conversion between dimensional physical units and dimensionless simulation units. Boundary conditions and initialisation procedures are described, including symmetry boundaries for multiphase simulations.

For efficient computation, the LBM is coded in the C programming language. Furthermore, to improve simulation speed, the model is parallelised, and different techniques including OpenMP and MPI are discussed. Performance results are evaluated in terms of million lattice updates per second (MLUPS). Results for OpenMP parallelisation of a 3D multiphase simulation showed maximum speeds of 52MLUPS. For MPI parallelisation, each of the multiphase models described in chapter 3 are compared in 2D. Speeds are found to increase linearly with the number of processes, with a maximum of 1126MLUPS for the pseudopotential method. In 3D, a maximum speed of 205MLUPS was achieved.

Finally, the 3D MRT model with no-slip, periodic and pressure boundary conditions was validated against analytical solutions to flow in a square duct, and the second-order accuracy of the model is confirmed.

---

### Wetting Model Evaluation and Development

---

#### 5.1 Introduction

As described in §3.2, there are numerous multiphase/ multicomponent models within the lattice Boltzmann framework. When solid surfaces are present in the simulation, each of these models can be modified to incorporate fluid-solid interaction (*wetting*). With Free-Energy based models, the Free-Energy functional is modified to account for the contribution of adhesive forces. Alternatively, for methods such as the HCZ model, wetting can be achieved by assigning walls an *effective* density, which is tuned for the desired contact angle. The same procedure is followed for colour-based models, where both colour-densities are assigned at solid walls. Soon after the development of the pseudopotential models [128, 129], modifications to allow for fluid-solid interactions (commonly referred to as *wetting models*) were presented and

promising results were achieved for both multiphase and multicomponent flows. Here, the adhesion force is computed alongside the cohesion force and incorporated into the LB algorithm through an appropriate forcing scheme. In this chapter, two key components of wetting models are evaluated, specifically, the form of the adhesion force model and the boundary treatment for the calculation of the inter-molecular force (cohesion force). Furthermore, a new wetting model is suggested which allows for control of adhesive forces over the liquid-vapour interface.

## 5.2 Multiphase Wetting Modelling

The ability to directly incorporate adhesive forces in the pseudopotential model makes it an attractive method to study wetting phenomena [189, 56, 190, 191, 192, 193, 64, 194]. Previous works investigating the performance of different wetting models have explored cases in which solid surfaces are chemically and topographically homogenous, e.g. [195], where the authors examined wetting model performance with different no-slip boundary schemes, such as the half-way bounce-back and Zou-He. Furthermore, upon suggesting a new wetting model, Li *et al.* [196] evaluated wetting model performance on smooth and structured solid surfaces, in which the Zou-He boundary was used. In these studies, key issues were identified when incorporating wetting models, such as the change of equilibrium densities close to boundaries and the generation of spurious velocities at the triple point. Typically, wetting models introduce an additional force to be incorporated into the LBM. The cohesive and adhesive force,  $\mathbf{F}_m$  and  $\mathbf{F}_{adh}$  respectively are incorporated into the LBM through a source term,  $S_i$ , which gives a general LB equation for a multiphase fluid as

$$f_i(\mathbf{x} + \mathbf{e}_i \Delta t, t + \Delta t) - f_i(\mathbf{x}, t) = \Omega_i(\mathbf{x}, t) + S_i(\mathbf{x}, t). \quad (5.1)$$

For the MRT method used throughout this thesis, the source term acts in moment space rather than population space. The source term for the D3Q19 velocity set is given in full in §3.3.1.

### 5.2.1 Existing Wetting Models

The different adhesion force models explored in this chapter can be expressed in the generalised form as

$$\mathbf{F}_{adh} = -G_{adh} \Phi_f(\mathbf{x}) \sum_i \omega(|\mathbf{e}_i|^2) \Phi_s(\mathbf{x} + \mathbf{e}_i \Delta t) s(\mathbf{x} + \mathbf{e}_i \Delta t) \mathbf{e}_i, \quad (5.2)$$

where  $G_{adh}$  is the fluid-solid adhesion strength parameter used for adjusting the wettability of the solid surface,  $s(\mathbf{x} + \mathbf{e}_i \Delta t)$  determines if a neighbouring node is solid ( $s = 1$ ) or fluid ( $s = 0$ ),  $\omega(|\mathbf{e}_i|^2)$  is a weighting coefficient, which is not required to be the same as those used in the chosen velocity set, finally,  $\Phi_f$  and  $\Phi_s$  are the fluid and solid potentials respectively.

The first wetting model proposed was by Martys and Chen [131], where  $\Phi_f(\mathbf{x}) = \rho(\mathbf{x})$  and  $\Phi_s = 1$ . Raiskinmaki *et al.* [191] then followed with  $\Phi_f(\mathbf{x}) = \psi(\mathbf{x})$  and  $\Phi_s = 1$ . Li *et al.* [196] suggested  $\Phi_f(\mathbf{x}) = \psi^2(\mathbf{x})$  and  $\Phi_s = 1$ . Zhu *et al.* [192] used  $\Phi_f(\mathbf{x}) = \rho(\mathbf{x})$  and  $\Phi_s = \psi(\mathbf{x})$ . It is common to categorise models based on the pre-sum fluid potential  $\Phi_f$ , which may be  $\rho$ ,  $\psi$  or  $\psi^2$ . Henceforth, wetting models are referred to as  $\rho$ -based,  $\psi$ -based or  $\psi^2$ -based.

A model proposed by Benzi *et al.* [189] assigns a fixed density value,  $\rho_w$ , at lattice nodes defined as solid ( $\mathbf{x}_w$ ). This gives the pseudopotential at solid walls as  $\psi(\rho(\mathbf{x}_w)) = \psi(\rho_w)$ , which enters the multiphase algorithm through

the calculation of the inter-molecular cohesion force rather than introducing an additional adhesion force. It is worth noting that if the standard pseudopotential model is used, where the sum of cohesive and adhesive force are used to update the momentum, then the wetting model can be equivalently expressed as an additional adhesive force term by setting  $\Phi_f(\mathbf{x}) = \psi(\mathbf{x})$ ,  $\Phi_s = \psi(\rho_w)$  and  $G_{adh} = G$ . However, the computation of the cohesion forces may need to be modified to ensure that  $\rho_w$  is not included twice. This is achieved by explicitly setting  $\psi(\mathbf{x}_w) = 0$ . Due to the MRT model with improved forcing used in this thesis, the total forces ( $\mathbf{F} = \mathbf{F}_m + \mathbf{F}_{adh}$ ), are treated differently from the adhesive forces individually, thus the two approaches are no longer equivalent.

Another approach frequently used within the multiphase LBM framework is the *geometric scheme* proposed by Ding and Spelt [197]. Similar to the model of Benzi *et al.* [189], this approach is incorporated into the multiphase algorithm through the calculation of the inter-molecular cohesion force and not an additional adhesion force term. This model is expressed as

$$\tan\left(\frac{\pi}{2} - \theta\right) = \frac{-\nabla\rho \cdot \mathbf{n}}{|\nabla\rho - (\mathbf{n} \cdot \nabla\rho)\mathbf{n}|}, \quad (5.3)$$

where  $\mathbf{n}$  is the unit normal to the solid surface. Once discretised, the computation of the gradient terms is used to set the density and pseudopotential in the solid nodes.

### 5.2.2 New Wetting Model

Regardless of the pre-sum factor for the adhesion force, there will be a smooth transition of the adhesion force from the liquid phase to the vapour phase over the width of the diffuse interface, which is typically large for LBM simulations. The effects of the artificially large interface compared to the

droplet diameter are described in [198], in which the authors show the resulting contact angles for Cassie-Baxter-type wetting of a micro-pillar array at increasing resolution. When the liquid-vapour interface width was comparable to the pillar size, a wetting transition state was observed resulting in incorrect contact angle determination. Whereas at higher resolution, no wetting transition occurred and the results converged towards the same contact angle measurement. Linked to this consideration is the work by Gao and McCarthy [23] in which the authors illustrate the importance of the contact line rather than the contact area in various wetting phenomena. Therefore, taking interface effects into consideration, a new wetting model is suggested which allows for modification of the wetting force over the droplet liquid-vapour interface, enabling surface-bulk and surface-interface adhesion to be controlled with greater precision. The new model is expressed as

$$\mathbf{F}_{adh} = \left[ -G_{adh}\psi^2(\mathbf{x}) \sum_i \omega(|\mathbf{e}_i|^2) s(\mathbf{x} + \mathbf{e}_i \Delta t) \mathbf{e}_i \right] (1 + |\nabla\varphi(\mathbf{x}) - (\mathbf{n} \cdot \nabla\varphi)\mathbf{n}| \chi), \quad (5.4)$$

where the terms in the square brackets give the standard wetting model of Li *et al.* [196] and the terms in the round brackets are used for modifying the adhesion force of the liquid-vapour interface. The variable  $\varphi(\mathbf{x})$  can be either the density or pseudopotential and  $\chi$  is used for tuning the liquid-vapour interface adhesion force. It is evident that the calculation of the adhesive force in the bulk, where  $|\nabla\varphi(\mathbf{x}) - (\mathbf{n} \cdot \nabla\varphi)\mathbf{n}| = 0$  i.e. away from the droplet interface, the standard wetting model of Li *et al.* [196] is recovered. The new model is henceforth referred to as the interface force modification (IFM) model. An illustration of the adhesion force profile is shown in figure 5.1 for the standard  $\psi^2$ -based model and the IFM model.

The additional gradient terms in equation 5.4 are computed numerically

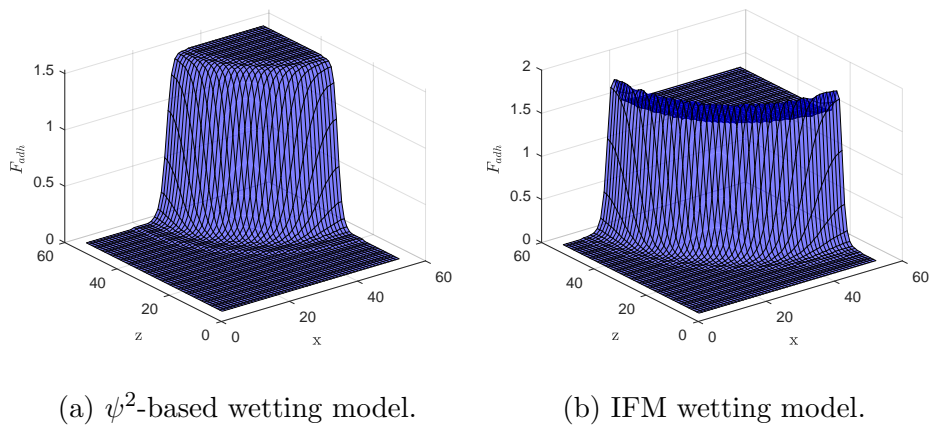


Figure 5.1: Profiles of adhesive force computed for different wetting models for a single droplet wetting a smooth surface. A quarter of the droplet is shown due to the symmetry boundary conditions.

with a standard centred  $2^{nd}$  order finite-difference scheme. However, special consideration is taken to ensure the gradient calculation only includes fluid nodes. To achieve this, if a solid node is included in the calculation of the gradient in the  $x$ ,  $y$  or  $z$  direction, the corresponding gradient(s) are set equal to zero, recovering the standard  $\psi^2$ -based wetting model. A consequence of this procedure is that the new model currently only modifies the adhesion force for solid walls aligned with a coordinate axis. However, ease of implementation is maintained.

### 5.2.3 Boundary Treatment

A key issue still to be explored in terms of adhesion force based wetting models is the fact that once solid boundaries are introduced, the calculation of the inter-molecular force (equation 3.47) at boundary nodes will be under-defined. This issue is illustrated in figure 5.2, in which the pseudopotential

values in the solid boundaries ( $\psi(\mathbf{x}_w)$ ) need to be specified. It is worth clarifying that this issue is also present for Zou-He (wet node) type boundaries, as the inter-molecular force is computed on these nodes also.

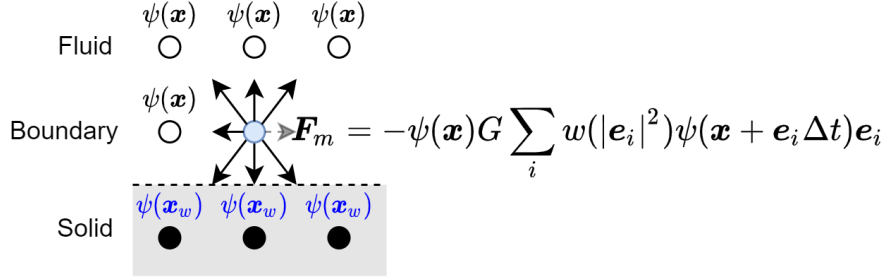


Figure 5.2: Illustration of the computation of cohesive forces at boundary nodes in which neighbouring pseudopotentials in solid nodes ( $\psi(\mathbf{x}_w)$ ) need to be defined.

One approach suggested by Sukop and Thorne [199] was to replace the unknown neighbouring pseudopotential terms with known ones in the direction normal to the boundary. This makes  $\partial_N \psi(\mathbf{x}_w) = 0$  and subsequently the cohesive force normal to the boundary zero. This results in an equilibrium contact angle of  $\theta \approx 90^\circ$  in the absence of additional forces. A drawback of this method is that boundary normals will need to be identified, and appropriate corrections applied accordingly. Variants of this boundary treatment are frequently used [200, 192, 193, 196, 201], however, it is often not explicitly stated, though it can be identified by the fact that the contact angle equilibrates to  $\theta \approx 90^\circ$  when the adhesion force is equal to zero.

It is often stated in the literature that a positive  $G_{adh}$  is required for simulating non-wetting fluids and a negative value required for wetting fluids, and for a neutrally wetting surface a value of  $G_{adh} = 0$  should be adopted [201, 196, 193, 192, 195]. However, this is only true for the previously de-

scribed boundary treatment. This confusion is made evident in [195], in which the authors make the aforementioned claim while subsequently showing that the adhesion strength parameter remains positive for both wetting and non-wetting fluids (see figure 17 in [195]).

It is therefore necessary to investigate the influence of the inter-molecular force calculation at boundary nodes on the wetting characteristics. To achieve this, three different treatments are considered. The first condition is to set pseudopotential values in solid walls equal to zero ( $\psi(\mathbf{x}_w) = 0$ ), this ensures that solid nodes are not included in the calculation of the intermolecular force. A second possible condition is to fix the wall pseudopotential to the value obtained from the equilibrium coexistence vapour density value  $\psi(\mathbf{x}_w) = \psi(\rho_v)$ . However, it is important to note that unlike the wetting model of Benzi *et al.* [189], these values are not used to achieve a desired contact angle. Finally, the model of Sukop and Thorne [199] is used in which the unknown pseudopotential values at the solid walls at the top and bottom of the domain are computed as  $\psi(\mathbf{x}_w) = \psi(\rho_{y\pm 2})$ .

### 5.3 Evaluation of Wetting Models

In the following sections wetting models are evaluated in terms of modelling aspects, such as the modification to the coexistence densities and the generation of spurious velocities. Furthermore, the static and dynamic results of droplets wetting are compared to theoretical predictions. For practical use as a simulation tool for wetting phenomena, it is desirable to set the equilibrium contact angle rather than the adhesion strength parameter,  $G_{adh}$ . Unfortunately, the relationship between  $G_{adh}$  and  $\theta$  is not known, thus for each wetting model and boundary treatment it is first required to perform

a preliminary investigation to obtain an approximate relationship between the two variables. Once an approximate relationship between  $G_{adh}$  and  $\theta$  is known for each model and boundary condition, the model performance can be evaluated under comparable scenarios.

### 5.3.1 Equilibrium Contact Angles on Homogeneous Surface

As previously mentioned, a preliminary study is required in order to determine the relationship between  $G_{adh}$  and the resulting equilibrium contact angle. This is achieved by simulating a static droplet on a smooth flat surface and measuring the resulting contact angles as  $G_{adh}$  is varied. In the absence of gravity, the droplet assumes the shape of a spherical cap, thus the contact angle can be determined as

$$\theta = 2 \tan^{-1} \left( \frac{2H}{D} \right), \quad (5.5)$$

where  $H$  and  $D$  are the droplets height and contact diameter respectively. For the following investigations, the half-way bounce back boundary is used, which places the physical boundary  $0.5\Delta x$  lattice spacing away from the boundary node. As the height and diameter can not be measured directly on this physical boundary, the nearest nodes are used, which for a solid floor is at the location  $y_0 = 1$ . The measurements taken from this height give  $D'$  and  $H'$  which are then related to the actual diameter and height as

$$D = \sqrt{4H(D - H)}, \quad (5.6)$$

where

$$R = \frac{2D'^2 + 4H'^2}{8H'} \text{ and } H' = H - y_0. \quad (5.7)$$

Due to the diffuse interface in multiphase simulations, which span several lattice nodes (illustrated in figure 5.3), there is ambiguity with precisely locating the *interface*. Therefore, two different definitions of the interface density  $\rho_{int}$  are defined as  $\rho_{int} = (\rho_l + \rho_v)/2$  and  $\rho_{int} = 2\rho_v$ . The location of these two densities is then linearly interpolated to give a precise location of the interface.

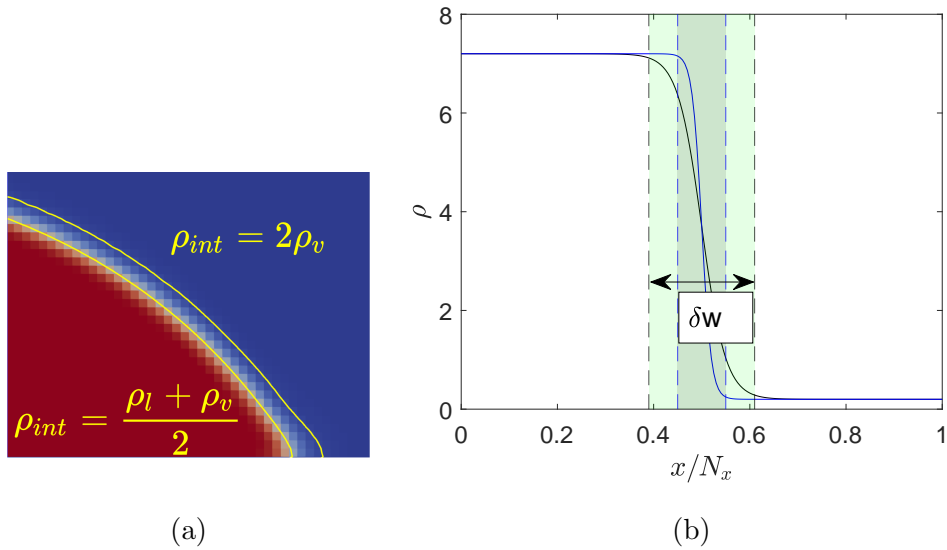


Figure 5.3: Illustration of the ambiguity in defining a precise *interface* location for diffuse interface models. (a) shows the density field for a droplet partially wetting a surface and (b) shows the density profile with different interface thicknesses.

### 5.3.2 Simulation Configuration

The effects of lattice resolution on results were first investigated. Using an arbitrary wetting model and wetting parameters, measurements of contact angles were taken for different lattice resolutions. The Peng-Robinson EOS is used, in which the temperature is  $T = 0.8T_c$ , the attraction parameter is  $a = 3/49$  and the repulsion parameter is  $b = 2/21$  giving coexistence densities of  $\rho_l \approx 7.2$  and  $\rho_v \approx 0.2$ . All relaxation times in the MRT model are set equal to 1 and  $\varepsilon = 0.085$ . Domain sizes of  $70 \times 37 \times 70$ ,  $110 \times 57 \times 110$  and  $150 \times 77 \times 150$  in the  $x$ ,  $y$  and  $z$  directions respectively were tested. For each lattice size, the droplet was set to one third the length in the  $x$  direction. Simulations ran until the convergence threshold of  $E = 10^{-6}$  for the density field was obtained. Comparing results of the recorded contact angle, the lattice resolution of  $110 \times 57 \times 110$  was determined to be sufficiently well resolved as the measured contact angles deviated by less than 3% from the finer resolution.

Therefore, using this configuration, approximate relationships for  $G_{adh}$  and the equilibrium contact angle can be obtained for each model by running a number of simulations determining a suitable polynomial relationship as

$$\theta = \sum_i k_i G_{adh}^i, \quad (5.8)$$

where  $k_i$  are coefficients for each  $G_{adh}^i$ . A total of 10 simulations are performed for each wetting model and boundary treatment. The symmetry boundary conditions described in §4.3.4 is used to increase computational speed. The following sections give the results for each of the wetting models.

### $\rho$ -based Wetting Model

The first wetting model extension of the pseudopotential method [131] was given for the multicomponent model. With this model, the pseudopotential was set equal to the density, thus the proposed wetting model was also based on the density and is expressed as

$$\mathbf{F}_{adh} = -G_{adh}\rho(\mathbf{x}) \sum_i w_i s(\mathbf{x} + \mathbf{e}_i \Delta t) \mathbf{e}_i. \quad (5.9)$$

The density based model was capable of producing a wide range of contact angles for each of the different boundary treatments. For boundary treatments  $\psi(\mathbf{x}_w) = \psi(\rho_v)$  and  $\psi(\mathbf{x}_w) = \psi(\rho_{y\pm 2})$  the relationships between  $\theta$  and  $G_{adh}$  are well approximated with a linear fit, as can be seen in figure 5.4a and 5.4b respectively. As for the boundary treatment of  $\psi(\mathbf{x}_w) = 0$ , the  $\theta$  and  $G_{adh}$  relationship is best fitted with a quadratic equation, figure 5.4a. The constants for the polynomial expressions are summarised in table 5.1.

wall treatment	$k_2$	$k_1$	$k_0$
$\psi(\mathbf{x}_w) = 0$	878.8	1743.8	878
$\psi(\mathbf{x}_w) = \psi(\rho_v)$	0.0	315.9	244.1
$\psi(\mathbf{x}_w) = \psi(\rho_{y\pm 2})$	0.0	152.7	89.5

Table 5.1: Polynomial coefficients for relating adhesion strength  $G_{adh}$  to equilibrium contact angle  $\theta$  with the  $\rho$ -based wetting model.

### $\psi$ -based Wetting Model

Depending on the method of incorporating forces into the model, the wetting models of Raiskinmaki *et al.* [191] and Benzi *et al.* [189] may be equivalent.

However, as the cohesive force ( $\mathbf{F}_m$ ) and total force ( $\mathbf{F}$ ) are incorporated individually in equation 3.57 (section 3.2), the models do in fact behave differently. Therefore, for the  $\psi$ -based model, the adhesive force is expressed as

$$\mathbf{F}_{adh} = -G_{adh}\psi(\mathbf{x}) \sum_i w_i s(\mathbf{x} + \mathbf{e}_i \Delta t) \mathbf{e}_i. \quad (5.10)$$

With this model, the range of achievable contact angles is found to be limited by simulation stability. For boundary treatments  $\psi(\mathbf{x}_w) = 0$  and  $\psi(\mathbf{x}_w) = \psi(\rho_v)$  the lowest contact angles obtainable were  $\theta \approx 102^\circ$  and  $\theta \approx 92^\circ$  respectively. The cause of the simulation instability at lower contact angles is assumed to be from the increased vapour density at boundary nodes. To overcome the simulation stability issue for boundary treatments  $\psi(\mathbf{x}_w) = 0$  and  $\psi(\mathbf{x}_w) = \psi(\rho_v)$ , the value of  $G_{adh}$  is changed from an initially stable value to the target value incrementally over a chosen number of time-steps at the beginning of the simulation. This allowed the two methods to generate a large range of contact angles. The boundary treatment  $\psi(\rho_{y\pm 2})$  was capable of modelling low contact angles, however, it was found to be limited to a maximum contact angle of  $\theta \approx 118^\circ$ . Here, the limitation was the generation of unphysical velocities, which increased in magnitude until the simulation became unstable. The cause of this additional unphysical velocity is beyond the scope of this thesis and it was not seen with other wetting models.

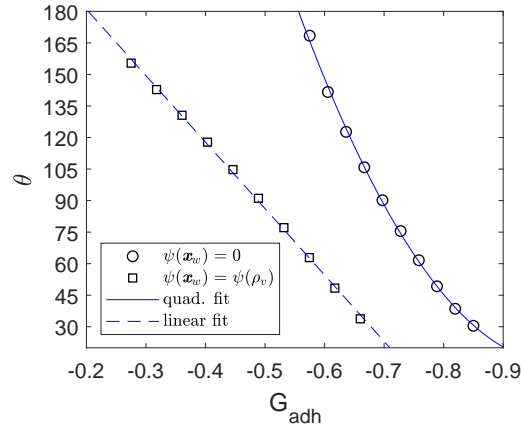
The aforementioned increased vapour density over solid surfaces causes the primary droplet to shrink as a result of ensuring that mass is conserved in the system. It is worth noting that difficulties in automatically measuring the contact angles arose from the presence of the increased vapour density above the solid surface, thus care must be taken to measure the droplet diameter at

the solid boundary. This was achieved by measuring the height and diameter from  $y_0 = 2$  in equation 5.7.

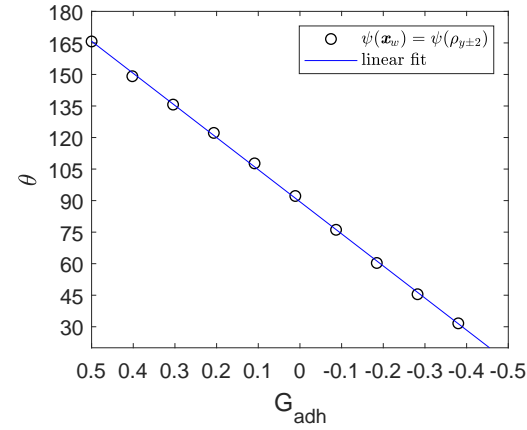
For both  $\psi(\mathbf{x}_w) = \psi(\rho_v)$  and  $\psi(\mathbf{x}_w) = 0$  a quadratic fit best describes the relationship between the adhesion strength  $G_{adh}$  and the equilibrium contact angle  $\theta$ , whereas the  $\psi(\mathbf{x}_w) = \psi(\rho_{y\pm 2})$  treatment again results in a linear fit as illustrated in figures 5.4c and 5.4d. The constants for polynomial fittings are displayed in table 5.2.

wall treatment	$k_2$	$k_1$	$k_0$
$\psi(\mathbf{x}_w) = 0$	25.9	171.33	275.66
$\psi(\mathbf{x}_w) = \psi(\rho_v)$	17	127	196.6
$\psi(\mathbf{x}_w) = \psi(\rho_{y\pm 2})$	0.0	74.11	91.15

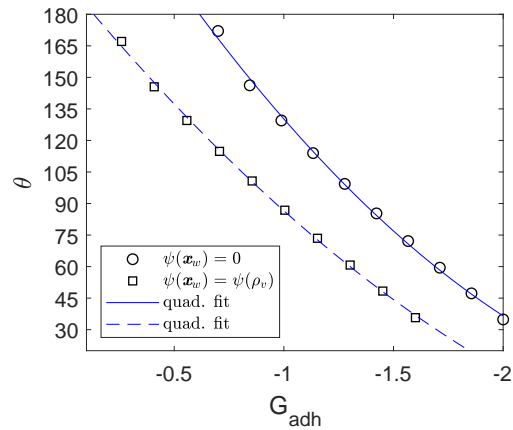
Table 5.2: Polynomial coefficients for relating adhesion strength  $G_{adh}$  to equilibrium contact angle  $\theta$  with the  $\psi$ -based wetting model.



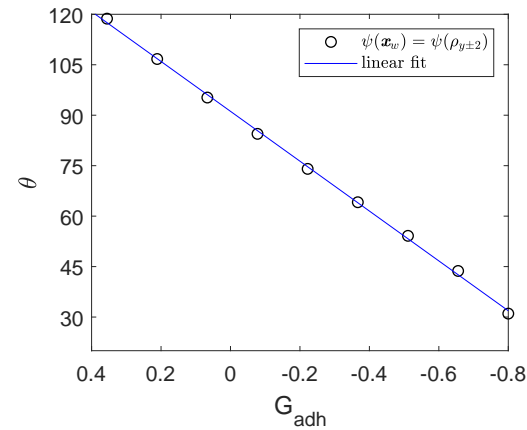
(a)  $\rho$ -based -  $\psi(\mathbf{x}_w)$  - fixed.



(b)  $\rho$ -based -  $\psi(\mathbf{x}_w)$  - variable.



(c)  $\psi$ -based -  $\psi(\mathbf{x}_w)$  - fixed.



(d)  $\psi$ -based -  $\psi(\mathbf{x}_w)$  - variable.

Figure 5.4: Equilibrium contact angles ( $\theta$ ) against adhesion strength parameter,  $G_{adh}$ , for  $\rho$ - and  $\psi$ -based wetting models.

### $\psi^2$ -based Wetting Model

To ensure that the adhesion force was the same order of magnitude as the cohesion force, Li *et al.* [196] suggested the adhesion force be expressed as

$$\mathbf{F}_{adh} = -G_{adh}\psi^2(\mathbf{x}) \sum_i w_i s(\mathbf{x} + \mathbf{e}_i \Delta t) \mathbf{e}_i. \quad (5.11)$$

The model was capable of simulating a wide range of contact angles with each boundary condition. For the boundary treatments of  $\psi(\mathbf{x}_w) = 0$  and  $\psi(\mathbf{x}_w) = \psi(\rho_v)$ , the relationship between  $\theta$  and  $G_{adh}$  is well fitted by a cubic and quadratic equation respectively, illustrated in figure 5.5a. The  $\psi(\mathbf{x}_w) = \psi(\rho_{y\pm 2})$  treatment again results in a linear fit as illustrated in figure 5.5b. The constants for polynomial fittings are displayed in table 5.3.

wall treatment	$k_3$	$k_2$	$k_1$	$k_0$
$\psi(\mathbf{x}_w) = 0$	2045.5	7215	8636.3	3553
$\psi(\mathbf{x}_w) = \psi(\rho_v)$	0.0	77.4	337.7	288.3
$\psi(\mathbf{x}_w) = \psi(\rho_{y\pm 2})$	0.0	0.0	97.3	90.68

Table 5.3: Polynomial coefficients for relating adhesion strength  $G_{adh}$  to equilibrium contact angle  $\theta$  with the  $\psi^2$ -based wetting model.

### IFM Wetting Model

For investigations with the IFM wetting model,  $\varphi = \rho'$ , therefore, the adhesion forces is expressed as

$$\mathbf{F}_{adh} = \left[ -G_{adh}\psi^2(\mathbf{x}) \sum_i w_i s(\mathbf{x} + \mathbf{e}_i \Delta t) \mathbf{e}_i \right] (1 + |\nabla \rho'(\mathbf{x}) - (\mathbf{n} \cdot \nabla \rho') \mathbf{n}| \chi), \quad (5.12)$$

where  $\chi = 0.3$  and  $\rho'$  is defined to ensure that the numerical calculation of the gradient only captures liquid-vapour variations and is not influenced by the presence of solid nodes as

$$\rho'(\mathbf{x} + e_{i\alpha}\Delta t) = \begin{cases} \rho(\mathbf{x} - e_{i\alpha}\Delta t) & \text{if } s(\mathbf{x} + e_{i\alpha}\Delta t) = 1, \\ \rho(\mathbf{x} + e_{i\alpha}\Delta t) & \text{if } s(\mathbf{x} + e_{i\alpha}\Delta t) \neq 1. \end{cases} \quad (5.13)$$

The gradient terms are then computed with a simple second order central difference scheme. For the boundary treatments of  $\psi(\mathbf{x}_w) = 0$  and  $\psi(\mathbf{x}_w) = \psi(\rho_v)$ , the relationship between  $\theta$  and  $G_{adh}$  is well fitted by a cubic and quadratic equation respectively, illustrated in figure 5.5c. The  $\psi(\mathbf{x}_w) = \psi(\rho_{y\pm 2})$  treatment again results in a linear fit as illustrated in figure 5.5d. The constants for polynomial fittings are displayed in table 5.4.

wall treatment	$k_3$	$k_2$	$k_1$	$k_0$
$\psi(\mathbf{x}_w) = 0$	10252	29423	28266	9133
$\psi(\mathbf{x}_w) = \psi(\rho_v)$	0.0	264.3	621.9	364.7
$\psi(\mathbf{x}_w) = \psi(\rho_{y\pm 2})$	0.0	0.0	124.5	90.7

Table 5.4: Polynomial coefficients for relating adhesion strength  $G_{adh}$  to equilibrium contact angle  $\theta$  with the IFM wetting model.

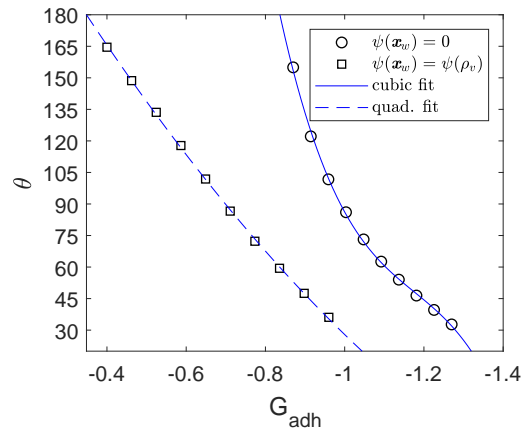
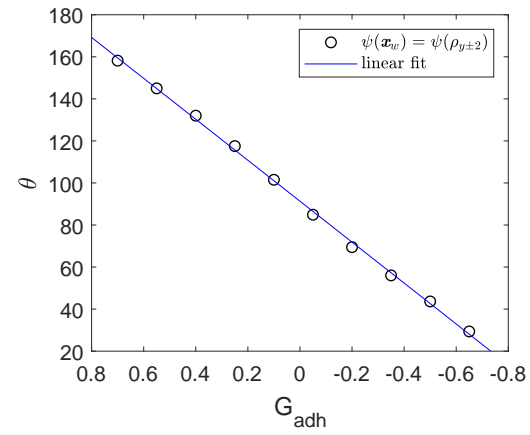
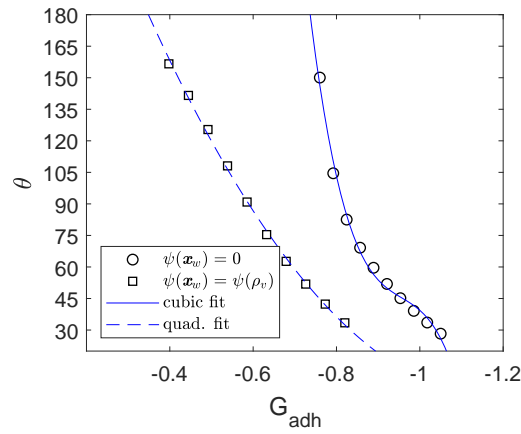
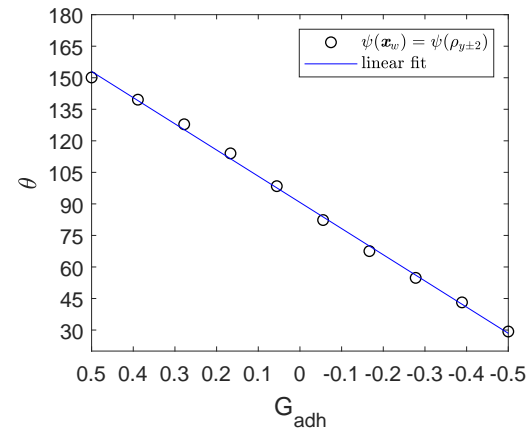
(a)  $\psi^2$ -based -  $\psi(\mathbf{x}_w)$  - fixed.(b)  $\psi^2$ -based -  $\psi(\mathbf{x}_w)$  - variable.(c) IFM model -  $\psi(\mathbf{x}_w)$  - fixed.(d) IFM model -  $\psi(\mathbf{x}_w)$  - variable.

Figure 5.5: Equilibrium contact angles ( $\theta$ ) against adhesion strength parameter,  $G_{adh}$ , for  $\psi^2$ -based and IFM wetting models.

## Geometric Wetting Model

Unlike the previous models in which an additional adhesion force is introduced into the model, the geometric model works by setting the values of the pseudopotential at the solid nodes, thus the aforementioned boundary problem no longer persists. An appealing feature of this model is the ability to specify the angle directly, without the need for a preliminary study. However, special gradient discretisations are required for boundaries located in different orientations. This makes the method challenging to implement for complex geometries and is more computationally demanding. For specifying the contact angle on a solid wall at the bottom of the simulation domain ( $y = 0$ ), the discrete geometric wetting model is expressed as

$$\rho_{x,0,z} = \rho_{x,2,z} + \tan\left(\frac{\pi}{2} - \theta\right)\zeta, \quad (5.14)$$

where

$$\zeta = \sqrt{(\rho_{x+1,1,z} - \rho_{x-1,1,z})^2 + (\rho_{x,1,z+1} - \rho_{x,1,z-1})^2}. \quad (5.15)$$

An additional strength of this approach is the ability to define the contact angle hysteresis [202]. First equation 5.3 is rearranged to solve for the contact angle at the current time-step, then this contact angle  $\theta$  is compared to specified advancing ( $\theta_A$ ) and receding ( $\theta_R$ ) angles. If  $\theta \leq \theta_R$ , then  $\theta$  in equation 5.14 is replaced by  $\theta_R$ . Alternatively, if  $\theta \geq \theta_A$ , then  $\theta$  is replaced with  $\theta_A$ . Finally, if the measured contact angle is between the advancing and receding angles, no changes are made. The measured contact angle compared to the specified angle is displayed in figure 5.6.

With the current implementation, the stability of the geometric scheme is found to depend on the size of the diffuse interface when simulating low

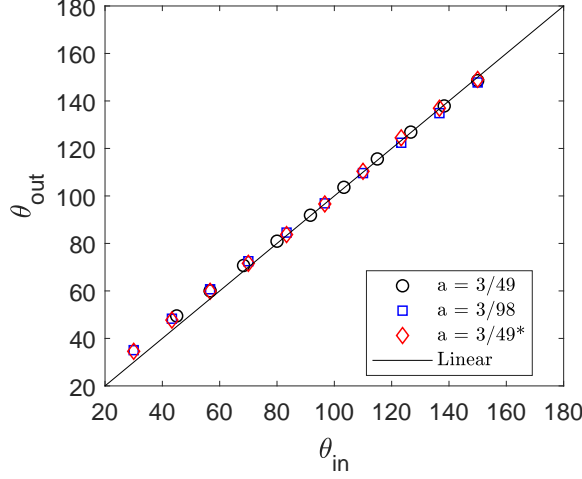


Figure 5.6: Equilibrium contact angles for geometric wetting model with different interface thicknesses and incorporated stability condition. The value marked with an asterisk is the model with improved stability (equation 5.16).

contact angles. The lowest achievable contact angle for the current model parameters was  $45^\circ$ . Increasing the interface thickness by setting  $a = \frac{3}{98}$  while ensuring the same reduced temperature to maintain the same density ratio, a contact angle of  $35^\circ$  was achievable. It is assumed that stability issues arise from errors in computing density gradients, which then result in erroneous values of the density/pseudopotential in the solid nodes. Therefore, a simple way to improve stability is to employ the following correction to the predicted density values in the solid nodes

$$\rho(\mathbf{x}_b) = \begin{cases} \rho_l^{eq} & \text{if } \rho(\mathbf{x}_b) > \rho_l^{eq}, \\ \rho_v^{eq} & \text{if } \rho(\mathbf{x}_b) < \rho_v^{eq}. \end{cases} \quad (5.16)$$

With this modification, contact angles of  $\theta = 30^\circ$  were easily achieved for the model with the standard interface size. Furthermore, the same linear trend

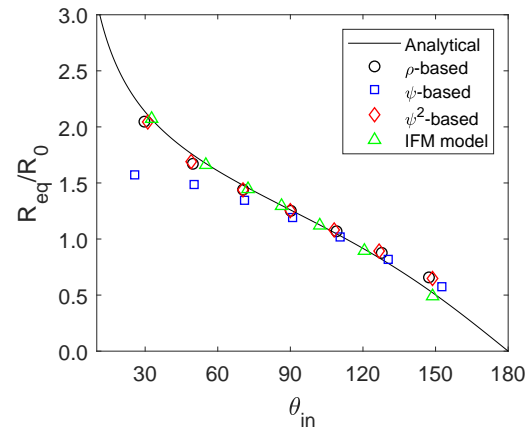
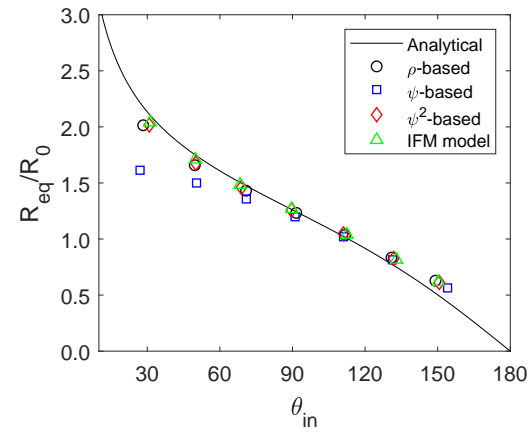
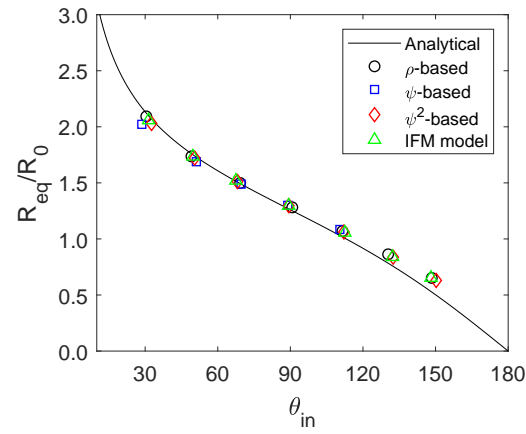
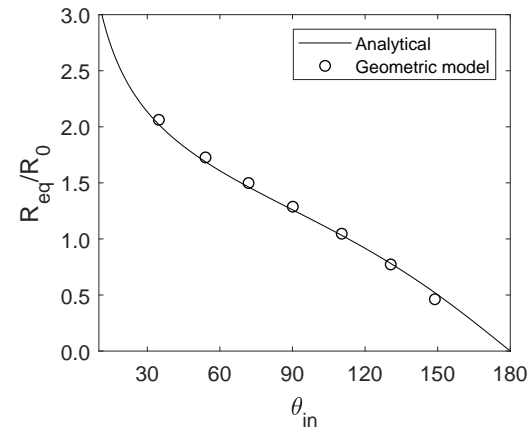
is observed between the prescribed and measured contact angles as in figure 5.6.

### Equilibrium Spreading Radius

For a given equilibrium contact angle, the maximum spreading factor determined by van Dam and Le Clerc [203] for a spherical cap approximation with conserved volume is expressed as

$$\frac{R_{eq}}{R_0} = \left( \frac{8}{\tan(\frac{\theta}{2})(3 + \tan^2(\frac{\theta}{2}))} \right)^{1/3}. \quad (5.17)$$

Using this prediction, the final spreading radius,  $R_{eq}$  for each model/ boundary treatment is compared to the predicted value for a range of contact angles in figure 5.7. For the  $\psi$ -based wetting model, the recorded spreading radius was significantly lower than the predicted value for both the  $\psi(\mathbf{x}_w) = 0$  and  $\psi(\mathbf{x}_w) = \psi(\rho_v)$  boundary treatments, figures 5.7a and 5.7b respectively. This is again due to a density increase in the vapour phase at boundary nodes, causing the main droplet size to decrease. The remaining wetting models/ boundary treatments all produced results agreeing well with the predicted value.

(a)  $\psi(\mathbf{x}_w) = 0$ .(b)  $\psi(\mathbf{x}_w) = \psi(\rho_v)$ .(c)  $\psi(\mathbf{x}_w) = \psi(\rho_{y\pm 2})$ .

(d) Geometric Wetting model.

Figure 5.7: Evaluation of equilibrium spreading factor for each wetting model and boundary treatment. Analytical solution obtained with equation 5.17.

### 5.3.3 Spurious Velocities

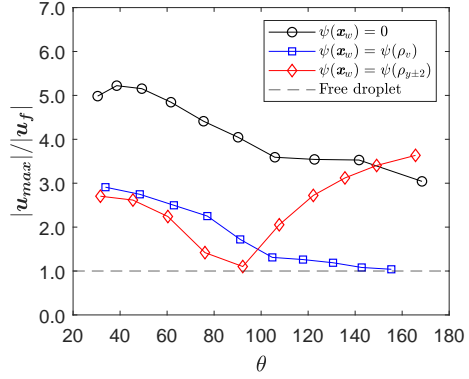
As previously described, spurious velocities are generated at the liquid-vapour interface even for a suspended droplet in a fully periodic domain. When there are additional forces added to the model to account for fluid-solid interactions, there are additional sources of momentum, causing the generation of more spurious velocities. These are unphysical and undesirable from a modelling perspective, especially if the magnitude of these velocities are comparable to characteristic velocities of the simulation. To compare the performance of different models and different solid node treatments, the maximum spurious velocity is recorded for a given equilibrium contact angle  $|\mathbf{u}_{max}|$  and normalised against the maximum spurious velocity of a droplet in a fully periodic domain,  $|\mathbf{u}_f|$ .

For the current model and temperature settings, the maximum spurious velocity magnitude of  $|\mathbf{u}_f| = 0.017149$  was observed. The results of each wetting model and boundary treatment are shown in figure 5.8. The  $\psi$ -based and geometric wetting model have very little influence on the spurious velocities, figures 5.8b and 5.8e respectively. Furthermore, each of the models in which the boundary is modelled as  $\psi(\mathbf{x}_w) = \psi(\rho_{y\pm 2})$  shows the lowest spurious velocity at  $\theta \approx 90^\circ$  and increases in magnitude either side of this contact angle, resembling a  $V$  shape, figures 5.8c, 5.8c and 5.8d.

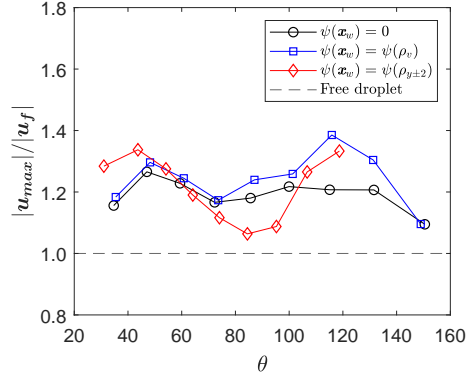
The  $\rho$ -based,  $\psi^2$ -based and new model display very similar trends, in that the spurious velocities are largest at low contact angles of  $\theta \approx 40^\circ$  for the boundary treatment  $\psi(\mathbf{x}_w) = 0$ . For contact angles larger than  $\theta \approx 40^\circ$ , the spurious velocities reduce at a similar rate for both  $\psi(\mathbf{x}_w) = 0$  and  $\psi(\mathbf{x}_w) = \psi(\rho_v)$  boundary treatments.

For each of the models tested, the spurious velocities are illustrated for the configuration in which the largest value was observed in figure 5.9. As the

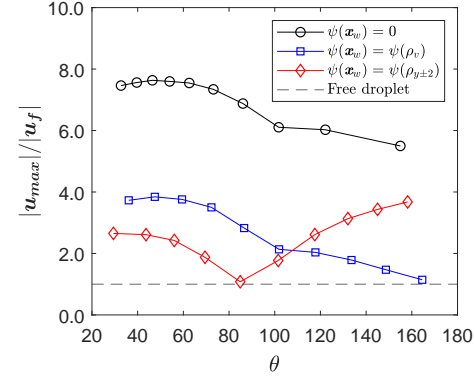
$\psi$ -based and the geometric model resulted in very low additional spurious velocities, the vectors are scaled by 200 for visibility, figures 5.9b and 5.9e respectively. The remaining wetting models produced significantly larger spurious velocities, thus the vectors are scaled by 70, figures 5.9c, 5.9c and 5.9. It is clear from these images that the largest spurious velocity occurs at the triple point.



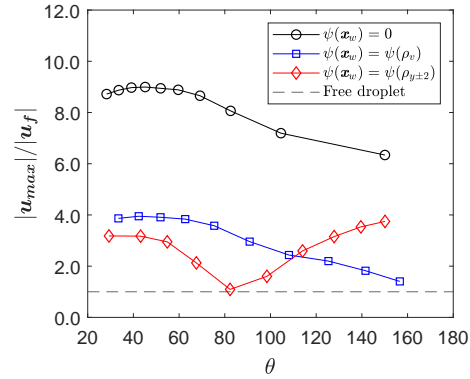
(a)  $\rho$ -based wetting model.



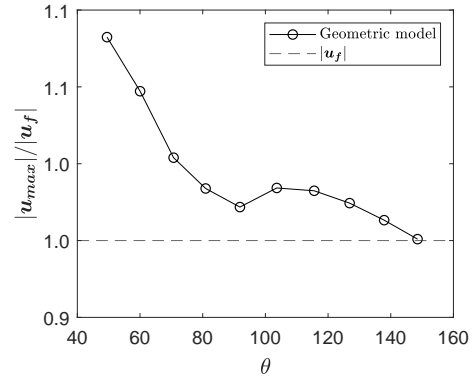
(b)  $\psi$ -based wetting model.



(c)  $\psi^2$ -based wetting model.



(d) IFM wetting model.



(e) Geometric wetting model.

Figure 5.8: Evaluation of maximum spurious velocities for different contact angles for each wetting model and boundary treatment. The velocity  $|u_{max}|$  is the maximum spurious velocity for a sessile droplet in equilibrium and  $|u_f|$  is the maximum spurious velocity for a droplet in a fully periodic domain.

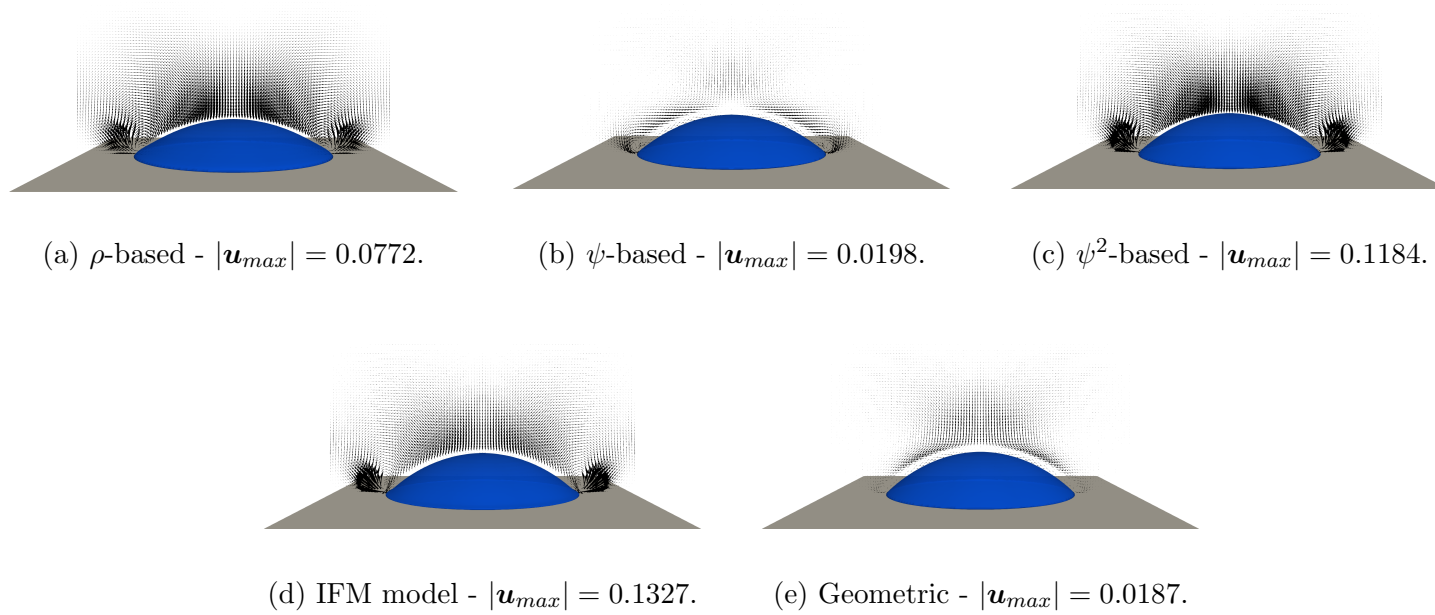


Figure 5.9: Illustration of velocity field for wetting model and boundary treatment configuration which resulted in the largest spurious velocity.

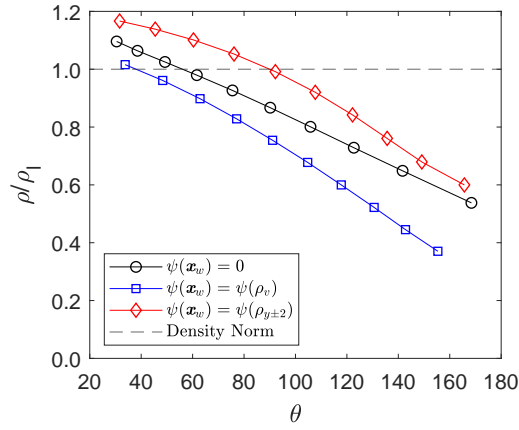
### 5.3.4 Maximum and Minimum Densities

The additional interaction force for fluid nodes at a solid boundary causes modification to the mechanical stability condition, which results in a change in density at these nodes. As alluded to previously, some wetting models can increase the vapour density to a value that approaches the coexistence liquid density when simulating low contact angles. Two different scenarios are investigated in terms of density change: liquid density change at the bottom surface of the wetting droplet and vapour density change at the solid wall situated at the top of the simulation domain. These locations are referred to as liquid- and vapour-phase regions respectively for the remainder of this chapter. The density was recorded at these two locations for a range of contact angles and normalised by the coexistence liquid and vapour densities respectively.

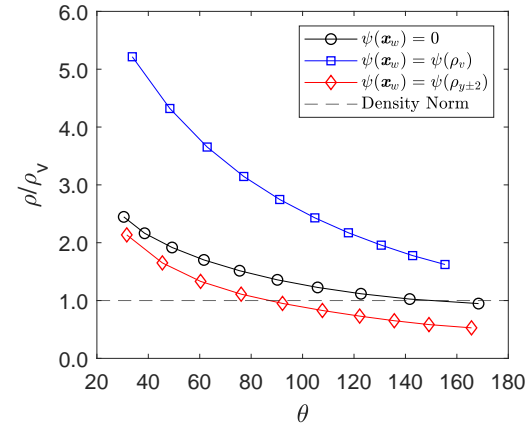
The values of density change for the  $\rho$ - and  $\psi$ -based model are displayed in figure 5.10. For the  $\rho$ -based model, the change in the liquid-phase is shown in figure 5.10a, where it can be seen that at low contact angles the density becomes larger than the coexistence value for each boundary treatment. Increasing the contact angle results in reduced density, as a diffuse interface between the solid and liquid grows. The same behaviour is seen in the vapour phase, highlighted in figure 5.10b.

For the  $\psi$ -based wetting model, the boundary treatments of  $\psi(\mathbf{x}_w) = 0$  and  $\psi(\mathbf{x}_w) = \psi(\rho_v)$  result in very similar density change values in both the liquid and vapour-phase regions, figures 5.10c and 5.10d respectively. For these boundary treatments, the density also never exceeds the coexistence liquid value at low contact angles. However, the density change in the vapour phase is significant, here at contact angles approaching  $\theta = 30^\circ$ , the density exceeds  $16\rho_v$ , making it close to the coexistence liquid value. This significant density

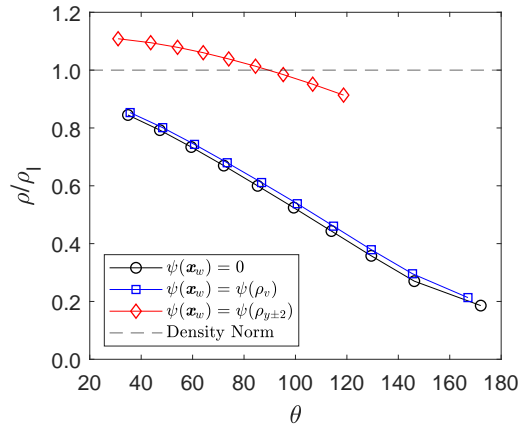
change results in mass loss from the droplet, responsible for the erroneous results in predicted spreading radius illustrated in figure [5.7](#).



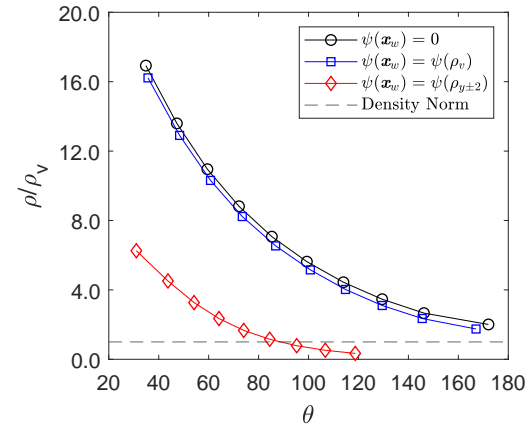
(a)  $\rho$ -based - Liquid phase.



(b)  $\rho$ -based - Vapour phase.



(c)  $\psi$ -based - Liquid phase.

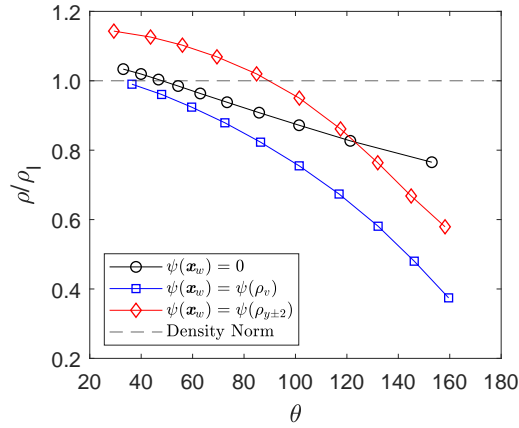


(d)  $\psi$ -based - Vapour phase.

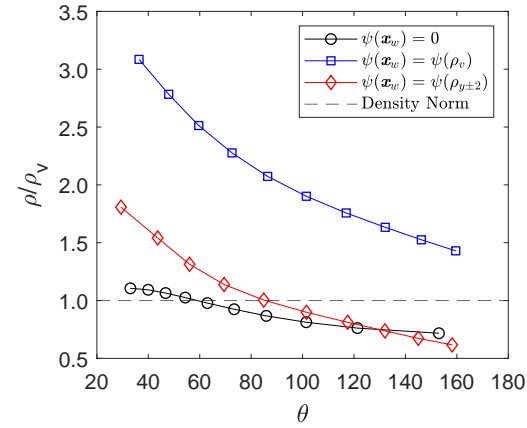
Figure 5.10: Deviation from coexistence density both in the liquid phase (boundary node beneath the droplet) and vapour phase (boundary node at the top of the simulation domain) for  $\rho$ - and  $\psi$ -based wetting models.

The density change results for the  $\psi^2$ -based and IFM model are displayed in figure 5.11. For both wetting models, the boundary treatment of  $\psi(\mathbf{x}_w) = \psi(\rho_{y\pm 2})$  is found to produce density values exceeding the coexistence liquid density for contact angles approximately lower than  $\theta = 80^\circ$ , figures 5.11a and 5.11c. In the vapour-phase, the boundary treatment of  $\psi(\mathbf{x}_w) = \psi(\rho_v)$  remains above the coexistence vapour density for the range of contact angles tested. For the IFM wetting model, the change in the vapour density is the lowest of all models tested.

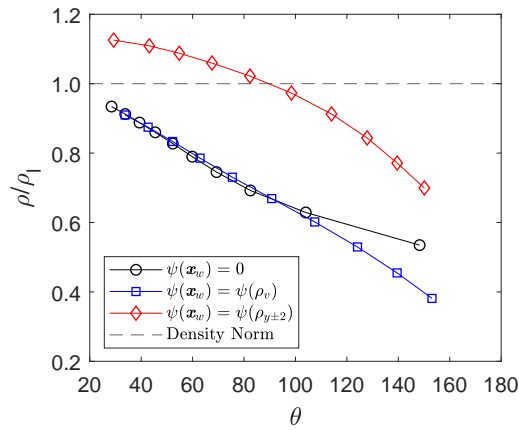
When using the geometric scheme, there are no additional force components, thus the mechanical stability is unaffected and densities remain unchanged.



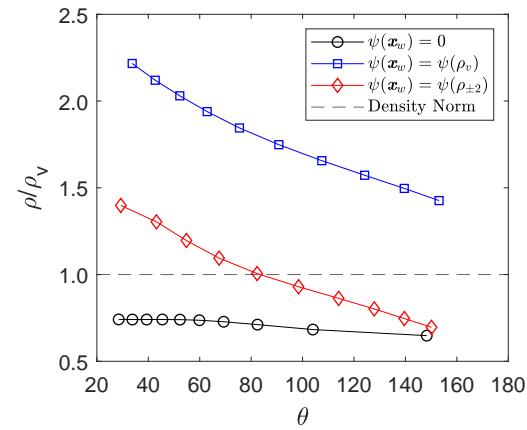
(a)  $\psi^2$ -based - Liquid phase.



(b)  $\psi^2$ -based - Vapour phase.



(c) IFM model - Liquid phase.



(d) IFM model - Vapour phase.

Figure 5.11: Deviation from coexistence density both in the liquid phase (boundary node beneath the droplet) and vapour phase (boundary node at the top of the simulation domain) for  $\psi^2$ -based and IFM wetting model.

### 5.3.5 Spreading on a Homogeneous Surface

Although the solid wall enforces a non-slip zero velocity boundary condition, the three-phase contact line is still able to move over the surface. This is due to the diffuse interface, which allows movement in an evaporation-condensation manner, as described in references [114, 204]. Each model's ability to capture the dynamics of spreading on a smooth surface is explored. Tanner's spreading law [25] gives a relationship between the evolution of a droplet's spreading radius and the time as  $r \sim t^n$ . For a partially wetting surface, the exponent  $n$  is found to be close to 0.5 in the early stages of droplet spreading for equilibrium contact angles approaching  $\theta = 0^\circ$  [205].

Using the same simulation parameters as described in the previous section as well as the determined relationships between  $G_{adh}$  and  $\theta$ , the evolution of a droplet's radius with equilibrium contact angle  $\theta = 40^\circ$  is recorded for each wetting model and wall/ boundary treatment, figure 5.12. The droplet radius is set to  $R_0 = 20$  and is initially located above the solid surface, with a centre height of  $y_0 = 22$  and as it spreads, the location of the interface is interpolated from the first layer of fluid nodes.

Due to simulation instability, the  $\psi$ -based wetting model could only be used with the  $\psi(\mathbf{x}_w) = \psi(\rho_{y\pm 2})$  boundary for contact angles of  $\theta = 40^\circ$ , figure 5.12b. The remaining boundary conditions required incremental change of the adhesion strength parameter during the early stages of the simulation, thus the wetting dynamics are affected.

Following molecular dynamic simulations [206], an exponential fitting of  $R/R_0 = 1.3t^{0.48}$  is included in each of the spreading plots to illustrate the similar performance between each model. However, it is noted that the boundary treatment of  $\psi(\mathbf{x}_w) = 0$  noticeably deviates from this prediction compared to the remaining boundary treatments, as can be seen in figures 5.12a, 5.12c

and 5.12d. The geometric model also agrees well with this fitting, figure 5.12e.

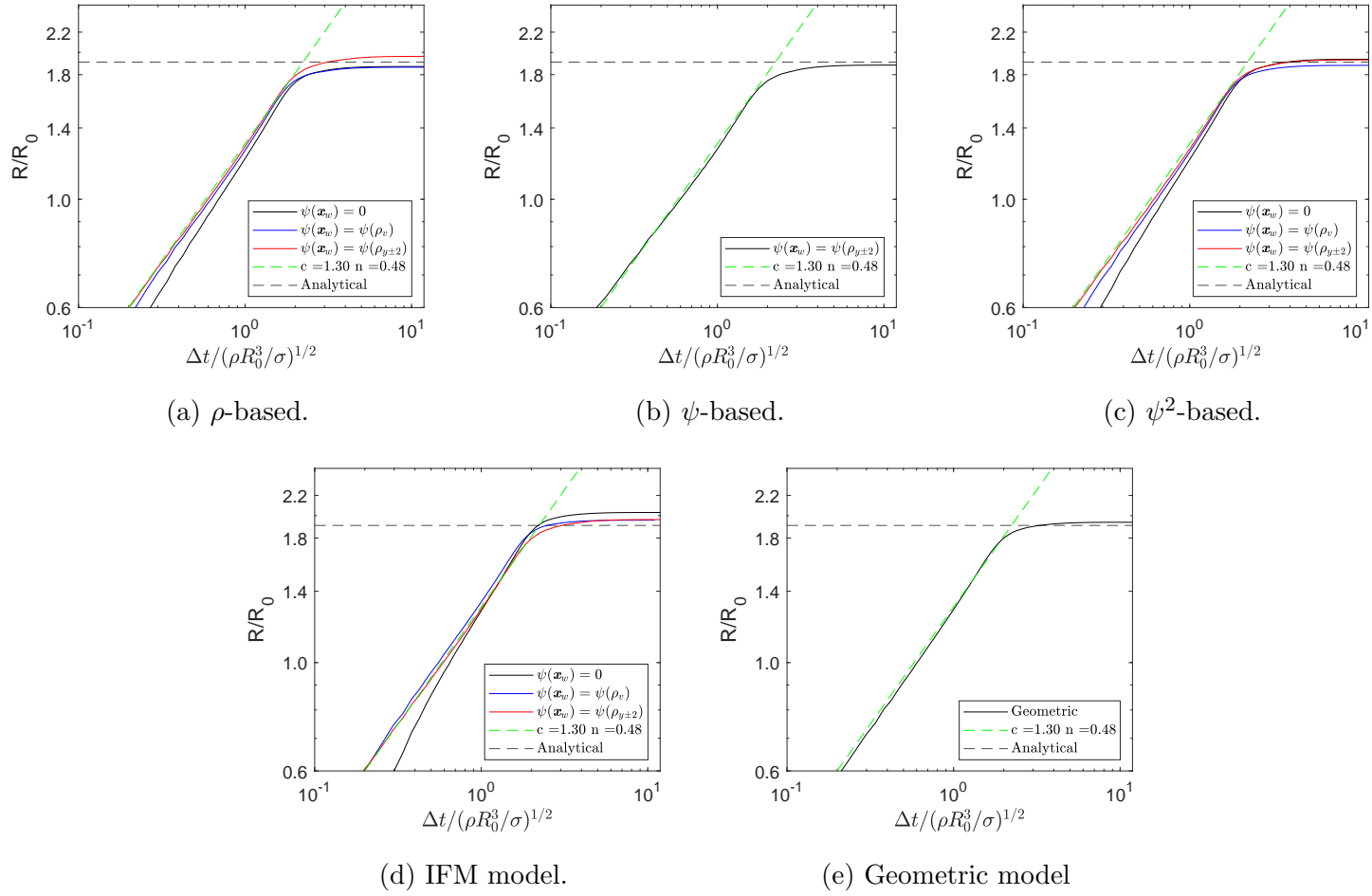


Figure 5.12: Evolution of droplet radius on a smooth surface with an equilibrium contact angle of  $\theta = 40^\circ$ . Equilibrium spreading factor determined by equation 5.17 and spreading power law exponent given by [206].

## 5.4 Wetting Chemically Heterogeneous Surfaces

Within the pseudopotential framework, there have been numerous studies looking at wetting of surfaces with localised changes in wettability with either the geometric wetting condition, where the prescribed contact angle varies with position  $\theta(\mathbf{x})$  [157, 158] or with the  $\psi(\rho_w)$  wetting model [189, 56, 207, 64]. This model allows for easily defining different wettabilities as density/pseudopotential values just need to be defined in solid nodes and the adhesive wetting forces are accounted for automatically. However, as shown in the previous section, these models can cause simulations to become unstable when simulating low contact angles. Previous investigations with the  $\psi(\rho_w)$  model have had low density ratios or time varying  $\rho_w$  values to maintain simulation stability. For adhesion based wetting models, the wetting is controlled by the parameter  $G_{adh}$ , which is usually a fixed value ensuring that the modelled chemical properties of the surface are homogeneous. To enable the modelling of surfaces with different local wettability, the adhesion force needs to be redefined. Firstly, the constant adhesion strength parameter is changed to a function of space,  $G_{adh} \rightarrow G_{adh}(\mathbf{x})$  and secondly the term  $s$  used for identifying solid nodes is changed to

$$s(\mathbf{x} + \mathbf{e}_i \Delta t) = \begin{cases} G_{adh}(\mathbf{x} + \mathbf{e}_i \Delta t) & \text{if } (\mathbf{x} + \mathbf{e}_i \Delta t) \text{ is solid,} \\ 0 & \text{otherwise.} \end{cases} \quad (5.18)$$

The adhesion force can then be expressed generally as

$$\mathbf{F}_{adh} = -\Phi_f(\mathbf{x}) \sum_i \omega(|\mathbf{e}_i|^2) \Phi_s(\mathbf{x} + \mathbf{e}_i \Delta t) s(\mathbf{x} + \mathbf{e}_i \Delta t) \mathbf{e}_i. \quad (5.19)$$

With these changes it is possible to use adhesion force based wetting modes

for locally varying wettabilities.

### 5.4.1 Spreading on Chemically Heterogeneous Surface

To explore each wetting model's performance on a chemically heterogeneous surface, a surface comprising hydrophilic and hydrophobic stripes is configured, as illustrated in figure 5.13.

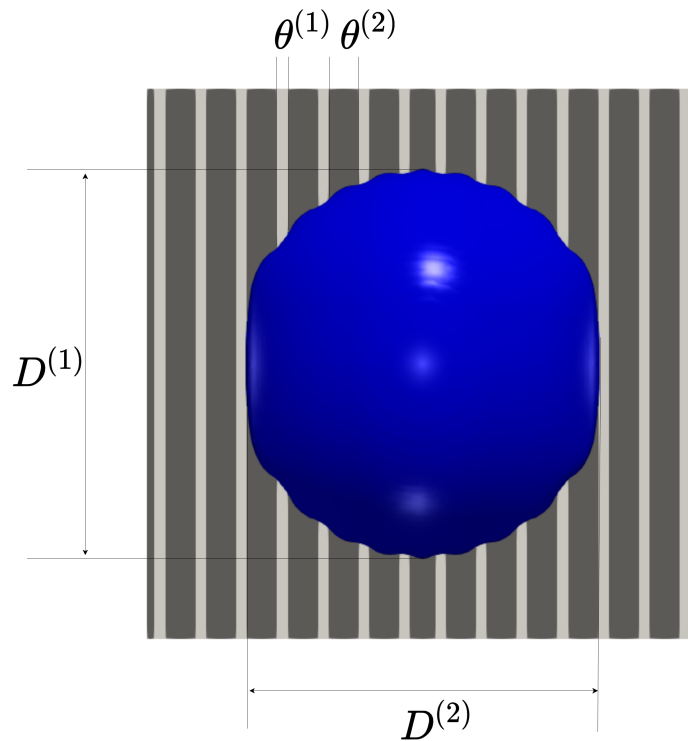


Figure 5.13: Illustration of a droplet deposited onto a chemically patterned surface. Different shaded regions represent regions with different intrinsic contact angles.

The equilibrium contact angle for a droplet on a smooth, chemically heterogeneous surface in which there are two distinct contact angles,  $\theta^{(1)}$  and  $\theta^{(2)}$

can be described by the Cassie-Baxter equation as

$$\cos(\theta_{App}) = f' \cos(\theta^{(1)}) + (1 - f') \cos(\theta^{(2)}), \quad (5.20)$$

where  $f'$  is the fraction of the surface occupied by wetting component 1. As the surface under consideration is comprised of stripes of equal width, the wetted fraction  $f' = 0.5$ . After defining contact angles  $\theta^{(1)}$  and  $\theta^{(2)}$ , the Cassie-Baxter equilibrium contact angle is then inserted into equation 5.17 to obtain the equilibrium spreading radius on a chemically patterned surface. The modelling of droplet spreading is explored for two surfaces: case (a) in which  $\theta^{(1)} = 30^\circ$  and  $\theta^{(2)} = 50^\circ$  and case (b) with  $\theta^{(1)} = 40^\circ$  and  $\theta^{(2)} = 140^\circ$ , giving Cassie-Baxter angles of  $\theta_{App} = 41^\circ$  and  $\theta_{App} = 90^\circ$  respectively. The stripy surface can cause anisotropy of the droplets equilibrium morphology, therefore diameters  $D^{(1)}$  and  $D^{(2)}$  (equally  $R^{(1)}$  and  $R^{(2)}$ ) are used to define the droplets size both parallel and perpendicular to the stripes respectively. The predicted equilibrium spreading radius,  $R^{(2)}$  is  $1.85R_0$  and  $1.26R_0$  for case (a) and (b) respectively. The evolution of the normalised droplets radius  $R^{(2)}/R_0$  for both surfaces is displayed in figure 5.14. For these investigations, the initial droplet radius was set to  $R_0 = 20$ , and the free relaxation times in the MRT set to 1.6. The width of each stripe was set to 4 lattice units for both regions. For each surface type, the  $\rho$ -based,  $\psi^2$ -based and IFM models are compared. Due to stability issues highlighted for the  $\psi$ -based model, it was omitted from the investigations.

For case (a), the  $\rho$ -based model slightly over-predicts the spreading radius for  $\psi(\mathbf{x}_w) = 0$  and  $\psi(\mathbf{x}_w) = \rho_v$  and comparatively good agreement is observed for the  $\psi(\mathbf{x}_w) = \psi(\rho_{y\pm 2})$ . For the  $\psi^2$ -based model, the boundary treatment  $\psi(\mathbf{x}_w) = 0$  results in the droplet radius deviating from the expected value as the simulation progresses, whereas the remaining boundary treatment perfor-

mance is comparatively better. For the IFM wetting model, each boundary treatment performs relatively well. For case (b), the  $\rho$ -based model performs best, with each boundary treatment giving results close to the analytical prediction. For the  $\psi^2$ -based and new model, significant deviations can be observed depending on the chosen boundary treatment. This is likely a result of the density deviation for each model/ boundary, which due to the large difference in contact angles can cause the droplet to pin or spread.

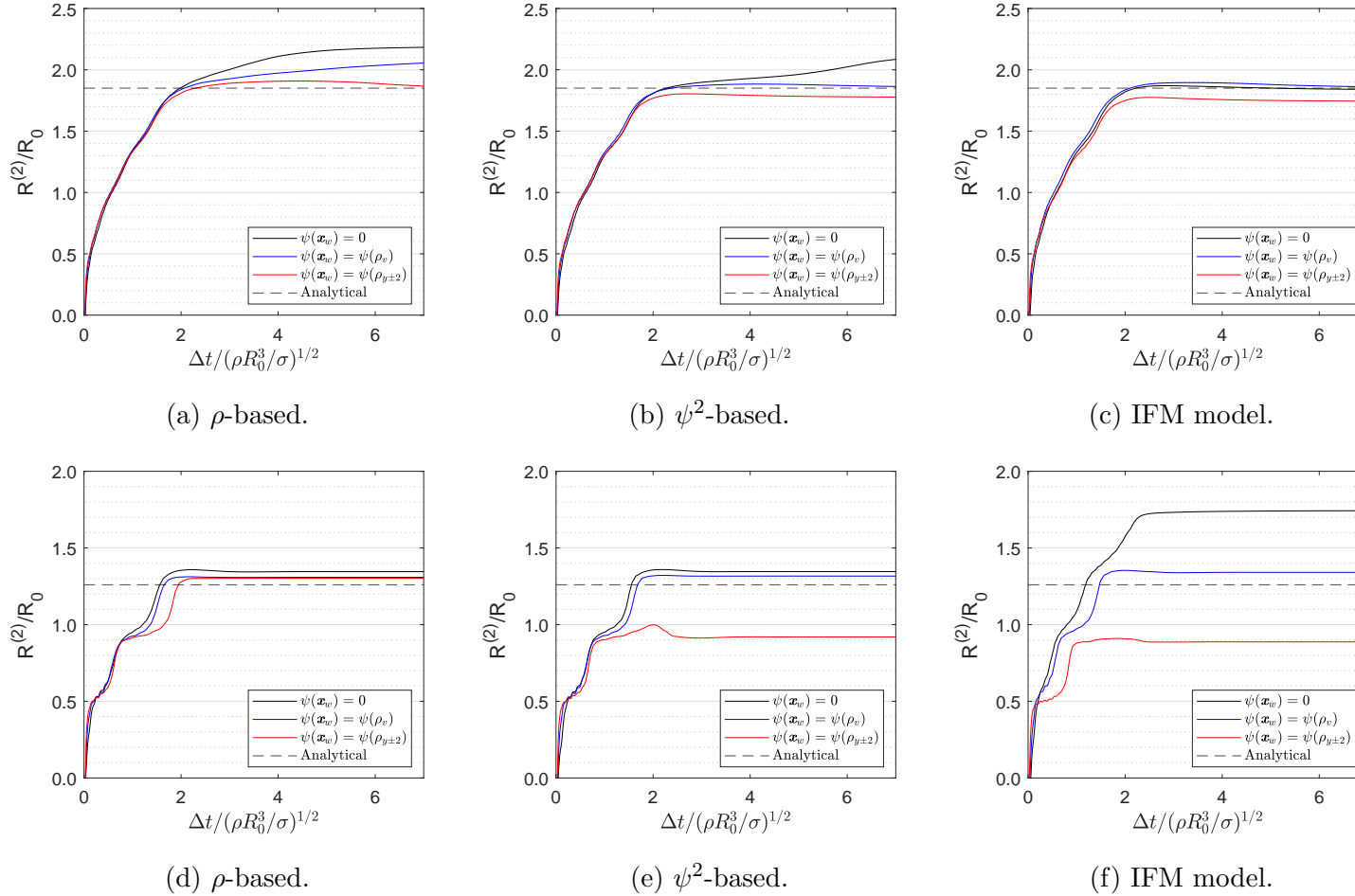


Figure 5.14: Evolution of droplet radius spreading on a chemically patterned surface. Figures (a), (b) and (c) have contact angles of  $\theta^{(1)} = 30^\circ$  and  $\theta^{(2)} = 50^\circ$ , giving an apparent contact angle of  $\theta_{App} = 41^\circ$ . Figures (d), (e) and (f) have contact angles of  $\theta^{(1)} = 40^\circ$  and  $\theta^{(2)} = 140^\circ$ , giving an apparent contact angle of  $\theta_{App} = 90^\circ$ . Equilibrium spreading factor given by equation 5.17.

## 5.5 Experimental Validation

To test the validity of the model at simulating real physical flows, simulation results are compared to experimentally obtained data for a single droplet impacting a solid surface. For inkjet printable droplets, Lim *et al.* [208] obtained data for the time evolution of the droplets height and radius. Their experiment consisted of a droplet of diameter  $D_0 = 48.1\mu m$  and a velocity of  $u_0 = 1.9ms^{-1}$ , giving dimensionless numbers of  $Re = 107$ ,  $We = 2.4$  and  $Oh = 0.015$ . The advancing and receding contact angles  $\theta_A$  and  $\theta_R$  were measured to be  $91^\circ$  and  $32^\circ$  respectively.

To distinguish between lattice and physical units, all lattice values are marked with a ( $\tilde{\phantom{x}}$ ). As with the previous investigations, the Peng-Robinson equation of state is used with a temperature of  $T = 0.8T_c$ , giving coexistence densities of  $\tilde{\rho}_l = 7.2$  and  $\tilde{\rho}_v = 0.2$ . The surface tension obtained from Young-Laplace validation is  $\tilde{\sigma} = 0.133$ . Finally, a droplet diameter of  $\tilde{D}_0 = 50$  was chosen. To ensure similarity between simulation and experiment, the dimensionless numbers are matched  $Re = \tilde{Re}$  and  $We = \tilde{We}$ . The free-fall velocity of the droplet was set first by

$$\tilde{u}_0 = \sqrt{\frac{We\tilde{\sigma}}{\tilde{\rho}_l\tilde{D}_0}}, \quad (5.21)$$

which is computed to be  $\tilde{u}_0 = 0.0298$ . Following which, the relaxation rates related to kinematic viscosity are set from the computed velocity and the target  $Re$  number as

$$\tilde{\tau}_\nu = \frac{\tilde{u}_0\tilde{D}_0}{\tilde{c}_s^2 Re} + 0.5, \quad (5.22)$$

which is computed to be  $\tilde{\tau}_\nu = 0.542$ . Although the lattice viscosity is now fixed, the requirement to have three unique conversion factors has not yet

been fulfilled, as the conversion factor for kinematic viscosity is the product of the previously determined conversion factor for length and velocity ( $C_\nu = C_l C_u$ ). Therefore, the final independent conversion factor is chosen to be the liquid density,  $C_\rho$ . These three unique conversion factors are then used to assign dimensions to the simulation results. The unique conversion factors are given explicitly as follows:  $C_l = D_0/\tilde{D}_0 = 0.962 \times 10^{-6}m$ ,  $C_u = u_0/\tilde{u}_0 = 60.46ms^{-1}$  and  $C_\rho = \rho_l/\tilde{\rho}_l = 138.89kgm^{-3}$ . The conversion factor for time is also required to compare with experiments and is computed as  $C_t = C_l/C_u = 0.0159 \times 10^{-6}s$ . Lastly, to improve simulation stability, the remaining relaxation times were set to  $\tilde{\tau} = 1.6$  and the initialisation of the liquid droplet used a higher liquid density of  $\tilde{\rho}_l = 7.5$ . The results of the simulation and experimental measurements are displayed in figure 5.15. Good agreement is observed for the height oscillation and radius pinning between experiment and LB model, even with the lower lattice resolution of  $\tilde{D}_0 = 34$ .

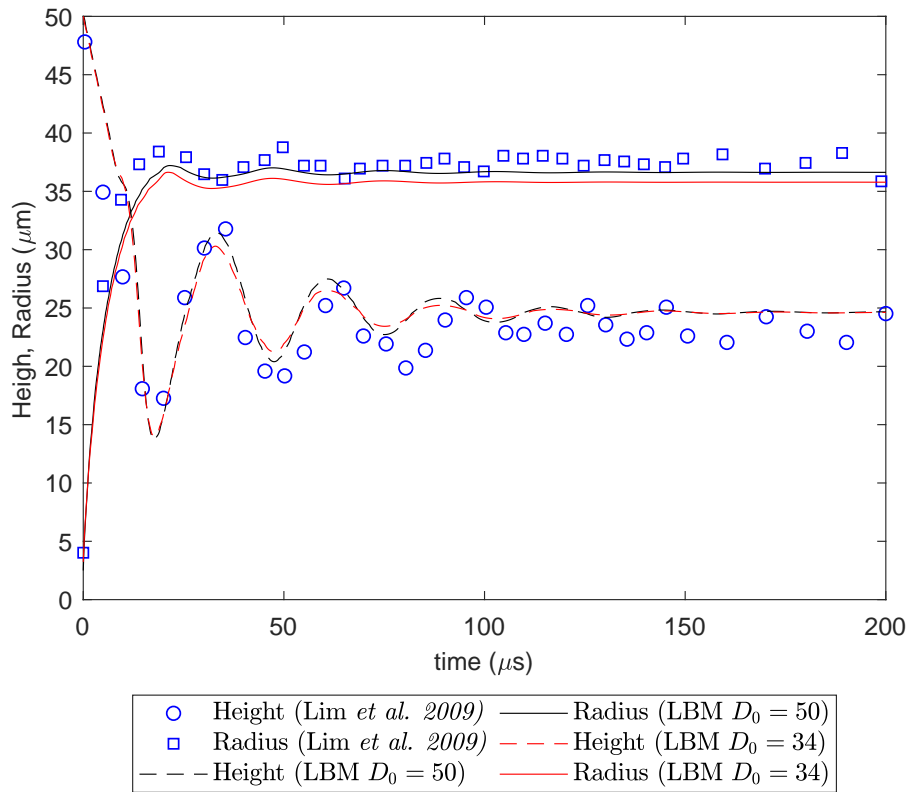


Figure 5.15: Experimental validation of multiphase model for simulating dynamical spreading and droplet height oscillation. Symbols are extracted data points from [208] and lines are LBM results.

-	$\rho$ -based	$\psi$ -based	$\psi^2$ -based	Geometric	IFM model
Equilibrium contact angles on homogeneous surface	✓ Wide range of contact angles.	✗ $\theta_{max} = 120$ for $\psi(\mathbf{x}_w) = \psi(\rho_{y\pm 2})$ . ✗ Reduced stability for $\theta$	✓ Wide range of contact angles.	✓ Wide range of contact angles.	✓ Wide range of contact angles.
Creation of additional spurious velocities ( $ \mathbf{u}_{max} $ )	✗ Large $ \mathbf{u}_{max} $ at low contact angles when $\psi(\mathbf{x}_w) = 0$ .	✓ Low $ \mathbf{u}_{max} $ for each boundary treatment.	✗ Large $ \mathbf{u}_{max} $ at low contact angles when $\psi(\mathbf{x}_w) = 0$ .	✓ Little influence on $ \mathbf{u}_{max} $ .	✗ Large $ \mathbf{u}_{max} $ at low contact angles when $\psi(\mathbf{x}_w) = 0$ .
Coexistence density Changes	✗ Vapour density increase at low contact angles.	✗ Vapour density increase at low contact angles.	✗ Liquid density increase at low contact angles.	-NA	✓ Lowest change in vapour density.
Spreading on homogeneous surface	✓ Good agreement with predicted spreading rate and maximum spreading radius.	✗ For $\theta = 40^\circ$ , $\psi(\mathbf{x}_w) = \psi(\rho_{y\pm 2})$ only stable boundary condition.	✓ Good agreement with predicted spreading rate and maximum spreading radius.	✓ Good agreement with predicted spreading rate and maximum spreading radius.	✓ Good agreement with predicted spreading rate and maximum spreading radius.
Spreading on heterogeneous surface	✗ Exaggerated spreading for low CB angle.	-NA	✓ Good agreement with analytical solution for maximum spreading radius.	-NA	✓ Good agreement with analytical solution for maximum spreading radius.

Table 5.5: Comparison of wetting model performance for static and dynamic scenarios.

## 5.6 Chapter Summary

This chapter explored two key components of wettability modelling within the pseudopotential multiphase model framework: the wetting model, and the boundary treatment for the calculation of the cohesion force. Furthermore, a new wetting model was suggested, referred to as the interface force modification (IFM) model which modifies the adhesion force over the diffuse liquid-vapour interface.

Preliminary studies are first performed, relating wetting model parameters to equilibrium contact angles. These are done for each wetting model and boundary treatment configuration.

Following this, models are compared for various wetting scenarios, including both static and dynamic and a table is constructed which summaries key modelling strengths and weaknesses (table 5.5). The new wetting model performed well in the benchmark tests and resulted in the smallest deviation from coexistence densities compared to other adhesion force based wetting models.

### 5.6.1 Further Considerations

Following completion of the wetting model investigations in this chapter, a new, recently proposed method [209] was discovered, which offers a dynamic solution to the cohesion force boundary issue highlighted in §5.2.3. For completeness, a brief evaluation of this condition is presented here, however, the performance with different adhesion models is left for future investigations. To avoid confusion with the previously proposed model, this model is referred to as the local average density (LAD) model henceforth. As the name suggests, the unknown density at the solid nodes is defined as

$$\rho_{ave}(\mathbf{x}_w) = \frac{\sum_i w_i \rho(\mathbf{x} + \mathbf{e}_i \Delta t) (1 - s(\mathbf{x} + \mathbf{e}_i \Delta t))}{\sum_i w_i (1 - s(\mathbf{x} + \mathbf{e}_i \Delta t))}. \quad (5.23)$$

With this boundary treatment the contact angle can then be varied with either an additional adhesive force [209, 210] or by modifying the density as

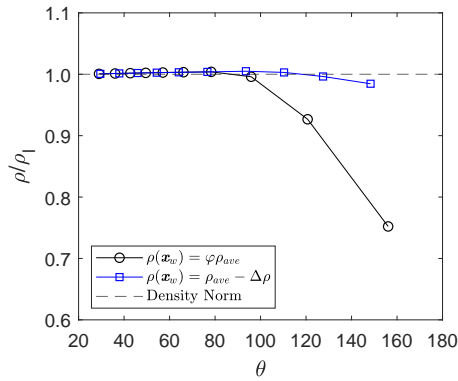
$$\rho(\mathbf{x}_w) = \begin{cases} \varphi \rho_{ave}, & \varphi \geq 1, \text{ for decreasing } \theta, \\ \rho_{ave} - \Delta\rho, & \Delta\rho \geq 0, \text{ for increasing } \theta, \end{cases} \quad (5.24)$$

where  $\varphi$  and  $\Delta\rho$  are constants. The motivation for the two different sets of parameters for modelling hydrophilic and hydrophobic conditions is apparent when looking at the density change over a range of contact angles, figure 5.16. For the modelling of low contact angle angles ( $\theta < 90^\circ$ ), the variation of the vapour density (figure 5.16a) shows the least deviation for  $\rho(\mathbf{x}_w) = \varphi \rho_{ave}$ . Alternatively, for contact angles larger than  $\theta > 90^\circ$ , the variation in the liquid phase density (figure 6.12b) shows the least deviation with the  $\rho(\mathbf{x}_w) = \rho_{ave} - \Delta\rho$  condition.

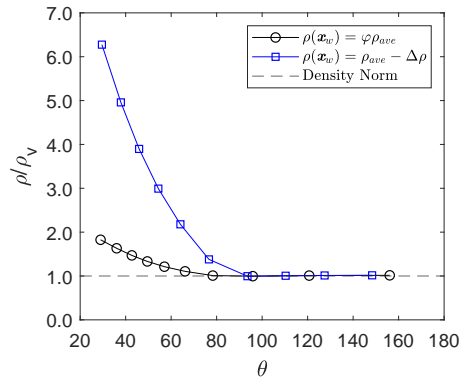
The maximum spurious velocities produced by the LAD are displayed in figure 5.17. The results are comparable to the  $\psi$ -based model, remaining relatively low throughout the range of contact angles tested.

The dynamic performance of the model agrees well with other models and the predicted spreading rate as shown in figure 5.18.

The preliminary investigations of the LAD model are promising, showing good performance in static and dynamic tests. However, further investigations are necessary to see how the model performance once combined with an adhesion force model.



(a) Liquid phase.



(b) Vapour phase.

Figure 5.16: Deviation from coexistence density both in the liquid phase (boundary node beneath the droplet) and vapour phase (boundary node at the top of the simulation domain) for the LAD model.

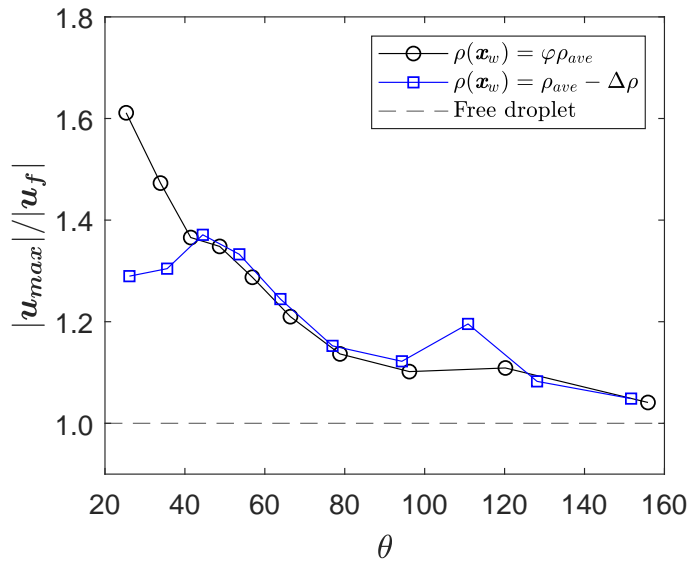


Figure 5.17: Evaluation of maximum spurious velocities for different contact angles for LAD model.

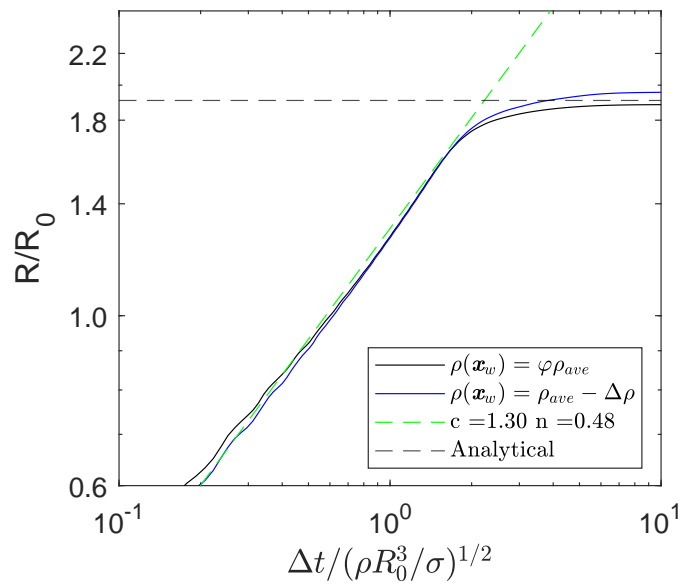


Figure 5.18: Evolution of droplet radius on smooth surface with an equilibrium contact angle of  $\theta = 40^\circ$  for the LAD model. Equilibrium spreading factor determined by equation 5.17 and spreading power law exponent given by [206].

## CHAPTER 6

---

### Droplet Deposition on Structured Surfaces

---

The research presented in this chapter was published in: F. F. Jackson, K. J. Kubiak, M. C. T. Wilson, M. Molinari, and V. Stetsyuk, “Droplet misalignment limit for inkjet printing into cavities on textured surfaces,” *Langmuir*, 2019. DOI: [10.1021/acs.langmuir.9b00649](https://doi.org/10.1021/acs.langmuir.9b00649)

---

#### 6.1 Introduction

This chapter explores the process of droplet deposition onto a chemically and topographically textured surface, specifically that of an idealised pixel geometry pertaining to organic light emitting diode displays (*square cavity*). Particular attention is given to the process of droplet self-alignment, mitigating droplet positioning errors. The multiphase model from §3.3 is used with the new (IFM) wetting model §5.2.2 to explore the dynamics of droplet deposition over a large parameter space and identify key attributes enhancing droplet self-alignment.

## 6.2 Deposition within a Square Micro-cavity

The idea of using chemical and topographically textured surfaces to control deposition is already utilised for the fabrication of devices via inkjet deposition. However, with demand for ever decreasing sizes of electrical components and the desire for display resolutions to increase, the requirement to precisely control droplets is requiring finer tolerances. This is problematic due to the nature of DOD inkjet printing (explained in §1.2), which requires the print head to be positioned a suitable distance away from the substrate for the formation of a droplet. Thus positional inaccuracies of the print head and angular deflection of the droplet once ejected from the nozzle (illustrated in figure 6.1) can lead to significant positioning errors.

In [4], the authors give the formula for the total positioning error,  $P$  as  $P = \sqrt{E_{PH}^2 + E_{\theta}^2 + E_u^2}$ , where  $E_{PH}$ ,  $E_{\theta}$  and  $E_u$  are the positional inaccuracy of the print head, angular deflection of the droplet exiting the nozzle and droplet in flight velocity error respectively. However, this does not give the maximum possible error as  $\sqrt{E_{PH}^2 + E_{\theta}^2 + E_u^2} \neq \sqrt{E_{PH}^2} + \sqrt{E_{\theta}^2} + \sqrt{E_u^2}$ . Nevertheless, their results still showed significant droplet placement errors with respect to the cavity under investigation. Furthermore, in [4], the cavities are circular, thus due to the symmetrical nature of the deposition, only the magnitude of each error was important. However, both  $E_{PH}$  and  $E_{\theta}$  are multi-dimensional, thus the positioning error is multi-dimensional,  $P = \sqrt{P_{\beta} + P_{\bar{\beta}}}$ , where  $\beta$  and  $\bar{\beta}$  represent orthogonal spatial dimensions. This will therefore influence deposition for non-circular cavities.

Prior research, both experimental and numerical focusing the droplet deposition into cavities include [211, 212, 52, 213, 58]. Furthermore, there are examples where the effects of droplet misalignment have been explored [51, 53, 59, 214]. However, these studies do not consider the limits of posi-

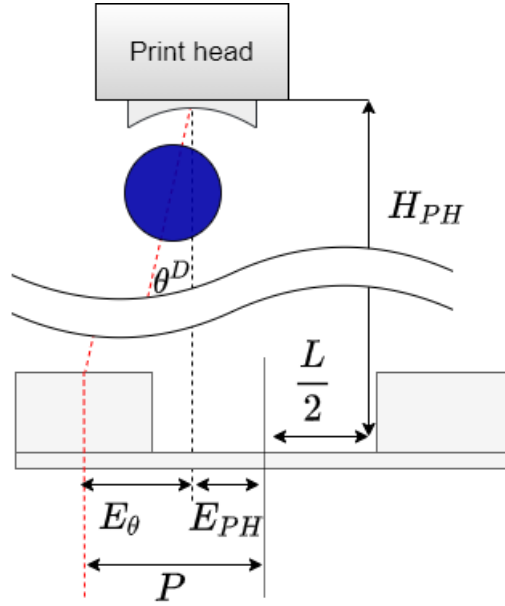


Figure 6.1: Illustration of droplet angular deflection ( $\theta^D$ ) and print-head positioning error ( $E_{PH}$ ) during droplet deposition. The droplet positional error,  $P$ , gives the distance away from the centre of the cavity and  $L$  gives the size of the cavity.

tional inaccuracy or the effects of dual-axis positional inaccuracy for the case of a square cavity.

The model used to explore the effects of positional inaccuracy is illustrated in figure 6.2. To reduce the size of the computational domain, the full flight path of the droplet from the print-head to the substrate,  $H_{PH}$ , is not modelled, rather the droplet is positioned above the cavity, with a pre-determined positioning error,  $P$ . Furthermore, as the droplet in-flight velocity is  $|\mathbf{u}| \approx u_y$ , the droplet is initialised with a single component of velocity in the  $y$ -axis only. The cavity dimensions,  $L$  and  $H$  give length and height respectively, the size of which is set in integer increments of  $\Delta x$ . The contact angle of the

substrate and cavity walls are controlled by  $\theta_s$  and  $\theta_w$  respectively.

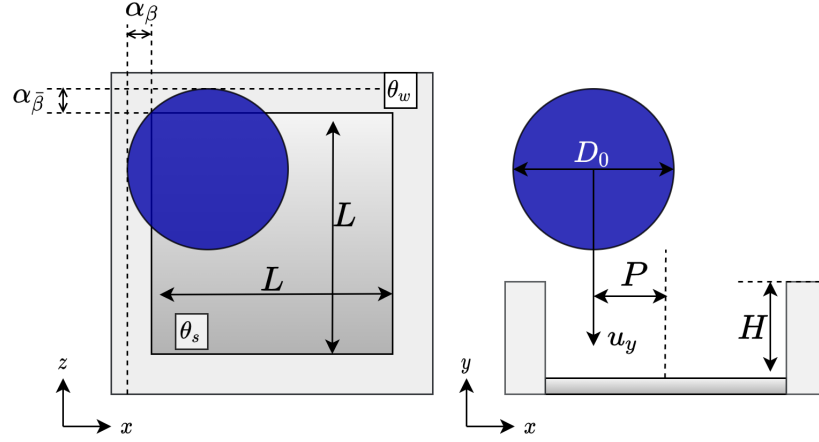


Figure 6.2: Idealised cavity geometry. Wetting of the substrate and cavity walls controlled by  $\theta_s$  and  $\theta_w$  respectively. Print-head misalignment,  $P$  gives droplets initial placement error,  $\alpha_\beta$  and  $\alpha_{\bar{\beta}}$  are the fraction of the droplet diameter overhanging the cavity walls in different directions.

To give a quantitative description of the wetting in the cavity, the wetted fraction (WF) is introduced, which describes the fraction of the cavity surface which is wetted by the droplet and is formally expressed as

$$\text{WF} = \frac{1}{L_x L_z} \sum_{x,z}^{L_x L_z} \text{H}(\rho_{x,2,z} - \rho_c), \quad (6.1)$$

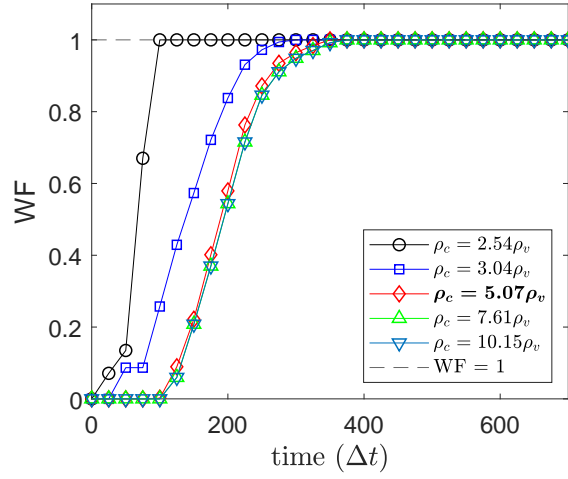
where  $L_x$  and  $L_z$  are the lattice nodes which are within the cavity in the  $x$  and  $z$  direction respectively,  $\text{H}$  is the Heaviside function, and  $\rho_c$  is a critical value of density, the value of which is determined in the following model validation section. The previously validated MRT multiphase model §3.3 is used with the new wetting model §5.2.2 which is subsequently parallelised with MPI (§4.4) to explore a large parameter space with quick computation.

### 6.2.1 Model Validation

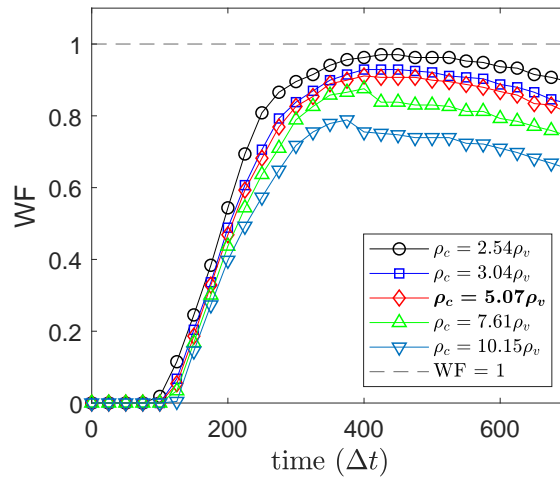
In order to accurately measure the wetted fraction within the cavity, nodes above the substrate need to be accurately classified as either wetted or non-wetted. To achieve this, an appropriate value of the critical density,  $\rho_c$  in equation 6.1 needs to be determined. The correct value will depend primarily on the models coexistence densities and also the chosen wetting model, as this affects the density values close to solid surfaces. To determine the critical value, a preliminary set of investigations is performed in which a droplet wets a cavity and the WF is recorded for different values of  $\rho_c$ . Both hydrophilic ( $\theta_s = \theta_w = 30^\circ$ ), and hydrophobic ( $\theta_s = \theta_w = 130^\circ$ ) cavities are investigated, to ensure the WF is accurately captured for a range of wetting conditions. The Reynolds and Weber numbers are set arbitrarily, with the only requirement being a sufficient droplet size for stability.

The resulting WF for different values of  $\rho_c$  are given in figure 6.3. For wetting of the hydrophilic cavity, figure 6.3a, it is evident that  $\rho_c < 5.07\rho_v$  results in significant deviation in the recorded WF, with the rate with which the cavity fills been over-predicted. For  $\rho_c \geq 5.07\rho_v$ , there is little deviation in the recorded WF. For wetting of the hydrophobic cavity, figure 6.3b, the WF results appear to be much more density to  $\rho_c$ . However, for  $3.04\rho_v \leq \rho_c \leq 5.07\rho_v$ , the WF results are in good agreement. Therefore, the critical density is chosen to be  $\rho_c = 5.07\rho_v$ , as this gives good predictions for both hydrophilic and hydrophobic wetting conditions.

It is worth noting that the new wetting model (§5.2.2) used for these investigations resulted in the least density change (for adhesion based models), which aids in the accurate determination of the WF.



(a) Hydrophilic cavity,  $\theta_s = \theta_w = 30^\circ$ .



(b) Hydrophobic cavity,  $\theta_s = \theta_w = 130^\circ$ .

Figure 6.3: Determination of suitable critical density value,  $\rho_c$ , for correctly computing the wetted fraction (equation 6.1) for both hydrophobic and hydrophilic cavities. Chosen  $\rho_c$  value highlighted in bold font.

### Lattice Independence Study

The effects of lattice resolution are investigated for the case of a single droplet impacting a neutrally wetting cavity ( $\theta_s = \theta_w = 90^\circ$ ). The smallest resolution

consisted of a droplet diameter of  $D_0 = 15.11$  falling into a square cavity with  $L = 20$  and  $H = 5$ . For each resolution the velocity was first set to ensure that  $We = 20$ , then the kinematic viscosity was set to ensure that  $Re = 20$ . Instead of the lattice time-step,  $\Delta t$ , the evolution of the WF is plotted against the dimensionless time,  $t^* = \Delta t u_0 / D_0$ , to allow for comparable results at different resolutions. It is important to note that the time taken to reach the substrate was slightly different for each of the domain sizes, this is likely due to the droplet experiencing viscous drag when falling towards the substrate, which increases with lattice resolution. For comparison across different lattice resolutions, the impact time ( $t_{impact}^*$ ) i.e. the time at which the droplet impacts the substrate, is subtracted from the dimensionless time  $t^* = t^* - t_{impact}^*$ , thus each WF plot starts from  $t^* = 0$ . From the initial resolution, the droplet diameter, cavity size and total domain size were scaled by 2, 4 and 8 and the evolution of the WF was recorded for each, figure 6.4. For all but the smallest resolution, which consisted of a droplet of  $D_0 = 15.1$  there is a clear linear trend in the early stages of wetting of  $WF \approx 1.8t^*$ , which is highlighted by the dashed red line. From  $t^* \approx 0.5$  onwards, the effects of the increased resolution result in a slightly longer time taken to fill the cavity ( $WF = 1$ ), although the trend for all but the smallest resolutions remain comparable. From these results, the minimum resolution for the droplet should be  $D_0 \approx 30.2$  for a cavity length  $L = 40$ , as this allows for the best compromise in terms of computational resources as well as a sufficiently well resolved simulation.

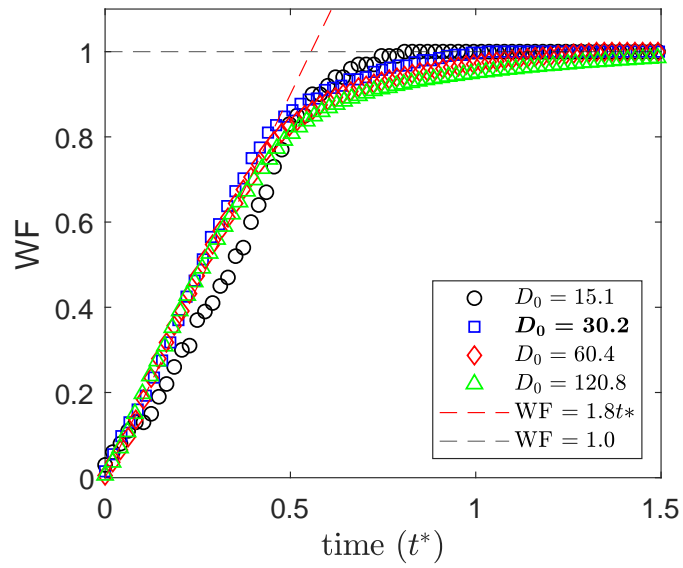


Figure 6.4: Determination of suitable lattice resolution through evaluation of the wetted fraction. Chosen lattice resolution highlighted in bold font.

## 6.2.2 Ideal Deposition into a Cavity

Before investigating the influence of positional inaccuracies on deposition, a base comparison is required. Therefore, the case of a droplet falling directly towards the centre of the cavity is explored. As the current multiphase model has a density ratio of  $\rho_R \approx 36$ , which is significantly smaller than that of physical printing systems, the influence of the dynamic viscosity ratio ( $\mu_R$ ) on the dynamic deposition process is explored. A droplet with a diameter of  $D_0 = 34$  with Re and We numbers of 30 and 13 respectively, is configured to fall directly into the centre of a cavity with dimensions  $45 \times 45 \times 10$  and equilibrium contact angles of  $\theta_s = \theta_w = 50^\circ$ . To expand the range of dynamic viscosity ratio of the liquid and vapour phases, the relaxation times which control the kinematic viscosity are varied locally as

$$\tau_\nu(\mathbf{x}) = \tau_{\nu,v} + (\tau_{\nu,l} - \tau_{\nu,v}) \frac{\rho(\mathbf{x}) - \rho_l}{\rho_l - \rho_v}, \quad (6.2)$$

where  $\tau_{\nu,v}$  and  $\tau_{\nu,l}$  are the relaxation times for the vapour and liquid kinematic viscosity respectively. The evolution of the WF is displayed in figure 6.5, where it is observed that as  $\mu_R$  increases above 60, no significant change in the evolution of the WF is exhibited, therefore this value is used for the following investigations. Illustrated in figure 6.6 are snapshots of droplets spreading with a dynamic viscosity ratio of  $\mu_R = 3.75$  and  $\mu_R = 240$ , figures 6.6a and 6.6b respectively. Here it is evident from the snapshot at  $t^* = 1.22$  that the inertial spreading of the droplet has been significantly damped by the increased viscosity of the surrounding vapour. These findings are in agreement with [58], in which the authors investigated the influence of density ratio on deposition with a kinematic viscosity ratio,  $\mu_R = 1$ .

As discussed in §1.2, there are ideal printing parameters in terms of Re and We which result in a fluid which is both printable and stable upon impact

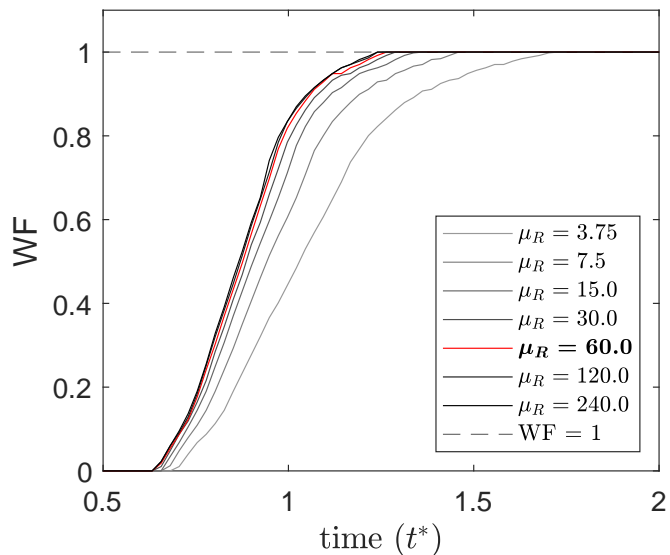
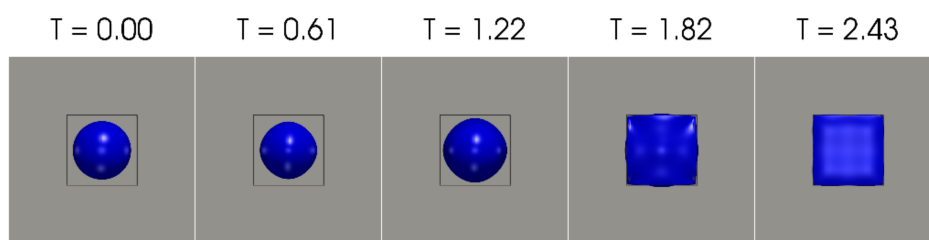
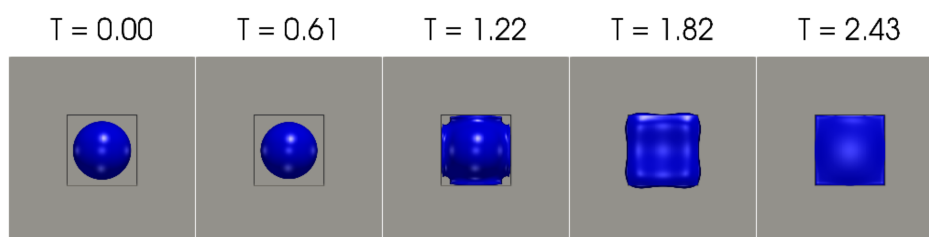


Figure 6.5: Evaluation of the effect of kinematic viscosity ratios  $\mu_R$  on the evolution of the WF. Darker lines correspond to larger kinematic viscosity ratio. Chosen viscosity ratio highlighted in bold.

with the substrate. The influence of  $Re$  and  $We$  within the printable regime (see figure 1.1 for illustration) is explored in terms of time taken to achieve a fully wetted cavity ( $t_{WF=1}^*$ ), figure 6.7. Here, either the  $Re$  or  $We$  is fixed while the other is varied ( $Oh(Re, We = 80)$  or  $Oh(We, Re = 30)$ ), then the two are combined to give the dimensionless parameter  $Z$ , which is the inverse of the Ohnesorge number. Included in the figure is a shaded region, illustrating the lower bound of  $Z$  highlighted in [15], as this is where a large difference in  $t_{WF=1}^*$  is observed for  $Oh(Re, We = 80)$ .



(a)  $\mu_R = 3.75$ .



(b)  $\mu_R = 240$

Figure 6.6: Snapshots of ideal droplet deposition into a cavity with different dynamic viscosity ratios.

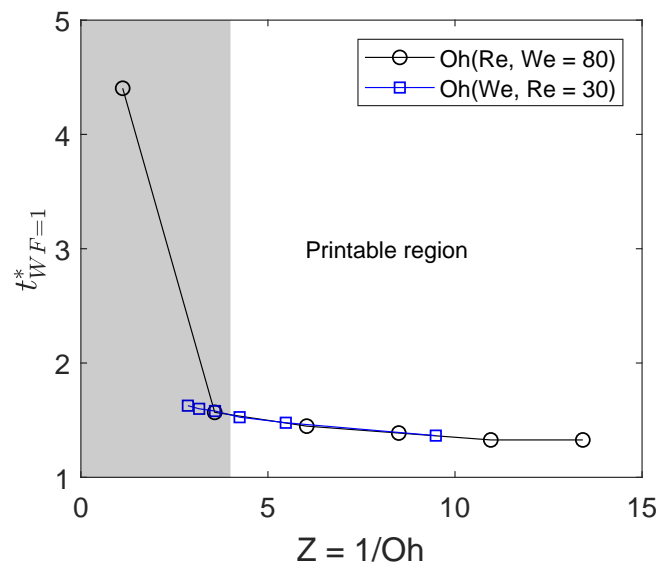


Figure 6.7: Dimensionless wetted time for ideal droplet deposition as a function of the inverse Ohnesorge number. The grey region illustrates Ohnesorge numbers below the critical value ( $Z = 4$ ) identified in [15].

## 6.3 Deposition with Single-axis Positional Inaccuracy

The topographical and chemical properties of the cavity aid in positioning the droplet to the desired location. Here, the effects of single-axis positional inaccuracies are explored in terms of the droplets ability to self-align i.e. move to the desired location and achieve  $WF = 1$ . As mentioned in the introduction to this chapter, there are numerous factors that contribute to positioning errors of the droplet. To generalise results for different droplet and cavity sizes, the overlap parameter  $\alpha_\beta$  is introduced (where  $\beta$  is the  $x$  or  $z$  direction), which describes the fraction of the droplet positioned outside of the cavity and is defined as

$$\alpha_\beta = \frac{1}{2} \left( 1 - \left( \frac{L}{D} - \frac{2P_\beta}{D} \right) \right). \quad (6.3)$$

For the case where a droplet is overhanging a single wall, the overlap parameter can conveniently be used to describe the fraction of the volume of the droplet initially positioned outside of the cavity, referred to as volume fraction VF and is expressed as

$$VF = 3\alpha_\beta^2 - 2\alpha_\beta^3. \quad (6.4)$$

### 6.3.1 Droplet Morphologies

The influence of the wettability of the substrate and cavity wall is first explored for the case of single-axis positional error, in which  $\alpha_\beta = 0.5$  ( $P_\beta = L/2$ ) and  $\alpha_{\bar{\beta}} = 0$ . The cavity dimensions and droplet properties are identical to the previous study with ideal deposition. Rather than monitoring convergence levels for each configuration, a maximum run time ( $t_{\max}^*$ )

is specified. The motivation for this is the varying time scales associated with different spreading regimes, which differ significantly depending on the wetting properties. To allow for comparable results for cases in which droplets are deposited ideally, the maximum run time is chosen to be  $t_{\max}^* = 8.51$ , as previous investigations ([58]) have shown that most dynamic behaviour has stabilised at times  $t^* < 8$ . Due to the use of a cut-off time, the droplet morphology at time  $t_{\max}^* = 8.51$  is referred to as the final-state morphology rather than the equilibrium morphology. The contact angles  $\theta_s$  and  $\theta_w$  are varied independently, for angles between  $30^\circ \leq \theta \leq 150^\circ$  for a total of 400 individual simulations. Snapshots of a small subset of the total 400 simulations are displayed in figure 6.8. As can be seen, the final-state morphologies vary significantly depending on the wetting properties, with only a few cases exhibiting ideal wetting properties, in which the droplet is fully confined within and fully wets the cavity.

Through measuring the WF inside the cavity, and determining if external wetting (EW) i.e. wetting on the surface of the surround cavity walls has occurred, four possible configurations are identifiable: ideal wetting where  $WF = 1$  and  $EW = 0$ , internal + external wetting where  $WF = 1$  and  $EW \neq 0$ , external wetting where  $WF \neq 1$  and  $EW \neq 0$  and finally partial wetting, where  $WF \neq 1$  and  $EW = 0$ . The resulting wetting types for each of the 400 simulations are displayed in figure 6.9. From this figure, it is clear that cavity wall contact angles lower than  $\theta_w \approx 75^\circ$  result in the droplet spreading and remaining outside of the cavity. Furthermore, it is found that if the substrate contact angle is above  $\theta_s \approx 105^\circ$  then only a partially wetted cavity is achieved, as the droplet either preferentially wets the cavity wall or remains confined within the cavity but fails to spread fully across the surface. Out of the 400 configurations, 133 (33.25%) resulted in ideal wetting.

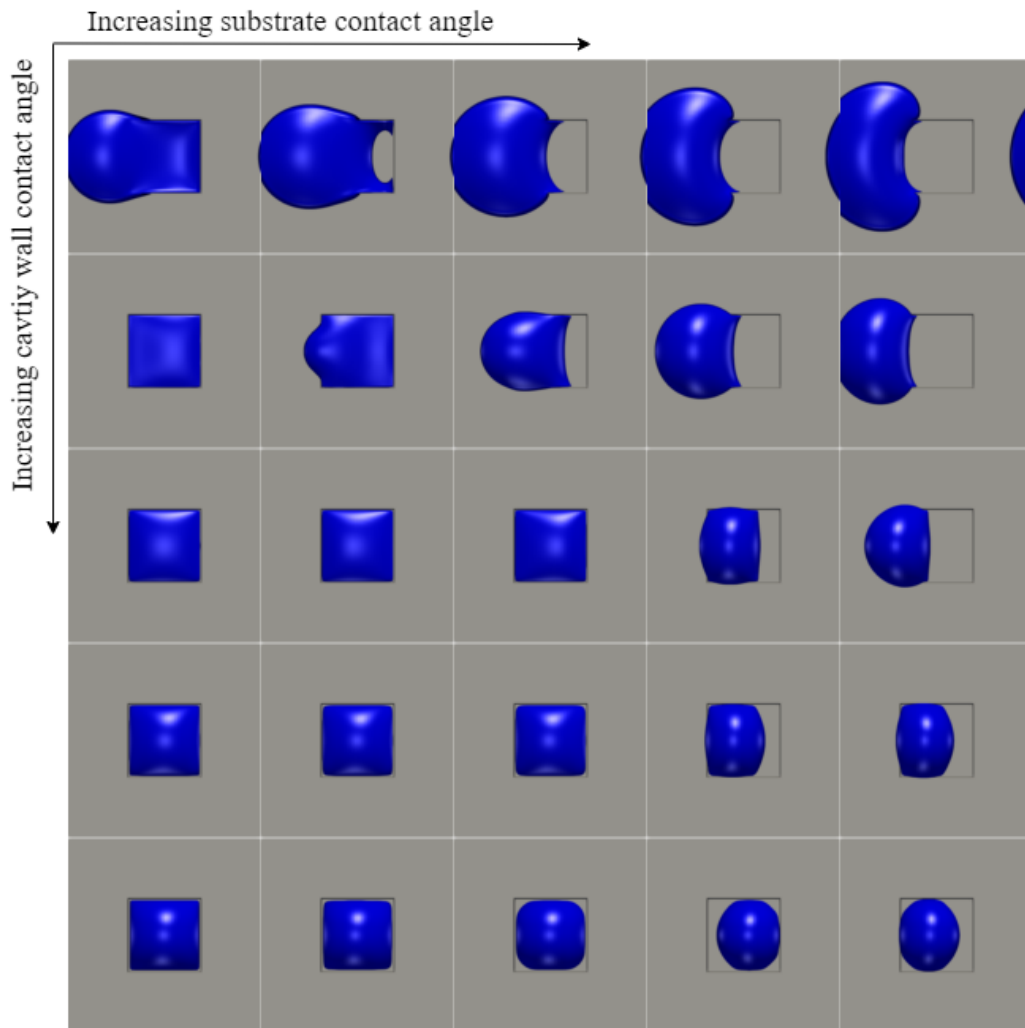


Figure 6.8: Distinct droplet morphologies for single-axis misalignment with overlap value of  $\alpha_\beta = 0.5$  and  $\alpha_{\bar{\beta}} = 0.0$ . Cavity wall contact angle ( $\theta_w$ ) increases from top to bottom and substrate contact angle ( $\theta_s$ ) increases from left to right.

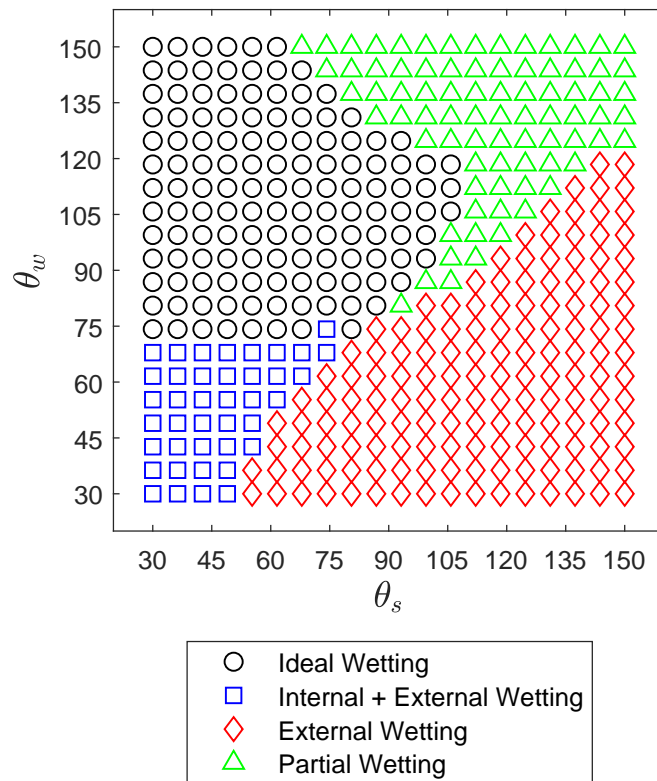


Figure 6.9: Identification of distinct droplet morphologies at  $t_{\max}^*$  for droplet deposition with single-axis misalignment ( $\alpha_\beta = 0.5$  and  $\alpha_{\bar{\beta}} = 0.0$ ).

### 6.3.2 Cavity Wetting Times

For the 133 configurations which resulted in an ideal deposition within the cavity (figure 6.9), the time taken to achieve a fully wetted cavity ( $t_{WF=1}^*$ ) is explored. The results are displayed in figure 6.10. For the cavity wall contact angle of  $\theta_w = 75^\circ$ , there is an approximately linear relationship between the substrate contact angle,  $\theta_s$  and the time taken to achieve a fully wetted cavity. Furthermore, the quickest wetting times are observed for low values of substrate contact angle. The shortest wetting time of  $t_{WF=1}^* = 2.578$  is observed when  $\theta_s = 30^\circ$  and  $\theta_w = 86.84^\circ$ . However, the results for  $\theta_w = 74.21^\circ$  to  $\theta_w = 86.84^\circ$  differ by less than 3%. It can be seen that wetting time is mainly governed by the substrate contact angle.

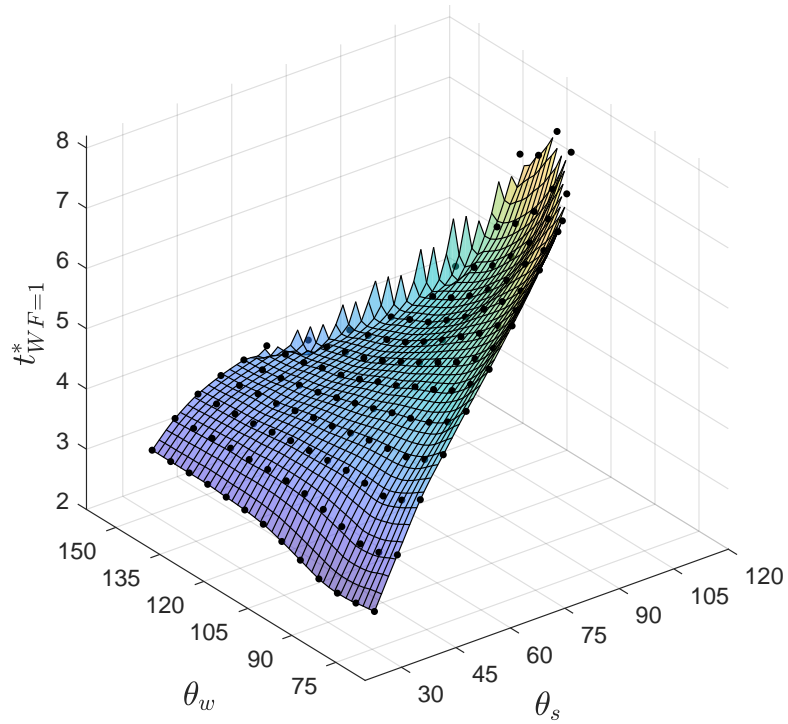


Figure 6.10: Wetting time for cavities in which ideal wetting is achieved for droplet deposition with single-axis misalignment ( $\alpha_\beta = 0.5$  and  $\alpha_{\bar{\beta}} = 0.0$ ).

### 6.3.3 Evolution of Wetted Fraction

The dynamic evolution of the WF is recorded at regular intervals throughout the simulation. In figure 6.11, the evolution of the WF is plotted for different wetting configurations. The solid-colour lines correspond to cases in which the substrate contact angle  $\theta_s = 60^\circ$  whereas the dashed lines represent substrate contact angles of  $\theta_s = 120^\circ$ . The different colours correspond to different contact angles of the cavity walls ( $\theta_w$ ). Highlighted in the figure are three shaded regions, which identify different spreading modes. The grey region shows the time at which the droplet is in free-fall, following this, the pink region illustrates the spreading regime dominated by the droplets inertia. In the green region, spanning from  $t^* \approx 0.9$  to  $t^* \approx 2.9$ , the spreading rate depends on the substrate contact angle  $\theta_s$ . Finally, the spreading is driven by the contact angle of the cavity wall  $\theta_w$ . From the results shown in figure 6.11, the case of  $\theta_s = 60^\circ$  and  $\theta_w = 120^\circ$  results in the shortest wetting time. When the substrate contact angle was increased to  $\theta_s = 120^\circ$  the droplet fails to fully wet the cavity and there is a clear recoil in the spreading at  $t^* \approx 6.0$ . Snapshots of the evolution of these two conditions are shown in figure 6.12. Here it can be seen how the part of the droplet which is wetting the cavity wall after impact is drawn back towards the rest of the droplet in the cavity, causing the WF to increase again at  $t^* \approx 2.43$ .

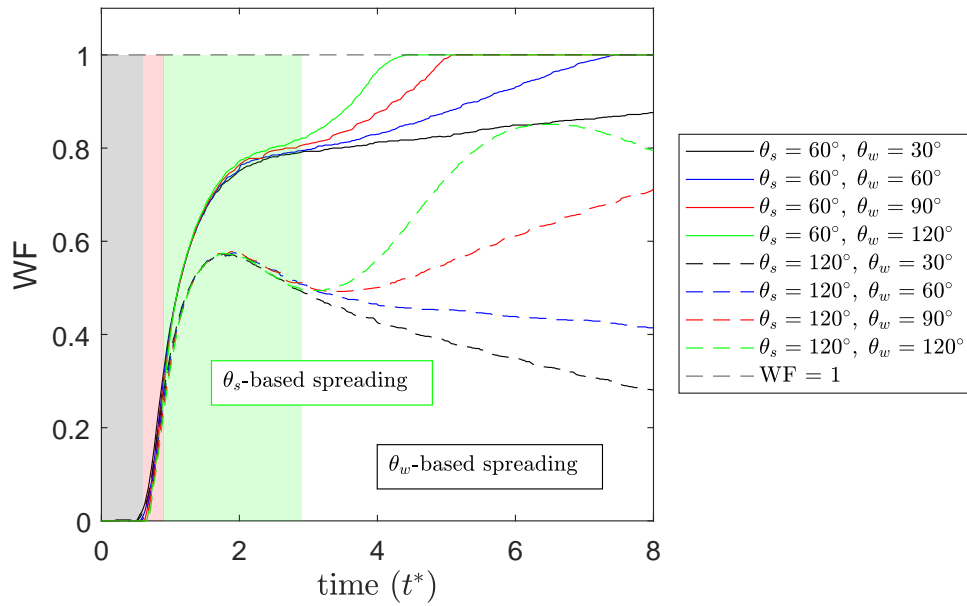
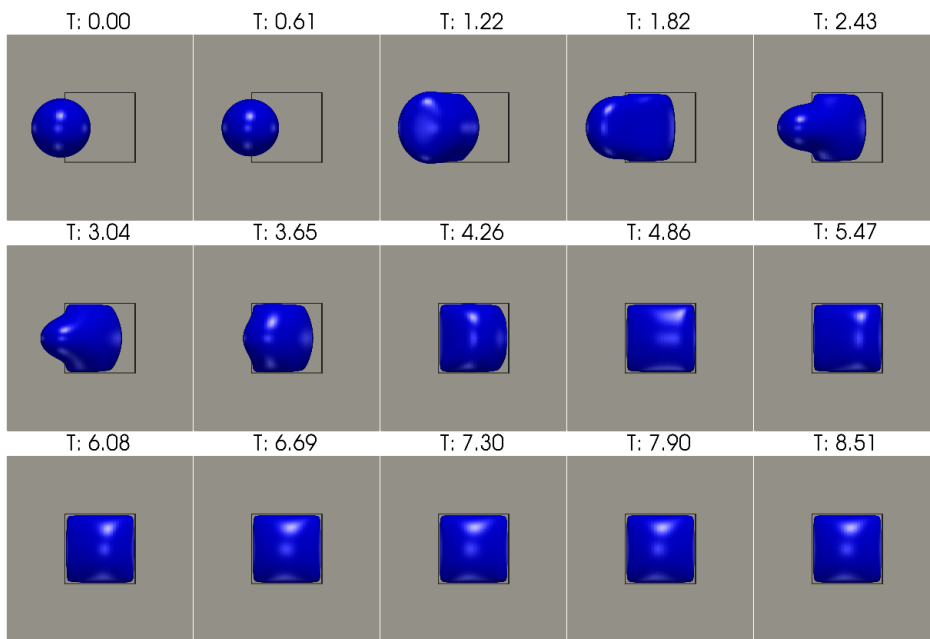
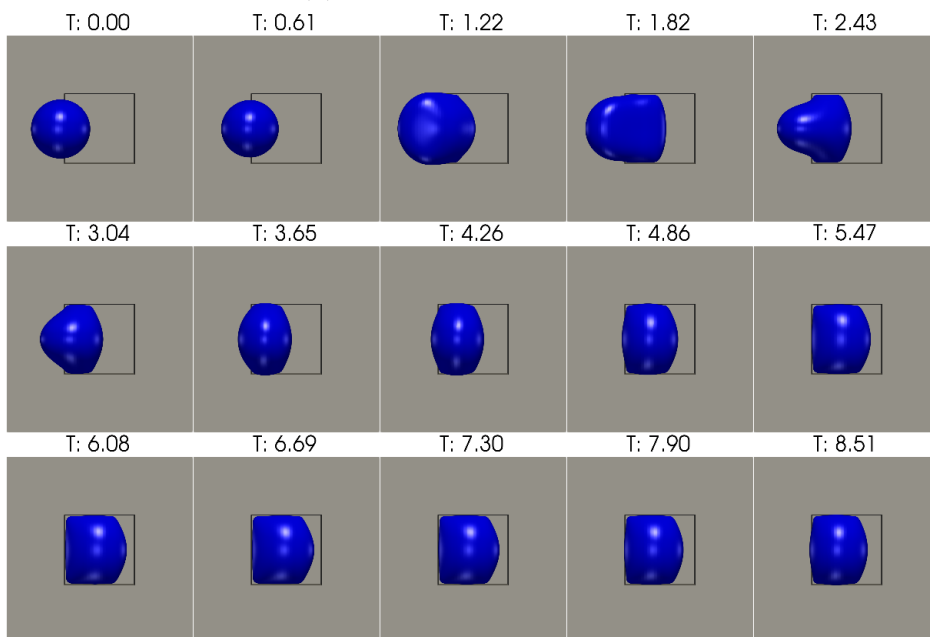


Figure 6.11: Evolution of wetted fraction for droplet deposition with single-axis misalignment ( $\alpha_\beta = 0.5$  and  $\alpha_{\bar{\beta}} = 0.0$ ). The grey shaded region illustrates the droplet free-fall regime, the pink shaded region illustrates the inertial spreading regime, the green shaded region is where the spreading is determined by the substrate contact angle ( $\theta_s$ ) and finally, the remaining white space illustrates the region in which the spreading is determined by the cavity wall contact angle ( $\theta_w$ ).



(a)  $\theta_s = 60^\circ$  and  $\theta_w = 120^\circ$



(b)  $\theta_s = 120^\circ$  and  $\theta_w = 120^\circ$

Figure 6.12: Illustrations of droplets spreading in cavities with different substrate and wall contact angles with single-axis misalignment ( $\alpha_\beta = 0.5$  and  $\alpha_{\bar{\beta}} = 0.0$ ).

## 6.4 Deposition with Dual-axis Positional Inaccuracy

As mentioned in the introduction, the positional inaccuracies are multidimensional and to the best of the author's knowledge, investigations of droplet deposition into cavities with positioning errors in two dimensions have not yet been explored. Here, the position relative to the cavity is still easily described by the overlap parameters  $\alpha_\beta$  and  $\alpha_{\bar{\beta}}$ , however, the VF becomes more complicated to compute, as two spherical caps intersect as illustrated in figure 6.13.

Below critical values of dual-axis overlap, the volume fraction can be computed as the sum of the individual volume fractions computed for each value of overlap (equation 6.4). However, if for a known value of overlap  $\alpha_{\bar{\beta}}$ , the other is above the critical value,  $\alpha_\beta^c$  additional consideration is required to account for the overlapping cap regions. The critical value for  $\alpha_\beta^c$  is expressed as

$$\alpha_\beta^c = \frac{1}{2} - \sqrt{\left(\frac{1}{2}\right)^2 - \left(\frac{1}{2} - \alpha_{\bar{\beta}}\right)^2}, \quad (6.5)$$

where  $\beta$  and  $\bar{\beta}$  are orthogonal coordinate axes. Alternatively, if  $\alpha_\beta = \alpha_{\bar{\beta}}$  then the critical value of overlap simplifies to  $\alpha_\beta^c = (2 - \sqrt{2})/4$ . If the misalignment is below these critical values, the cap volume equations can be computed simply as

$$\begin{aligned} V_\beta^c &= \frac{1}{3}\pi(\alpha_\beta 2R_0)^2(3R_0 - \alpha_\beta 2R_0), \\ V_{\bar{\beta}}^c &= \frac{1}{3}\pi(\alpha_{\bar{\beta}} 2R_0)^2(3R_0 - \alpha_{\bar{\beta}} 2R_0). \end{aligned} \quad (6.6)$$

When the two spherical caps overlap, the additional *wedge* volume ( $V_w$ ) needs

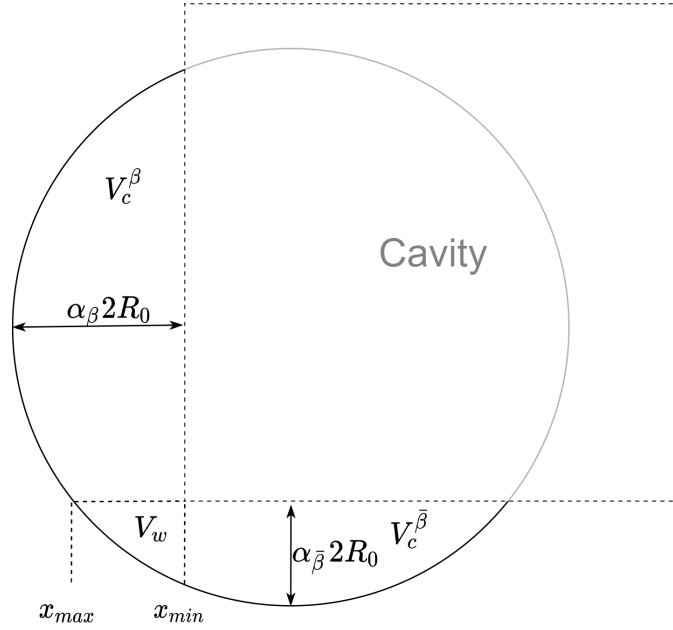


Figure 6.13: Illustration of the volume of droplet initially placed outside of the cavity for dual-axis positioning error ( $\alpha_\beta$  and  $\alpha_{\bar{\beta}} > 0$ ).  $R_0$  is the droplet radius,  $V_c^\beta$ ,  $V_c^{\bar{\beta}}$  and  $V_w$  are the spherical cap volumes and wedge volume respectively.  $x_{max}$  and  $x_{min}$  are the limits used in determining the volume,  $V_w$ .

to be removed from the above calculation, the wedge volume is computed with the following integral

$$V_w = \int_{x_{min}}^{x_{max}} R(x)^2 \cos^{-1} \left( 1 - \frac{h(x)}{R(x)} \right) - (L) \sqrt{2h(x)R(x) - h(x)^2} dx, \quad (6.7)$$

where,  $x_{min}$  and  $x_{max}$  are the limits illustrated in figure 6.13,  $R(x) = \sqrt{R_0^2 - x^2}$ ,  $h(x) = R(x) - L$  and  $L = r_0 - \alpha_\beta 2R_0$ . Therefore, the total VF is calculated as follows

$$VF = \frac{3(V_{\beta}^c + V_{\bar{\beta}}^c - V_w)}{4\pi R_0^3}. \quad (6.8)$$

The relationship between the VF and the values of overlap for dual-axis misalignment is illustrated in figure 6.14, where dashed lines are used to illustrate overlap values which results in  $VF = 0.5$  for comparison with earlier results.

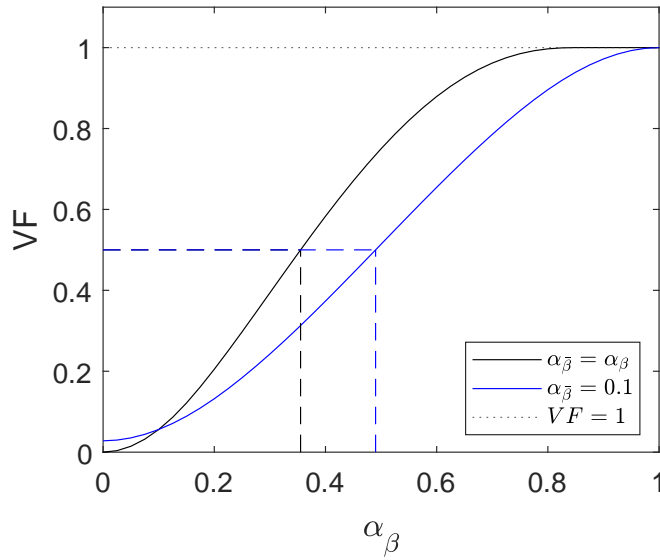


Figure 6.14: Volume fraction for different configurations of dual-axis misalignment.

By making the assumption that the dual-axis value of overlap (when  $\alpha_{\beta} = \alpha_{\bar{\beta}}$ ) is equal to the single-axis value of overlap divided by  $\sqrt{2}$ , a reasonable approximation of the dual-axis VF can be made as

$$VF \approx 6\alpha_{\bar{\beta}}^2 - 4\sqrt{2}\alpha_{\bar{\beta}}^3. \quad (6.9)$$

This assumption is compared to the exact solution obtained by equation 6.8 in figure 6.15, and good agreement is seen up until the value of  $\alpha_{\beta} = 1/\sqrt{2}$  as

this is where the assumption gives a VF of 1, the maximum possible value. Furthermore, a bad approximation is included in which the VF is calculated from individual cap volumes without considering the overlapping *wedge*.

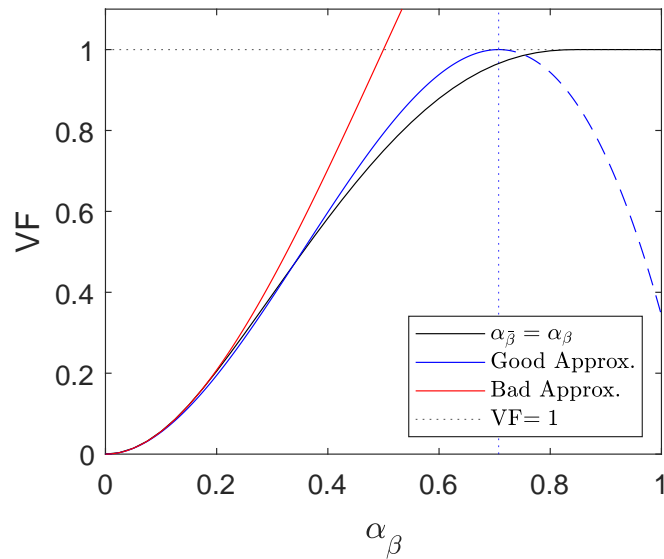


Figure 6.15: Approximations for the volume fraction with dual-axis overlap. The solid black line is the analytical solution (equation 6.8), the blue line is the *good* approximation (equation 6.9) and the red line is the *bad* approximation. The blue dotted line is at the point  $\alpha_\beta = 1/\sqrt{2}$ , where the *good* approximation equals 1.

### 6.4.1 Droplet Morphologies

In order to compare results between dual-axis and single-axis positional inaccuracy, the initial VF is matched in both cases. Therefore, in order to achieve a  $VF = 0.5$  when  $\alpha_\beta = \alpha_{\bar{\beta}}$ , the dual-axis overlap needs to be 0.355216. Applying this value of overlap, simulations are run as before, varying the contact angles of the substrate and cavity walls independently. Snapshots of a small subset of the 400 total simulations are displayed in figure 6.16. The final state configuration of each of the 400 simulations is displayed in figure 6.17. Out of the 400 configurations, 122 resulted in ideal wetting of the cavity (30.5%, which is 2.75% less than the single overlap results).

### 6.4.2 Cavity Wetting Time

Taking the 122 configurations in which ideal wetting occurs, the wetting time is investigated, figure 6.18. Interestingly, the shortest wetting time of  $t_{WF=1}^* = 3.50$  for the dual-axis positioning error case is observed for  $\theta_s = 30^\circ$  and  $\theta_w = 150^\circ$ , whereas for the single-axis misalignment the quickest wetted time was achieved with wall contact angle of  $\theta_w = 86.84^\circ$ . It is also evident that increasing the wall contact angle reduces the wetting time for all substrate contact angles, which differs from the results for the single value of overlap.

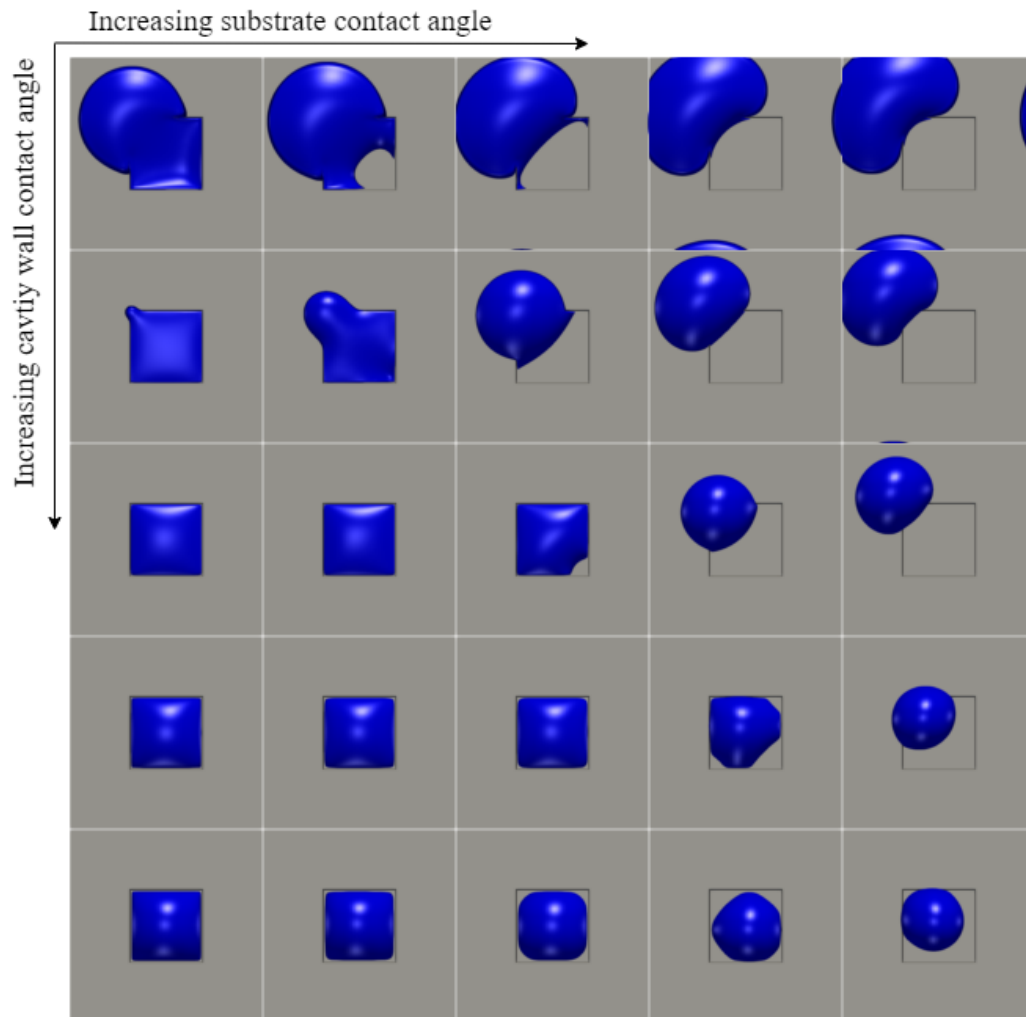


Figure 6.16: Distinct droplet morphologies for dual-axis misalignment with overlap values of  $\alpha_\beta = \alpha_{\bar{\beta}} = 0.355216$  ( $\text{VF} = 0.5$ ). Cavity wall contact angle ( $\theta_w$ ) increases from top to bottom and substrate contact angle ( $\theta_s$ ) increases from left to right.

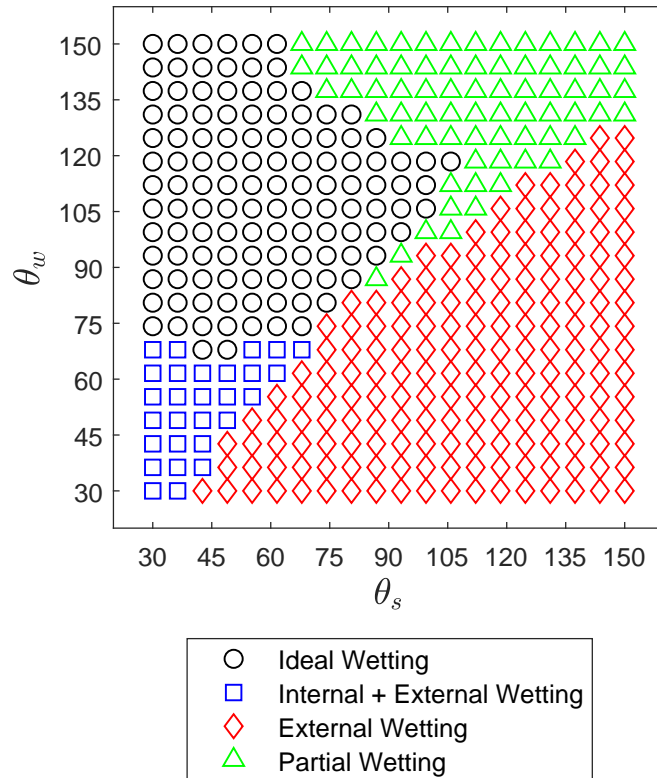


Figure 6.17: Identification of distinct droplet morphologies at  $t = t_{max}$  for droplet deposition with dual-axis misalignment  $\alpha_\beta = \alpha_{\bar{\beta}} = 0.355216$  (VF = 0.5).

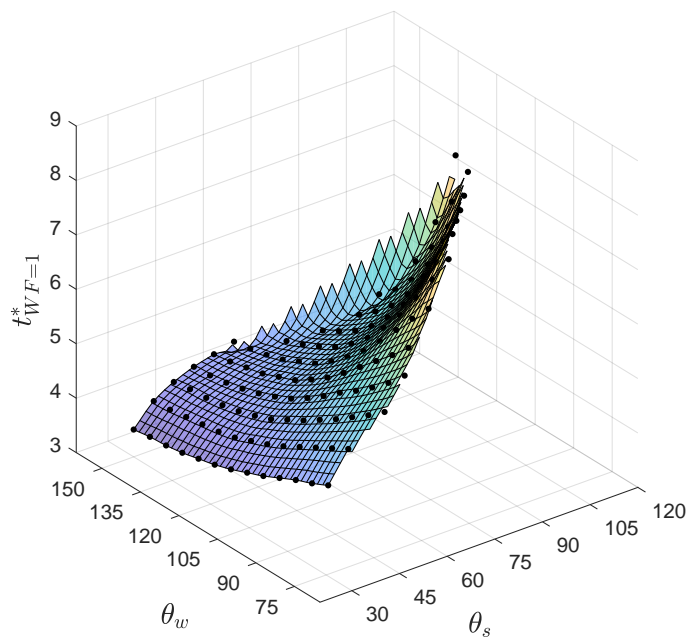


Figure 6.18: Wetting time for cavities in which ideal wetting is achieved for droplet deposition with dual-axis misalignment  $\alpha_\beta = \alpha_{\bar{\beta}} = 0.355216$  (VF = 0.5).

### 6.4.3 Evolution of Wetted Fraction

The time dependence of the wetted fraction for dual-axis positioning error is illustrated in figure 6.19. As with the single-axis positioning error results (figure 6.11), there are different spreading regimes that can be identified. The majority of the wetting configurations gave similar evolution of the wetted fraction compared to the single-axis positioning error case. There is, however, notably different dynamics for the cavity with  $\theta_s = 120^\circ$  and  $\theta_w = 90^\circ$ . Where, for the single-axis case (figure 6.11), the wetted fraction increases after the substrate spreading regime. Alternatively, for the dual-axis case, the wetted fraction remains approximately constant after the substrate spreading regime. This is attributed to the droplet spreading over a concave corner for the case of a dual-axis positioning error, which due to the contact angle of cavity wall,  $\theta_w = 90^\circ$ , draws the droplet backwards (towards the corner). This is supported by the results of the case where the wall contact angle is increased to  $\theta_w = 120^\circ$ , as after the substrate spreading regime the wetted fraction increases, as the droplet is now pushed away from the corner.

Snapshots of the droplet evolution in a cavity with different substrate contact angles and dual-axis positioning error are displayed in figure 6.20. For the case where the substrate contact angle is  $\theta_s = 60^\circ$ , figure 6.20a, the droplet can be seen to impact the top corner of the cavity wall, spread, then be drawn into the cavity, giving a fully wetted cavity (WF = 1). For the case where the substrate contact angle is increased to  $\theta_s = 120^\circ$ , figure 6.20b, the droplet impacts the top corner of the cavity wall, spreads and is slowly drawn into the cavity. However, complete wetting is not achieved, and the final-state morphology resembles an irregular heptagon.

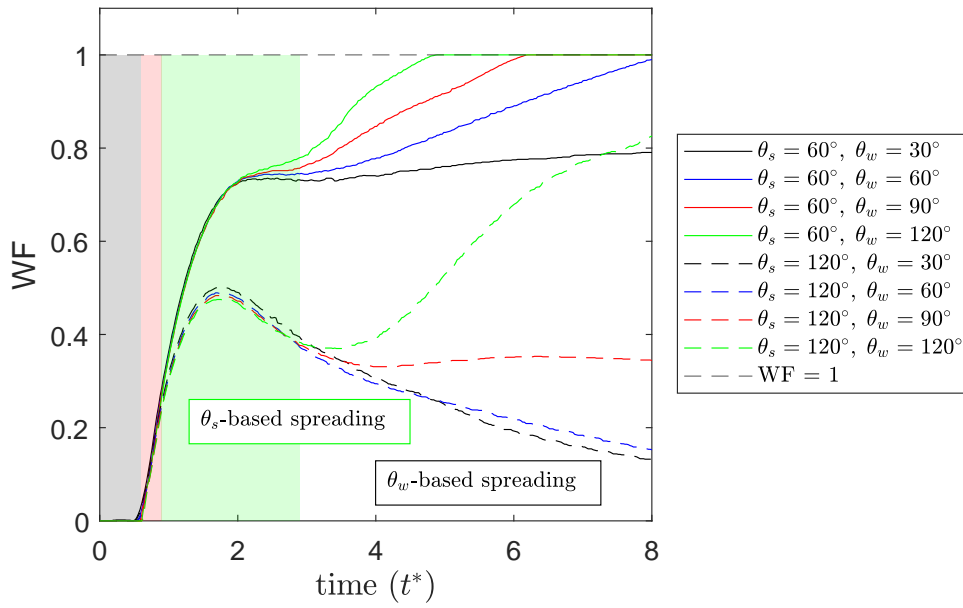
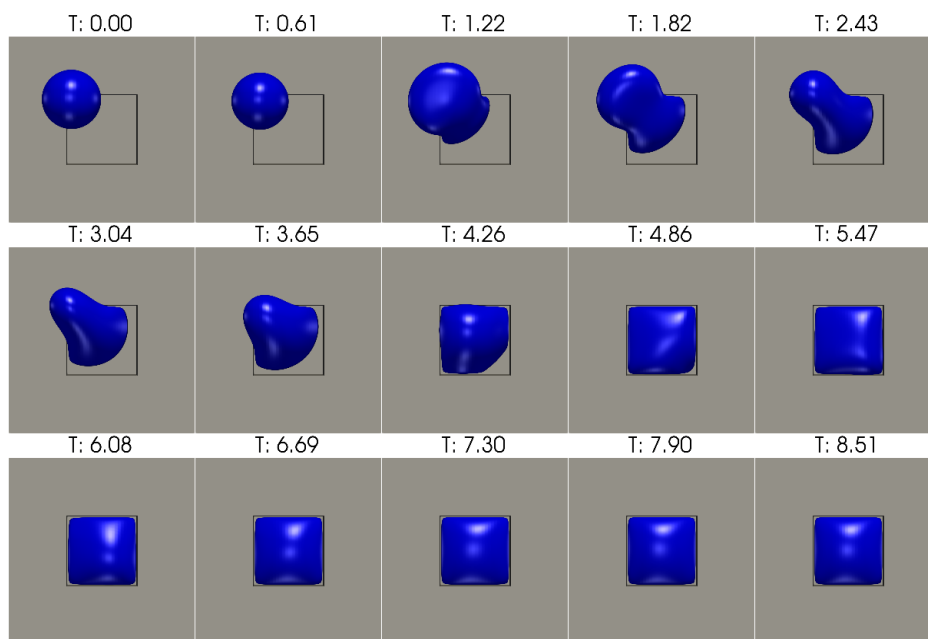
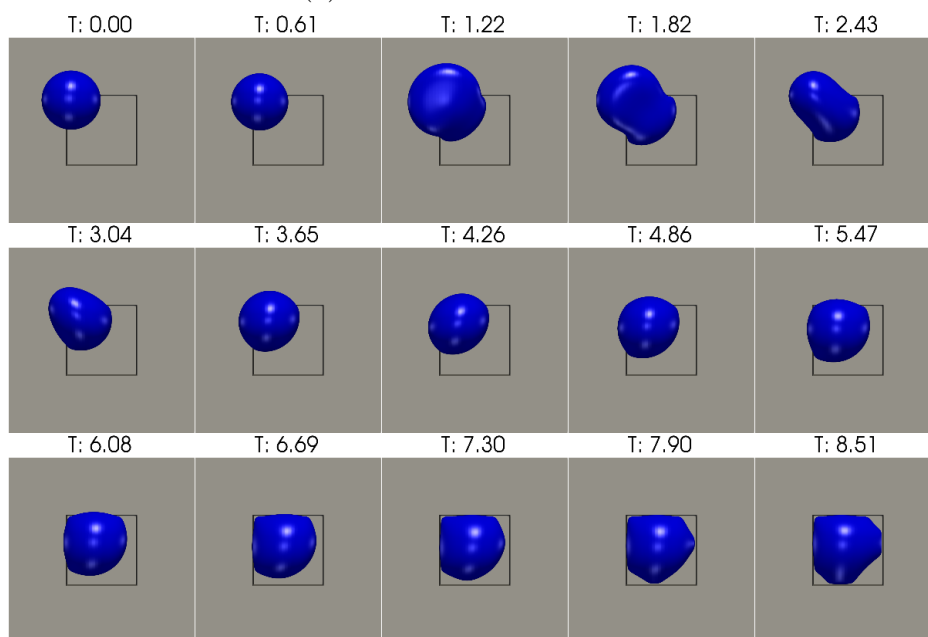


Figure 6.19: Evolution of wetted fraction for droplet deposition with dual-axis misalignment  $\alpha_\beta = \alpha_{\bar{\beta}} = 0.355216$  ( $\text{VF} = 0.5$ ). The grey shaded region illustrates the droplet free-fall regime, the pink shaded region illustrates the inertial spreading regime, the green shaded region is where the spreading is determined by the substrate contact angle ( $\theta_s$ ) and finally, the remaining white space illustrates the region in which the spreading is determined by the cavity wall contact angle ( $\theta_w$ ).



(a)  $\theta_s = 60^\circ$  and  $\theta_w = 120^\circ$



(b)  $\theta_s = 120^\circ$  and  $\theta_w = 120^\circ$

Figure 6.20: Illustrations of droplets spreading in cavities with different substrate and wall contact angles with dual-axis misalignment ( $\alpha_\beta = \alpha_{\bar{\beta}} = 0.355216$ ).

#### 6.4.4 Additional Dual-Axis Positional Inaccuracy Configuration

An additional case of dual-axis misalignment is explored where  $\alpha_\beta \neq \alpha_{\bar{\beta}}$ . Again, ensuring the VF remains comparable to the prior investigations, the overlap values are set as  $\alpha_\beta = 0.49015$ ,  $\alpha_{\bar{\beta}} = 0.1$  giving  $\text{VF} = 0.5$ . The identification of droplet morphology types are comparable to figures 6.9 and 6.17 and out of the 400 configurations tested, 123 resulted in ideal wetting of the cavity (30.75%) which is between the values of the single axis positioning error case ( $\alpha_\beta = 0.5$  and  $\alpha_{\bar{\beta}} = 0$ ) and dual-axis case ( $\alpha_\beta = \alpha_{\bar{\beta}} = 0.355216$ ). Furthermore, the results for wetting time and dynamic evolution of the wetted fraction remain comparable to the single and dual-axis cases (figures 6.10, 6.11, 6.18, 6.19), thus have been omitted.

## 6.5 Maximum Permissible Positioning Error

The investigations of the previous sections highlighted suitable wetting characteristics of the cavity. For the substrate contact angle, it is evident and intuitive that low contact angles  $\theta_s \leq 30^\circ$  are preferable. Through investigating the time taken to fully wet the cavity for single- and dual-axis misalignment, the ideal cavity wall contact angle range was found to be between  $75^\circ \leq \theta_w \leq 150^\circ$ .

There is however an important consideration when determining the maximum possible positional error, the fact that for display pixels there are multiple cavities in close proximity to each other, as illustrated in figure 6.21. Here  $W$  is the spacing between each cavity.

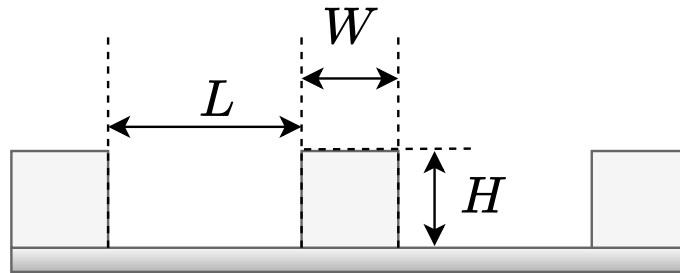


Figure 6.21: Illustration of cavity spacing for display configuration.

Considering the cavity geometry alone, the maximum positional error before the droplet is positioned closer to a neighbouring cavity is simply

$$P = \frac{1}{2}(L + W). \quad (6.10)$$

It is straightforward to see if this positional limit is attainable for a printer with known print head positioning error,  $E_{PH}$  and angular deflection  $E_\theta = H_{PH} \cdot \tan(\theta^D)$  by ensuring

$$E_\theta + E_{\text{PH}} < \frac{1}{2}(L + W), \quad (6.11)$$

However, meeting this condition alone does not ensure the droplet will wet the cavity ideally i.e. the full droplet confined within the cavity and a wetted fraction of one.

As highlighted earlier in the chapter, the wetting properties have a strong influence on the ability of the droplet to self-align. Furthermore, the droplet size relative to the cavity will significantly affect printability. Therefore, to determine the maximum permissible positioning error, the parameter  $\alpha_{\text{MAX}}$  is introduced, which described the maximum permissible overlap while still achieving a successful print. This value depends on the wetting and topography of the cavity, as will be described in §6.5.3. The benefit of using  $\alpha_{\text{MAX}}$  is that the maximum permissible positioning error,  $P_{\text{MAX}}$  can be given in terms of droplet and cavity size as

$$P_{\text{MAX}} = \frac{D}{2}(2\alpha_{\text{MAX}} - 1) + \frac{L}{2}. \quad (6.12)$$

This makes the determination of minimum cavity size possible for known positioning errors, as if  $P < P_{\text{MAX}}$  a successful deposit will be achieved.

### 6.5.1 Influence of Dual-axis Misalignment on Deposition

The effects of cavity height,  $H$ , and spacing,  $W$ , are explored for both single- and dual-axis overlap. The wetting properties of the cavity are set based on the results from the previous investigations to  $\theta_s = 30^\circ$  and  $\theta_w = 112.5^\circ$ . The width and height are changed independently for values between  $2 \leq W, H \leq 20$  for a total of 100 simulations. For each configuration, the outcome either

results in print success, with ideal wetting or print failure for any other wetting type. Curves are fitted to the boundaries of the parameter space for print success and failure and are plotted in figure 6.22. For equal volume fractions, the dual-axis overlap configuration was able to achieve a successful print across a larger range in the parameter space.

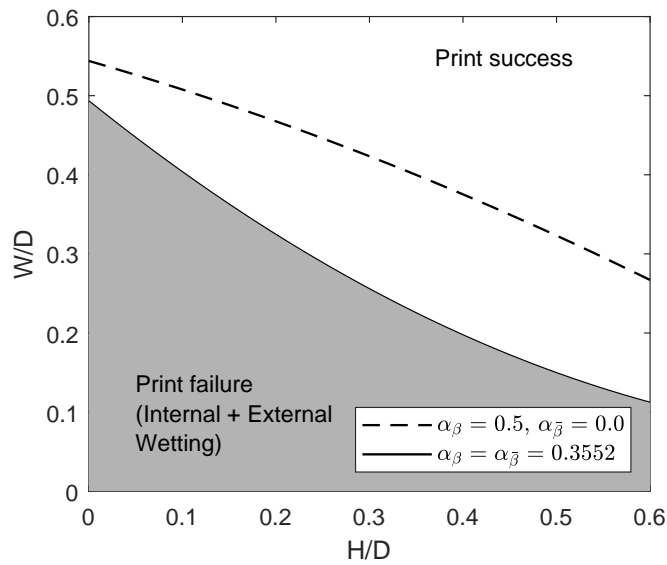
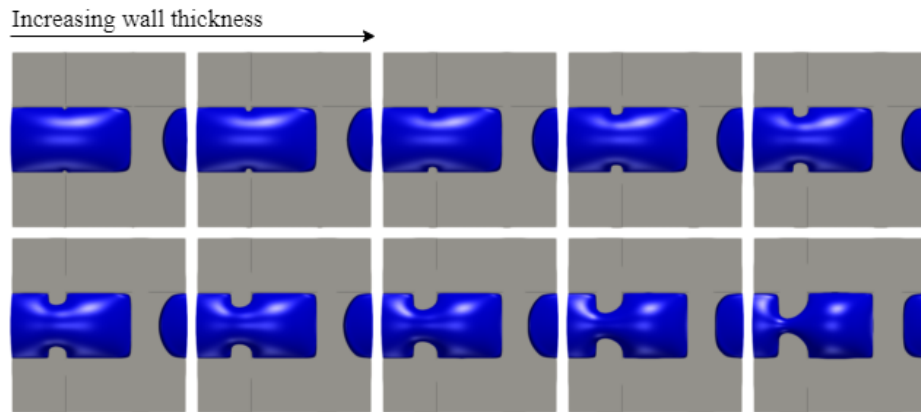


Figure 6.22: Investigation of print success for varying cavity height  $H/D$ , width  $W/D$  for single- and dual-axis misalignment. Dashed line shows results for single-axis misalignment,  $\alpha_\beta = 0.5$ ,  $\alpha_{\bar{\beta}} = 0$  ( $VF = 0.5$ ) and solid line shows results for dual-axis misalignment,  $\alpha_\beta = \alpha_{\bar{\beta}} = 0.3552$  ( $VF = 0.5$ )

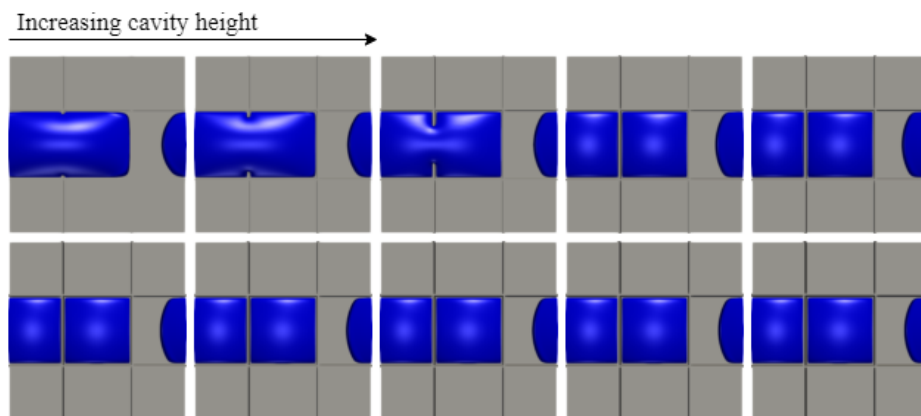
For a single-axis value of overlap, the resulting droplet morphologies for cavities in which the height or width is equal to 2 ( $H/D$  or  $W/D = 1/17$ ) is displayed in figure 6.23. The effects of the wall thickness are shown in figure 6.23a, where the droplet spreads over the wall, wetting the two neighbouring cavities and connects the two by a liquid *bridge*. The width of the bridge connecting the two neighbouring cavities decreases with increasing width.

The effects of increasing cavity height are shown in figure 6.23b. Here, the connecting liquid bridge is only observed for the first few cases, up to a height of  $H/D = 3/17$ , after which the droplet is split between the neighbouring cavities.

The resulting droplet morphologies for dual-axis overlap, in which the height or width is equal to 2 ( $H/D$  or  $W/D = 1/17$ ) is displayed in figure 6.24. The effects of increasing the wall thickness are shown in figure 6.24a. For widths of  $W/D = 3/17$  and lower, the droplet spreads over the cavity walls and wets three neighbouring cavities, and each of the cavities is connected by a liquid bridge. Above this width, the droplet wets just two of the neighbouring cavities. Increasing the width further, to  $W/D = 9/17$ , a successful print is obtained. The effects of increasing the cavity height are illustrated in figure 6.24b. As with the width study, it is found that heights of  $H/D = 3/17$  and lower, that the droplet spreads over the cavity walls and wets three neighbouring cavities. For heights above this, the droplet spreads into two of the neighbouring cavities.

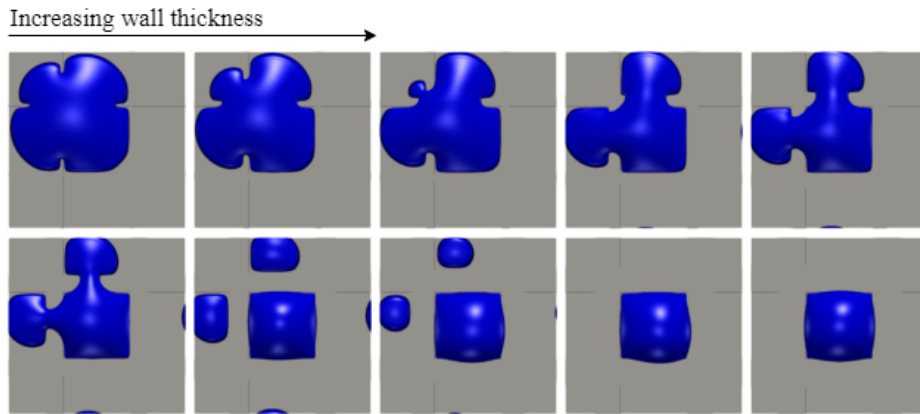


(a)  $0.059 \leq \frac{W}{D} \leq 0.588$ ,  $\frac{H}{D} = 0.059$

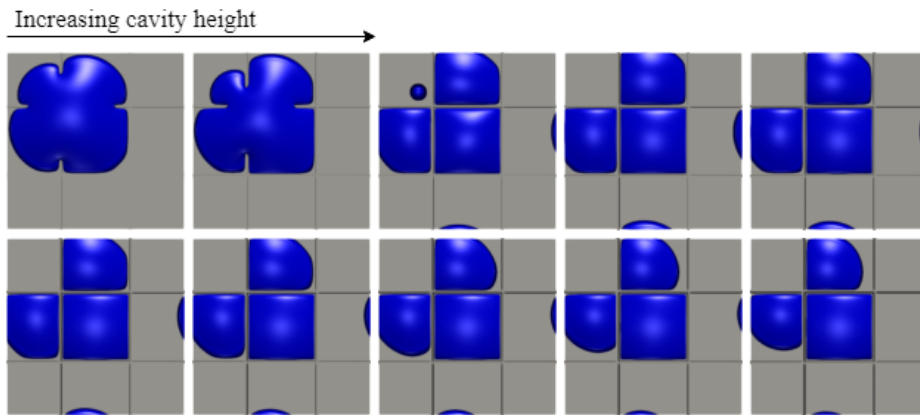


(b)  $0.059 \leq \frac{H}{D} \leq 0.588$ ,  $\frac{W}{D} = 0.059$

Figure 6.23: Final state morphologies for droplet impact cavity with a single-axis overlap. Variations in (a) different wall thicknesses, and (b) different cavity heights.



(a)  $0.059 \leq \frac{W}{D} \leq 0.588$ ,  $\frac{H}{D} = 0.059$



(b)  $0.059 \leq \frac{H}{D} \leq 0.588$ ,  $\frac{W}{D} = 0.059$

Figure 6.24: Final state morphologies for droplet impact cavity with a dual-axis overlap. Variations in (a) different wall thicknesses, and (b) different cavity heights.

## 6.5.2 Influence of Droplet Properties on Deposition

To investigate how droplet properties affect the droplet ability to self-align for different cavity heights and widths, the Weber number,  $We$ , is varied within the printable parameter range described in §1.2. The maximum permissible  $We$ , ensuring  $Z \geq 4$ , with a Reynolds number of  $Re = 30$  is  $We = 56.25$ . The minimum value, ensuring  $Z \leq 14$ , is  $We = 4.59$ . The droplet is deposited with single-axis misalignment, with an overlap value  $\alpha_\beta = 0.5$ . The height and width are varied individually over 100 simulations for each of the  $We$  numbers. The results are displayed in figure 6.25. The curves displayed are fitted from the discrete parameter space explored with the simulations. As the  $We$  number is reduced, the parameter space in which a successful print is achieved increases.

Snapshots of the evolution of the droplet for the different  $We$  numbers tested are shown in figure 6.26. Here the cavity height and width are  $H/D = W/D = 7/17$ . For the  $We$  number of  $We = 56.25$ , figure 6.26a, the droplet impacts the cavity wall with enough inertia to split into two, wetting the neighbouring cavity as well as the primary. For the smaller  $We$  number of  $We = 4.59$ , figure 6.26b, the droplet impacts the cavity wall but does not split, resulting in a successful print.

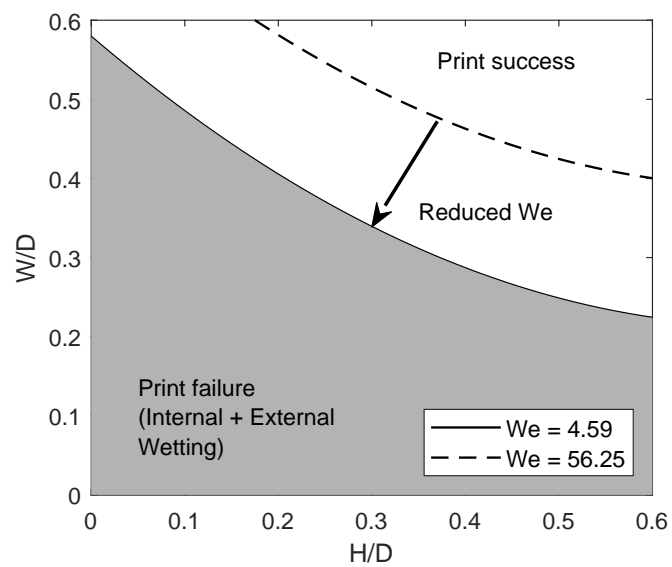
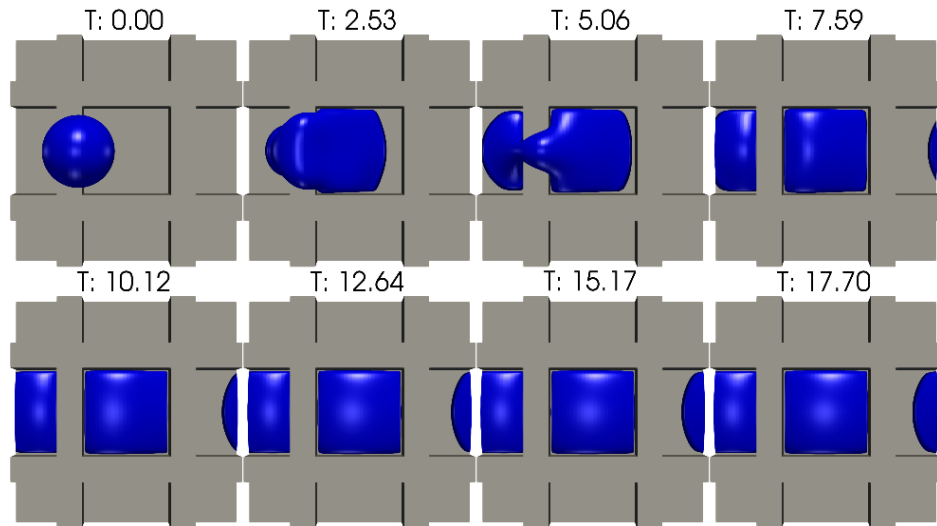
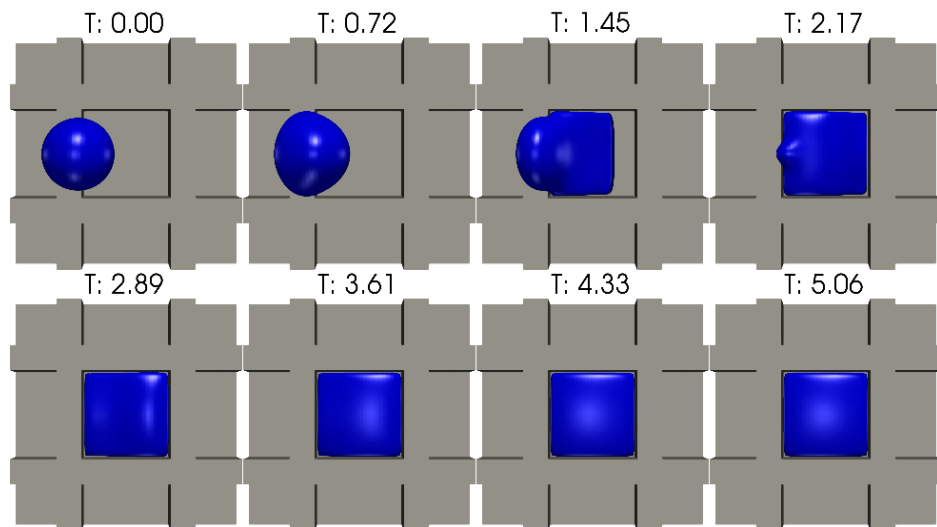


Figure 6.25: Investigation of print success for varying cavity height  $H/D$ , width  $W/D$  and We number. Dashed line illustrates results for  $Re = 30$  and  $We = 56.25$  ( $Z = 4$ ) and solid line illustrates results for  $Re = 30$  and  $We = 4.59$  ( $Z = 14$ ).



(a) Weber Number  $We = 56.25$ .



(b) Weber Number  $We = 4.59$ .

Figure 6.26: Snapshots of the droplet evolution with high and low  $We$  numbers. Cavity height ( $H/D$ ) and width ( $W/D$ ) are 0.41.

### 6.5.3 Determination of Maximum Permissible Overlap

As identical cavities are situated next to each other, separated by distance  $W$ , if the droplet position error is larger than  $P = 0.5(L + W)$  the droplet will no longer be directed towards the intended cavity. This positioning error is therefore the maximum permissible value when considering the geometry. However, as shown in the previous sections, the ability for the droplet to self-align to achieve a successful print is affected by the wetting properties of the cavity, droplet properties such as  $We$  number, type of overlap i.e. single- or dual-axis and the cavity height. These properties determine the maximum permissible overlap  $\alpha_{\text{MAX}}$ .

The ideal cavity wetting properties,  $We$  number, and type of overlap have been determined from the previous investigations. For simplicity, the maximum overlap is investigated in terms of single-axis positional error. To determine the maximum overlap, simulations are run with incremental increases of overlap until print failure. To achieve an accurate value of  $\alpha_{\text{MAX}}$ , simulations are first performed with a large increment size to obtain a rough approximation of the boundaries between print success and failure. Then the simulations are run again between these boundaries, with finer incremental sizes to obtain a reasonable prediction of the maximum overlap, resulting in a total of 224 simulations. Four different cavity heights are investigated and the results are shown in figure 6.27. The grey shaded region corresponds to the limit in overlap ( $\alpha_{\text{LIMIT}}$ ) before the droplet is no longer positioned closest to the intended cavity,  $\alpha_{\text{LIMIT}} = 0.5W/D + 0.5$ . As can be seen for the lowest height tested,  $H/D = 0.059$  at  $W/D = 0.059$  (point (a) in figure 6.27), the maximum achievable overlap is  $\alpha_{\text{MAX}} = 0$ , this is due to the large droplet volume compared to the cavity, which results in overfilling, illustrated in figure 6.28a. Increasing the cavity height typically allowed for a larger value

of overlap to be reached, however, for  $H/D = 0.59$  and  $W/D = 0.59$  (point (b) in figure 6.27), the droplet impacted the wall, became pinned on the wall corners and failed to wet the cavity, thus the maximum attainable overlap was reduced, illustrated in figure 6.28b.

With the normalised cavity height as  $H/D = 0.41$  and the width  $W/D = 0.588$ , the maximum achievable overlap was found to be  $\alpha_{\text{MAX}} = 0.762$ , which gives a volume fraction of  $\text{VF} = 0.857$ . The corresponding dual-axis overlap case is  $\alpha_{\beta} = \alpha_{\bar{\beta}} = 0.5798$ , which was found to give print success also.

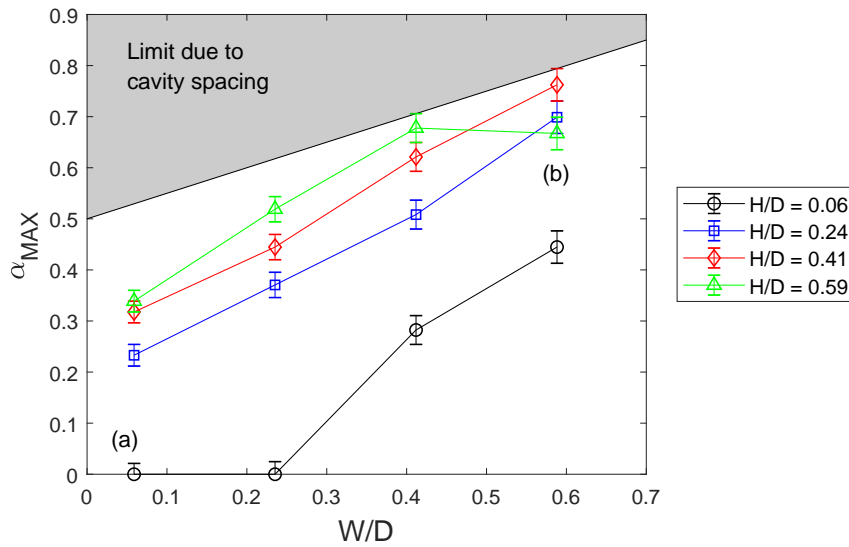


Figure 6.27: Determination of maximum achievable overlap for different cavity wall widths and heights. Error bars indicate incremental step size in overlap parameter.

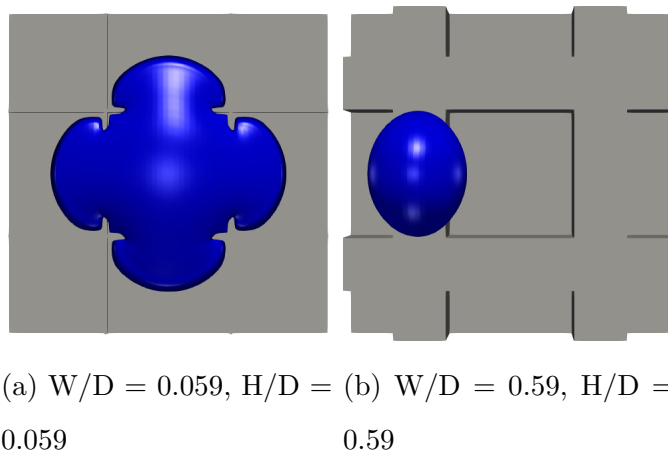


Figure 6.28: Illustration of final state morphologies for points (a) and (b) highlighted in figure 6.27.

### 6.5.4 Printable Parameter Map

Using the computed maximum overlap value,  $\alpha_{\text{MAX}}$ , a printing parameter map is constructed, in terms of positioning error,  $P/L$  and droplet size  $D/L$ , which can be used to determine if a print will be successful for given positioning errors and cavity sizes, figure 6.29. First, an approximation for the minimum droplet size required to fill the cavity with a given substrate contact angle,  $\theta_s$ , can be made by first considering the spreading ratio, which is rewritten for clarity as

$$r(\theta_s) = \left( \frac{8}{\tan(\frac{\theta_s}{2})(3 + \tan^2(\frac{\theta_s}{2}))} \right)^{1/3}. \quad (6.13)$$

Then by setting the cavity substrate area equal to the area wetted by a droplet and rearranging, an approximate expression for the minimum drop size can be given as

$$\frac{2}{\sqrt{\pi}r(\theta_s)} = \frac{D}{L}. \quad (6.14)$$

Which for a substrate contact angle of  $\theta_s = 30^\circ$ , gives the minimum ratio of  $D/L = 0.5287$ . Additionally, equating the cavity volume and droplet volume and rearranging, an expression is given for the maximum droplet size for a cavity as

$$\frac{2}{L} \left( \frac{3L^2H}{4\pi} \right)^{1/3} = \frac{D}{L}. \quad (6.15)$$

Which for  $L = 45$  and  $H = 14$  gives the maximum ratio of  $D/L = 0.8407$ .

Finally, to validate the printing parameter map, 200 simulations were performed with varying drop size and positioning errors, figure 6.30. Within the limits of a single drop filling a cavity, the simulations results which resulted in print success are well predicted by the map. Above  $D/L = 0.8407$ , the

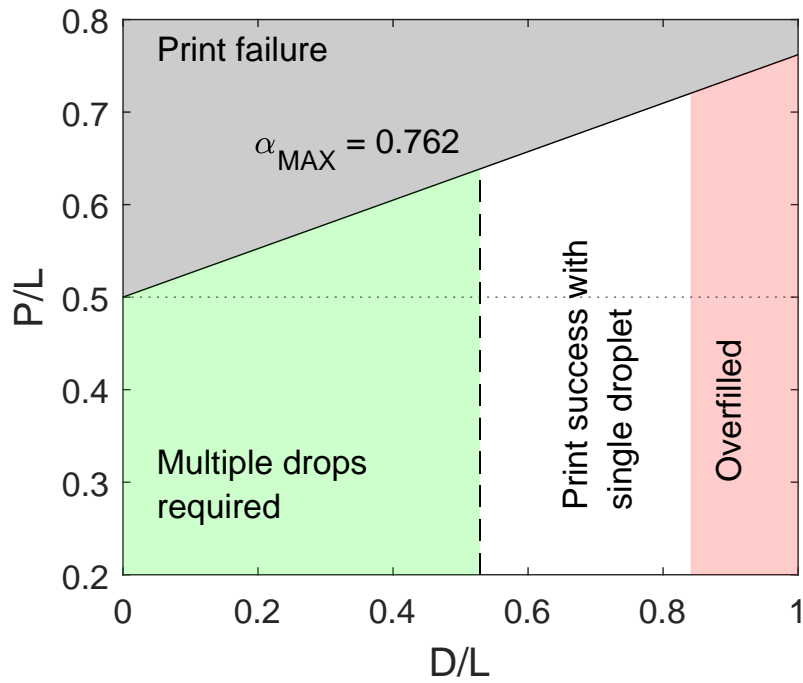


Figure 6.29: Printable parameter map based on determined maximum overlap value,  $\alpha_{MAX}$ .

red dashed line, the maximum allowable overlap begins to reduce, as external wetting sets in.

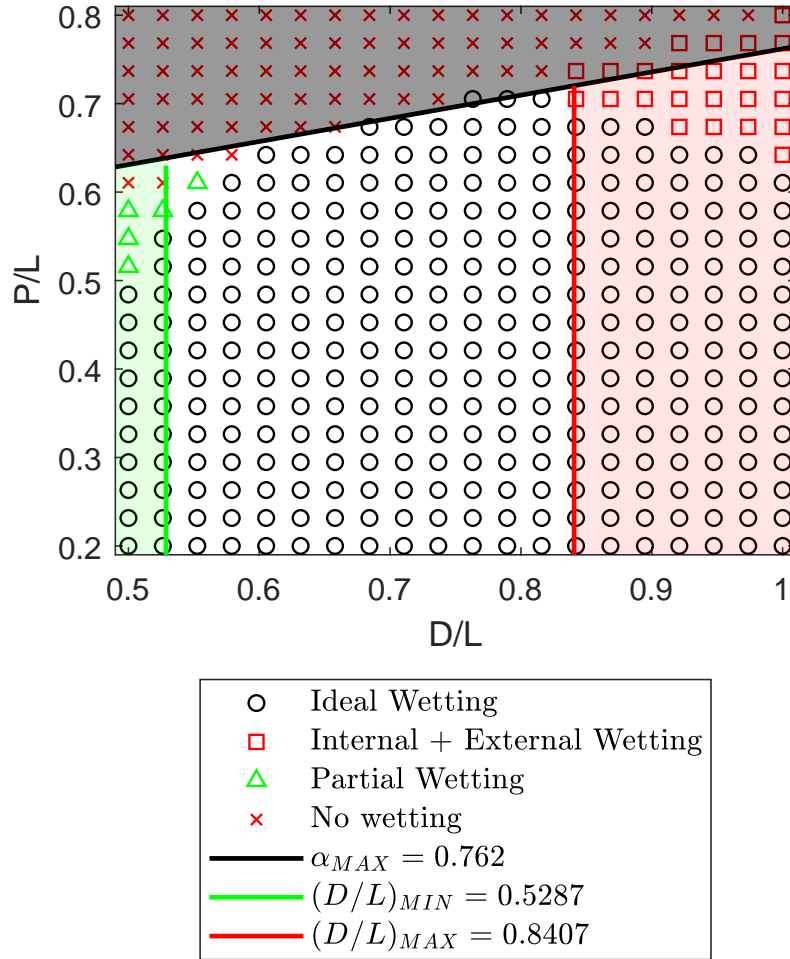


Figure 6.30: Validation of printable parameter map. Green region shows where multiple droplets are required, pink region shows where overfilling occurs and grey region shows where overlap exceeds  $\alpha_{LIMIT}$ .

## 6.6 Chapter Summary

In this chapter, the previously validated multiphase model is used with the newly developed wetting model to explore droplet deposition into cavities with positional inaccuracies. A parametric investigation of droplet self-alignment for different substrate and cavity wall contact angles is conducted for both single- and dual-axis positional inaccuracies. Using the MPI parallelised version of the code (described in §4), simulation run-time was reduced by over 98%, with simulations taking on average 41.49 seconds to complete, running on 121 processes on HPC cluster ARC4 (University of Leeds). The quick computation speeds allowed for well resolved (400 simulations each) parameter studies.

Using the ideal wetting conditions found from the parametric investigation, it was found that dual-axis positioning error results in a greater print success rate compared to single-axis positioning error. Furthermore, it is found that reducing the Weber number also aids in attaining successful prints, as it limits the spreading over the cavity walls. The limits of achievable positioning error for cavities placed in close proximity are investigated and used to determine the maximum achievable droplet overlap. This overlap value is used to construct a printing map that illustrates parameters that lead to successful deposition into a cavity. Simulation results of different droplet sizes and positioning inaccuracy agree well with the constructed printing map.

## CHAPTER 7

---

### Evaporation on Textured Surfaces

---

#### 7.1 Introduction

In the previous chapter, the parameters affecting droplet self-alignment under positioning errors were explored and optimised to increase the likelihood of print success. In this chapter, the evaporation dynamics of a droplet in a heated cavity is explored. The previously validated pseudopotential model is coupled with a finite-difference solver for an energy equation, which is then validated and used to explore the influence of the cavity wall and substrate contact angle on evaporation rate, internal flows and particle deposition.

## 7.2 Background

To enable inkjet deposition to become a commercially viable method of fabricating organic light emitting diodes (OLEDs), a uniform deposit of the functional material needs to be deposited in a precise and repeatable manner. To control the positioning of the inkjet printed droplet(s), chemically and topographically patterned surfaces are used, which are in the form of a substrate with a low contact angle and surrounding walls of a higher contact angle (a cavity). However, in comparison to flat surfaces, in which there has been much research on the evaporation and deposit morphologies (see §1), the understanding of evaporation in cavities is limited.

The evaporation dynamics of single and binary solvents has been explored experimentally in [215]. Evaporation was found to be enhanced in the corners of square cavities, which in turn resulted in more deposition in these areas. Other investigations have focused on the final deposit morphology alone, and not the dynamics [7]. Ely *et al.* [216] investigated some of the factors influencing the final deposit morphology, including the contact angle of the cavity wall, surface roughness and particle concentration. Sáenz *et al.* [217] have studied the deposits of geometrically controlled droplets [217], where preferential deposition is seen in sharp corners due to enhanced evaporation rate.

Numerical investigations on droplets evaporating in cavities are limited, however, Son [218] investigated the influence of cavity sidewalls on the deposition and evaporation of droplets using a level-set method. In their study of evaporation, however, the droplet did not make contact with the cavity walls, although they noted that the evaporation rate was reduced compared to the case of a free sessile droplet.

Recently, multiphase (pseudopotential) lattice Boltzmann models have been

coupled with energy equations to explore evaporation dynamics. The evaporation of free droplets with forced convection in two- and three-dimensions have successfully modelled Marangoni effects [219, 165]. Furthermore, evaporation on chemically patterned flat surfaces have been explored both in two- and three-dimensions [157, 158]. With these models, the lattice Boltzmann model is coupled to a finite-difference scheme, solving an energy equation that is coupled through the equation of state. These models have captured stick-slip mode of evaporation as well as spherical cap deviation and internal flows due to temperature induced Marangoni stresses. Evaporation on non-flat surfaces have also been explored in two dimensions for textured and rough surfaces [159, 160, 166]. Where the models have successfully captured changes in evaporation rate due to changes in the surface topography.

This chapter aims at further developing the understanding of the dynamics of evaporation from within a heated cavity, to elucidate the mechanism affecting deposit morphology.

### 7.3 Thermal Model Validation

The pseudopotential model from the previous chapters is extended to model thermal flows by adding a finite-difference based solver for an additional energy equation, which is rewritten for clarity as

$$\frac{\partial T}{\partial t} = -\mathbf{u} \cdot \nabla T + \frac{1}{\rho C_v} \left( \lambda \nabla^2 T + \nabla \lambda \cdot \nabla T \right) - \frac{T}{\rho C_v} \left( \frac{\partial p_{EOS}}{\partial T} \right) \nabla \cdot \mathbf{u}, \quad (7.1)$$

where  $C_v$  is the specific heat and  $\lambda$  is the thermal conductivity. As described in §3.4, a fourth order Runge-Kutta method is adopted to solve the equation numerically. The last term on the right-hand side is a source term due to phase change. However, due to the spurious velocities of the pseudopotential

method, the divergence at the liquid-vapour interface is non-zero, therefore, a free droplet will heat up gradually as the simulation evolves. These effects are mitigated by ensuring spurious velocities are small, thus an increased temperature is used. For the following simulations, the temperature is increased to  $T = 0.86T_c$ , corresponding to a density ratio  $\rho_R \approx 17$ , as this is typically used without issue [157, 158, 160, 161].

The source term on the right-hand side responsible for phase change is derived from a local balance law of entropy in [220], here the authors also show how to derive the specific latent heat for the Peng-Robinson equation of state by first computing the enthalpy as

$$h = \left[ aT \cdot \eta(\omega) \cdot \sqrt{\alpha(T)} \cdot \frac{1}{\sqrt{T \cdot T_c}} + a\alpha(T) \right] \cdot \frac{1}{2\sqrt{2}b} \times \ln \left| \frac{2b^2\rho - 2b - 2\sqrt{2}b}{2b^2\rho - 2b + 2\sqrt{2}b} \right|, \quad (7.2)$$

where  $\eta(\omega) = (0.37464 + 1.5422\omega - 0.26992\omega^2)$  and  $\alpha(T) = [1 + (0.37464 + 1.54226\omega - 0.26992\omega^2)(1 - \sqrt{T/T_c})]^2$ . The enthalpy for the liquid,  $h_l$  and vapour,  $h_v$  are obtained by inserting  $\rho_l$  and  $\rho_v$  into equation 7.2 respectively, then the latent heat,  $h_{fg}$ , is obtained as

$$h_{fg} = h_v - h_l. \quad (7.3)$$

Equation 7.1 is derived under the assumption of negligible viscous dissipation. The validity of this assumption can be checked by evaluating the Brinkman number (Br), which describes the ratio of viscous heat generation to external heating, and is defined as

$$\text{Br} = \frac{\mu u^2}{\lambda(T_{wall} - T_{sat})}, \quad (7.4)$$

which for the resulting velocities in the following investigations result in a small number,  $\text{Br} \ll 1$ .

### 7.3.1 Dirichlet Boundary Conditions

A simple validation case for the multiphase thermal model is the well-known  $D^2$  law for droplet vaporisation [221, 160]. Here, the diameter squared of the droplet is shown to decrease at a constant rate as it evaporates ( $D^2(t)/D_0^2 = 1 - kt$ ), where  $D_0$  is the initial droplet diameter and  $k$  is the evaporation rate. A droplet of diameter,  $D_0 = 50$ , is initialised at the centre of a fully periodic domain, comprising of  $151^3$  lattice nodes. The droplet temperature is set to  $T_{sat} = 0.86T_c$  and the boundaries of the domain are fixed to a higher temperature of  $T_{vap} = T_{sat} + \Delta T$ , where  $\Delta T$  is the superheat, set to  $0.14T_c$ . The kinematic viscosity set to  $\nu = 0.1$  ( $\tau_\nu = 0.8$ ). The requirements of the  $D^2$  law are no buoyancy, negligible viscous heat dissipation and constant thermophysical properties. As such, the specific heat is set to  $C_v = 5$  and the thermal conductivity is set to either  $\lambda = 1/3$  or  $\lambda = 2/3$ . Having a constant thermal diffusivity simplifies equation 7.1, as the term  $\nabla\lambda \cdot \nabla T$  vanishes. For the first 5000 time-steps, the temperature solver is switched off to allow the droplet to relax to an equilibrium state, after which the temperature solver is included and the droplet begins to evaporate due to the temperature difference. The results for the two different thermal conductivities are displayed in figure 7.1. As can be seen, both cases show a constant rate of reduction for the droplet diameter squared, with  $k = 6.98 \times 10^{-6}$  and  $k = 1.38 \times 10^{-5}$  for  $\lambda = 1/3$  and  $\lambda = 2/3$  respectively.

#### Solid Boundaries

For the implementation of the *no-slip* boundary, the standard bounce-back method is used, as this allows for straightforward implementation and accurate boundaries for walls aligned with lattice nodes. To control the wetting, the geometric boundary condition, described in §5.3, is used as this model

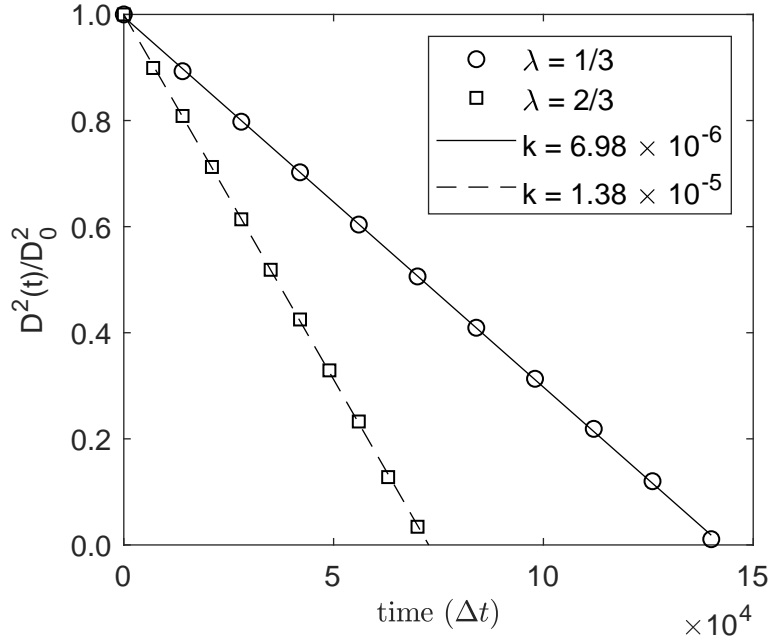


Figure 7.1: Validation of  $D^2$  law for droplet vaporisation with hybrid pseudopotential model. Thermal conductivities of  $\lambda = \frac{1}{3}$  and  $\lambda = \frac{2}{3}$  for circle and square symbols respectively.

allows for directly specifying contact angles irrespective of the temperature, generates low spurious velocities and has the ability to control contact angle hysteresis.

To validate the thermal multiphase model in the presence of solid boundaries, heat conduction between two fixed temperature walls is simulated. A quasi-one-dimension domain, comprising  $3 \times 100 \times 3$  lattice nodes in the  $x$ ,  $y$  and  $z$  direction respectively is configured, with periodic boundaries at all faces apart from the top and bottom, which are solid. The temperature at the bottom layer of solid nodes is heated to  $T = T_{sat} + \Delta T$  and the solid nodes at the top of the domain are fixed to  $T = T_{sat}$ . Here, the thermal

conductivity is non-constant and is computed as  $\lambda = C_v \rho \chi$ , where  $\chi$  is the thermal diffusivity. Liquid fills the bottom portion of the domain, and has thermal conductivity,  $\lambda_l$ , whereas vapour fills the rest of the domain and has thermal conductivity,  $\lambda_v$  (illustrated in figure 7.2a). In order to compare the simulation results of the temperature distribution to an analytical solution, the temperature used in computing pseudopotential is fixed at the saturation temperature ( $\psi(T_{sat})$ ), resulting in uniform density in the liquid and vapour phases. Different ratios of liquid and vapour are explored, with results showing good agreement with analytical solutions, figure 7.2b.

For the scenarios where the pseudopotential varies with temperature and solid nodes are assigned a fixed temperature value, special consideration is required for the geometric boundary condition. The pseudopotential is a function of density and temperature ( $\psi(\rho, T)$ ), for which the density is assigned through the geometric condition. However, assigning the fixed wall temperature to the value of the pseudopotential results in the incorrect temperature profile. Using the temperature of the nearest neighbouring fluid node results in the correct temperature profile

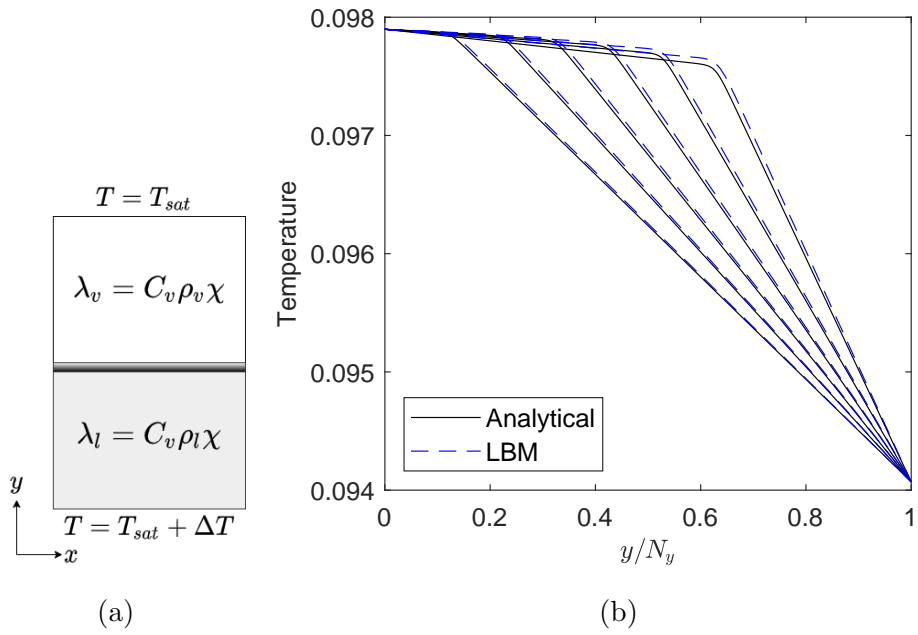


Figure 7.2: Validation of temperature distribution in a multiphase system in which different fluid-vapour levels are explored. (a) shows the model schematic and (b) shows the simulation results compared with the analytical solution. Black lines show analytical solution and blue lines show LBM results (both in lattice units).

### 7.3.2 Outflow Boundary Condition

In addition to accurately modelling temperature boundary conditions, the pressure boundary condition also needs to be correctly implemented to simulate evaporation [222]. To enforce pressure boundary conditions in the following simulations, the Zou-He boundary condition, as described in §4.3 is used. When assigning a pressure boundary to a 3D simulation, the  $y$ -component of velocity will be determined by the Zou-He method, and the  $x$ - and  $z$ -components of velocity are set to 0. However, this was found to generate flow into the domain (before the temperature solver is switched on), even if the boundary pressure/density is set to enforce  $\partial_y \rho = 0$ . To avoid this, the total mass is computed at the beginning of the simulation,  $M_0$ , then at subsequent time-steps, the mass is computed everywhere apart from on Zou-He boundary nodes ( $\bar{M}_t$ ). The difference is then divided by the number of Zou-He boundary nodes to give the density value ensuring conserved mass. The evolution of the system mass is shown in figure 7.3, where it can be seen that the modified boundary conserves the system mass.

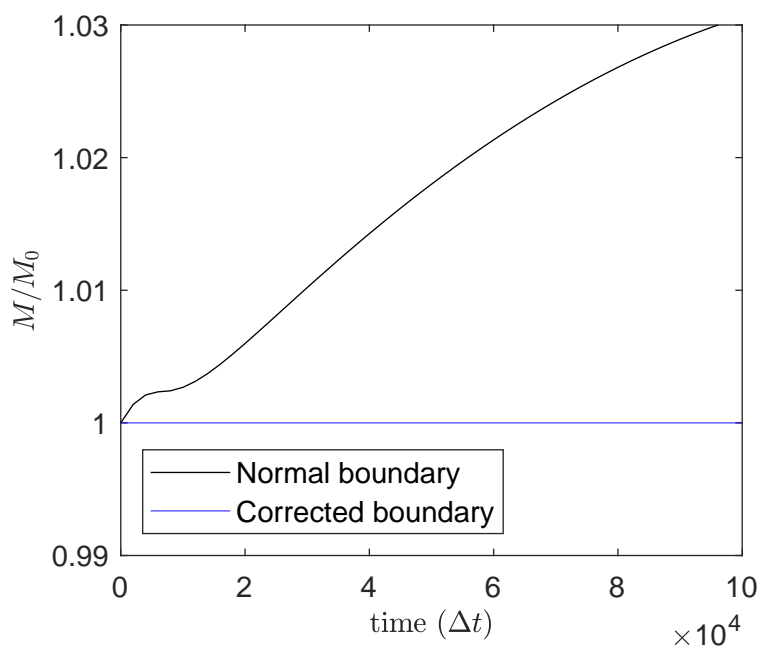


Figure 7.3: Open boundary condition effects on system mass. The black line is the original Zou-He boundary and the blue line is the mass conserving version.

## 7.4 Sessile Droplet Evaporation

As with previous investigations in this thesis, the Peng-Robinson equation of state is used. However, in order to reduce the spurious velocities at the liquid-vapour interface, the size of the diffuse interface is increased. This is achieved by reducing the parameter  $a$  in the equation of state (equation 3.55). The relationship between the attraction parameter and the interface thickness is illustrated in figure 7.4. Similarly to the findings in [141], the interface size is found to be approximately proportional to  $1/\sqrt{a}$ . For a saturation temperature of  $T_{sat} = 0.86T_c$ , reducing the attraction parameter from  $a = 3/49$  to  $a = 2/49$  resulted in an increase in interface thickness by approximately  $2.2\Delta x$ , giving the total interface thickness of approximately  $12\Delta x$ . This reduced the maximum spurious velocity from  $|\mathbf{u}_f| = 4.865 \times 10^{-3}$  to  $|\mathbf{u}_f| = 2.748 \times 10^{-3}$ .

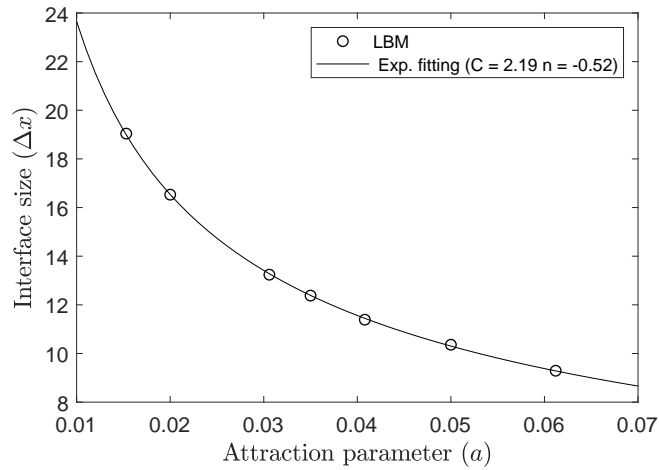


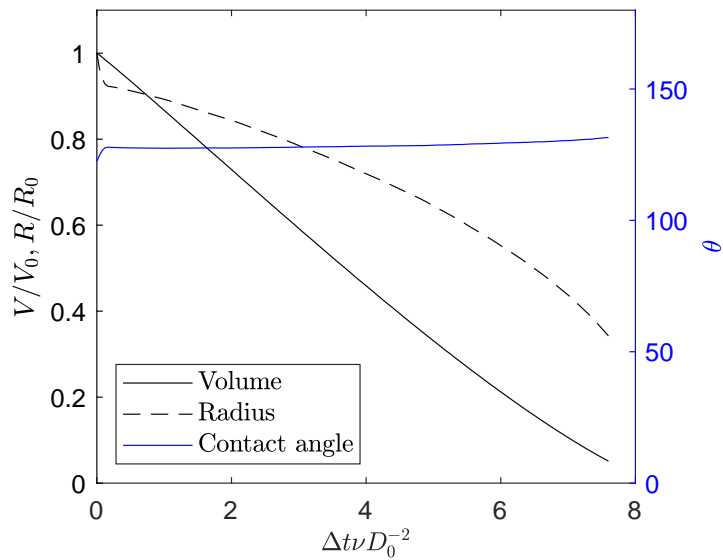
Figure 7.4: Relationship between attraction parameter in Peng-Robinson EOS and liquid-vapour interface thickness.

To further explore the thermal models capabilities, evaporation in the con-

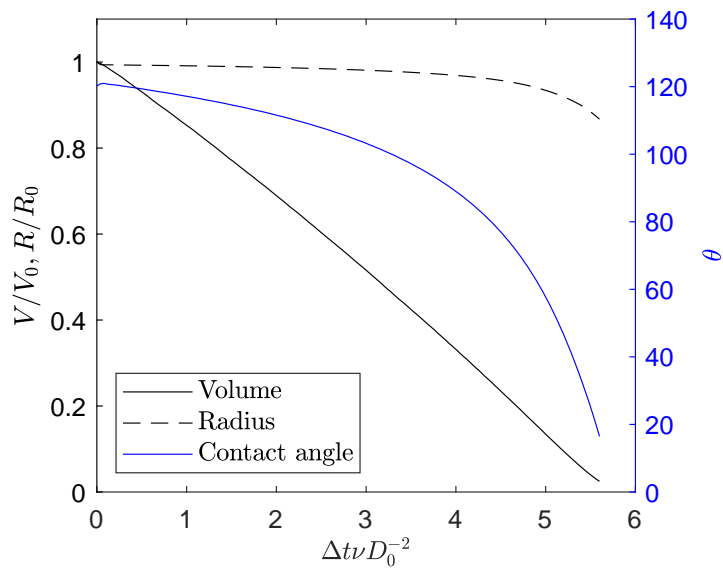
stant contact angle (CCA) and constant contact radius (CCR) modes are investigated. A domain comprising of  $101^3$  lattice nodes is constructed. The bottom surface is a no-slip solid wall, with a constant temperature of  $T_{wall} = T_{sat} + \Delta T$ , where  $\Delta T$  is the superheat which is set to  $\Delta T = 0.02T_c$ . The specific heat is set to  $C_v = 2$  and the thermal diffusivity is set to  $\chi = 0.125$ . The top nodes are set to enforce a zero pressure gradient with the Zou-He boundary and held at fixed temperature,  $T_{wall} = T_{sat}$ . A droplet of diameter  $D_0 = 50$  is initialised just above the solid surface. The kinematic viscosity is varied in the liquid and vapour phases, with the liquid kinematic viscosity of  $\nu = 0.063$  ( $\tau_\nu = 0.689$ ) and a vapour kinematic viscosity of  $\nu = 0.253$  ( $\tau_\nu = 1.26$ ). To model the CCA and CCR evaporation regimes, an advancing contact angle is chosen arbitrarily as  $\theta_A = 90^\circ$ , then the receding angle is set as either  $\theta_R = 90^\circ$  or  $\theta_R = 0^\circ$  for CCA and CCR modes respectively. After  $10,000\Delta t$ , the droplet has equilibrated and the temperature solver is switched on.

The transient evolution of the droplet volume, radius and contact angle for evaporating droplets is displayed in figure 7.5, where results are plotted against dimensionless time ( $\Delta t\nu D_0^{-2}$ ). The transient results for CCA and CCR, figures 7.5a and 7.5b respectively, show good qualitative agreement with experiments [223, 224, 225].

The two modes of evaporation are also illustrated in figure 7.6, where density contours show the droplet at different times. The plots show half the droplet, with the height and radius normalised by the radius of the initial droplet,  $R_0$ . For the CCA mode in figure 7.6a, the droplet is clearly observed to shrink in a self-similar fashion. Alternatively, for the CCR mode, figure 7.6b, the radius is observed to remain fixed in position, and the height and angle decrease as evaporation proceeds.

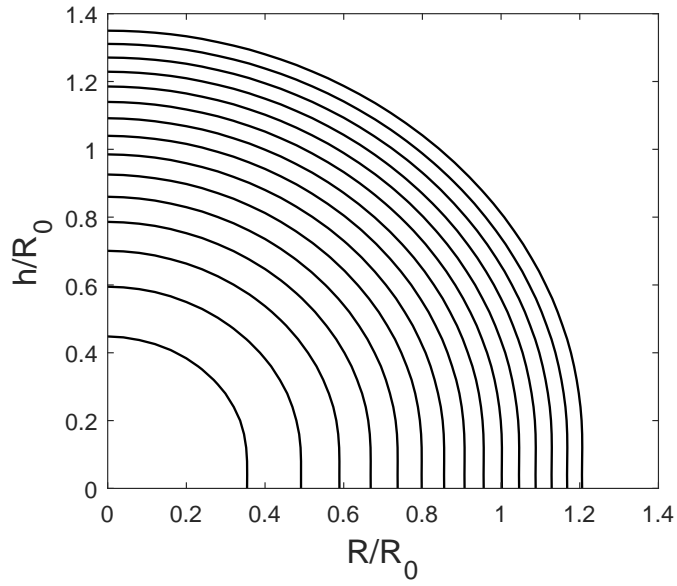


(a) CCA

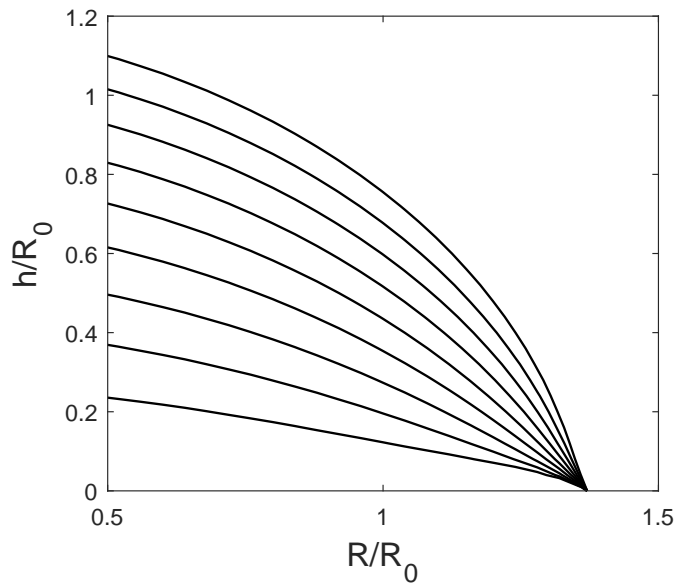


(b) CCR

Figure 7.5: Transient evolution of normalised volume, normalised radius and contact angle for droplet evaporating in CCA and CCR modes.



(a) CCA mode.



(b) CCR mode.

Figure 7.6: Density contours at different stages of the evaporation processes for droplets evaporating in either the CCA or CCR mode on a flat heated surface.

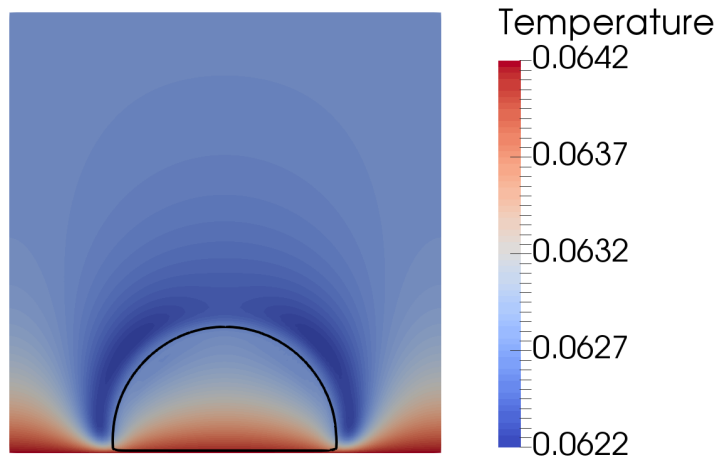
### 7.4.1 Evaporative Cooling

The last term in equation 7.1 is a source term, which is responsible for capturing the evaporative cooling effects. The effects of evaporative cooling are clearly observed during the simulation of evaporation, figure 7.7. For both the CCA and CCR modes, figures 7.7a and 7.7b respectively, the coldest regions are seen at the liquid-vapour interface. This generates a temperature gradient inside the droplet, with reducing temperature towards the apex of the drop.

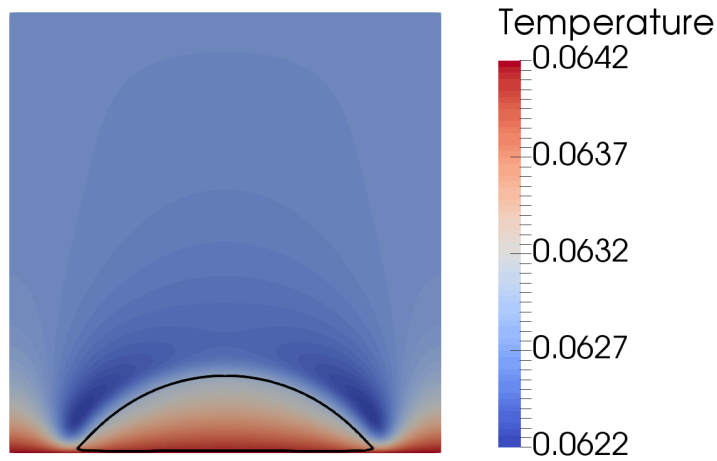
### 7.4.2 Internal Flow of Evaporating Droplets

As the temperature is non-uniform within the droplet due to the heated surface and evaporative cooling at the liquid-vapour interface, the surface tension is non-uniform, with lower values at the base of the droplet and higher values in cooler regions. The effect of non-uniform surface tension is an internal recirculating flow, referred to as Marangoni convection. This flow is captured in the simulation, as illustrated by figure 7.8, where velocity vectors show the internal flow both before the temperature solver is switched on, figure 7.8a and shortly after the temperature solver is switched on, figure 7.8b. Once the temperature solver is switched on, two counter-rotating flow patterns can be observed, which at the droplet interface flow from the bottom (low surface tension) towards the droplets peak (high surface tension). In the centre of the droplet, the flow is directed down towards the substrate.

The average velocity inside the droplet is recorded for both CCA and CCR evaporation modes, figure 7.9. Once the droplet reached equilibrium, but before the temperature solver was switched on, the average velocity inside the droplet was found to be approximately  $|\mathbf{u}|_{avg} \approx 1.79 \times 10^{-4}$ . Once the



(a) CCA mode.



(b) CCR mode.

Figure 7.7: Temperature distribution (in lattice units) of evaporating sessile droplets in which effects of evaporative cooling are observed.

temperature solver was switched on and the Marangoni flows developed, the two modes of evaporation showed different average velocities. The CCA mode recorded larger velocities than the CCR mode, of  $|\mathbf{u}|_{avg} \approx 3.99 \times 10^{-4}$  and  $|\mathbf{u}|_{avg} \approx 3.38 \times 10^{-4}$  respectively. This may be due to the larger droplet height in CCA mode, which due to heat conduction within the droplet creates

a larger temperature gradient and thus stronger Marangoni flows.

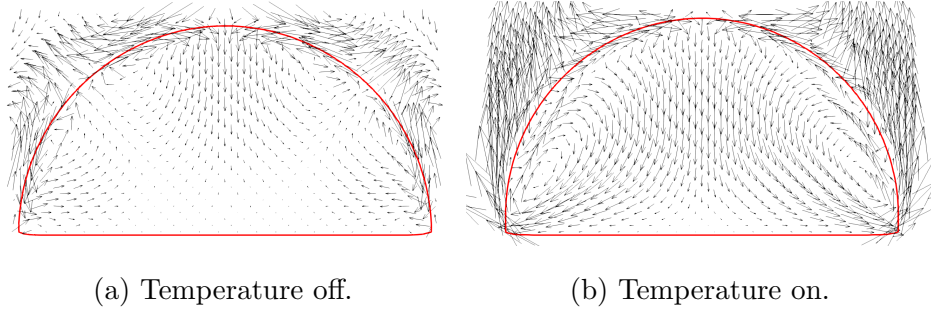
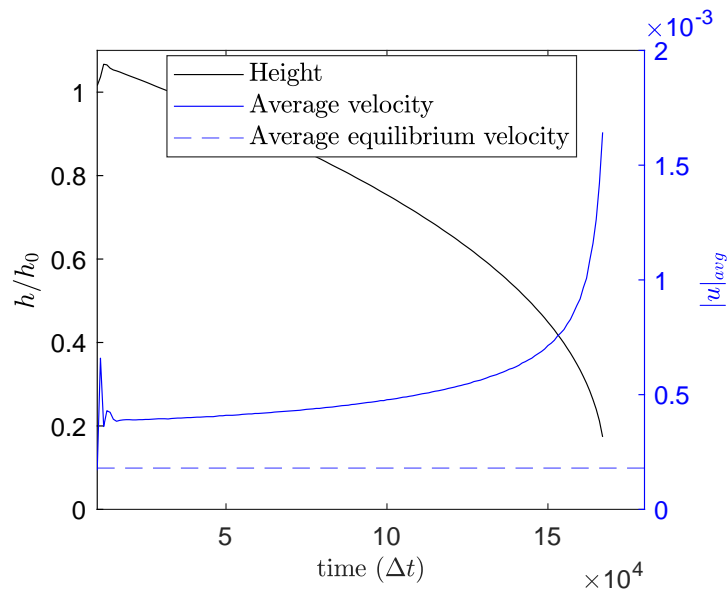
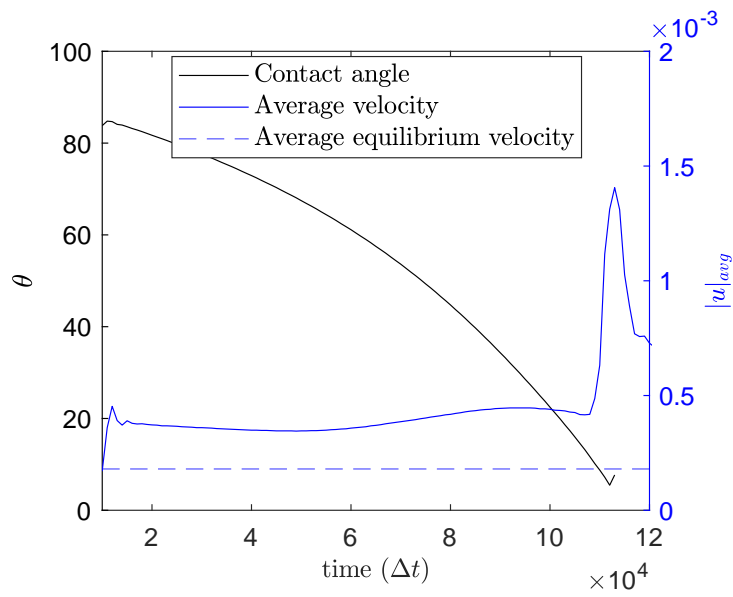


Figure 7.8: Velocity streamlines highlighting Marangoni flows in sessile droplet evaporation. Vectors scales by 8000 for visibility.



(a) CCA mode.



(b) CCR mode.

Figure 7.9: Average velocity magnitude for evaporating droplets in CCA and CCR mode.

## 7.5 Evaporation in Cavities

The simulation configuration is illustrated in figure 7.10. As with the previous investigations into evaporation on smooth surfaces, the geometric wetting boundary condition is used. However, the implementation of this wetting condition is not straightforward for complex geometries, and numerous discrete forms are needed depending on the location of the boundary node. Details on the identification of boundary node types and unique discrete expressions are given in the appendix B.2. This technique has proven successful for isothermal simulations of deposition into cavities [58, 59].

The cavity dimensions are based on the finding in the previous chapter, however, due to the increased interface thickness, the cavity dimensions of length and height are set to  $L = 69$  and  $H = 21$ . Using the minimum and maximum droplet size to cavity ratios determined in the previous chapter (§6.5), the minimum and maximum droplet sizes are found to be  $D_0 = 36.5$  and  $D_0 = 58.0$  respectively. The total simulation is comprised of  $99 \times 101 \times 99$  lattice nodes in the  $x$ ,  $y$  and  $z$  axes respectively, which due to the periodic boundary conditions resembles closely packed cavities in a display. It is assumed that effects of reduced surface temperature have negligible effect on the resulting dynamics, thus a constant temperature at all solid surfaces,  $T(\mathbf{x}_b) = T_{sat} + \Delta T$ , is applied while the saturation temperature is held at the outflow boundary of  $T_{sat} = 0.86T_c$ .

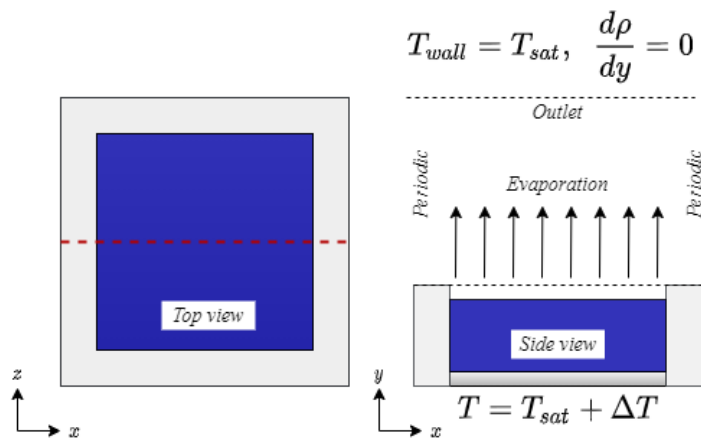


Figure 7.10: Illustration of simulation configuration for evaporating droplet in a heated cavity.

### 7.5.1 Influence of Cavity Wettability on Evaporation Rate

The evaporation from within a cavity is now investigated. The simulation is configured as in figure 7.10, where the cavity is initially empty, and a droplet of diameter  $D_0 = 63.8$  is placed in the centre of the domain. The droplet is initialised with a small  $y$ -component of velocity,  $u_y = -0.03$ , to allow it to fall into the cavity and fill it. The kinematic viscosity of the liquid was set to  $\nu = 0.063$  ( $\tau_\nu = 0.689$ ), and the kinematic viscosity of the vapour was set to  $\nu = 0.252$  ( $\tau_\nu = 1.255$ ). The wall superheat is set to  $\Delta T = 0.02T_c$ , the specific heat is set to  $C_v = 2$  and the thermal diffusivity is set to  $\chi = 0.125$ . The temperature solver is added after  $10,000\Delta t$ , once the droplet has settled in the cavity. For the first investigation, a cavity of neutral wetting and zero hysteresis ( $\theta_R = \theta_A = 90^\circ$ ) is investigated, figure 7.11. Different evaporation regimes are identifiable, which are illustrated in figure 7.12. Initially, due to the large volume of the droplet relative to the cavity, it evaporated with a fixed contact line. Once the droplet volume equals the cavity volume, it begins to evaporate with constant surface area, which slows down the evaporation rate. Finally, as the liquid surface lowers within the cavity, it detaches from walls and forms a droplet in the centre of the cavity. This stage shows the lowest evaporation rate, which is due to a combination of reduced temperature, as it detaches from the fixed temperature cavity walls and begins to evaporate in the CCA mode, which is slower than the CCR mode.

Next, the influence of contact line pinning is investigated. The same simulation parameters as before are used, with the exception of the receding contact angles of the substrate and cavity wall, which are both fixed to  $1^\circ$ . The resulting evaporation rate is shown in figure 7.13, and snapshots of the

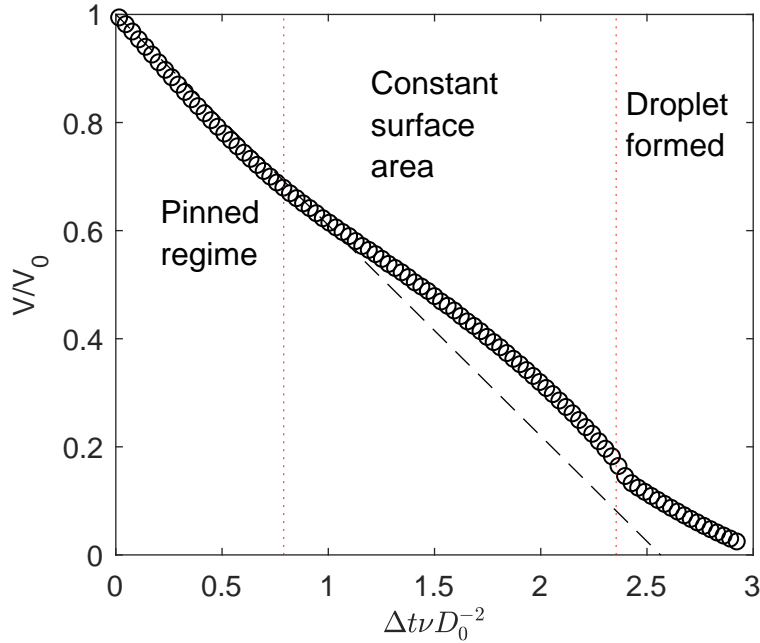


Figure 7.11: Time dependence of non-dimensional droplet volume evaporating in a square cavity with no hysteresis. Substrate contact angles of  $\theta_s^A = \theta_s^R = 90^\circ$  and cavity wall contact angles of  $\theta_w^A = \theta_w^R = 90^\circ$ .

evaporation process are illustrated in figure 7.14. As the contact line remains pinned to the edge of the cavity wall, the surface of the droplet changes from convex, to flat, to concave as the simulation progresses. Eventually, the droplet contacts the substrate in the centre of the cavity, and a hole is made. At this point, the evaporation rate drastically slows down. However, this is assumed to be an unphysical artefact of the model, as the geometric boundary condition is trying to enforce a pinned contact and the liquid level is reducing due to evaporation.

The ideal wetting conditions highlighted in §6 are used to assign the advancing contact angles of the substrate and cavity wall, and the effects of receding

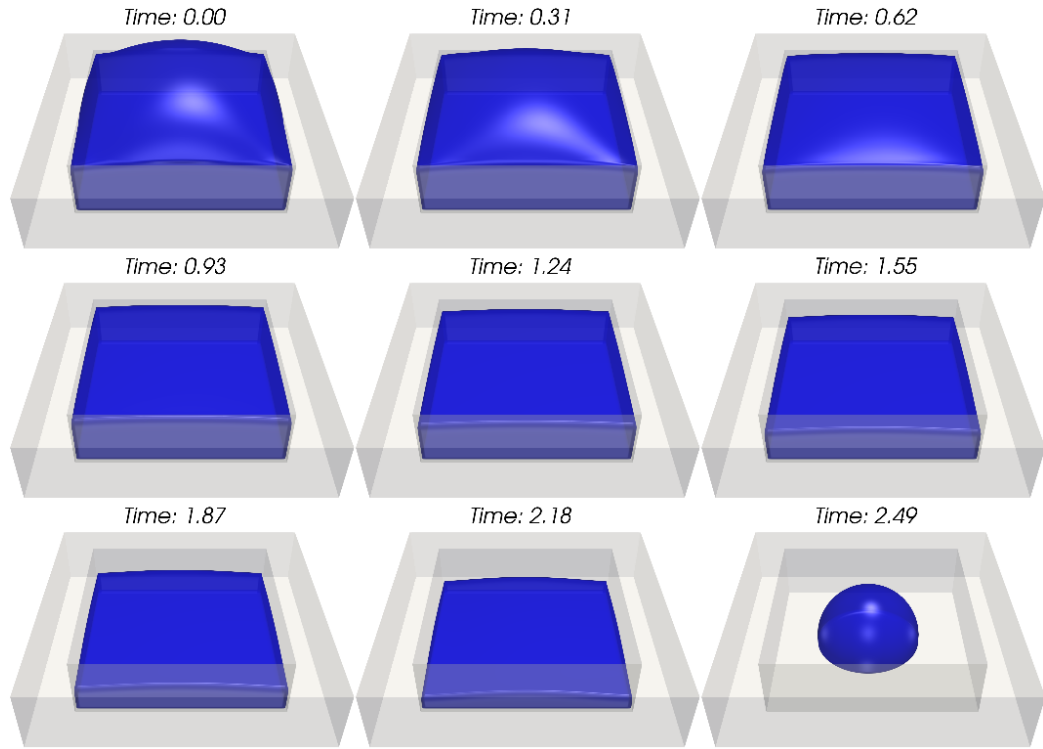


Figure 7.12: Snapshots of droplet evaporation in a square cavity with  $\theta = 90^\circ$  and no hysteresis (corresponding to figure 7.11). The superheat of the cavity is  $\Delta T = 0.02T_c$ .

contact angles of the cavity wall are explored, figure 7.15. The substrate is modelled with zero hysteresis, thus  $\theta_s^A = \theta_s^R = 30^\circ$  and the cavity walls have receding angles of  $90^\circ$ ,  $70^\circ$  and  $30^\circ$ . Initially, all droplets evaporate at the same rate, as the droplet overfills the cavity. Once the droplet volume reduces below the cavity volume, the evaporation results begin to differ, with the lowest receding angle evaporating fastest. As with the neutrally wetting, zero hysteresis case, the cavity with  $\theta_w^R = 90^\circ$  results in liquid evaporation until it detaches from the cavity walls to make a droplet in the centre of the cavity. The receding angles of  $\theta_w^R = 70^\circ$  and  $\theta_w^R = 30^\circ$  result in the liquid

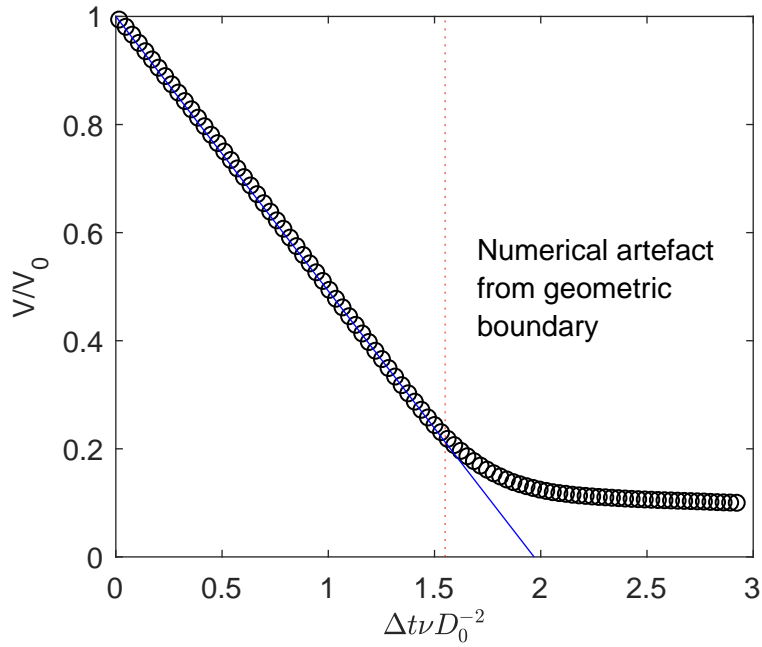


Figure 7.13: Time dependence of non-dimensional droplet volume evaporating in a square cavity with pinned contact lines. Substrate contact angles of  $\theta_s^A = 90^\circ$ ,  $\theta_s^R = 1^\circ$  and cavity wall contact angles of  $\theta_w^A = 90^\circ$  and  $\theta_w^R = 1^\circ$ .

forming a hole, as the liquid in the centre of the cavity reaches the substrate first. Illustrations of the droplets morphology at time  $\Delta t\nu D_0^{-2} = 2.49$  are shown in figure 7.16.

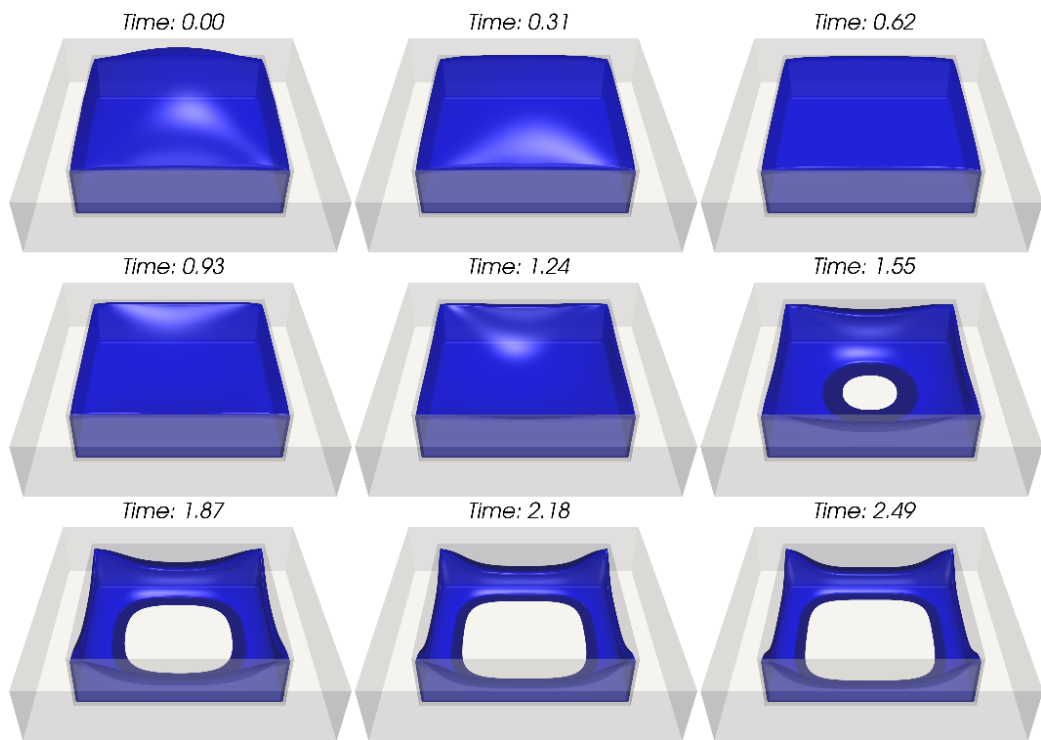


Figure 7.14: Snapshots of droplet evaporation in a square cavity with pinned contact lines (corresponding to figure 7.13). The superheat of the cavity is  $\Delta T = 0.02T_c$ .

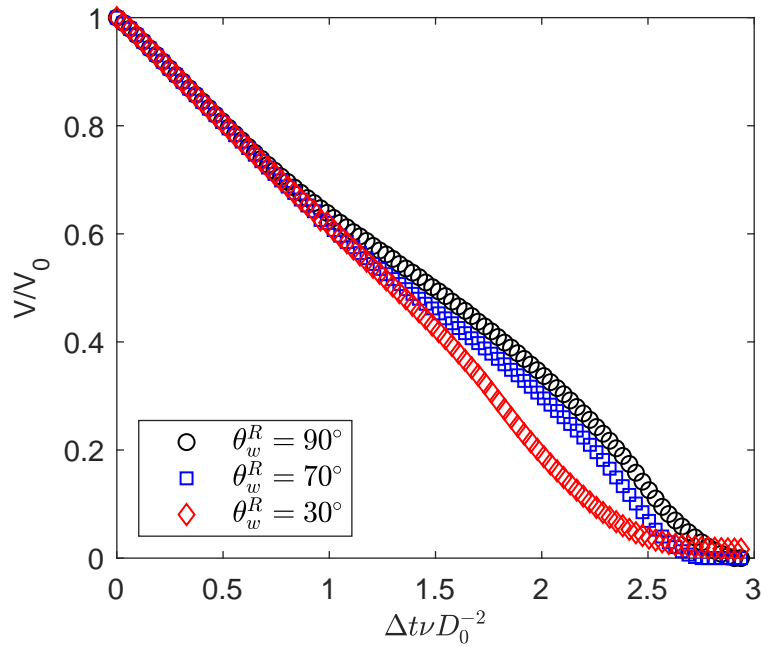


Figure 7.15: Time dependence of non-dimensional droplet volume evaporating in a square cavity with different receding contact angles.

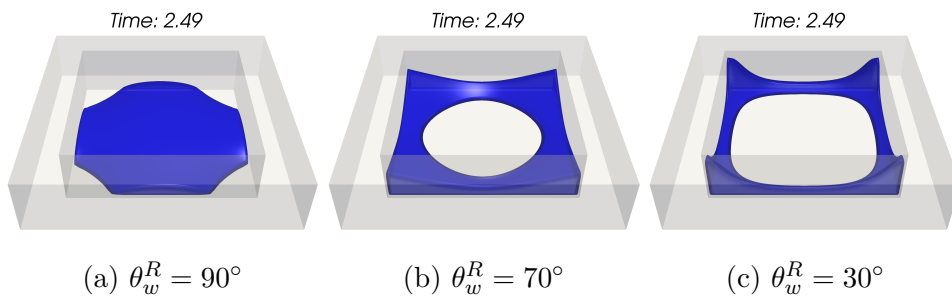


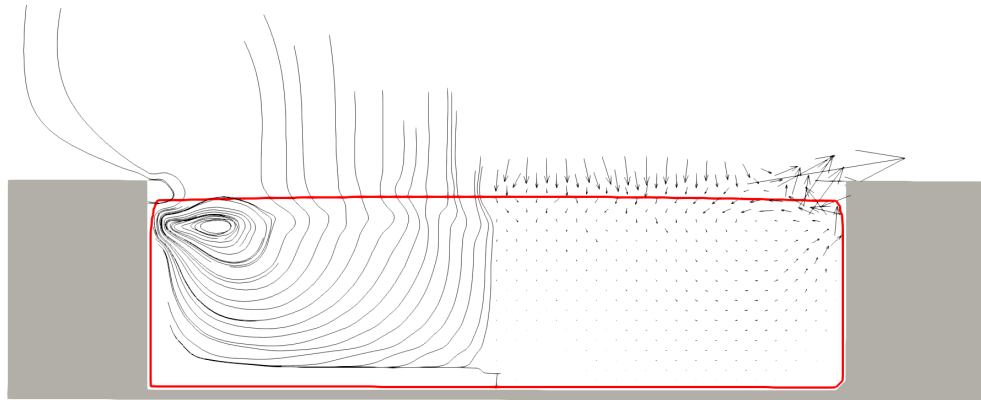
Figure 7.16: Snapshots of droplet morphologies during evaporating in a square cavity with different receding contact angles. Examples correspond to figure 7.15.

## 7.5.2 Internal Flow of Droplets Evaporating in Cavity

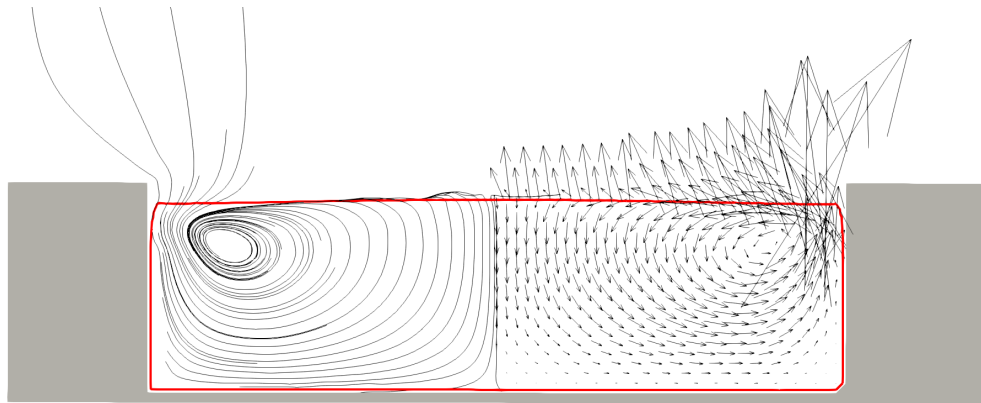
As previously shown, the model is capable of capturing thermal Marangoni flows in sessile droplets. Now, the effects on the velocity field are investigated for a heated square cavity. The model parameters remain unchanged from the previous study, with the exception of the droplet diameter, as a liquid layer inside the cavity is initialised instead. The height of the liquid layer is set 17, as to be lower than the cavity height. Both streamlines and velocity vectors of a plane cutting the centre of the cavity are illustrated in figure 7.17. Before the temperature solver is switched on, there are non-zero spurious velocities at the liquid-vapour interface, figure 7.17a. The velocity profile shortly after the temperature solver is switched on is illustrated in figure 7.17b. The heated cavity walls cause a temperature gradient along the surface of the droplet, and as a result, a surface tensions driven (Marangoni) flow develops, flowing towards the centre of the cavity.

To give a quantitative description of the resulting flows, the average velocity magnitude inside the liquid is recorded. First, the average velocity results for a neutrally wetting cavity, with no hysteresis are displayed in figure 7.18. The approximate averaged velocity before the temperature solver is switched on is found to be  $|\mathbf{u}|_{\text{avg}} \approx 3.6 \times 10^{-5}$ . Once the temperature solver is switched on, at  $10,000\Delta t$ , the averaged velocity increases up to  $|\mathbf{u}|_{\text{avg}} \approx 2.25 \times 10^{-4}$ , over six times larger than the equilibrium velocity. The maximum velocity inside the liquid, averaged over space and time, with the temperature solver on was found to be  $|\mathbf{u}|_{\text{max}} \approx 1.35 \times 10^{-3}$ .

The influence of the receding contact angle on the velocity is then investigated. For the case where both the substrate and cavity wall have a receding contact angle of  $\theta_R = 30^\circ$ , the resulting averaged velocity is shown in figure 7.19. The time-averaged value is found to be approximately the same as the



(a) Temperature solver off.



(b) Temperature solver on.

Figure 7.17: Illustration of thermal Marangoni flows inside a heated square cavity. Left-hand side shows streamlines and right-hand side shows velocity vectors. In both figures vectors are scaled by 8000 for visibility. The superheat of the cavity is  $\Delta T = 0.02T_c$ .

cavity with no hysteresis, although the averaged maximum value is reduced to  $|\mathbf{u}|_{\max} \approx 9.0 \times 10^{-4}$ . However, as the simulation progresses, the centre of the concave droplet surface contacts the substrates and quickly generates a hole (illustrated in figure 7.16c), which is why there is a large spike in velocity at time  $\Delta t \approx 5.6 \times 10^4$ .

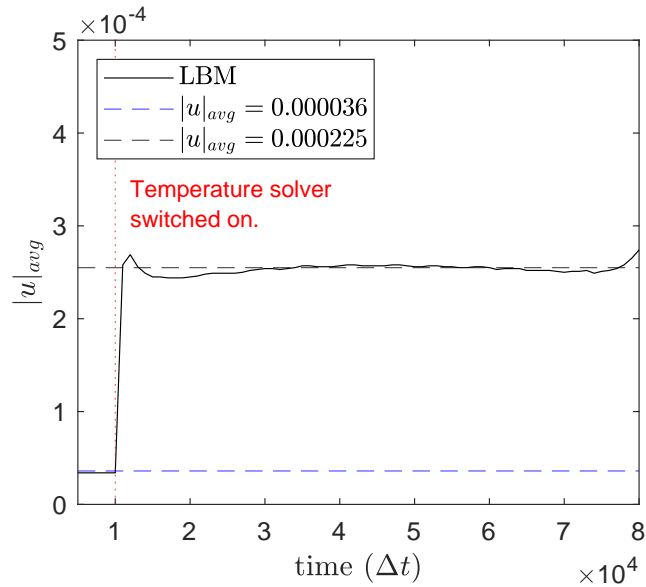


Figure 7.18: Time dependence of spatial averaged velocity magnitude of a droplet evaporating in a heated square cavity with no hysteresis.

Finally, the case where the contact line remains pinned is investigated. Both the cavity wall and substrate are assigned receding contact angles of  $\theta_R = 1^\circ$ . The resulting averaged velocity is displayed in figure 7.20, where a slight increase is noted compared to the previous cases. At the time  $\Delta t \approx 5.6 \times 10^4$ , the averaged velocity increases slightly, which is due to contact of the concave droplet contacting the centre of the substrate. However, as the contact line is pinned, the sharp velocity spike which was seen in figure 7.19 is not observed. The maximum velocity is found to be  $|\mathbf{u}|_{\max} \approx 9.0 \times 10^{-4}$ , the same as the case for the  $30^\circ$  receding contact angle.

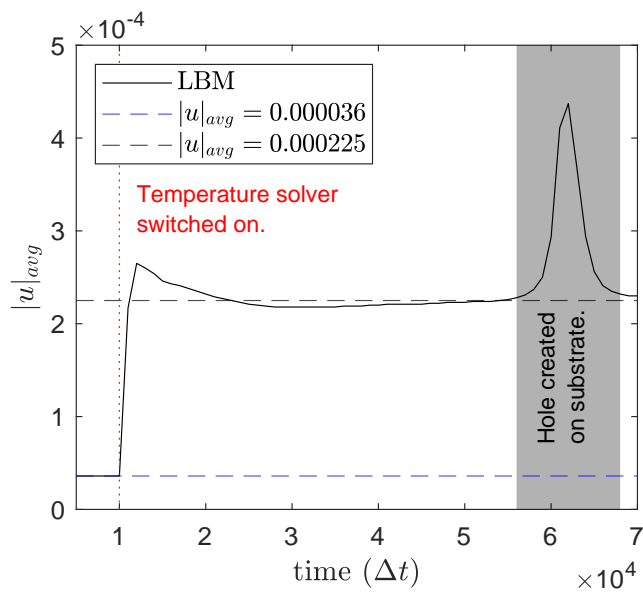


Figure 7.19: Time dependence of spatial averaged velocity magnitude of a droplet evaporating in a heated square cavity with  $30^\circ$  receding contact angle on cavity wall. The grey shaded region illustrates the time at which the droplet forms a hole on the substrate surface.

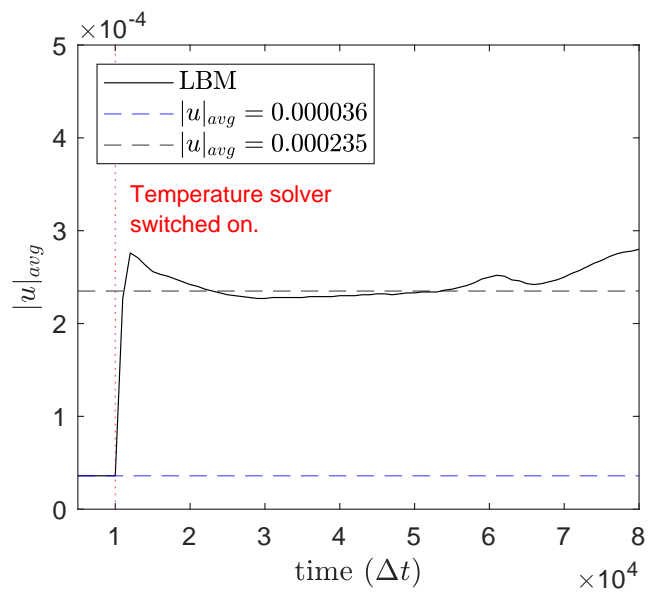


Figure 7.20: Time dependence of spatial averaged velocity magnitude of a droplet evaporating in a heated square cavity with pinned contact line.

## 7.6 Deposits

In order to investigate the particle deposits characteristics of drops evaporating in cavities, an additional solver is required. Here, instead of using a particle based solver to individually track each particle, a macroscopic approach is used to reduce computation cost and model complexity. An additional lattice Boltzmann equation is introduced to solve an advection-diffusion equation for particle concentration,  $\phi_c$ . The additional LBM solver is applied to a D3Q7 velocity set and is expressed as

$$g_i(\mathbf{x} + \mathbf{e}_i \Delta t, t + \Delta t) - g_i(\mathbf{x}, t) = -\frac{1}{\tau_g} (g_i(\mathbf{x}, t) - g_i^{eq}(\mathbf{x}, t)) \Delta t, \quad (7.5)$$

where,  $g_i$  is the distribution function for the concentration of particles,  $\tau_g$  is the relaxation time which controls the particle diffusivity and  $g_i^{eq}$  is the equilibrium distribution function, which is expressed as

$$g_i^{eq}(\mathbf{x}, t) = w_{g,i} \phi_c \left[ 1 + \frac{\mathbf{u}_c \cdot \mathbf{e}_i}{c_s^2} \right], \quad (7.6)$$

where  $w_{g,i}$  are the velocity set weights, which are equal to  $w_{g,0} = 1/4$  and  $w_{g,1,\dots,6} = 1/8$ . The particle concentration is equal to the sum of  $g_i$ , and modified velocity,  $\mathbf{u}_c$  is computed as follows

$$\mathbf{u}_c = \mathbf{u} + k \frac{\mathbf{F}_m}{2\rho}, \quad (7.7)$$

where  $k$  is a free parameter chosen to control the particle repulsion from the liquid-vapour interface, keeping the particle concentration inside the droplet. The particle diffusivity,  $D_c$ , is controlled with the relaxation time,  $\tau_g$ , as

$$D_c = c_s^2 (\tau_g - 0.5). \quad (7.8)$$

The final consideration is the boundary conditions, for which the bounce-back boundary condition is applied to solid surfaces, to give a no-flux condition. During initialisation, a larger particle concentration is added to the liquid phase ( $\phi_c, h = 0.3$ ), and a lower concentration is added elsewhere ( $\phi_{c,l} = 0.016$ ).

The Péclet number (Pe), described the ratio between the convection and diffusion of particles and is expressed as

$$\text{Pe} = \frac{Lu}{D_c}. \quad (7.9)$$

For droplets evaporating on a smooth surface, the Pe number can be used to determine if a uniform particle deposit will result. When the  $\text{Pe} < 1$ , uniform deposits can be expected, whereas for  $\text{Pe} > 1$ , non-uniform deposition results [29, 30].

### 7.6.1 Deposition on a Smooth Surface

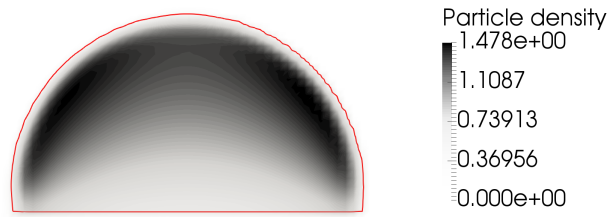
Due to the movement of the liquid-vapour interface and the resulting modification to internal flows, droplets evaporating in CCA mode do not leave ring-like deposits on the substrate. Furthermore, for Péclet numbers greater than one, particles are uniformly distributed inside the droplet, due to preferential diffusive time scales. To validate the particle concentration model, the evaporation of a droplet is investigated for both high and low Péclet numbers.

A lattice domain of  $101^3$  is configured, with a solid boundary at the bottom, modified Zou-He pressure boundary at the top and remaining boundary conditions set as periodic. A droplet of  $D_0 = 52$  is initialised above the solid surface, and the wetting condition of  $\theta = 90^\circ$  is applied, without hysteresis. The thermal settings remain unchanged from the previous in-

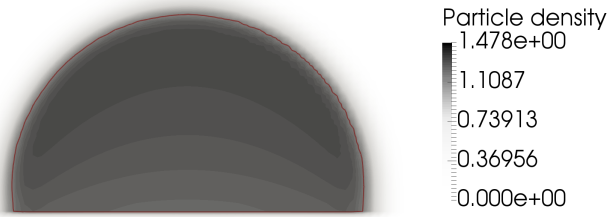
vestigations. To modify the Pe number, the particle diffusivity was set as either  $D_c = 0.01$  ( $\tau_g = 0.53$ ) or  $D_c = 0.16$  ( $\tau_g = 1.0$ ). Measurements of the maximum velocity inside the droplet, once the temperature solver was added were found to be  $|\mathbf{u}|_{\max} \approx 1.7 \times 10^{-3}$ , giving Pe numbers of  $Pe \approx 8.81$  and  $Pe \approx 0.53$  respectively. Similarly, using the thermal diffusivity of  $\chi = 0.125$ , the thermal Péclet number ( $Pe^T$ ) is found to be  $Pe^T \approx 0.71$ . The free parameter to control the particle-interface repulsion is set to  $k = 2$ , as this was found suitable for keeping the bulk of the particle inside the droplet through the whole evaporation stage. The results for CCA evaporation are illustrated in figure 7.21, where planes intersecting the centre of the droplet show the particle concentration at the time  $\Delta t = 80,000$ . For the higher Pe number, figure 7.21a, the particle concentration is largest towards the sides of the droplet. Alternatively, for the lower Pe number, figure 7.21b, the particle concentration is shown to be much more uniformly distributed, as expected.

Isothermal evaporation is modelled by modifying the Zou-He boundary condition to assign an outflow velocity at the top of the simulation domain. To give evaporation times comparable to the thermal model, an outflow velocity of  $u_y = 0.002$  was chosen. The resulting concentration for isothermal CCA evaporation is illustrated in figure 7.21c. Here, the concentration can be seen to be slightly more pronounced towards the apex of the droplet, but much less so than the thermally driven case in which Marangoni flows are present (figure 7.21a).

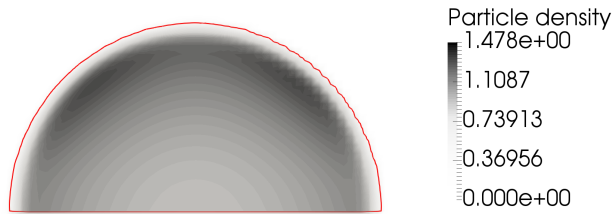
For the case of CCR evaporation, particles can be expected to travel toward the contact line due to increased evaporation rate and internal replenishing flow. The results for this mode of evaporation are illustrated in figure 7.22. The results are taken at the same time as the CCA mode,  $\Delta t = 80,000$ . As can be seen for the  $Pe > 1$  case, figure 7.22a, the overall particle con-



(a)  $Pe \approx 8.81$



(b)  $Pe \approx 0.53$



(c)  $Pe \approx 6.7$  (Isothermal)

Figure 7.21: Illustration of particle concentration in evaporating droplets in CCA mode for different Péclet numbers.

centration is much more pronounced around the entire surface of the drop compared to the CCA case, this is because more of the droplet has evaporated, reducing the droplet to particle ratio. Furthermore, there is a high particle concentration at the edge of the droplet, meaning the Marangoni flows were insufficient to remove the coffee-ring effect completely. As before, the lower  $Pe$  number results in a much more uniform particle concentration, figure 7.22b.

The isothermal evaporation case is illustrated in figure 7.22c. Here, due to internal capillary flow towards the contact line, the particle concentration is pronounced in this region only, as there are no Marangoni flows to direct the particles back towards the apex of the droplet. This demonstrates the models ability to capture the well-documented coffee-ring effect [27].

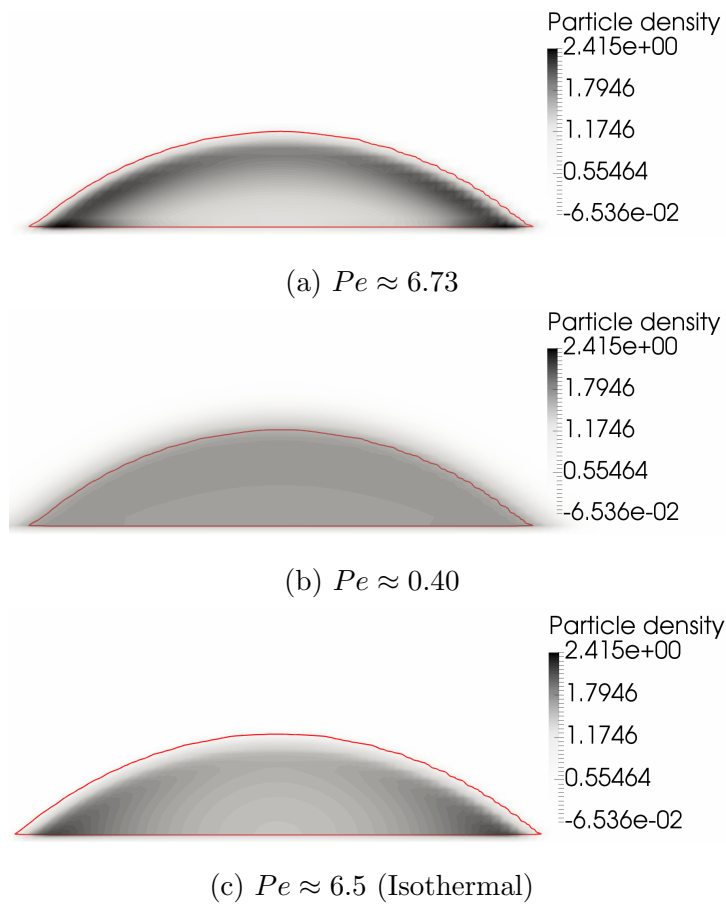


Figure 7.22: Illustration of particle concentration in evaporating droplets in CCR mode for different Péclet numbers.

## 7.6.2 Deposition in a Square Cavity

For the following investigations, the effects of receding contact angle and internal flows on deposition are explored. At low Pe numbers, the particle motion is primarily driven by diffusion and uniform deposits are achieved. However, to investigate the effects of internal flows, Péclet numbers greater than one are considered, where the characteristic length is taken to be the cavity width of  $L = 69$  and the particle diffusivity is equal to  $D_c = 0.01$ .

To instigate the influence of internal flows, the evaporation is either thermally driven, with the simulation configured identically to §7.5.1, or driven by a density gradient, where the Zou-He boundary condition is used to assign an outward flow at the boundary. For both cases, the parameters for the particle solver remain unchanged from the previous study.

To compare thermal and isothermal results, times are non-dimensionalised by the time at which the droplet has fully evaporated. For a neutrally wetting cavity ( $\theta = 90^\circ$ ), with no hysteresis, the evolution of the particle concentration on the cavity substrate is illustrated in figure 7.23. It is important to note that the scale changes in each figure, due to the naturally increasing particle concentration as the droplet evaporates, which would make visualisation challenging if a fixed scale were used. As the simulations evolve, the particle concentration becomes more concentrated around the edges of the cavity, particularly in the cavity corners.

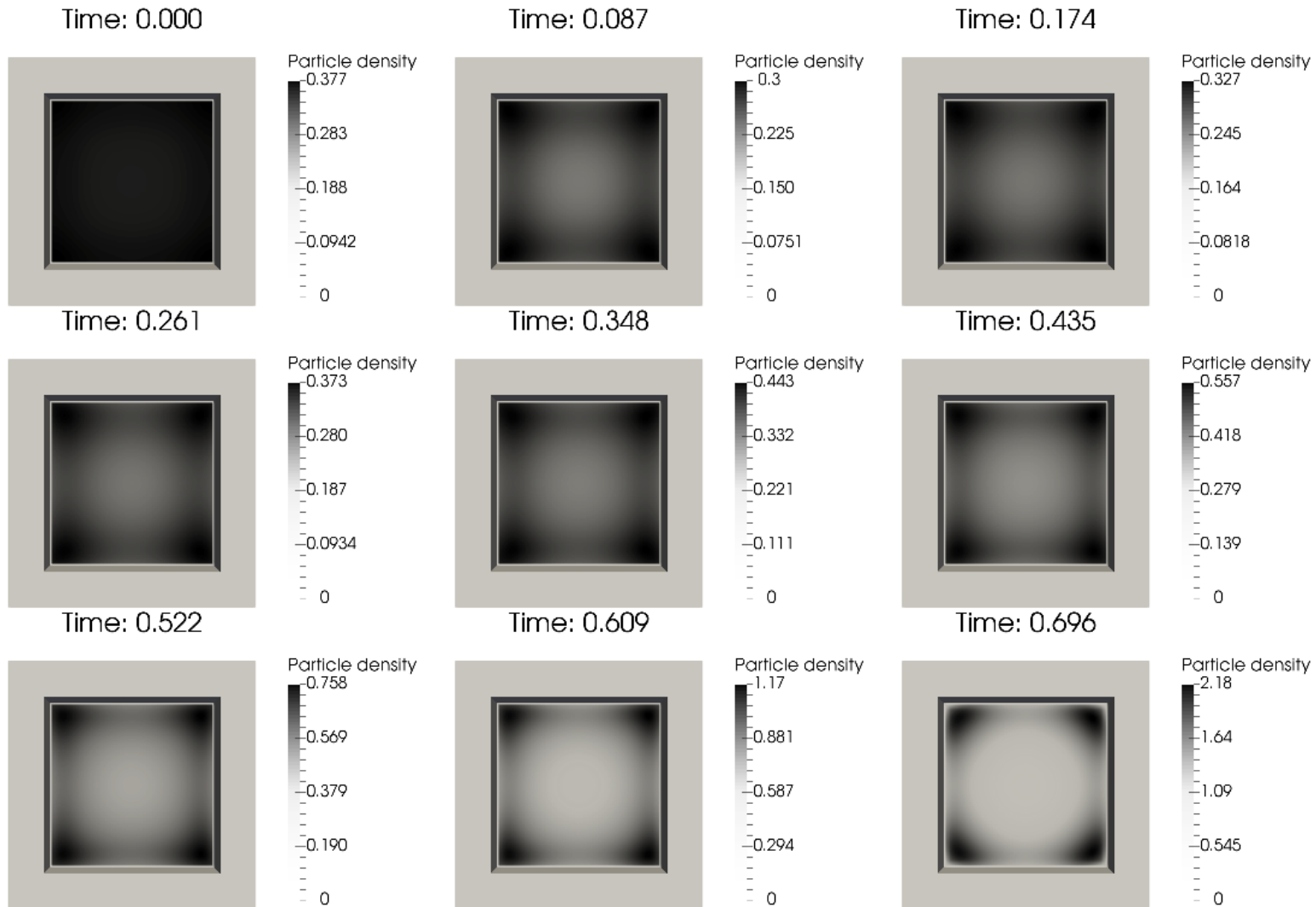


Figure 7.23: Snapshots illustrating the evolution of particle concentration on the substrate surface for a droplet evaporating in a heated cavity with  $Pe \approx 9.315$ . Cavity contact angles of  $\theta = 90^\circ$  and with no hysteresis.

Snapshots of the particle density concentration from the side, at a plane intersecting the centre of the cavity are illustrated in figure 7.24 for both thermal and isothermal evaporation. For the case of thermally driven evaporation, figure 7.24a, the particle concentration can be seen to increase toward to apex of the droplet, due to the presence of Marangoni flows. For the isothermal case, figure 7.24b, a uniform particle deposit is maintained throughout evaporation. This is to be expected as the evaporative flux will be uniform over the flat liquid-vapour interface, thus resulting internal flows are also uniform.

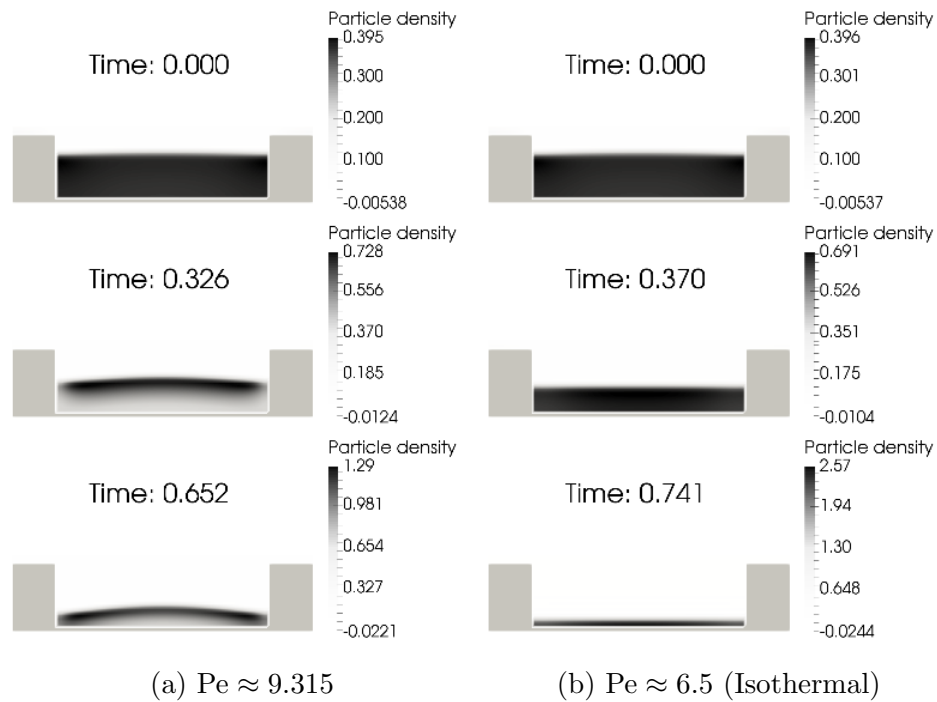


Figure 7.24: Snapshots of particle concentration for thermal and isothermal evaporation in a cavity. Cavity contact angles of  $\theta = 90^\circ$  and with no hysteresis.

The particle concentration snapshots for the case where the cavity wall has a receding contact angle of  $\theta_R = 30^\circ$  are displayed in figure 7.25. At the early

stages of evaporation, up to the time of approximately  $t \approx 0.178$ , the particle concentration increases at the edges and corners of the cavity. After this point, the concentration increases toward the centre of the cavity. Eventually, the droplet contacts the substrate in the centre, while the contact line on the cavity walls remains in place, causing a hole to be created. This drives the particle concentration towards the edges of the cavity as the contact line on the substrate recedes.

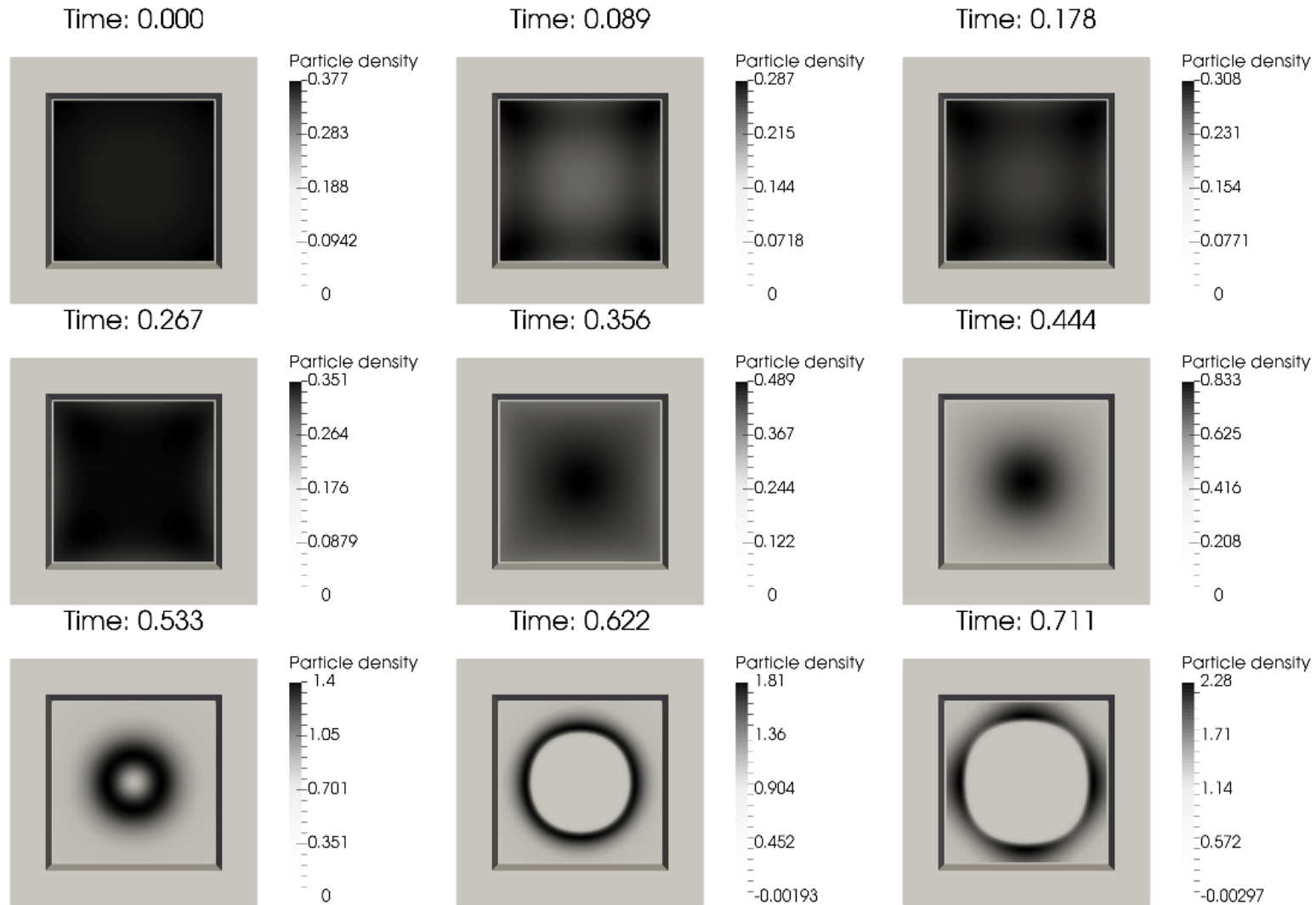


Figure 7.25: Snapshots illustrating the evolution of particle concentration on the substrate surface for a droplet evaporating in a heated cavity with  $Pe \approx 6.21$ . Cavity contact angles of  $\theta_A = 90^\circ$  and receding contact angle of  $\theta_R = 30^\circ$ .

Snapshots on the particle concentration from the side are illustrated in figure 7.26. For the thermally driven evaporation, figure 7.26a, the particle concentration increases towards the apex of the droplet, where it remains as the shape becomes more concave.

For the isothermal case, figure 7.26b, the concentration is greatest towards the centre of the cavity. It is worth noting, however, that in the case of colloidal fluids the creation of the hole in the centre of the cavity is quite unlikely, due to the increased viscosity and gelling effect. Therefore, the contact angle of the cavity walls will control the uniformity of the deposit.

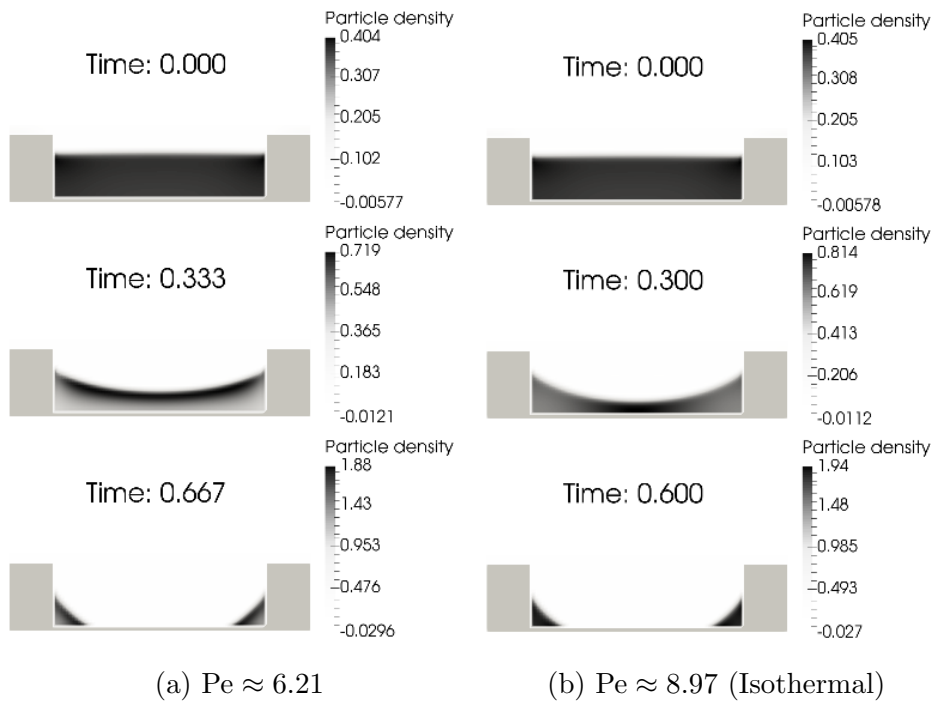


Figure 7.26: Snapshots of particle concentration for thermal and isothermal evaporation in a cavity. Cavity contact angles of  $\theta_A = 90^\circ$  and receding contact angle of  $\theta_R = 30^\circ$ .

## 7.7 Chapter Summary

In this chapter, the multiphase pseudopotential model is coupled with an energy equation to investigate thermally driven evaporation. First, the model is validated against analytical expressions of heat conduction as well as qualitatively with experiments of sessile droplet evaporation on a heated surface. The validated model is then used to study evaporation in a heated square cavity. The cavity wetting properties were shown to affect the evaporation rate similarly to the case of droplet evaporation on a flat surface. Depending on the receding contact angle, the droplet will either form a bump or a hole on the substrate during the late stages of evaporation. Therefore, depending on the desired result, the contact angle of the cavity walls can be used to control the deposit morphology and obtain a uniform deposit.

Marangoni flows are observed in the droplet inside the heated cavity are investigated qualitatively and quantitatively, with measurements of the average and maximum velocity over time.

Finally, an additional LBM solver is added to model particle concentration within the droplet. The model is validated with simulations of droplet evaporation in constant contact angle and constant contact radius modes on flat surfaces, where the coffee-ring stain can be observed for high Péclet numbers and pinned contact lines. The deposits within a square cavity are investigated both for thermal and isothermal evaporation, where the spatial variation of the particle concentration over time can be observed depending on the receding contact angle of the cavity wall and internal flows. Furthermore, the presence of Marangoni flows within the droplet resulted in the particle concentration increasing at the liquid-vapour interface.

## CHAPTER 8

---

### Conclusions

---

#### 8.1 Conclusions

Inkjet printing is seen as a promising fabrication technique for many functional devices, including but not limited to, organic light emitting diodes (OLEDs). To print OLEDs, chemical and topographical features are used to aid in positioning the droplet once deposited from the print head. However, as OLEDs are used for displays, which required smaller pixels as resolutions increase, ensuring the printed droplet lands in the desired location becomes increasingly challenging. Furthermore, even once the droplet is in the cavity, there are challenges in achieving a uniform particle deposit once the carrier solvent has evaporated.

The research conducted in this thesis aimed to develop the understanding of the dynamics of inkjet deposited droplets onto idealised pixel geometries

(square cavity) and also the evaporation of the droplet from within the cavity. To achieve this, a multiphase lattice Boltzmann method is developed which is capable of modelling thermal flows and running in parallel on high performance computers.

In chapter 2, the background of the lattice Boltzmann is given both in terms of its origins in cellular automata and its physical foundations. A discussion on model extensions leads to the adoption of the multiple-relaxation-time (MRT) collision operator, which improves simulation stability and accuracy.

In chapter 3, popular extensions for modelling multiphase and multicomponent flows are presented. From reviewing the strengths and weaknesses of different models, the pseudopotential approach is adopted, due to its inherently simple algorithm and ability to incorporate realistic equations of state. Following recent developments in the literature, the model is subsequently modified to achieve better thermodynamic consistency with the MRT algorithm. This is subsequently validated by comparing simulation results of coexistence densities to analytical solutions obtained from the maxwell equal-area construct rule. Finally, extensions to allow for thermal multiphase flows are presented and an energy equation is chosen which captures phase change effects.

In chapter 4, numerical implementation is discussed, including conversion between simulation and physical units, boundary conditions for velocity, pressure, and symmetry (with multiple phases) and finally initialisation procedures are presented. Computing aspects are described, where the processes of parallelising the multiphase algorithm for MPI is given and model performance in terms of million lattice updates per second (MLUPS) is found to increase from 1MLUPS to 205MLUPS for a 3D simulation running on 1 and 256 processes respectively. This, therefore, allows for very fast computational

speeds compared to other more conventional multiphase solvers.

In chapter 5, different wetting models for the pseudopotential model are summarised and a new wetting model is suggested, which allows for control of the adhesion strength over the liquid-vapour interface, which is typically large in LBM simulations. Furthermore, a key issue relating to the calculation of the cohesion force and boundary nodes is identified. Three different boundary treatments are proposed and subsequently evaluated with each of the wetting models (including the new wetting model).

The results from static and dynamic tests revealed that there is no one clear choice when it comes to choosing a wetting model, and different models are found to exhibit different strengths and weaknesses. The same is also true for the boundary treatments. For example, one of the boundary treatments was found to be beneficial, as it had a minimum effect on the coexistence densities at boundary nodes, however, this same treatment was also found to produce the largest additional spurious velocities. Therefore, after evaluation of each of the different wetting models and boundary treatments, a table is presented which summarises the strength and weaknesses for different scenarios. Nevertheless, the new wetting model performed comparatively well in each of the benchmark studies. However, it still suffers from some common drawbacks seen with other models, such as additional spurious velocities at the triple point.

In chapter 6, the validated multiphase lattice Boltzmann model is used with the new wetting model proposed in chapter 5, to investigate the process of droplet deposition into idealised pixel geometries (square cavities). Particular attention is given to cases in which droplets are deposited with positioning errors, which arise from print head positioning errors and angular deflections upon ejection from the nozzle.

The MPI parallelised version of the code is used for large scale parametric studies to determine preferential parameters for print success in which the droplet are deposited with both single- and dual-axis positional errors. To quantitatively describe the print quality, the nodes above the substrate are monitored to determine the fraction of the cavity wetted by the droplet. First, the influence of the substrate and cavity wall contact angles are investigated. Here, a minimum contact angle is found for the cavity wall of  $75^\circ$ , and a maximum value for the substrate of  $105^\circ$ . Further evaluating the wetting conditions which resulted in fully wetting the cavity, it is found that the substrate contact angle has a strong influence on the time taken to fully fill the cavity.

Using the wetting conditions which resulted in the shortest cavity filling time, the influence of the cavity height and spacing, i.e., distance to neighbouring cavity are explored, where it was found that for comparable configurations, dual-axis positioning error is better than single-axis in terms of droplet self-alignment within the cavity. Furthermore, investigating the influence of the Weber number, within the printable fluid regime showed that lower values are preferable to avoid droplets contaminating neighbouring cavities.

The upper limits of positioning errors are then explored. With increasing the cavity height, a successful print could be achieved with positioning errors close to the limit determined by the cavity length and spacing. Finally, using the determined upper limit for positioning error defined in terms of droplet size and cavity length, a parameter map is produced, which gives the conditions required for a successful print. Expressions are also derived for giving the minimum single droplet size required to fully wet the cavity substrate, and the maximum size to avoid overfilling.

In chapter 7, the pseudopotential model is coupled with an energy equa-

tion to investigate droplet evaporation in heated cavities. The model is first validated quantitatively with comparisons to analytical solutions of heat conduction and qualitatively against experiments for sessile droplet evaporation. The validated model is then used to investigate droplet evaporation in a square cavity, where the receding contact angle of the cavity wall was found to influence the evaporation rate and resulting droplet morphologies. Receding contact angles lower than  $90^\circ$  would cause the droplet to make a hole once the centre of the concave droplet reached the substrate. Alternatively, when the receding contact angle of the wall and substrate was set to  $90^\circ$ , different evaporation modes were identified, such as pinning to the top of the cavity walls, reduction inside the cavity with constant surface area, and finally, the droplet dewetting the cavity walls and forming a droplet in the centre of the substrate.

The internal flows were investigated, and Marangoni flows were found to develop due to temperature gradients along the surface of the droplet. Finally, an additional LBM solver is added to investigate particle deposition, where instead of tracking individual particles, a macroscopic approach is used, showing the particle concentration. The model is validated for sessile droplet evaporation on a smooth surface, with thermally driven evaporation and isothermal, diffusion driven evaporation, where the coffee-ring effect was observed. The validated model is then used to explore the deposits of droplets evaporating in square cavities, where again the influence of the cavity wall contact angle is found to affect the evolution of the particle concentration. With heated cavities, the particle concentration was also found to increase at the liquid-vapour interface.

Based on the results obtained in this thesis, recommendations on cavity wetting properties can be made. High wettability substrates of  $30^\circ$  are recom-

mended, as this aids in the self-positioning of the droplet within the cavity. For the surrounding cavity walls, contact angles of  $112.5^\circ$  were found to mitigate single- and dual-axis positioning errors. Furthermore, during evaporation, receding angles greater than  $90^\circ$  are recommended for improving the final particle deposit morphology, as this avoids the likelihood of forming holes. For heated cavities, the resulting Marangoni flows are shown to enhance particle concentration towards the liquid-vapour interface, this would likely improve the final deposit due to the increased viscosity hindering further particle transport.

## 8.2 Future Work

Although the research conducted in this thesis has highlighted key aspects of wettability modelling, droplet deposition and self-alignment and evaporation dynamics. The investigations have opened up new areas for further investigation.

Starting with the base lattice Boltzmann algorithm, implementing a multiple-relaxation-time model based on a non-orthogonal transformation matrix can minimise computational overhead compared to the standard orthogonal matrix while still retaining stability and accuracy improvements. Furthermore, as highlighted in section 3.3, there are numerous extensions to allow for independent tuning of the surface tension and density ratio which would increase modelling capabilities.

Although satisfactory simulation speeds were achieved through parallelisation of the LBM algorithm with OpenMP and MPI, there are limits to the achievable speed with the simple one-dimensional domain decomposition used. Therefore, implementing more advanced domain decompositions could

result in a further increase of simulation speeds. Alternatively, implementation on graphical processing units could result in a significant simulation speed increase.

Through investigating wettability modelling in chapter 5, it was found that the adhesion force based wetting models naturally capture some contact angle hysteresis effects. Further dynamic studies of wetting models and boundary conditions are required to quantitatively describe the levels of hysteresis. The newly proposed IFM wetting model has alternate configurations to be explored. Furthermore, extensions are required in order to enable investigations on boundaries not aligned with a coordinate axis. Wetting with the boundary treatment based on a locally average density needs to be explored with different adhesion force based wetting models.

The investigations of droplet deposition and self-alignment used the case of an idealised square cavity with a single droplet of commensurate size. There are however different shape cavities to explore, some of which would require the deposition of multiple droplets. This, therefore, increases the parameter space, and thus a more efficient multi-objective optimisation strategy could be used to explore the limits of droplet self-alignment for these scenarios. The deposition is explored for a Newtonian fluid, however, depending on the concentration of functional materials in the ink, the fluid can become non-Newtonian. Therefore, the droplet self-alignment properties of non-Newtonian fluids can be explored.

Finally, for investigations of evaporation and particle concentration dynamics, model extensions could be implemented to account for changes in viscosity due to increased local particle concentration. Alternatively, the multiphase model could be coupled with a particle model to capture the actual deposition process.

# APPENDIX A

---

## Publications and Presentations

---

### Publications

- F. F. Jackson, K. J. Kubiak, M. C. T. Wilson, M. Molinari, and V. Stetsyuk, “Droplet misalignment limit for inkjet printing into cavities on textured surfaces,” *Langmuir*, 2019.

### Presentations

- Modelling of Inkjet Deposition into Cavities with Print-head Misalignment - UK Consortium on Mesoscale Engineering Sciences (UKCOMES) 14<sup>th</sup> December 2020.
- Simulation of Droplet Deposition and Evaporation in Square Cavities - UK Fluids Network (UKFN) - Droplets and Surface Interactions, 16<sup>th</sup> May 2019, University of Edinburgh.

## APPENDIX B

---

### Geometric Wetting Boundary

---

#### B.1 Identification of Node Types

In order to implement the geometric boundary condition, density gradients tangential to the solid surface need to be evaluated numerically, as they are used to set the density value at solid nodes to control the wetting. For flat surfaces, this is straightforward, however, for the cavity geometry used in this thesis, implementation is cumbersome, due to the many different discretisations required. The first step required the identification of different surface types i.e. bottom wall node, corner node, edge node, etc. Figure [B.1](#) illustrates the different node types in a cavity, for which individual conditions need to be applied to control the wetting. A total of 66 unique sites are identified.

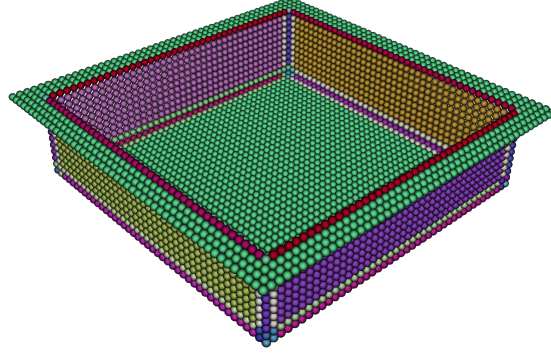


Figure B.1: Identification of unique node types within a square cavity for discretisation of the geometric boundary condition to control wetting.

## B.2 Discretisation

Example discretisations are presented for various node types. The geometric boundary condition is expressed as

$$\tan\left(\frac{\pi}{2} - \theta\right) = \frac{-\nabla\rho \cdot \mathbf{n}}{|\nabla\rho - (\mathbf{n} \cdot \nabla\rho)\mathbf{n}|}. \quad (\text{B.1})$$

A mixture of second-order central-difference, forward- and backward-difference schemes are used to evaluate the gradient terms depending on the type of node which is identified. An example for a bottom wall surface is presented, here, the normal direction is the  $y$ -axis,  $\mathbf{n} = [0, 1, 0]^T$ . First, the gradient of density is evaluated as

$$\nabla\rho = \frac{\partial\rho}{\partial x}\hat{e}_x + \frac{\partial\rho}{\partial y}\hat{e}_y + \frac{\partial\rho}{\partial z}\hat{e}_z, \quad (\text{B.2})$$

which is then used with the normal unit vector to compute the dot product as

$$-\nabla\rho\cdot\mathbf{n}=-\frac{\partial\rho}{\partial y}, \quad (\text{B.3})$$

and additionally,

$$|\nabla\rho-(\mathbf{n}\cdot\nabla\rho)\mathbf{n}|=\left|\frac{\partial\rho}{\partial x}\hat{e}_x+\frac{\partial\rho}{\partial z}\hat{e}_z\right|. \quad (\text{B.4})$$

These expressions are then replaced with second-order central-difference schemes, for example

$$\frac{\partial\rho}{\partial y}\Big|_{x,1,z}\approx\frac{\rho_{x,2,z}-\rho_{x,0,z}}{2\Delta x}, \quad (\text{B.5})$$

where  $\rho_{x,1,z}$  is the density at the node directly above the bottom surface and  $\rho_{x,0,z}$  is the density in the solid node. Similarly, the second-order central-difference is applied to  $|\nabla\rho-(\mathbf{n}\cdot\nabla\rho)\mathbf{n}|=\zeta$  to give

$$\frac{1}{2\Delta x}\left|\frac{\partial\rho}{\partial x}\hat{e}_x+\frac{\partial\rho}{\partial z}\hat{e}_z\right|\approx\sqrt{(\rho_{x+1,1,z}-\rho_{x-1,1,z})^2+(\rho_{x,1,z+1}-\rho_{x,1,z-1})^2}. \quad (\text{B.6})$$

Inserting these discrete expressions back into equation B.1, one can obtain the final form for describing the density at the solid node as

$$\rho_{x,0,z}=\rho_{x,2,z}+\tan\left(\frac{\pi}{2}-\theta\right)\sqrt{(\rho_{x+1,1,z}-\rho_{x-1,1,z})^2+(\rho_{x,1,z+1}-\rho_{x,1,z-1})^2}. \quad (\text{B.7})$$

Note how  $2\Delta x$  has cancelled out when combining the all the discrete expressions.

### B.2.1 Corner Treatment

When dealing with corners, there is no formal mathematical definition of a normal vector. A simple approach to assigning densities to corner nodes is

illustrated in figure B.2. Here the solid red nodes are corner nodes, which need to be assigned a density value and the red outlined nodes are where the density value is taken from.

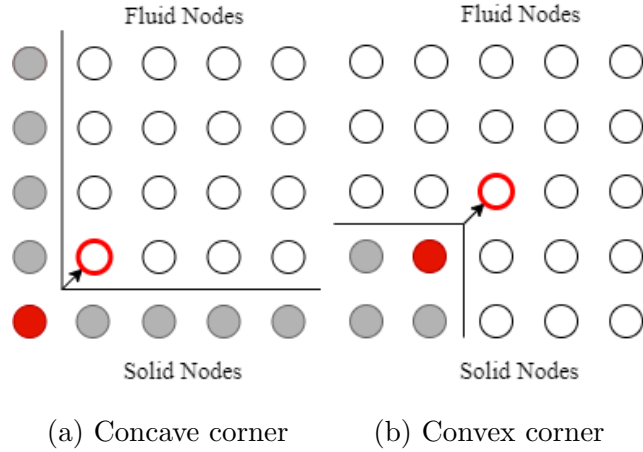


Figure B.2: Illustration of solid ghost nodes in convex and concave corners.

For wall nodes neighbouring corners, different numerical schemes are used to compute the gradient terms. An example is illustrated in figure B.3, where the wall node above the corner is shown in solid red. Gradient terms need to be evaluated at the fluid node next to the boundary (blue outline, red fill). The gradient in the  $y$ -axis is evaluated with a forward difference scheme (blue nodes with a white fill), and gradients in the  $z$ -axis (going into the page) are evaluated with a central difference scheme. Finally, the density at the node can be determined as

$$\rho_{x,y,z} = \rho_{x+2,y,z} + \tan\left(\frac{\pi}{2} - \theta\right)\zeta, \quad (\text{B.8})$$

with



## APPENDIX C

---

### Lattice Isotropy

---

For the D2Q9 and D3Q19 velocity sets used to recover the Navier-Stokes equations, the lattice isotropy is as follows

$$\begin{aligned}\sum_i w_i &= 1, \\ \sum_i w_i e_{i\alpha} &= 0, \\ \sum_i w_i e_{i\alpha} e_{i\beta} &= c_s^2 \delta_{\alpha\beta}, \\ \sum_i w_i e_{i\alpha} e_{i\beta} e_{i\gamma} &= 0, \\ \sum_i w_i e_{i\alpha} e_{i\beta} e_{i\gamma} e_{i\mu} &= c_s^4 (\delta_{\alpha\beta} \delta_{\gamma\mu} + \delta_{\alpha\gamma} \delta_{\beta\mu} + \delta_{\alpha\mu} \delta_{\beta\gamma}), \\ \sum_i w_i e_{i\alpha} e_{i\beta} e_{i\gamma} e_{i\mu} e_{i\nu} &= 0.\end{aligned}\tag{C.1}$$

## C.1 Moments of the Equilibrium Distribution Function

With the equilibrium distribution function given as

$$f_i^{eq} = w_i \rho \left( 1 + \frac{e_{i\alpha} u_\alpha}{c_s^2} + \frac{u_\alpha u_\beta (e_{i\alpha} e_{i\beta} - c_s^2 \delta_{\alpha\beta})}{2c_s^4} \right), \quad (\text{C.2})$$

the macroscopic moments of the equilibrium distribution function are obtained with use of equation C.1 to give

$$\begin{aligned} \Pi^{eq} &= \sum_i f_i^{eq} = \rho, \\ \Pi_\alpha^{eq} &= \sum_i f_i^{eq} e_{i\alpha} = \rho u_\alpha, \\ \Pi_{\alpha\beta}^{eq} &= \sum_i f_i^{eq} e_{i\alpha} e_{i\beta} = \rho c_s^2 \delta_{\alpha\beta} + \rho u_\alpha u_\beta, \\ \Pi_{\alpha\beta\gamma}^{eq} &= \sum_i f_i^{eq} e_{i\alpha} e_{i\beta} e_{i\gamma} = \rho c_s^2 (u_\alpha \delta_{\beta\gamma} + u_\beta \delta_{\alpha\gamma} + u_\gamma \delta_{\alpha\beta}). \end{aligned} \quad (\text{C.3})$$



---

## Bibliography

---

- [1] P. F. Moonen, I. Yakimets, and J. Huskens, “Fabrication of transistors on flexible substrates: from mass-printing to high-resolution alternative lithography strategies,” *Advanced Materials*, vol. 24, no. 41, pp. 5526–5541, 2012. [1](#)
- [2] R. G. Scalisi, M. Paleari, A. Favetto, M. Stoppa, P. Ariano, P. Pandolfi, and A. Chiolerio, “Inkjet printed flexible electrodes for surface electromyography,” *Organic Electronics*, vol. 18, pp. 89–94, 2015. [1](#)
- [3] P. Calvert, “Inkjet printing for materials and devices,” *Chemistry of Materials*, vol. 13, no. 10, pp. 3299–3305, 2001. [1](#), [2](#)
- [4] T. Shimoda, K. Morii, S. Seki, and H. Kiguchi, “Inkjet printing of light-emitting polymer displays,” *Materials Research Society Bulletin*, vol. 28, no. 11, pp. 821–827, 2003. [1](#), [2](#), [146](#)

- [5] M. Gao, L. Li, and Y. Song, “Inkjet printing wearable electronic devices,” *Journal of Materials Chemistry C*, vol. 5, no. 12, pp. 2971–2993, 2017. [1](#)
- [6] A. Islam, M. Rabbani, M. H. Bappy, M. A. R. Miah, and N. Sakib, “A review on fabrication process of organic light emitting diodes,” in *Informatics, Electronics & Vision (ICIEV), 2013 International Conference on*, pp. 1–5, IEEE. [2](#)
- [7] H. Gorter, M. J. J. Coenen, M. W. L. Slaats, M. Ren, W. Lu, C. J. Kuijpers, and W. A. Groen, “Toward inkjet printing of small molecule organic light emitting diodes,” *Thin Solid Films*, vol. 532, pp. 11–15, 2013. [2](#), [195](#)
- [8] M. Singh, H. M. Haverinen, P. Dhagat, and G. E. Jabbour, “Inkjet printing—process and its applications,” *Advanced materials*, vol. 22, no. 6, pp. 673–685, 2010. [2](#)
- [9] M. Robin, W. Kuai, M. Amela-Cortes, S. Cordier, Y. Molard, T. Mohammed-Brahim, E. Jacques, and M. Harnois, *Epoxy Based Ink as Versatile Material for Inkjet-Printed Devices*, vol. 7. 2015. [2](#)
- [10] J. Alamán, R. Alicante, J. I. Peña, and C. Sánchez-Somolinos, “Inkjet printing of functional materials for optical and photonic applications,” *Materials*, vol. 9, no. 11, p. 910, 2016. [2](#)
- [11] I. M. Hutchings and G. Martin, *Inkjet technology for digital fabrication*. Chichester, West Sussex, United Kingdom: John Wiley & Sons Ltd., 2013. [2](#)

- [12] B. Derby, “Inkjet printing of functional and structural materials: fluid property requirements, feature stability, and resolution,” *Annual Review of Materials Research*, vol. 40, pp. 395–414, 2010. [3](#), [5](#)
- [13] S. D. Hoath, *Fundamentals of Inkjet Printing: The Science of Inkjet and Droplets*. DE: Wiley-VCH, 2016. [3](#), [10](#), [15](#)
- [14] N. Reis and B. Derby, “Ink jet deposition of ceramic suspensions: Modeling and experiments of droplet formation,” *MRS Online Proceedings Library*, vol. 624, no. 1, pp. 65–70, 2000. [4](#)
- [15] D. Jang, D. Kim, and J. Moon, “Influence of fluid physical properties on ink-jet printability,” *Langmuir*, vol. 25, no. 5, pp. 2629–2635, 2009. [4](#), [154](#), [156](#)
- [16] D. Deganello, *Printing techniques for the fabrication of OLEDs*, pp. 360–385. Woodhead Publishing, 2013. [6](#)
- [17] Y. Wang, H. Guo, J.-j. Chen, E. Sowade, Y. Wang, K. Liang, K. Marcus, R. R. Baumann, and Z.-s. Feng, “Paper-based inkjet-printed flexible electronic circuits,” *ACS Applied Materials & Interfaces*, vol. 8, no. 39, pp. 26112–26118, 2016. [6](#)
- [18] H. Sirringhaus, T. Kawase, R. H. Friend, T. Shimoda, M. Inbasekaran, W. Wu, and E. P. Woo, “High-resolution inkjet printing of all-polymer transistor circuits,” *Science*, vol. 290, no. 5499, pp. 2123–2126, 2000. [6](#)
- [19] C. Gerard and P. Y. D. Marc, “Inkjet printing of conductive materials: a review,” *Circuit World*, vol. 38, no. 4, pp. 193–213, 2012. [6](#)

- [20] V. V. Bergeron, D. Bonn, J. Y. Martin, and L. Vovelle, “Controlling droplet deposition with polymer additives,” *Nature*, vol. 405, no. 6788, pp. 772–5, 2000. [6](#)
- [21] R. N. Wenzel, “Resistance of solid surfaces to wetting by water,” *Industrial & Engineering Chemistry*, vol. 28, no. 8, pp. 988–994, 1936. [9](#)
- [22] A. B. D. Cassie and S. Baxter, “Wettability of porous surfaces,” *Transactions of the Faraday Society*, vol. 40, no. 0, pp. 546–551, 1944. [9](#)
- [23] L. Gao and T. J. McCarthy, “Wetting 101°,” *Langmuir*, vol. 25, no. 24, pp. 14105–14115, 2009. [9](#), [102](#)
- [24] R. Rioboo, M. Marengo, and C. Tropea, “Time evolution of liquid drop impact onto solid, dry surfaces,” *Experiments in Fluids*, vol. 33, no. 1, pp. 112–124, 2002. [10](#)
- [25] L. H. Tanner, “The spreading of silicone oil drops on horizontal surfaces,” *Journal of Physics D: Applied Physics*, vol. 12, no. 9, p. 1473, 1979. [10](#), [129](#)
- [26] D. Brutin, *Droplet wetting and evaporation: from pure to complex fluids*. Academic Press, 2015. [10](#)
- [27] R. D. Deegan, O. Bakajin, T. F. Dupont, G. Huber, S. R. Nagel, and T. A. Witten, “Capillary flow as the cause of ring stains from dried liquid drops,” *Nature*, vol. 389, no. 6653, pp. 827–829, 1997. [10](#), [229](#)
- [28] F. Giorgiutti-Dauphiné and L. Pauchard, “Drying drops,” *The European Physical Journal E*, vol. 41, no. 3, p. 32, 2018. [10](#)

- [29] A. F. Routh and W. B. Zimmerman, “Distribution of particles during solvent evaporation from films,” *Chemical Engineering Science*, vol. 59, no. 14, pp. 2961–2968, 2004. [11](#), [226](#)
- [30] J. Sun, B. Bao, M. He, H. Zhou, and Y. Song, “Recent advances in controlling the depositing morphologies of inkjet droplets,” *ACS Applied Materials & Interfaces*, vol. 7, no. 51, pp. 28086–28099, 2015. [11](#), [226](#)
- [31] R. G. Picknett and R. Bexon, “The evaporation of sessile or pendant drops in still air,” *Journal of Colloid and Interface Science*, vol. 61, no. 2, pp. 336–350, 1977. [11](#)
- [32] P. J. Smith, *The Behaviour of a Droplet on the Substrate*. Singapore: World Scientific, 2009. [11](#)
- [33] D. Orejon, K. Sefiane, and M. E. R. Shanahan, “Stick–slip of evaporating droplets: substrate hydrophobicity and nanoparticle concentration,” *Langmuir*, vol. 27, no. 21, pp. 12834–12843, 2011. [11](#)
- [34] L. E. Scriven and C. V. Sternling, “The marangoni effects,” *Nature*, vol. 187, no. 4733, pp. 186–188, 1960. [11](#)
- [35] Y. Tsoumpas, S. Dehaeck, A. Rednikov, and P. Colinet, “Effect of marangoni flows on the shape of thin sessile droplets evaporating into air,” *Langmuir*, vol. 31, no. 49, pp. 13334–13340, 2015. [11](#)
- [36] H. Hu and R. G. Larson, “Marangoni effect reverses coffee-ring depositions,” *The Journal of Physical Chemistry B*, vol. 110, no. 14, pp. 7090–7094, 2006. [11](#)

- [37] G. D. Smith, *Numerical solution of partial differential equations: finite difference methods*. Oxford university press, 1985. [13](#)
- [38] O. C. Zienkiewicz, R. L. Taylor, P. Nithiarasu, and J. Z. Zhu, *The finite element method*. Oxford: Elsevier/Butterworth-Heinemann, sixth edition ed., 2005. [13](#)
- [39] H. K. Versteeg and W. Malalasekera, *An introduction to computational fluid dynamics: the finite volume method*. Pearson education, 2007. [13](#)
- [40] C. W. Hirt and B. D. Nichols, “Volume of fluid (vof) method for the dynamics of free boundaries,” *Journal of Computational Physics*, vol. 39, no. 1, pp. 201–225, 1981. [13](#)
- [41] E. Olsson and G. Kreiss, “A conservative level set method for two phase flow,” *Journal of Computational Physics*, vol. 210, no. 1, pp. 225–246, 2005. [13](#)
- [42] M. P. Allen and D. J. Tildesley, *Computer simulation of liquids*. Oxford: Clarendon Press, 1989. [13](#)
- [43] D. Frenkel and B. Smit, “Understanding molecular simulation: From algorithms to applications,” 2002. [14](#)
- [44] T. Krüger, H. Kusumaatmaja, A. Kuzmin, O. Shardt, G. Silva, and E. M. Viggen, *The lattice Boltzmann method*, vol. 10 of *Springer International Publishing*. 2017. [14](#), [15](#), [16](#), [30](#), [37](#), [39](#), [50](#), [61](#), [74](#), [76](#), [85](#)
- [45] P. J. Hoogerbrugge and J. M. V. A. Koelman, “Simulating microscopic hydrodynamic phenomena with dissipative particle dynamics,” *EPL (Europhysics Letters)*, vol. 19, no. 3, p. 155, 1992. [15](#)

- [46] M. B. Liu, G. R. Liu, L. W. Zhou, and J. Z. Chang, “Dissipative particle dynamics (dpd): An overview and recent developments,” *Archives of Computational Methods in Engineering*, vol. 22, no. 4, pp. 529–556, 2015. [15](#)
- [47] M. C. T. Wilson and K. J. Kubiak, “Simulation of drops on surfaces,” *Fundamentals of Inkjet Printing: The Science of Inkjet and Droplets*, 2015. [15](#)
- [48] S. Mirjalili, S. S. Jain, and M. Dodd, “Interface-capturing methods for two-phase flows: An overview and recent developments,” *Center for Turbulence Research Annual Research Briefs*, vol. 2017, no. 117-135, p. 13, 2017. [15](#)
- [49] N. A. Patankar and Y. Chen, “Numerical simulation of droplet shapes on rough surfaces,” in *2002 International Conference on Modeling and Simulation of Microsystems-MSM 2002*, pp. 116–119. [16](#)
- [50] G. Fischer, M. Bigerelle, K. J. Kubiak, T. G. Mathia, Z. Khatir, and K. Anselme, “Wetting of anisotropic sinusoidal surfaces—experimental and numerical study of directional spreading,” *Surface Topography: Metrology and Properties*, vol. 2, no. 4, pp. 044003–044003, 2014. [16](#)
- [51] A. S. Yang, M. T. Yang, and M. C. Hong, “Numerical study for the impact of liquid droplets on solid surfaces,” *Proceedings of the Institution of Mechanical Engineers, Part C: Journal of Mechanical Engineering Science*, vol. 221, no. 3, pp. 293–301, 2007. [16](#), [146](#)
- [52] T. Liou, C. Chan, C. Fu, and K. Shih, “Effects of impact inertia and surface characteristics on deposited polymer droplets in microcavities,”

- Journal of Microelectromechanical Systems*, vol. 17, no. 2, pp. 278–287, 2008. [16](#), [146](#)
- [53] Y. Suh and G. Son, “Numerical simulation of droplet deposition and self-alignment on a microstructured surface,” *Numerical Heat Transfer, Part A: Applications*, vol. 57, no. 6, pp. 415–430, 2010. [16](#), [146](#)
- [54] T. D. Blake, “The physics of moving wetting lines,” *Journal of Colloid and Interface Science*, vol. 299, no. 1, pp. 1–13, 2006. [16](#)
- [55] J. De Coninck and T. D. Blake, “Wetting and molecular dynamics simulations of simple liquids,” *Annual Review of Materials Research*, vol. 38, pp. 1–22, 2008. [16](#)
- [56] J. R. Castrejon-Pita, E. S. Betton, K. J. Kubiak, M. C. T. Wilson, and I. M. Hutchings, “The dynamics of the impact and coalescence of droplets on a solid surface,” *Biomicrofluidics*, vol. 5, no. 1, pp. 014112–014112, 2011. [16](#), [99](#), [132](#)
- [57] X. Cheng, Y. Zhu, L. Zhang, D. Zhang, and T. Ku, “Lattice boltzmann simulation of droplets coalescence in a film patterning process on nonideal surfaces,” *Computers & Fluids*, 2018. [16](#)
- [58] L. Zhang, T. Ku, X. Cheng, Y. Song, and D. Zhang, “Inkjet droplet deposition dynamics into square microcavities for oleds manufacturing,” *Microfluidics and Nanofluidics*, vol. 22, no. 4, p. 47, 2018. [16](#), [146](#), [153](#), [158](#), [212](#)
- [59] L. Zhang, X. Cheng, T. Ku, Y. Song, and D. Zhang, “Lattice boltzmann study of successive droplets impingement on the non-ideal recessed microchannel for high-resolution features,” *International Jour-*

*nal of Heat and Mass Transfer*, vol. 120, pp. 1085–1100, 2018. [16](#), [146](#), [212](#)

- [60] K. H. A. Al-Ghaithi, O. G. Harlen, N. Kapur, and M. C. T. Wilson, “Morphologies and dynamics of micro-droplet impact onto an idealised scratch,” *Journal of Fluid Mechanics*, vol. 925, p. A23, 2021. [16](#)
- [61] H. Rashidian, M. Sellier, and P. Mandin, “Dynamic wetting of an occlusion after droplet impact,” *International Journal of Multiphase Flow*, vol. 111, pp. 264–271, 2019. [16](#)
- [62] X. Frank and P. Perré, “Droplet spreading on a porous surface: A lattice boltzmann study,” *Physics of Fluids*, vol. 24, no. 4, p. 042101, 2012. [16](#), [58](#)
- [63] A. S. Joshi and Y. Sun, “Lattice boltzmann simulation of colloidal drop dynamics on patterned substrates for printable electronics fabrication,” in *2009 Flexible Electronics Displays Conference and Exhibition*, pp. 1–8. [16](#)
- [64] T. Pravinraj and R. Patrikar, “Modelling and investigation of partial wetting surfaces for drop dynamics using lattice boltzmann method,” *Applied Surface Science*, vol. 409, pp. 214–222, 2017. [16](#), [99](#), [132](#)
- [65] S. Gong and P. Cheng, “Numerical investigation of droplet motion and coalescence by an improved lattice boltzmann model for phase transitions and multiphase flows,” *Computers and Fluids*, vol. 53, 2012. [16](#)
- [66] Z. Guo and C. Shu, *Lattice Boltzmann method: and its applications in engineering*, vol. 3. World Scientific, 2013. [16](#), [43](#)

- [67] H. Huang, M. Sukop, and X. Lu, *Multiphase lattice Boltzmann methods: Theory and application*. John Wiley and Sons, 2015. [16](#), [50](#), [51](#), [54](#), [56](#), [57](#)
- [68] J. von Neumann, *The general and logical theory of automata*, pp. 1–41. Oxford, England: Wiley, 1951. [21](#)
- [69] S. Wolfram, “Statistical mechanics of cellular automata,” *Reviews of Modern Physics*, vol. 55, no. 3, pp. 601–644, 1983. [21](#)
- [70] M. Gardner, “The fantastic combinations of jhon conway’s new solitaire game’life,” *Scientific American*, vol. 223, pp. 20–123, 1970. [22](#)
- [71] M. Gardner, “Geometric fallacies: hidden errors pave the road to absurd conclusions,” *Scientific American*, vol. 224, no. 4, pp. 114–117, 1971. [22](#)
- [72] M. Gardner, “On cellular automata, self-reproduction, the garden of eden and the game” life”,” *Scientific American*, vol. 224, pp. 112–117, 1971. [22](#)
- [73] M. Gardner, “The orders of infinity, the topological nature of dimensions and “supertasks”,” *Scientific American*, vol. 224, no. 3, pp. 106–109, 1971. [22](#)
- [74] J. Hardy, Y. Pomeau, and O. De Pazzis, “Time evolution of a two-dimensional model system. i. invariant states and time correlation functions,” *Journal of Mathematical Physics*, vol. 14, no. 12, pp. 1746–1759, 1973. [23](#)

- [75] U. Frisch, B. Hasslacher, and Y. Pomeau, “Lattice-gas automata for the navier-stokes equation,” *Physical Review Letters*, vol. 56, no. 14, p. 1505, 1986. [23](#)
- [76] G. R. McNamara and G. Zanetti, “Use of the boltzmann equation to simulate lattice-gas automata,” *Physical Review Letters*, vol. 61, no. 20, pp. 2332–2335, 1988. [24](#)
- [77] F. J. Higuera and J. Jiménez, “Boltzmann approach to lattice gas simulations,” *EPL (Europhysics Letters)*, vol. 9, no. 7, p. 663, 1989. [24](#)
- [78] S. Chen, H. Chen, D. Martnez, and W. Matthaeus, “Lattice boltzmann model for simulation of magnetohydrodynamics,” *Physical Review Letters*, vol. 67, no. 27, p. 3776, 1991. [24](#)
- [79] J. M. V. A. Koelman, “A simple lattice boltzmann scheme for navier-stokes fluid flow,” *EPL (Europhysics Letters)*, vol. 15, no. 6, p. 603, 1991. [24](#)
- [80] Y. H. Qian, D. d’Humières, and P. Lallemand, “Lattice bgk models for navier-stokes equation,” *EPL (Europhysics Letters)*, vol. 17, no. 6, p. 479, 1992. [24](#), [28](#)
- [81] P. L. Bhatnagar, E. P. Gross, and M. Krook, “A model for collision processes in gases. i. small amplitude processes in charged and neutral one-component systems,” *Physical Review A*, vol. 94, no. 3, p. 511, 1954. [24](#), [27](#), [29](#)
- [82] H. Grad, “On the kinetic theory of rarefied gases,” *Communications on pure and applied mathematics*, vol. 2, no. 4, pp. 331–407, 1949. [25](#)

- [83] X. He and L.-S. Luo, “A priori derivation of the lattice boltzmann equation,” *Physical Review E*, vol. 55, no. 6, p. R6333, 1997. [27](#)
- [84] X. He and L.-S. Luo, “Theory of the lattice boltzmann method: From the boltzmann equation to the lattice boltzmann equation,” *Physical Review E*, vol. 56, no. 6, p. 6811, 1997. [27](#)
- [85] S. Chapman and T. G. Cowling, *The mathematical theory of non-uniform gases*. Cambridge, England: The University press, 1939. [32](#)
- [86] D. d’Humières, I. Ginzburg, M. Krafczyk, P. Lallemand, L.-S. Luo, and D. Bushnell, “Multiple-relaxation-time lattice boltzmann models in 3d,” [37](#), [39](#)
- [87] Y. Wu, N. Gui, X. Yang, J. Tu, and S. Jiang, “Improved stability strategies for pseudo-potential models of lattice boltzmann simulation of multiphase flow,” *International Journal of Heat and Mass Transfer*, vol. 125, pp. 66–81, 2018. [38](#), [62](#)
- [88] M. Geier, M. Schönherr, A. Pasquali, and M. Krafczyk, “The cumulant lattice boltzmann equation in three dimensions: Theory and validation,” *Computers & Mathematics with Applications*, vol. 70, no. 4, pp. 507–547, 2015. [38](#), [40](#)
- [89] Q. Liu, Y.-L. He, D. Li, and Q. Li, “Non-orthogonal multiple-relaxation-time lattice boltzmann method for incompressible thermal flows,” *International Journal of Heat and Mass Transfer*, vol. 102, pp. 1334–1344, 2016. [38](#)
- [90] M. Geier, A. Greiner, and J. G. Korvink, “Cascaded digital lattice boltzmann automata for high reynolds number flow,” *Physical Review E*, vol. 73, no. 6, p. 066705, 2006. [40](#)

- [91] L. Fei, K. H. Luo, and Q. Li, “Three-dimensional cascaded lattice boltzmann method: Improved implementation and consistent forcing scheme,” *Physical Review E*, vol. 97, no. 5, p. 053309, 2018. [40](#)
- [92] S. Ansumali and I. V. Karlin, “Entropy function approach to the lattice boltzmann method,” *Journal of Statistical Physics*, vol. 107, no. 1-2, pp. 291–308, 2002. [41](#)
- [93] I. V. Karlin, S. Succi, and S. S. Chikatamarla, “Comment on “numerics of the lattice boltzmann method: Effects of collision models on the lattice boltzmann simulations”,,” *Physical Review E*, vol. 84, no. 6, p. 068701, 2011. [41](#)
- [94] L.-S. Luo, W. Liao, X. Chen, Y. Peng, and W. Zhang, “Numerics of the lattice boltzmann method: Effects of collision models on the lattice boltzmann simulations,” *Physical Review E*, vol. 83, no. 5, p. 056710, 2011. [41](#)
- [95] F. J. Alexander, S. Chen, and J. D. Sterling, “Lattice boltzmann thermohydrodynamics,” *Physical Review E*, vol. 47, no. 4, p. R2249, 1993. [42](#)
- [96] Y. Chen, H. Ohashi, and M. Akiyama, “Thermal lattice bhatnagar-gross-krook model without nonlinear deviations in macrodynamic equations,” *Physical Review E*, vol. 50, no. 4, pp. 2776–2783, 1994. [42](#)
- [97] B. J. Palmer and D. R. Rector, “Lattice boltzmann algorithm for simulating thermal flow in compressible fluids,” *Journal of Computational Physics*, vol. 161, no. 1, pp. 1–20, 2000. [42](#)

- [98] D. H. Rothman and J. M. Keller, “Immiscible cellular-automaton fluids,” *Journal of Statistical Physics*, vol. 52, no. 3-4, pp. 1119–1127, 1988. [45](#), [48](#)
- [99] A. K. Gunstensen, D. H. Rothman, S. Zaleski, and G. Zanetti, “Lattice boltzmann model of immiscible fluids,” *Physical Review A*, vol. 43, no. 8, p. 4320, 1991. [46](#)
- [100] D. Grunau, S. Chen, and K. Eggert, “A lattice boltzmann model for multiphase fluid flows,” *Physics of Fluids A*, vol. 5, no. 10, pp. 2557–2562, 1993. [46](#)
- [101] M. Latva-Kokko and D. H. Rothman, “Diffusion properties of gradient-based lattice boltzmann models of immiscible fluids,” *Physical Review E*, vol. 71, no. 5, p. 056702, 2005. [46](#), [48](#)
- [102] H. Liu, A. J. Valocchi, and Q. Kang, “Three-dimensional lattice boltzmann model for immiscible two-phase flow simulations,” *Physical Review E*, vol. 85, no. 4, p. 046309, 2012. [49](#)
- [103] Z. Cheng, Y. Ba, J. Sun, C. Wang, S. Cai, and X. Fu, “A numerical study of droplet dynamic behaviors on a micro-structured surface using a three dimensional color-gradient lattice boltzmann model,” *Soft Matter*, vol. 14, no. 5, pp. 837–847, 2018. [49](#)
- [104] T. Akai, M. J. Blunt, and B. Bijeljic, “Pore-scale numerical simulation of low salinity water flooding using the lattice boltzmann method,” *Journal of Colloid and Interface Science*, vol. 566, pp. 444–453, 2020. [49](#)
- [105] T. Akai, B. Bijeljic, and M. J. Blunt, “Wetting boundary condition for the color-gradient lattice boltzmann method: Validation with analyt-

- ical and experimental data,” *Advances in Water Resources*, vol. 116, pp. 56–66, 2018. [49](#)
- [106] M. R. Swift, W. R. Osborn, and J. M. Yeomans, “Lattice boltzmann simulation of nonideal fluids,” *Physical Review Letters*, vol. 75, no. 5, pp. 830–833, 1995. [50](#)
- [107] J. S. Rowlinson and B. Widom, *Molecular theory of capillarity*. Courier Corporation, 2013. [50](#)
- [108] C. M. Pooley and K. Furtado, “Eliminating spurious velocities in the free-energy lattice boltzmann method,” *Physical Review E*, vol. 77, no. 4, p. 046702, 2008. [51](#)
- [109] D. J. Holdych, D. Rovas, J. G. Georgiadis, and R. O. Buckius, “An improved hydrodynamics formulation for multiphase flow lattice-boltzmann models,” *International Journal of Modern Physics C*, vol. 9, no. 08, pp. 1393–1404, 1998. [51](#)
- [110] H. Zheng, C. Shu, and Y.-T. Chew, “A lattice boltzmann model for multiphase flows with large density ratio,” *Journal of Computational Physics*, vol. 218, no. 1, pp. 353–371, 2006. [51](#)
- [111] A. Fakhari and M. H. Rahimian, “Phase-field modeling by the method of lattice boltzmann equations,” *Physical Review E*, vol. 81, no. 3, p. 036707, 2010. [52](#)
- [112] T. Inamuro, T. Ogata, S. Tajima, and N. Konishi, “A lattice boltzmann method for incompressible two-phase flows with large density differences,” *Journal of Computational Physics*, vol. 198, no. 2, pp. 628–644, 2004. [52](#)

- [113] X. He and G. D. Doolen, “Thermodynamic foundations of kinetic theory and lattice boltzmann models for multiphase flows,” *Journal of Statistical Physics*, vol. 107, no. 1-2, pp. 309–328, 2002. [52](#)
- [114] A. J. Briant, A. J. Wagner, and J. M. Yeomans, “Lattice boltzmann simulations of contact line motion. i. liquid-gas systems,” *Physical Review E*, vol. 69, no. 3, p. 031602, 2004. [52](#), [129](#)
- [115] H. Kusumaatmaja, J. Léopoldès, A. Dupuis, and J. M. Yeomans, “Drop dynamics on chemically patterned surfaces,” *EPL (Europhysics Letters)*, vol. 73, no. 5, pp. 740–746, 2006. [52](#)
- [116] J. M. Yeomans and H. Kusumaatmaja, “Modelling drop dynamics on patterned surfaces,” *Bulletin of the Polish Academy of Sciences: Technical Sciences*, pp. 203–210–203–210, 2007. [52](#)
- [117] H. Kusumaatmaja, R. J. Vrancken, C. W. M. Bastiaansen, and J. M. Yeomans, “Anisotropic drop morphologies on corrugated surfaces,” *Langmuir*, vol. 24, no. 14, pp. 7299–7308, 2008. [52](#)
- [118] M. L. Blow, H. Kusumaatmaja, and J. M. Yeomans, “Imbibition through an array of triangular posts,” *Journal of Physics: Condensed Matter*, vol. 21, no. 46, p. 464125, 2009. [52](#)
- [119] M. R. Swift, E. Orlandini, W. R. Osborn, and J. M. Yeomans, “Lattice boltzmann simulations of liquid-gas and binary fluid systems,” *Physical Review E*, vol. 54, no. 5, pp. 5041–5052, 1996. [53](#)
- [120] X. He, S. Chen, and R. Zhang, “A lattice boltzmann scheme for incompressible multiphase flow and its application in simulation of rayleigh–taylor instability,” *Journal of Computational Physics*, vol. 152, no. 2, pp. 642–663, 1999. [53](#), [54](#), [56](#)

- [121] X. He, X. Shan, and G. D. Doolen, “Discrete boltzmann equation model for nonideal gases,” *Physical Review E*, vol. 57, no. 1, p. R13, 1998. [53](#)
- [122] A. R. Davies, *The fundamental applications of single and multiphase lattice Boltzmann methods to engineering flows*. Thesis, 2004. [55](#), [76](#)
- [123] R. Zhang, X. He, and S. Chen, “Interface and surface tension in incompressible lattice boltzmann multiphase model,” *Computer Physics Communications*, vol. 129, no. 1, pp. 121–130, 2000. [55](#)
- [124] A. G. Yiotis, J. Psihogios, M. E. Kainourgiakis, A. Papaioannou, and A. K. Stubos, “A lattice boltzmann study of viscous coupling effects in immiscible two-phase flow in porous media,” *Colloids and Surfaces A: Physicochemical and Engineering Aspects*, vol. 300, no. 1-2, pp. 35–49, 2007. [57](#), [58](#)
- [125] T. Lee and L. Liu, “Lattice boltzmann simulations of micron-scale drop impact on dry surfaces,” *Journal of Computational Physics*, vol. 229, no. 20, pp. 8045–8063, 2010. [57](#)
- [126] L. Amaya-Bower and T. Lee, “Single bubble rising dynamics for moderate reynolds number using lattice boltzmann method,” *Computers & Fluids*, vol. 39, no. 7, pp. 1191–1207, 2010. [57](#)
- [127] T. Lee and C.-L. Lin, “A stable discretization of the lattice boltzmann equation for simulation of incompressible two-phase flows at high density ratio,” *Journal of Computational Physics*, vol. 206, no. 1, pp. 16–47, 2005. [57](#)
- [128] X. Shan and H. Chen, “Lattice boltzmann model for simulating flows with multiple phases and components,” *Physical Review E*, vol. 47, no. 3, pp. 1815–1815, 1993. [58](#), [60](#), [98](#)

- [129] X. Shan and H. Chen, “Simulation of nonideal gases and liquid-gas phase transitions by the lattice boltzmann equation,” *Physical Review E*, vol. 49, no. 4, p. 2941, 1994. [58](#), [98](#)
- [130] X. Shan, “Pressure tensor calculation in a class of nonideal gas lattice boltzmann models,” *Physical Review E*, vol. 77, no. 6, p. 066702, 2008. [59](#)
- [131] N. S. Martys and H. Chen, “Simulation of multicomponent fluids in complex three-dimensional geometries by the lattice boltzmann method,” *Physical Review E*, vol. 53, no. 1, pp. 743–750, 1996. [61](#), [100](#), [109](#)
- [132] Q. Kang, D. Zhang, and S. Chen, “Displacement of a three-dimensional immiscible droplet in a duct,” *Journal of Fluid Mechanics*, vol. 545, pp. 41–66, 2005. [61](#)
- [133] J. Bao and L. Schaefer, “Lattice boltzmann equation model for multi-component multi-phase flow with high density ratios,” *Applied Mathematical Modelling*, vol. 37, no. 4, pp. 1860–1871, 2013. [61](#)
- [134] C. D. Stiles and Y. Xue, “High density ratio lattice boltzmann method simulations of multicomponent multiphase transport of h2o in air,” *Computers & Fluids*, vol. 131, pp. 81–90, 2016. [61](#)
- [135] Q. Li, K. H. Luo, Q. J. Kang, Y. L. He, Q. Chen, and Q. Liu, “Lattice boltzmann methods for multiphase flow and phase-change heat transfer,” *Progress in Energy and Combustion Science*, vol. 52, pp. 62–105, 2016. [61](#), [69](#)
- [136] H. B. Callen, “Thermodynamics and an introduction to thermostatistics,” 1998. [61](#)

- [137] P. Yuan and L. Schaefer, “Equations of state in a lattice boltzmann model,” *Physics of Fluids*, vol. 18, no. 4, p. 042101, 2006. [61](#), [62](#)
- [138] Q. Li and K. H. Luo, “Thermodynamic consistency of the pseudopotential lattice boltzmann model for simulating liquid–vapor flows,” *Applied Thermal Engineering*, vol. 72, no. 1, pp. 56–61, 2014. [63](#)
- [139] C. E. Colosqui, G. Falcucci, S. Ubertini, and S. Succi, “Mesoscopic simulation of non-ideal fluids with self-tuning of the equation of state,” *Soft Matter*, vol. 8, no. 14, pp. 3798–3809, 2012. [63](#)
- [140] Q. Li, K. H. Luo, and X. Li, “Forcing scheme in pseudopotential lattice boltzmann model for multiphase flows,” *Physical Review E*, vol. 86, no. 1, p. 016709, 2012. [64](#), [68](#)
- [141] Q. Li, K. H. Luo, and X. J. Li, “Lattice boltzmann modeling of multiphase flows at large density ratio with an improved pseudopotential model,” *Physical Review E*, vol. 87, no. 5, p. 053301, 2013. [64](#), [68](#), [204](#)
- [142] R. R. Nourgaliev, T. N. Dinh, T. G. Theofanous, and D. Joseph, “The lattice boltzmann equation method: theoretical interpretation, numerics and implications,” *International Journal of Multiphase Flow*, vol. 29, no. 1, pp. 117–169, 2003. [68](#)
- [143] L.-S. Luo, “Unified theory of lattice boltzmann models for nonideal gases,” *Physical Review Letters*, vol. 81, no. 8, pp. 1618–1621, 1998. [68](#)
- [144] Z. Guo, C. Zheng, and B. Shi, “Discrete lattice effects on the forcing term in the lattice boltzmann method,” *Physical Review E*, vol. 65, no. 4, p. 046308, 2002. [68](#)

- [145] X. He, X. Shan, and G. Doolen, “Discrete boltzmann equation model for nonideal gases,” *Physical Review E*, vol. 57, no. 1, p. R13, 1998. [68](#)
- [146] A. L. Kupershtokh, “New method of incorporating a body force term into the lattice boltzmann equation,” in *Proc. 5th International EHD Workshop, University of Poitiers, Poitiers, France*, pp. 241–246, 2004. [68](#)
- [147] H. Huang, M. Krafczyk, and X. Lu, “Forcing term in single-phase and shan-chen-type multiphase lattice boltzmann models,” *Physical Review E*, vol. 84, no. 4, p. 046710, 2011. [68](#)
- [148] D. Lycett-Brown and K. H. Luo, “Improved forcing scheme in pseudopotential lattice boltzmann methods for multiphase flow at arbitrarily high density ratios,” *Physical Review E*, vol. 91, no. 2, p. 023305, 2015. [68](#)
- [149] M. Sbragaglia, R. Benzi, L. Biferale, S. Succi, K. Sugiyama, and F. Toschi, “Generalized lattice boltzmann method with multirange pseudopotential,” *Physical Review E*, vol. 75, no. 2, p. 026702, 2007. [68](#)
- [150] S. F. Kharmiani, H. Niazmand, and M. Passandideh-Fard, “An alternative high-density ratio pseudo-potential lattice boltzmann model with surface tension adjustment capability,” *Journal of Statistical Physics*, 2019. [68](#)
- [151] Q. Li and K. H. Luo, “Achieving tunable surface tension in the pseudopotential lattice boltzmann modeling of multiphase flows,” *Physical Review E*, vol. 88, no. 5, p. 053307, 2013. [68](#)

- [152] A. Xu, T. S. Zhao, L. An, and L. Shi, “A three-dimensional pseudo-potential-based lattice boltzmann model for multiphase flows with large density ratio and variable surface tension,” *International Journal of Heat and Fluid Flow*, vol. 56, pp. 261–271, 2015. [68](#)
- [153] S. Ammar, G. Pernaudat, and J.-Y. Trépanier, “A multiphase three-dimensional multi-relaxation time (mrt) lattice boltzmann model with surface tension adjustment,” *Journal of Computational Physics*, vol. 343, pp. 73–91, 2017. [68](#)
- [154] X. Shan, “Analysis and reduction of the spurious current in a class of multiphase lattice boltzmann models,” *Physical Review E*, vol. 73, no. 4, p. 047701, 2006. [68](#)
- [155] R. Zhang and H. Chen, “Lattice boltzmann method for simulations of liquid-vapor thermal flows,” *Physical Review E*, vol. 67, no. 6, p. 066711, 2003. [69](#)
- [156] Q. Li, Q. J. Kang, M. M. Francois, Y. L. He, and K. H. Luo, “Lattice boltzmann modeling of boiling heat transfer: The boiling curve and the effects of wettability,” *International Journal of Heat and Mass Transfer*, vol. 85, pp. 787–796, 2015. [69](#)
- [157] Q. Li, P. Zhou, and H. J. Yan, “Pinning–depinning mechanism of the contact line during evaporation on chemically patterned surfaces: A lattice boltzmann study,” *Langmuir*, vol. 32, no. 37, pp. 9389–9396, 2016. [69](#), [132](#), [196](#), [197](#)
- [158] Y. Yu, Q. Li, C. Q. Zhou, P. Zhou, and H. J. Yan, “Investigation of droplet evaporation on heterogeneous surfaces using a three-dimensional thermal multiphase lattice boltzmann model,” *Applied*

- Thermal Engineering*, vol. 127, pp. 1346–1354, 2017. [69](#), [132](#), [196](#), [197](#)
- [159] W.-Z. Yuan and L.-Z. Zhang, “Pinning–depinning mechanisms of the contact line during evaporation of microdroplets on rough surfaces: A lattice boltzmann simulation,” *Langmuir*, vol. 34, no. 26, pp. 7906–7915, 2018. [69](#), [196](#)
- [160] Q. Li, Q. J. Kang, M. M. Francois, and A. J. Hu, “Lattice boltzmann modeling of self-propelled leidenfrost droplets on ratchet surfaces,” *Soft Matter*, vol. 12, no. 1, pp. 302–312, 2016. [69](#), [196](#), [197](#), [198](#)
- [161] Q. Li, P. Zhou, and H. J. Yan, “Improved thermal lattice boltzmann model for simulation of liquid-vapor phase change,” *Physical Review E*, vol. 96, no. 6, p. 063303, 2017. [69](#), [197](#)
- [162] A. Zarghami, N. Looije, and H. Van den Akker, “Assessment of interaction potential in simulating nonisothermal multiphase systems by means of lattice boltzmann modeling,” *Physical Review E*, vol. 92, no. 2, p. 023307, 2015. [69](#)
- [163] W. Yang, H. Huang, and W. Yan, “Thermal lattice boltzmann simulation of evaporating thin liquid film for vapor generation,” *Applied Sciences*, vol. 8, no. 5, p. 798, 2018. [69](#)
- [164] S. Sohrabi and Y. Liu, “Modeling thermal inkjet and cell printing process using modified pseudopotential and thermal lattice boltzmann methods,” *Physical Review E*, vol. 97, no. 3-1, pp. 033105–033105, 2018. [69](#)
- [165] D. L. Albernaz, G. Amberg, and M. Do-Quang, “Simulation of a suspended droplet under evaporation with marangoni effects,” *Interna-*

*tional Journal of Heat and Mass Transfer*, vol. 97, pp. 853–860, 2016.  
[69](#), [196](#)

- [166] S. Dou and L. Hao, “Numerical study of droplet evaporation on heated flat and micro-pillared hydrophobic surfaces by using the lattice boltzmann method,” *Chemical Engineering Science*, vol. 229, p. 116032, 2021. [69](#), [196](#)
- [167] G. Hazi and A. Markus, “On the bubble departure diameter and release frequency based on numerical simulation results,” *International Journal of Heat and Mass Transfer*, vol. 52, no. 5, pp. 1472–1480, 2009. [69](#)
- [168] A. Márkus and G. Házi, “Simulation of evaporation by an extension of the pseudopotential lattice boltzmann method: A quantitative analysis,” *Physical Review E*, vol. 83, no. 4, p. 046705, 2011. [69](#), [70](#)
- [169] Q. Li and K. H. Luo, “Effect of the forcing term in the pseudopotential lattice boltzmann modeling of thermal flows,” *Physical Review E*, vol. 89, no. 5, p. 053022, 2014. [70](#)
- [170] P. A. Skordos, “Initial and boundary conditions for the lattice boltzmann method,” *Physical Review E*, vol. 48, no. 6, p. 4823, 1993. [76](#)
- [171] A. J. C. Ladd, “Numerical simulations of particulate suspensions via a discretized boltzmann equation. part 1. theoretical foundation,” *Journal of Fluid Mechanics*, vol. 271, pp. 285–309, 1994. [76](#)
- [172] T. Inamuro, M. Yoshino, and F. Ogino, “A non-slip boundary condition for lattice boltzmann simulations,” *Physics of Fluids*, vol. 7, no. 12, pp. 2928–2930, 1995. [76](#)

- [173] D. R. Noble, S. Chen, J. G. Georgiadis, and R. O. Buckius, “A consistent hydrodynamic boundary condition for the lattice boltzmann method,” *Physics of Fluids*, vol. 7, no. 1, pp. 203–209, 1995. [76](#)
- [174] Q. Zou and X. He, “On pressure and velocity boundary conditions for the lattice boltzmann bgk model,” *Physics of Fluids*, vol. 9, no. 6, pp. 1591–1598, 1997. [76](#), [79](#)
- [175] M. Bouzidi, M. Firdaouss, and P. Lallemand, “Momentum transfer of a boltzmann-lattice fluid with boundaries,” *Physics of Fluids*, vol. 13, no. 11, pp. 3452–3459, 2001. [76](#)
- [176] G. Zhao-Li, Z. Chu-Guang, and S. Bao-Chang, “Non-equilibrium extrapolation method for velocity and pressure boundary conditions in the lattice boltzmann method,” *Chinese Physics*, vol. 11, no. 4, p. 366, 2002. [76](#)
- [177] Z. Guo, C. Zheng, and B. Shi, “An extrapolation method for boundary conditions in lattice boltzmann method,” *Physics of Fluids*, vol. 14, no. 6, pp. 2007–2010, 2002. [76](#)
- [178] P. Lallemand and L.-S. Luo, “Lattice boltzmann method for moving boundaries,” *Journal of Computational Physics*, vol. 184, no. 2, pp. 406–421, 2003. [76](#)
- [179] A. A. Mohamad and S. Succi, “A note on equilibrium boundary conditions in lattice boltzmann fluid dynamic simulations,” *The European Physical Journal Special Topics*, vol. 171, no. 1, pp. 213–221, 2009. [76](#)
- [180] X. He, Q. Zou, L.-S. Luo, and M. Dembo, “Analytic solutions of simple flows and analysis of nonslip boundary conditions for the lattice

boltzmann bgk model,” *Journal of Statistical Physics*, vol. 87, no. 1, pp. 115–136, 1997. [76](#)

[181] J. Latt, B. Chopard, O. Malaspinas, M. Deville, and A. Michler, “Straight velocity boundaries in the lattice boltzmann method,” *Physical Review E*, vol. 77, no. 5, p. 056703, 2008. [76](#)

[182] R. W. Nash, H. B. Carver, M. O. Bernabeu, J. Hetherington, D. Groen, T. Krüger, and P. V. Coveney, “Choice of boundary condition for lattice-boltzmann simulation of moderate-reynolds-number flow in complex domains,” *Physical Review E*, vol. 89, no. 2, p. 023303, 2014. [76](#)

[183] Q. Lou, Z. Guo, and B. Shi, “Evaluation of outflow boundary conditions for two-phase lattice boltzmann equation,” *Physical Review E*, vol. 87, no. 6, p. 063301, 2013. [76](#)

[184] S. H. Kim and H. Pitsch, “A generalized periodic boundary condition for lattice boltzmann method simulation of a pressure driven flow in a periodic geometry,” *Physics of Fluids*, vol. 19, no. 10, p. 108101, 2007. [77](#)

[185] D. P. Ziegler, “Boundary conditions for lattice boltzmann simulations,” *Journal of Statistical Physics*, vol. 71, no. 5, pp. 1171–1177, 1993. [78](#)

[186] M. Hecht and J. Harting, “Implementation of on-site velocity boundary conditions for d3q19 lattice boltzmann simulations,” *Journal of Statistical Mechanics: Theory and Experiment*, vol. 2010, no. 01, p. P01018, 2010. [79](#)

[187] Q. Zhang, C. Zhu, and M. Zhu, “Three-dimensional numerical simulation of droplet evaporation using the lattice boltzmann method

- based on gpu-cuda accelerated algorithm,” *Communications in Computational Physics*, vol. 23, no. 4, pp. 1150–1166, 2018. [85](#)
- [188] F. M. White and I. Corfield, *Viscous fluid flow*, vol. 3. McGraw-Hill New York, 2006. [92](#)
- [189] R. Benzi, L. Biferale, M. Sbragaglia, S. Succi, and F. Toschi, “Mesoscopic modeling of a two-phase flow in the presence of boundaries: The contact angle,” *Physical Review E*, vol. 74, no. 2, p. 021509, 2006. [99](#), [100](#), [101](#), [105](#), [109](#), [132](#)
- [190] K. J. Kubiak and T. G. Mathia, “Anisotropic wetting of hydrophobic and hydrophilic surfaces—modelling by lattice boltzmann method,” *Procedia Engineering*, vol. 79, no. Supplement C, pp. 45–48, 2014. [99](#)
- [191] P. Raiskinmäki, A. Koponen, J. Merikoski, and J. Timonen, “Spreading dynamics of three-dimensional droplets by the lattice-boltzmann method,” *Computational Materials Science*, vol. 18, no. 1, pp. 7–12, 2000. [99](#), [100](#), [109](#)
- [192] Y. Zhu, M. Shan, Y. Yang, Q. Han, C. Zhu, and X. Zhang, “Effect of wettability on collapsing cavitation bubble near solid surface studied by multi-relaxation-time lattice boltzmann model,” *Applied Sciences*, vol. 8, no. 6, 2018. [99](#), [100](#), [104](#)
- [193] S. Son, L. Chen, Q. Kang, D. Derome, and J. Carmeliet, “Contact angle effects on pore and corner arc menisci in polygonal capillary tubes studied with the pseudopotential multiphase lattice boltzmann model,” *Computation*, vol. 4, no. 1, 2016. [99](#), [104](#)

- [194] F. F. Jackson, K. J. Kubiak, M. C. T. Wilson, M. Molinari, and V. Stetsyuk, “Droplet misalignment limit for inkjet printing into cavities on textured surfaces,” *Langmuir*, 2019. [99](#)
- [195] S. Khajepour, J. Cui, M. Dewar, and B. Chen, “A study of wall boundary conditions in pseudopotential lattice boltzmann models,” *Computers & Fluids*, 2018. [99](#), [104](#), [105](#)
- [196] Q. Li, K. H. Luo, Q. J. Kang, and Q. Chen, “Contact angles in the pseudopotential lattice boltzmann modeling of wetting,” *Physical Review E*, vol. 90, no. 5, p. 053301, 2014. [99](#), [100](#), [102](#), [104](#), [113](#)
- [197] H. Ding and P. D. M. Spelt, “Wetting condition in diffuse interface simulations of contact line motion,” *Physical Review E*, vol. 75, no. 4, p. 046708, 2007. [101](#)
- [198] K. Connington and T. Lee, “Lattice boltzmann simulations of forced wetting transitions of drops on superhydrophobic surfaces,” *Journal of Computational Physics*, vol. 250, pp. 601–615, 2013. [102](#)
- [199] M. C. Sukop and D. T. J. Thorne, *Lattice Boltzmann Modeling*. Springer, Berlin, Heidelberg: Springer, Berlin, Heidelberg, 2006. [104](#), [105](#)
- [200] A. Ghassemi and A. Pak, “Numerical study of factors influencing relative permeabilities of two immiscible fluids flowing through porous media using lattice boltzmann method,” *Journal of Petroleum Science and Engineering*, vol. 77, no. 1, pp. 135–145, 2011. [104](#)
- [201] L. Chen, Q. Kang, Y. Mu, Y.-L. He, and W.-Q. Tao, “A critical review of the pseudopotential multiphase lattice boltzmann model: Methods

- and applications,” *International Journal of Heat and Mass Transfer*, vol. 76, pp. 210–236, 2014. [104](#)
- [202] L. Wang, H.-b. Huang, and X.-Y. Lu, “Scheme for contact angle and its hysteresis in a multiphase lattice boltzmann method,” *Physical Review E*, vol. 87, no. 1, p. 013301, 2013. [116](#)
- [203] D. B. van Dam and C. Le Clerc, “Experimental study of the impact of an ink-jet printed droplet on a solid substrate,” *Physics of Fluids*, vol. 16, no. 9, pp. 3403–3414, 2004. [118](#)
- [204] A. J. Briant and J. M. Yeomans, “Lattice boltzmann simulations of contact line motion. ii. binary fluids,” *Physical Review E*, vol. 69, no. 3, p. 031603, 2004. [129](#)
- [205] J. C. Bird, S. Mandre, and H. A. Stone, “Short-time dynamics of partial wetting,” *Physical Review Letters*, vol. 100, no. 23, p. 234501, 2008. [129](#)
- [206] K. G. Winkels, J. H. Weijs, A. Eddi, and J. H. Snoeijer, “Initial spreading of low-viscosity drops on partially wetting surfaces,” *Physical Review E*, vol. 85, no. 5, p. 055301, 2012. [129](#), [131](#), [144](#)
- [207] J. R. Castrejón-Pita, K. J. Kubiak, A. A. Castrejón-Pita, M. C. T. Wilson, and I. M. Hutchings, “Mixing and internal dynamics of droplets impacting and coalescing on a solid surface,” *Physical Review E*, vol. 88, no. 2, p. 023023, 2013. [132](#)
- [208] T. Lim, S. Han, J. Chung, J. T. Chung, S. Ko, and C. P. Grigoropoulos, “Experimental study on spreading and evaporation of inkjet printed pico-liter droplet on a heated substrate,” *International Journal of Heat and Mass Transfer*, vol. 52, no. 1, pp. 431–441, 2009. [137](#), [139](#)

- [209] Q. Li, Y. Yu, and K. H. Luo, “Implementation of contact angles in pseudopotential lattice boltzmann simulations with curved boundaries,” *Physical Review E*, vol. 100, no. 5, p. 053313, 2019. [141](#), [142](#)
- [210] J. Yang, L. Fei, X. Zhang, X. Ma, K. H. Luo, and S. Shuai, “Improved pseudopotential lattice boltzmann model for liquid water transport inside gas diffusion layers,” *International Journal of Hydrogen Energy*, vol. 46, no. 29, pp. 15938–15950, 2021. [142](#)
- [211] V. V. Khatavkar, P. D. Anderson, P. C. Duineveld, and H. H. E. Meijer, “Diffuse interface modeling of droplet impact on a pre-patterned solid surface,” *Macromolecular Rapid Communications*, vol. 26, no. 4, pp. 298–303, 2005. [146](#)
- [212] H. J. Subramani, T. Al-Housseiny, A. U. Chen, M. Li, and O. A. Basaran, “Dynamics of drop impact on a rectangular slot,” *Industrial & Engineering Chemistry Research*, vol. 46, no. 19, pp. 6105–6112, 2007. [146](#)
- [213] T.-M. Liou, C.-Y. Chan, and K.-C. Shih, “Study of the characteristics of polymer droplet deposition in fabricated rectangular microcavities,” *Journal of Micromechanics and Microengineering*, vol. 19, no. 6, p. 065028, 2009. [146](#)
- [214] P. Kant, A. Hazel, M. Dowling, A. B. Thompson, and A. Juel, “Sequential deposition of microdroplets on patterned surfaces,” *Soft Matter*, 2018. [146](#)
- [215] B. Kazmierski, *The Drying of Inkjet Printed Drops on Patterned Substrates*. Thesis, 2018. [195](#)

- [216] F. Ely, C. O. Avellaneda, P. Paredez, V. C. Nogueira, T. E. A. Santos, V. P. Mammanna, C. Molina, J. Brug, G. Gibson, and L. Zhao, “Patterning quality control of inkjet printed pedot:pss films by wetting properties,” *Synthetic Metals*, vol. 161, no. 19, pp. 2129–2134, 2011. [195](#)
- [217] P. J. Sáenz, A. W. Wray, Z. Che, O. K. Matar, P. Valluri, J. Kim, and K. Sefiane, “Dynamics and universal scaling law in geometrically-controlled sessile drop evaporation,” *Nature communications*, vol. 8, no. 1, pp. 1–9, 2017. [195](#)
- [218] G. Son, “Numerical simulation of microdroplet impact and evaporation on a solid surface,” *Journal of Heat Transfer*, vol. 134, no. 10, pp. 101502–101502–10, 2012. [195](#)
- [219] D. Albernaz, M. Do-Quang, and G. Amberg, “Multirelaxation-time lattice boltzmann model for droplet heating and evaporation under forced convection,” *Physical Review E*, vol. 91, no. 4, p. 043012, 2015. [196](#)
- [220] S. Gong and P. Cheng, “Lattice boltzmann simulation of periodic bubble nucleation, growth and departure from a heated surface in pool boiling,” *International Journal of Heat and Mass Transfer*, vol. 64, pp. 122–132, 2013. [197](#)
- [221] C. K. Law, “Recent advances in droplet vaporization and combustion,” *Progress in energy and combustion science*, vol. 8, no. 3, pp. 171–201, 1982. [198](#)

- [222] A. Zarghami and H. E. A. Van den Akker, “Thermohydrodynamics of an evaporating droplet studied using a multiphase lattice boltzmann method,” *Physical Review E*, vol. 95, no. 4, p. 043310, 2017. [202](#)
- [223] S. Dash and S. V. Garimella, “Droplet evaporation dynamics on a superhydrophobic surface with negligible hysteresis,” *Langmuir*, vol. 29, no. 34, pp. 10785–10795, 2013. [205](#)
- [224] C. Sodtke, V. S. Ajaev, and P. Stephan, “Evaporation of thin liquid droplets on heated surfaces,” *Heat and Mass Transfer*, vol. 43, no. 7, pp. 649–657, 2007. [205](#)
- [225] M. Gao, P. Kong, L.-X. Zhang, and J.-N. Liu, “An experimental investigation of sessile droplets evaporation on hydrophilic and hydrophobic heating surface with constant heat flux,” *International Communications in Heat and Mass Transfer*, vol. 88, pp. 262–268, 2017. [205](#)